AUSTRALIAN NATIONAL ANTARCTIC RESEARCH EXPEDITIONS

ANARE RESEARCH NOTES 69

Australian upper atmospheric and space physics research in Antarctica, 1988

Edited by Mark Conde and Helen Beggs

ANTARCTIC DIVISION
AUSTRALIA

ANARE RESEARCH NOTES (ISSN 0729-6533)

This series allows rapid publication in a wide range of disciplines. Copies of this and other *ANARE Research Notes* are available from the Antarctic Division. Any person who has participated in Australian National Antarctic Research Expeditions is invited to publish through this series. Before submitting manuscripts authors should obtain a style guide from:

The Publications Office
Antarctic Division
Channel Highway
Kingston
Tasmania 7050
Australia

Published September 1989
ISBN: 0 642 14785 X

CONTENTS

AUSTRALIAN UPPER ATMOSPHERE AND SPACE PHYSICS RESEARCH IN ANTARCTICA, 1988

edited by Mark Conde and Helen Beggs

Antarctic Division
Department of the Arts, Sport, the Environment, Tourism and Territories
Kingston, Tasmania, Australia

PREFACE

Most of the papers in this collection were presented in the solar terrestrial physics specialist lectures at the eighth Australian Institute of Physics conference held at the University of New South Wales, Sydney, between 25 and 29 January 1988. Papers 9, 16 and 17 were not presented at the conference but are considered to be of interest to scientists studying the upper atmosphere at high southern latitudes. The final two papers are an expansion of poster presentations outlining the established research facilities at Australia's four permanent stations, Macquarie Island, Mawson, Davis and Casey. In particular, the last section is intended to indicate to researchers the type of data available from routine observatory style experiments, and the provision of timing and data logging facilities for those planning to establish experiments in Antarctica.

The majority of papers are preliminary and are intended as a summary of current directions of Australian upper atmospheric and space physics research in Antarctica. It is anticipated that the results will appear in appropriate journals.

1. THE WORLD IONOSPHERE-THERMOSPHERE STUDY

K.D. Cole[1] and C.H. Liu[2]

[1]Department of Physics
La Trobe University
Bundoora Vic 3083
Australia

[2]Department of Electrical and Computer Engineering
University of Illinois
USA

ABSTRACT

The World Ionosphere-Thermosphere Study (WITS) is an international interdisciplinary program of research organised by the Scientific Committee on Solar-Terrestrial Physics (SCOSTEP). WITS is a 3-year program that started 1 July 1987, and will continue until December 1989. Its aim is to increase substantially our understanding of the global dynamics of the ionosphere and thermosphere as a coupled system and also of the irregularities in the ionosphere. The study will include coupling with the magnetosphere and lower atmosphere.

1.1 GLOBAL IONOSPHERE/THERMOSPHERE DYNAMICS

Under this heading come many interrelated studies including inputs from energy from the Sun (via EUV radiation), from the solar wind (via polar electrodynamic processes), from the magnetosphere (generally energetic particles), from the lower atmosphere (via tides and planetary-scale and acoustic gravity waves) and from meteorites. The dynamic and aeronomical interactions between ionised and neutral species in the region are also included. These studies should incorporate the asymmetries of the geomagnetic field vis a vis the asymmetries of the thermosphere and atmosphere generally.

1.2 IONOSPHERIC IRREGULARITIES

Ionospheric inhomogeneities are created in a wide range of temporal and spatial scales. These include field-aligned irregularities in equatorial, polar and mid-latitude regions; irregularities caused by acoustic gravity waves (e.g. travelling ionospheric disturbances (TIDs)); hydromagnetic waves and a variety of plasma instabilities. The source of energy and the conditions and mechanisms of formation and their differing manifestations in different parts of the globe need further elucidation.

1.3 PROJECTS

As part of the project plan of conducting WITS in manageable units, the following projects have either been established or are being incorporated in WITS.

1.3.1 *Global Ionosphere-Thermosphere Coupling and Dynamics (GITCAD)*

GITCAD involves the study (and subsequent analysis and modelling) on a near-global scale of the response of the upper thermosphere and *F* region ionospheric plasma to forcing by solar EUV and precipitating energetic particles (auroral zone and low latitude), the long-range propagation of disturbances via winds, waves and fields and the effects of coupling between the thermosphere and ionosphere during these periods.

1.3.2 *Lower Thermosphere Coupling Study (LTCS)*

LTCS is a co-ordinated investigation of the lower thermosphere (80-150 km), combining observational and numerical modelling efforts with the ultimate goal of better understanding the dynamic and electrodynamic processes coupling the mesosphere, lower thermosphere and upper thermosphere atmospheric regions.

1.3.3 *World Acoustic Gravity Wave Study (WAGS)*

WAGS is to study the global generation and propagation of gravity waves in the ionosphere. Efforts will be concentrated on the identification of the cause-effect relation for aurora-generated TIDs, and the relation of *F* region gravity waves and the gravity wave spectra generated in the lower atmosphere.

1.3.4 *The Sundial Program*

Sundial is a global-scale program focused on advancing fundamental understanding and predictive capabilities relevant to ionospheric phenomena at all points and at all times. The effort systematically combines theoretical and empirical modelling with measurements that include a global network of seventy ionospheric monitoring stations. Solar, interplanetary, magnetospheric and thermospheric data are also obtained in campaigns of a minimum of 8 days' duration, which are scheduled every 9 months with specific scientific rationale applied to this ascending phase of the solar cycle.

1.3.5 *Global Irregularity Study*

This is a global study of the sources, evolution and decay of irregularities with scale sizes ranging from hundreds of kilometres to a few metres. Campaigns for high-latitude plasma structures and low- and mid-latitude plasma irregularities will be conducted.

1.3.6 *Ionospheric Perturbations and Geomagnetic Pulsations*

Occasionally, clear associations of oscillations of ionospheric parameters (e.g. the phase-height of isopycnic levels) with the oscillation of the geomagnetic field at the ground are observed. This clear association of a known cause and a known effect provides a powerful opportunity to test basic theory for a class of ionospheric disturbance in which the cause is not only known but independently observable.

1.3.7 *Solar Activity-Induced Variations in the Ionosphere and Thermosphere*

The project will make use of existing instruments to measure the solar soft *X*-ray flux (1-8 angstroms) and UV spectral irradiance (120-400 nm). The EUV flux will be modelled by using the coronal *X* ray and *F* 10 data to estimate the coronal EUV fluxes and by using the chromospheric Mg II *h* and *k* lines at 280 nm to estimate the chromospheric EUV flux on the basis of relations derived from current Atmospheric Explorer (AE)-E EUV measurements and soft *X*-ray and Mg II *h* and *k* line data.

1.3.8 *General Real-Time Support of WITS Projects*

The Space Environment Services Centre (Boulder, Colorado) is a 24-hour real-time space environment monitoring and forecasting centre that is operated jointly by the National Oceanic and Atmospheric Administration (US Department of Commerce) and the US Air Force Air Weather Service. Its objective is support of other projects.

Its organisers anticipate that WITS will not only lead to deeper understanding of physical processes in the ionosphere/thermosphere system, but will also usher in improvements in

communications at all frequencies, from VLF to SHF, based upon predictions of ionospheric irregularities and better ionospheric models. Such applications are expected to emerge in techniques of mineral exploration, navigation, transmission of time and frequency standards, ionospheric prediction and forecasting, HF remote sensing, VHF and *S* band remote sensing, radio astronomy and plasma physics.

At the recent meeting of the International Union of Geodesy and Geophysics (IUGG) in Vancouver, Canada, a WITS workshop outlined outstanding problems to be addressed in the next 3 years. At the 1989 meeting of the International Association of Geomagnetism and Aeronomy (IAGA) at Exeter, UK, scientific results of WITS projects will be presented.

Further information on WITS projects may be obtained from the SCOSTEP Secretariat, Department of Electrical and Computer Engineering, University of Illinois, 1406 W. Green Street, Urbana, IL 61801.

2. A NEW CONCEPT OF THE SOLAR CYCLE

P.R. Wilson
Department of Applied Mathematics
University of Sydney
NSW 2006
Australia

ABSTRACT

It has long been recognised that solar activity has an important influence on our terrestrial environment. Not only do solar flares give rise to particle streams which interfere with radio communication and create hazards for space exploration, but the periodic variations in activity, known as the solar cycle, apparently give rise to climatic variations which are, as yet, imperfectly understood. For example, an apparent interruption to the solar cyclic processes during the 17th century coincided with a period known as the 'Little Ice Age'. An understanding of the cycle and an ability to predict its future variations is of some importance for an understanding of our terrestrial environment.

The cycle has been defined in terms of a sequential periodic variation in sunspot numbers, the period being the interval between successive minima, and currently averaging 11.2 years. However, a number of observations have indicated that the activity cycle may begin at higher latitudes prior to the emergence of the first sunspots of the new cycle. Results from sunspot cycle 21 are reported. Taken together with earlier results, they indicate that sunspot activity is simply the major phase of a more extended cycle which begins at high latitudes prior to the maximum of a given sunspot cycle and progresses towards the equator during the next 18-22 years, merging with the conventional 'butterfly diagram' (the plot of the latitudes of emerging sunspots against time) as it enters sunspot latitudes. This extended cycle may be understood in the perspective of a model of giant convective rolls which generate dynamo waves propagating from pole to equator.

2.1 INTRODUCTION

The small overlap of successive sunspot cycles in the butterfly diagram has long been known. However, during the 1950s, coronal observers (e.g. Trellis 1957, Waldmeier 1957, Bretz and Billings 1959) noted that, in addition to the strong maxima in the emission of the 5303 (green) line at sunspot latitudes, a zone of enhanced emission appears at high latitudes in each hemisphere several years before the beginning of the sunspot cycle and migrates equatorwards, reaching latitude ~40° in coincidence with the appearance of new-cycle spots at this latitude, apparently extending the butterfly diagram back in time to higher latitudes. Similar suggestions have been made by Leroy and Noens (1983) following a study of the variance of the 5303 coronal emissivity from 1944-74.

During sunspot cycle 20, Harvey and Martin (1973), Harvey et al. (1975) and Martin and Harvey (1979) studied the properties of small magnetic bipoles without sunspots, called ephemeral regions (ERs), and found that they followed the declining number of active regions during the latter part of the cycle, although minimum occurred 1 or 2 years earlier for ERs. Further, they identified a high-latitude band of ERs in 1973 and 1975 and also noted a small but identifiable statistical tendency for the high-latitude ERs to follow the Hale-Nicholson orientation law for cycle 21 rather than 20. In a different context, Legrand and Simon (1981) noted that enhanced geomagnetic activity related to the solar cycle arises from two components, one the high-speed wind streams originating from high-latitude coronal holes and the other from sunspot activity. They pointed out that the high-latitude streams are closely related to coronal holes which form shortly after the polar field reversal and last for 9 or 10 years, suggesting that these streams mark the beginning of a new cycle. In this regard, McIntosh (private communication)

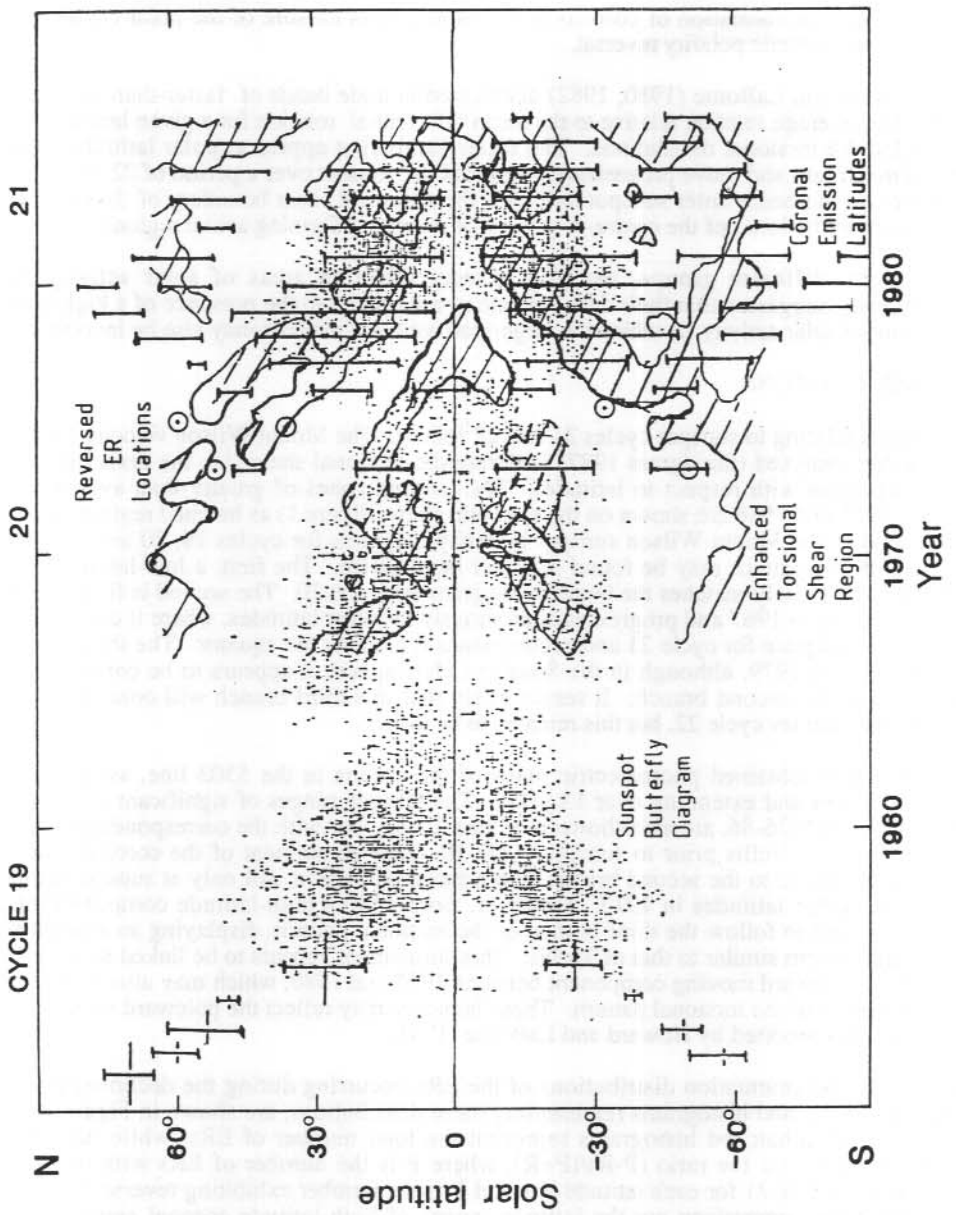

Figure 1. Superimposed on the Mount Wilson butterfly diagrams for cycles 19, 20 and 21 are the greater-than-average shear zones of the torsional oscillations pattern from 1967 to 1984, indicated by the hatched region within the contour lines, together with the green line emission maxima at high latitudes prior to cycle 19, from data given by Trellis in 1973 and from 1976 to 1986, from Altrock's data. The vertical extent of the line represents the latitude range of significant emission during a given year. The circles represent the typical locations of predominantly reversed polarity ERs observed during cycle 20 by Martin and Harvey.

suggested that the formation of coronal holes, shortly after closure of the polar crown gap, is related to the magnetic polarity reversal.

Later Howard and LaBonte (1980, 1982) discovered latitude bands of faster-than-average and slower-than-average rotation relative to the mean differential rotation for a given latitude, which they called the torsional oscillations. The faster bands first appear at polar latitudes prior to sunspot maximum and move progressively towards the equator over a period of 22 years. They noted that, as the bands enter sunspot latitudes, the poleward shear boundary of the faster band corresponds to the locus of the centre-of-gravity of the newly forming active regions.

Thus several different groups, working in very different areas of solar activity, have independently suggested that their data indicate or are related to the presence of a high latitude component of solar activity, in which the large-scale velocity patterns may also be involved.

2.2 OBSERVATIONS

New results relating to sunspot cycles 21 and 22 follow. The Mount Wilson velocity data have been further analysed (Snodgrass 1987) to derive the torsional shear (i.e. the derivative of the torsional pattern with respect to latitude). The latitude zones of greater-than-average shear between 1967 and 1986 are shown on the synoptic chart (Figure 1) as hatched regions against a background of the Mount Wilson sunspot butterfly diagrams for cycles 19, 20 and 21. Three branches of this pattern may be found in either hemisphere. The first, a low-latitude branch from 1967-79, closely matches the butterfly diagram for cycle 20. The second is first identified at high latitudes in 1967 and progresses continuously to lower latitudes, where it connects with the butterfly diagram for cycle 21 and accompanies it towards the equator. The third begins at high latitudes in 1979, although in the Southern Hemisphere it appears to be connected by a bifurcation to the second branch. It seems likely that this third branch will connect with the butterfly diagram for cycle 22, but this remains to be tested.

Again, we have obtained photoelectric maps of the corona in the 5303 line, averaged over several rotations and extending over 13 years. The latitude ranges of significant emission for 1973, and from 1976-86, are also shown in Figure 1, together with the corresponding emission data obtained by Trellis prior to sunspot cycle 19. One component of the coronal emission clearly corresponds to the second branch of the torsional pattern, not only at sunspot latitudes but also at higher latitudes in 1973. However, from 1980 a high-latitude component of the emission is seen to follow the third branch of the torsional pattern, displaying an equatorward progressing pattern similar to that of Trellis. This component appears to be linked to the second branch by a poleward moving component between 1975 and 1980, which may also be related to a similar branch of the torsional pattern. These branches may reflect the poleward motion of the large-scale flux reported by Howard and LaBonte (1981).

The latitude and orientation distributions of the ERs occurring during the declining phase of sunspot cycle 21, and histograms representing these distributions, are shown in Figure 2(a) for 1982-86. The unhatched histograms represent the total number of ERs, while the hatched histograms represent the ratio (P-R)/(P+R), where P is the number of ERs with orientation appropriate to cycle 21 for each latitude box and R is the number exhibiting reverse orientation. Also shown for comparison are the latitude ranges of high-latitude coronal emission. The observed ER populations have not been corrected for a visibility function, and thus the lower-latitude populations are more heavily weighted. Nevertheless, subsidiary high-latitude maxima or extensions of the ER populations may be distinguished between 1982 and 1985, particularly in the Southern Hemisphere, at latitudes corresponding to the coronal emission. Further, as indicated by negative values of (P-R)/(P+R) in 1983, 1985 and 1986, the high-latitude populations exhibit a preference for orientations contrary to the Hale-Nicholson law for cycle 21 but consistent with that for cycle 22.

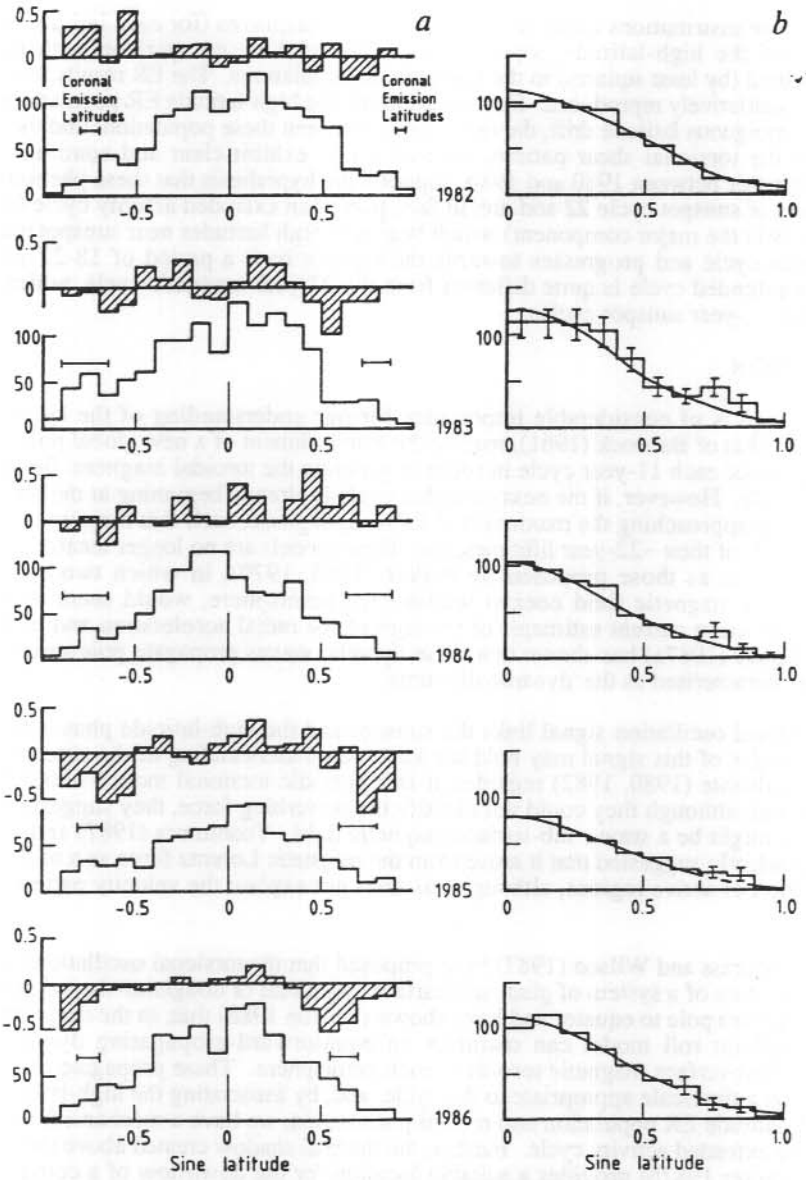

Figure 2(a).The unhatched histograms represent the total ER populations, P + R, plotted against sine latitude for the years 1982-86. The hatched histograms show the relative excess of normally oriented ERs (with respect to cycle 21), (P-R)/(P+R). Thus, negative values indicate a preference for orientations appropriate to cycle 22. Also shown are the high-latitude ranges of the coronal emission for these years.

Figure 2(b).The histograms show the populations for the sine latitude ranges of Figure 2 averaged over north and south hemispheres. The error bars, determined as described in the text, are shown for all latitude bins in 1983 and at selected latitudes in other years. The curve represents the corresponding Gaussian distributions.

In Figure 2(b) the distributions are averaged over both hemispheres (for each latitude box) and the presence of the high-latitude populations is indicated by comparison with Gaussian distributions fitted (by least squares) to the low-latitude populations. The ER results for cycle 20 are therefore qualitatively reproduced. Further, although the high-latitude ER populations do not exhibit an unambiguous latitude drift, the relationship between these populations and the coronal emission and the torsional shear pattern, both of which exhibit clear and continuous drifts towards the equator between 1980 and 1986, supports the hypothesis that these phenomena are the forerunners of sunspot cycle 22 and are, in fact, part of an extended activity cycle (of which sunspot activity is the major component) which begins at high latitudes near sunspot maximum of the previous cycle and progresses towards the equator over a period of 18-22 years. In addition, this extended cycle is quite different from the 22-year magnetic cycle, which simply consists of two 11-year sunspot cycles.

2.3 DISCUSSION

This new concept is of considerable importance for our understanding of the cycle. Some models, such as that of Babcock (1961), require the establishment of a new global poloidal field at the conclusion of each 11-year cycle in order to generate the toroidal magnetic fields for the next 11-year cycle. However, if the next extended cycle is already beginning at the poles while its predecessor is approaching the maximum of its sunspot phase, such that they are overlapped for more than half of their ~22-year lifetimes, then these models are no longer tenable. Dynamo wave models, such as those proposed by Parker (1955, 1970), in which two sub-surface toroidal bands of magnetic field coexist within each hemisphere, would seem to be more appropriate. But using current estimates of the sign of the radial acceleration and of cyclonic convection, Parker (1987a) has shown that these dynamo waves propagate polewards, a result which he has characterised as the 'dynamo dilemma'.

Since the torsional oscillation signal links the sunspot and the high-latitude phases of activity together, the origin of this signal may hold the key to an understanding of the extended cycle. Howard and LaBonte (1980, 1982) regarded it as a periodic torsional motion about the solar rotation axis, and, although they could not identify the perturbing force, they suggested that the restoring force might be a strong sub-surface magnetic field. Yoshimura (1987) and Schussler (1981) independently suggested that it arose from the magnetic Lorentz force as a back reaction to the generation of active regions, although this does not explain the velocity pattern at high-latitudes.

Elsewhere, Snodgrass and Wilson (1987) have proposed that the torsional oscillations represent the surface signature of a system of giant sub-surface azimuthal or doughnut-shaped convection rolls migrating from pole to equator and have shown (Wilson 1988) that, in the deep convection zone, the doughnut roll model can maintain an equatorward-propagating dynamo wave, generating two subsurface magnetic toroids in each hemisphere. These propagate from high to low latitudes on a timescale appropriate to the cycle, and, by associating the high-latitude toroid with the high-latitude ER population and related phenomena, we have a mechanism which may account for the extended activity cycle. Further, the thermal shadow created above the toroid (as proposed by Parker 1987b) provides a suitable location for the downflow of a convective roll system so that, as the dynamo wave drives the magnetic toroid towards the equator, it is accompanied by the moving pattern of convective rolls, at least during its high-latitude phase. In this regard, it is of interest that Kuhn et al. (1987) have suggested that the limb-temperature-minima, which they found near latitude 50° in 1983, 1984 and 1985, may be associated with the large-scale convection.

The evidence from cycle 21 supports and extends the earlier suggestions of an extended activity cycle, and, in order to place this in some perspective, we propose a system of azimuthal convective rolls forming near the poles every 11 years. This system provides the driving mechanism for a dynamo wave and generates the toroidal magnetic fields. At high-latitudes it is assumed that the rolls are complete and the magnetic toroid gives rise to only the weaker forms

of activity (the ERs and the coronal emission features). As the wave progresses to lower latitudes, the author suggests that the rolls break up into giant cells having an east-west velocity component, and the large active regions are generated from the sub-surface toroid, possibly after the manner suggested by McIntosh and Wilson (1985). Thus a coherent picture of a plausible mode of operation of the extended cycle and the large scale convection is beginning to emerge and should provide a basis for further testing during the current sunspot cycle.

2.4 ACKNOWLEDGMENTS

This work was carried out in collaboration with R.C. Altrock and K.L. Harvey of the National Solar Observatory, S.F. Martin of the Big Bear Solar Observatory and H.B. Snodgrass of Lewis and Clark College, USA. The author was supported by a grant from the Australian Research Grants Committee.

2.5 REFERENCES

Babcock, H.W. (1961). *Astrophysical Journal 133*:572-587.
Bretz, M.C. *and* Billings, D.E. (1959). *Astrophysical Journal 129*:134-145.
Harvey, K.L., Harvey, J.W. *and* Martin, S.F. (1975). *Solar Physics 40*:87-102.
Harvey, K.L. *and* Martin, S.F. (1973). *Solar Physics 32*:389-402.
Howard, R., *and* LaBonte, B.J. (1980). *Astrophysical Journal Letters 239*:L33-36.
Howard, R.F. *and* LaBonte, B.J. (1981). *Solar Physics 74*:131.
Kuhn, J.R., Libbrecht, K.G. *and* Dicke, R.H. (1987). *Nature 328*:326-327.
LaBonte, B.J. *and* Howard, R. (1982). *Solar Physics 75*:161-178.
Legrand, J.P. *and* Simon, P.A. (1981). *Solar Physics 70*:173-195.
Leroy, J.L. *and* Noens, J.C. (1983). *Astronomy and Astrophysics 20*:L1-2.
Martin, S.F. *and* Harvey, K.L. (1979). *Solar Physics 64*:93-108.
McIntosh, P.S., *and* Wilson, P.R. (1985). *Solar Physics 97*:59-79.
Parker, E.N. (1955). *Astrophysical Journal 122*:293-314.
Parker, E.N. (1970). *Annual Review of Astronomy and Astrophysics 8*:1.
Parker, E.N. (1987a). *Solar Physics 110*:11-22.
Parker, E.N. (1987b). *Astrophysical Journal 312*:868.
Schussler, M. (1981). *Astronomy and Astrophysics 94*:L17-L18.
Snodgrass, H.B. (1987). *Solar Physics 110*:35-50.
Snodgrass, H.B. *and* Wilson, P.R. (1987). *Nature 328*:696-699.
Trellis, M. (1957). *Annales d'Astrophysique Number 5*.
Waldmeier, M. (1957). *Die Sonnenkorona II*. Birkhauser, Basel.
Wilson, P.R. (1988). *Solar Physics 117*:217-226.
Yoshimura, H. (1987). *Astrophysical Journal 247*:1102-1112.

3. THE RISE OF SOLAR CYCLE NUMBER 22

R.J. Thompson
IPS Radio and Space Services
PO Box 1548
Chatswood NSW 2057
Australia

ABSTRACT

The new solar cycle, denoted cycle 22, has risen faster than any of the previous cycles, indicating that the cycle is likely to be of large amplitude. Moreover, the rapid rise suggests that the cycle could be arriving early, perhaps similar to the phase advance which occurred during cycles 1-4. The rapid early rise of cycle 22 also suggests that there might be a connection with the period of extraordinarily low geomagnetic activity centred on 1980. If this is the case, then the suppression of geomagnetic activity is the first sign of a new cycle, approximately 7 years prior to the 'official' start of the cycle. This idea is consistent with recent ideas on the solar cycle and has significant implications for geomagnetic disturbance forecasting.

3.1 INTRODUCTION

In the 16 months since solar minimum in September 1986, the new solar cycle has been rising quickly. There have been bursts of active region growth in October 1986, April-May 1987, July-August 1987, October 1987 and January 1988. The yearly smoothed sunspot number had climbed from its minimum value of 12.3 in September 1986 to 31 by July 1987. The yearly-smoothed sunspot number for January 1988 looks likely to be at least 45.

The rapid rise of the new cycle makes it an appropriate time to compare this rise with those observed for previous solar cycles. In particular, this comparison might make it possible to confirm or refute existing predictions of the eventual amplitude and timing of the peak of the cycle.

The amplitude of the new cycle has already been predicted by a variety of techniques, a summary of which has been published by Brown (1984a). The most highly-regarded of these is known as the 'precursor' technique. This operates on the notion that the solar cycle really begins some years before solar minimum, the first manifestation being the formation of stable large-scale magnetic structures known as coronal holes. Coronal holes are the origin of high speed solar wind streams which produce disturbances to the terrestrial ionosphere and magnetic field. Most variants of the precursor technique correlate the number and strength of these terrestrial disturbances with the ultimate amplitude of the solar cycle.

A large peak in magnetic disturbance occurred during the period 1982-84 after a period of extremely low geomagnetic activity centred on 1980. This peak of geomagnetic activity is generally assumed to be the precursor of the next cycle, in this case cycle 22, suggesting a cycle of large amplitude. This has led to predictions for the peak sunspot number of roughly 150.

Table 1 summarises some recent predictions of the amplitude of cycle 22 using precursor techniques (Brown 1984b, Dicke 1978, Feynman 1982, Kane 1987, Kataja 1984, Sargent 1987, Schatten 1984, Schatten and Sofia 1987, Snodgrass and Wilson 1987). These have an average of 149 which would make it considerably higher than the long-term average cycle amplitude of slightly more than 100. However, the cycle would continue the sequence of large cycles during the last five cycles. The sequence includes cycle 19 which was the largest cycle on record (peak sunspot number of 201, and cycle 21 which was the second largest on record (peak sunspot number of 165).

Table 1. Some recent predictions of the peak sunspot number for cycle 22.

Author	Predicted Sunspot Number
Brown (1984)	120
Kane (1987)	190
Kataja (1984)	140
Sargent (1987)	118
Schatten (1984)	109
Schatten and Sofia (1987)	170
Thompson (1985)	159
Thompson (1987)	163
Brown (1988)	174

3.2 THE RISE OF PREVIOUS SOLAR CYCLES

The rise (ΔR) of each historical solar cycle has been calculated here using the following formula:

$$\Delta R = \left(\frac{\sum_{i=1}^{i=N} R_i}{N} \right) - R_{min}$$

where

ΔR is the rise in the sunspot number of the cycle, N months after solar minimum,
R_i is the monthly sunspot number,
R_{min} is the yearly smoothed sunspot number at solar minimum,
and the summation is taken over the N months following the solar minimum.

The rise, as defined above, is the average sunspot number in the N months after solar minimum with the sunspot number at solar minimum having been subtracted. For this study, attention was restricted to the last twenty-one solar cycles for which there are reliable monthly sunspot numbers.

The rise of a solar cycle might be expected to correlate with the eventual amplitude of the cycle. Figure 1 illustrates how this correlation changes as the interval from solar minimum is increased from 9 to 24 months. In each panel in Figure 1, the dots represent the observed sunspot number rise and the amplitudes for each of the twenty-one solar cycles. The numbers alongside some of

the dots give the solar cycle number. The solid line in the figure is the least squares best fit to the data. The solid vertical line in the first three panels indicates the rise in the sunspot number observed for cycle 22.

The sequence of panels in Figure 1 shows that the relationship between cycle rise and the peak sunspot number is weak for the shorter intervals. For these intervals the relationship is probably influenced by factors such as the shape of the cycle, the height of the minimum and perhaps the amplitude of the previous cycle (which might advance or delay solar minimum depending on its amplitude). For longer intervals the correlation improves, and by 24 months the relationship gives a good prediction of the peak sunspot value.

Table 2 ranks historical cycles in order of their rapidity of rise according to equation (1). The five fastest rising cycles are listed in order after intervals from solar minimum of 9, 12, 15, 18 and 24 months, as well as the order at solar maximum. Each panel also gives the eventual peak sunspot number for each of the top five cycles as well as the average peak sunspot number for the five cycles.

Table 2 shows that, despite the general trend for large cycles to rise most quickly, there are some notable variations. For example, the largest cycle on record (cycle 19) did not rise particularly quickly in its early stages and does not appear in the top five listing until 15 months. Even at this stage it is ranked equal fifth. However, by 24 months it has moved to the top of the order.

Cycle 21, the second highest on record, is similar in that it does not appear in the top five until more than 18 months after solar minimum. However, by 24 months it has moved to third in the order.

Cycles 2 and 4 are particularly interesting. Cycle 2 rates as the fastest rising cycle for intervals from 9 months until 21 months, yet it was only slightly larger than average in terms of its peak sunspot number. The cycle reached a peak sunspot number of 115 making it the tenth largest of the twenty-one solar cycles. Cycle 4 also rose rapidly in its early stages, being rated second fastest from intervals from 9 months through to 24 months. Its eventual peak sunspot number is 141, making it a strong cycle, but still only sixth largest of the twenty-one cycles.

If amplitude is not the sole reason for the rapid early rise of cycles 2 and 4 then it is interesting to speculate as to the reason. Both cycles were remarkable compared with the other nineteen cycles. Cycle 2 was the shortest cycle in duration of any of the cycles, lasting 9 years. On the other hand, cycle 4 was remarkable because it was the longest cycle in duration, lasting 13.6 years in total with a very long decline (10.2 years) from solar maximum to the following solar minimum. The rise of the cycle from its minimum to maximum was in fact relatively short, taking 3.4 years.

The contrast in the duration of the two cycles suggests that the rapid rise of the cycles could result from a phase advance in the timing of solar maximum. This possibility was suggested by Dicke (1978) who noted that the short intervals between the maxima of cycles 1, 2, 3 and 4 resulted in a phase advance of solar maximum by 5.6 years. This advance was totally corrected by the long duration of the decline of cycle 4. This can be seen in Figure 2 which shows the phase, in years, of the observed solar maxima since 1750. This phase has been calculated relative to a constant cycle of 11 years in duration. The anomaly for cycles 2-5 is readily visible, with the phase of the solar maximum for cycle 4 occurring almost 6 years earlier than the average phase.

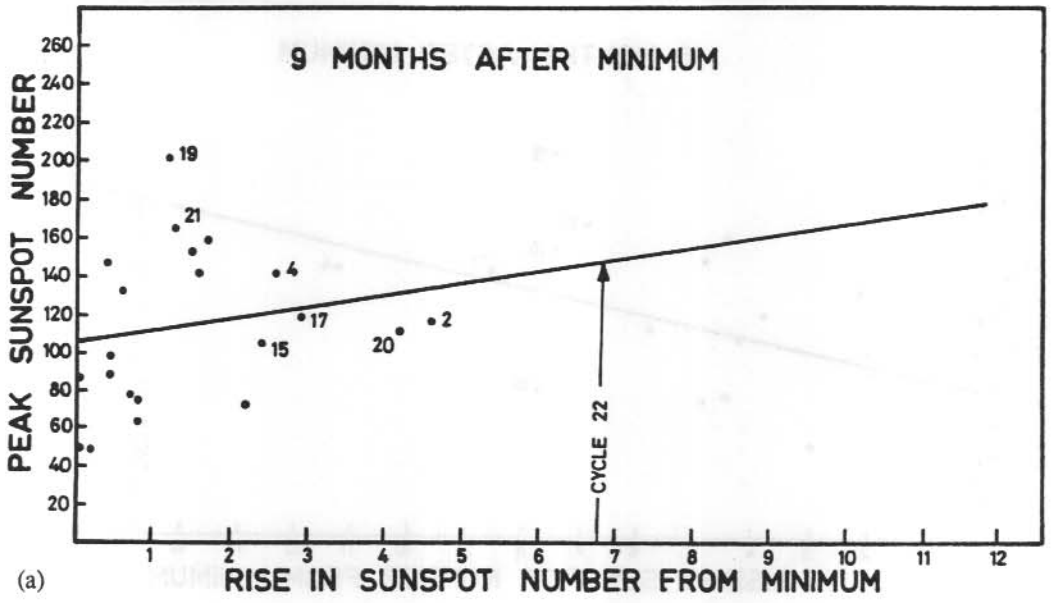

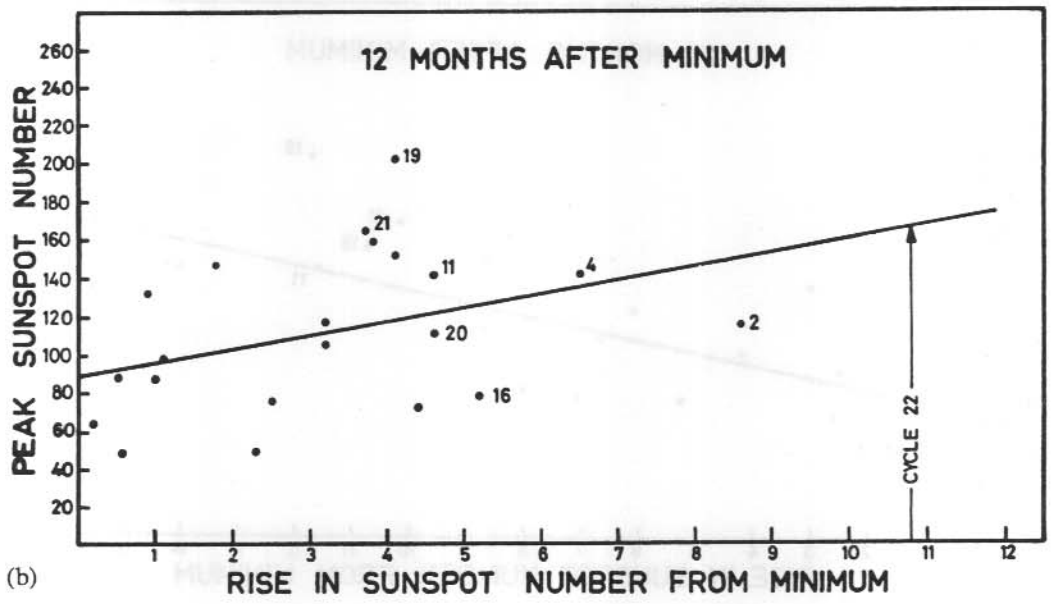

Figure 1(a - e). The relationship between the rise in the sunspot number in the early part of a solar cycle and the eventual amplitude of the cycle. The dots represent the observed rise for each of the twenty-one solar cycles. The vertical solid line in the first three panels is the rise observed for cycle 22. The solid line is the least squares best fit to the data.

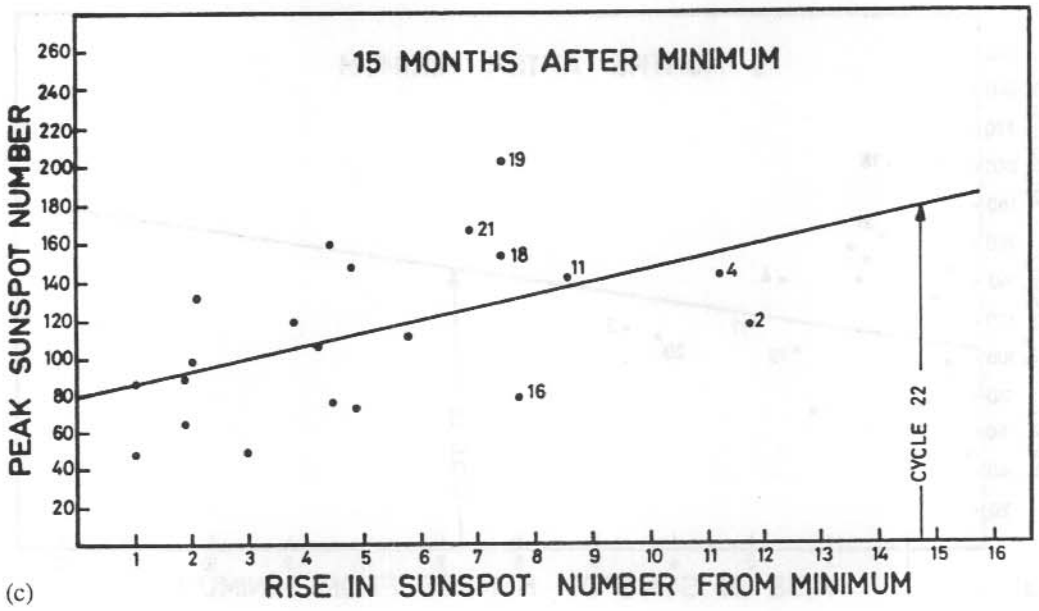
15 MONTHS AFTER MINIMUM
PEAK SUNSPOT NUMBER
RISE IN SUNSPOT NUMBER FROM MINIMUM
CYCLE 22
19
21
18
11
4
2
16

(c)

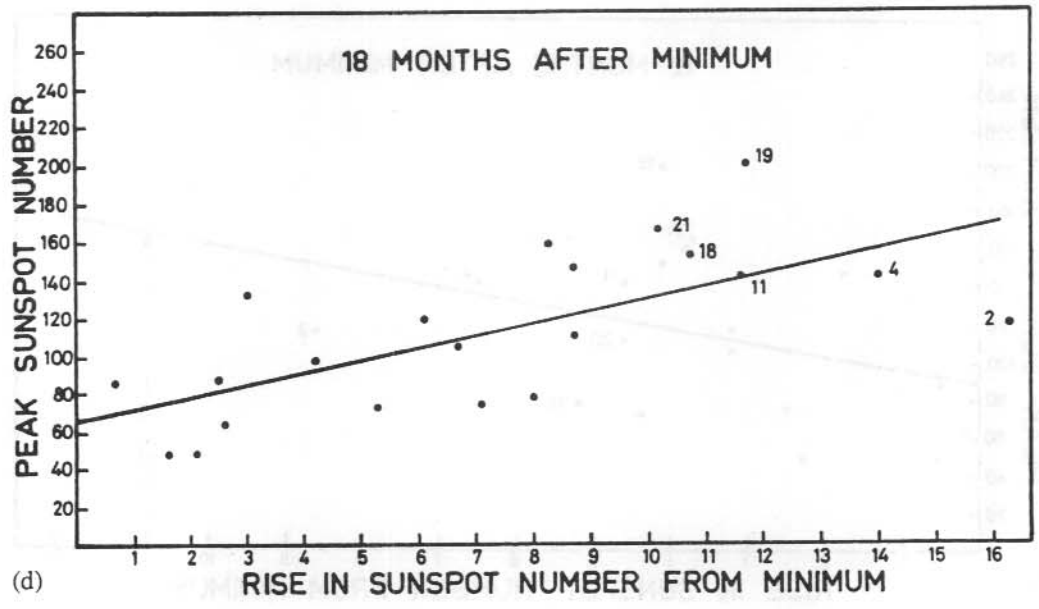
18 MONTHS AFTER MINIMUM
PEAK SUNSPOT NUMBER
RISE IN SUNSPOT NUMBER FROM MINIMUM
19
21
18
11
4
2

(d)

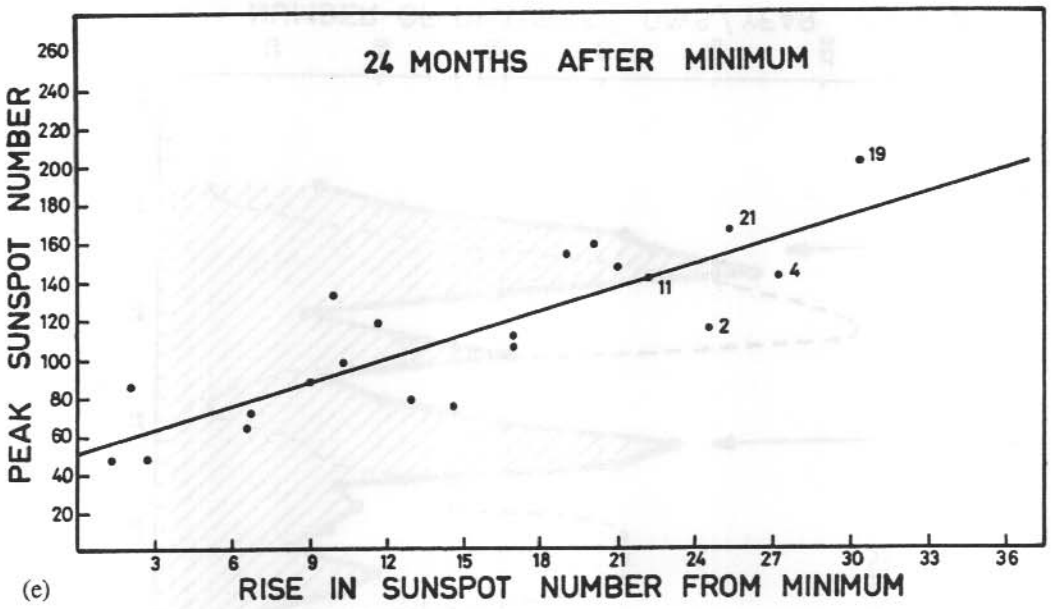

(e)

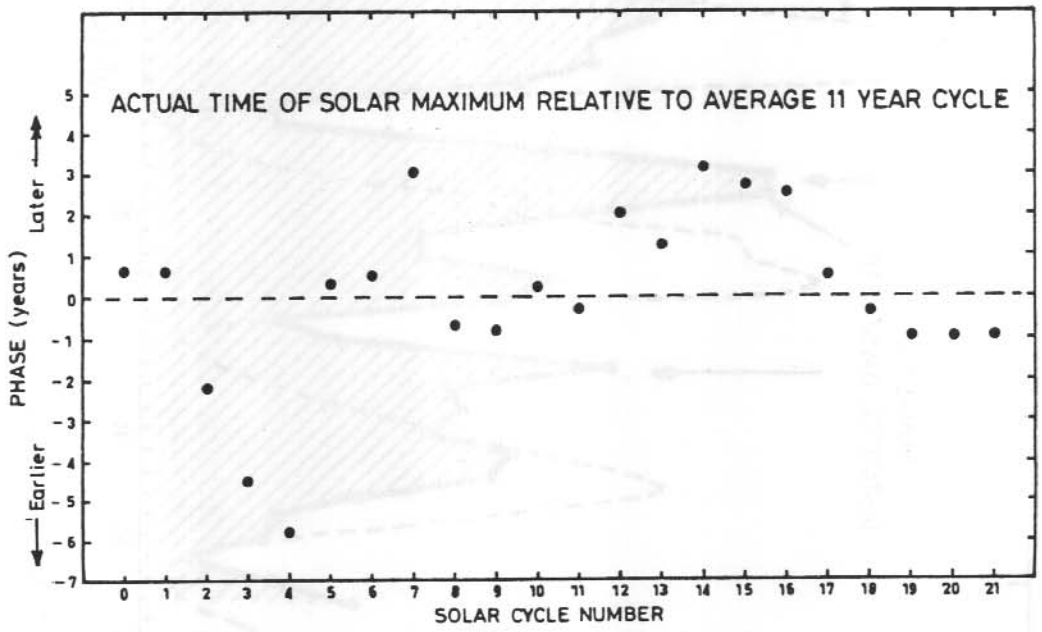

Figure 2. The difference between the actual time of solar maximum for cycles 1-21 and an exact 11 year cycle.

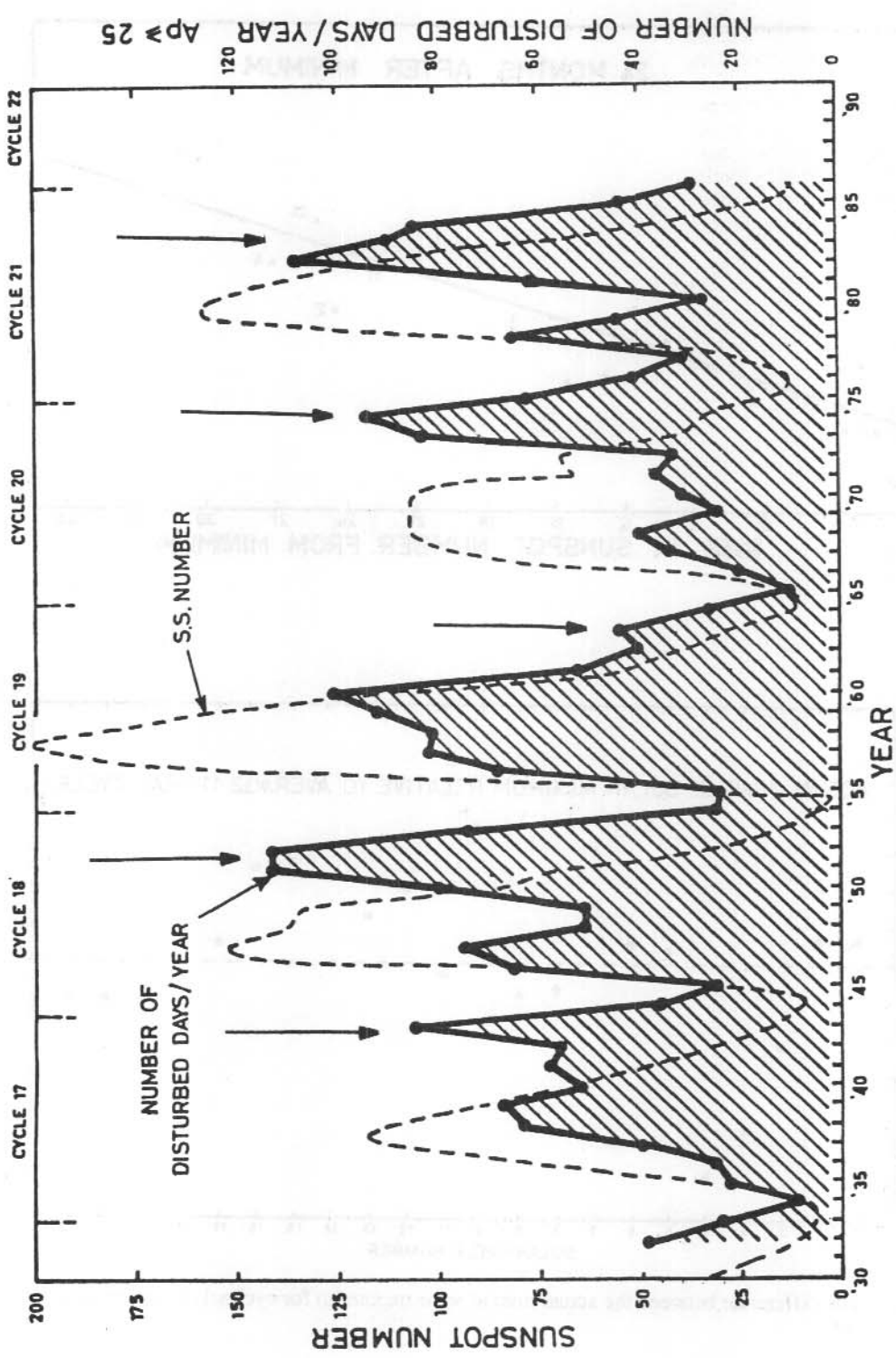

Figure 3. The variation of the yearly-averaged sunspot number since 1930 (solid line).

3.3 THE RISE OF CYCLE 22

The rapid rise of cycle 22 is strikingly illustrated in Figure 1 by the positions of the vertical bar in each of the first three panels. In each of these panels, cycle 22 is the fastest rising cycle by a substantial margin. The two most obvious reasons for the rapid rise of cycle 22 are the possibility of a very large amplitude cycle or the possibility of a phase anomaly such as that observed for cycles 2-5. The predictions for the amplitude of the cycle, listed in Table 1, have an average of 149 which would make the cycle a large one, but not outstanding.

If a large amplitude is not the only reason for the rapid early rise of cycle 22 then a phase anomaly similar to that observed during cycles 2-5 might be an explanation. The possibility that cycle 22 may be coming early is supported by the early arrival of the 'precursor' geomagnetic activity for cycle 22. This is illustrated in Figure 3 which shows the variation of smoothed sunspot number (dashed line) and the level of terrestrial magnetic disturbance during the last five solar cycles. This latter quantity has been defined by the number of days in each year for which the planetary magnetic disturbance index (Ap) equalled or exceeded a value of 25.

Figure 3 suggests that there are two components which seem to be important in determining the level of magnetic disturbance. Firstly, there is a component which varies in phase with the solar cycle producing a peak of disturbances during the high sections of each solar cycle. There is some tendency for the amplitude of this peak to correlate with the amplitude of the solar cycle (i.e. larger cycles produce more disturbances). Then there is a second component which produces a peak of disturbances in the declining phase of solar cycles which are indicated in Figure 3 by arrows. The amplitudes of these peaks do not correlate well with the amplitude of the same solar cycle but there does appear to be a correlation with the amplitude of the following solar cycle. The decomposition of the variation of the level of geomagnetic disturbance into these two components has been discussed by Feynman (1982).

An example of a large peak of disturbances can be seen during 1950-53 in the declining phase of cycle 18. This was followed by cycle 19 which reached a record peak sunspot number of 201. Likewise, there was another large peak of disturbances in 1973-75 in the declining phase of cycle 20 preceding cycle 21 which was the second highest cycle on record. On the other hand, the disturbance peak observed in the declining phase of cycle 19 was small, preceding cycle 20 which was only average in amplitude. The correlation between declining phase magnetic activity and the amplitude of the next solar cycle forms the basis of the 'precursor technique' for predicting the amplitude of a solar cycle.

The large peak of magnetic disturbances in the declining phase of cycle 21 has been used to predict a large amplitude for solar cycle 22. However, an interesting feature of this declining phase peak is that it occurred only 2.5 years after solar maximum and ended before solar minimum. This contrasts with the two earlier large precursor peaks. The peak in the declining phase of cycle 18 reached its peak some 4.5 years after solar maximum. Likewise the peak in cycle 20 occurred 5.5 years after solar maximum.

3.4 THE LOW LEVEL OF GEOMAGNETIC DISTURBANCE IN 1980

The early arrival of the cycle 22 precursor geomagnetic activity was preceded by a very unusual period of low magnetic activity centred on the year 1980. This was a year of high solar activity and was close to the maximum of the second largest cycle on record. There was no lack of solar activity such as solar flares, but the level of geomagnetic disturbance was extremely low.

Figure 4 (adapted from Feynman 1982) shows the yearly average of the aa magnetic disturbance index for each year during the period 1869-1975 plotted against the average sunspot number for that year. The dots represent the individual years with the solar maximum years indicated by a square. The dashed line is Feynman's extreme locus below which there are no data points. Feynman used this line to separate the two components of geomagnetic activity - one correlated

Table 2. The rise of historical solar cycles.

After 9 Months

Ranking	*Cycle Number*	*Sunspot Number*
1	2	116
2	20	111
3	17	119
4	4	141
5	15	105

Average Sunspot Number = 118

After 12 Months

Ranking	*Cycle Number*	*Sunspot Number*
1	2	116
2	4	141
3	16	78
4	11	141
4	20	111

Average Sunspot Number = 117

After 15 Months

Ranking	*Cycle Number*	*Sunspot Number*
1	2	116
2	4	141
3	11	141
4	16	78
5	18	152
5	19	201

Average Sunspot Number = 131

After 18 Months

Ranking	*Cycle Number*	*Sunspot Number*
1	2	116
2	4	141
3	19	201
4	11	141
5	18	152

Average Sunspot Number = 150

After 24 Months

Ranking	*Cycle Number*	*Sunspot Number*
1	19	201
2	4	141
3	21	165
4	2	116
5	11	141

Average Sunspot Number = 153

At Solar Maximum

Ranking	*Cycle Number*	*Sunspot Number*
1	19	201
2	21	165
3	3	159
4	18	152
5	8	147

Average Sunspot Number = 165

Table 3. The variation in the geoeffectiveness of solar flares.

Year	76-77	78	79	80	81	82	83	84	Total
Number of X flares	8	20	25	18	35	42	6	7	161
Number Ap>25 on Day 2	2	10	9	0	13	20	3	5	62
Expected Number Ap>25	0.5	3.3	2.9	1.1	5.2	10.3	1.5	1.5	26.3
Percent Above Expected	19%	34%	24%	-6%	22%	23%	25%	50%	22%

with sunspot number and the other a 'precursor' of future sunspot number. For any point that lies on the line, the level of geomagnetic activity would be due solely to factors associated with sunspot number. For points lying above the line the level of geomagnetic activity would be due to a combination of sunspot-related factors and precursor activity.

A 'plus' sign represents the position of the year 1980 in Figure 4. It lies considerably lower than Feynman's extreme locus making 1980 unique in more than one hundred years of magnetic records.

It is tempting to connect the extraordinarily low magnetic activity in 1980 with the early arrival of precursor geomagnetic activity in 1982 and the record rapid rise of cycle 22. For such a connection it is necessary to postulate that the first effect of a new solar cycle is not the enhancement of geomagnetic activity in the declining phase of the previous cycle. Rather, the first effect is to suppress geomagnetic activity just prior to the onset of the precursor geomagnetic activity.

The idea that information about a solar cycle is present as early as 7 years before its official start is consistent with recent ideas on the structure of the Sun and the solar cycle. Snodgrass and Wilson (1987) have suggested the existence of giant convective rolls which start at the poles and migrate to the equator in a period of 18-22 years. As they reach middle to low latitudes, the rolls are manifest in the formation of sunspot regions, this being the usual solar cycle. Prior to reaching sunspot latitudes, the convective rolls associated with a strong solar cycle evidently enhance the ability of coronal holes to penetrate to equatorial latitudes and to cause geomagnetic disturbances. Even earlier still, the effect appears to be a suppression of geomagnetic activity, perhaps by inhibiting coronal holes from reaching equatorial latitudes.

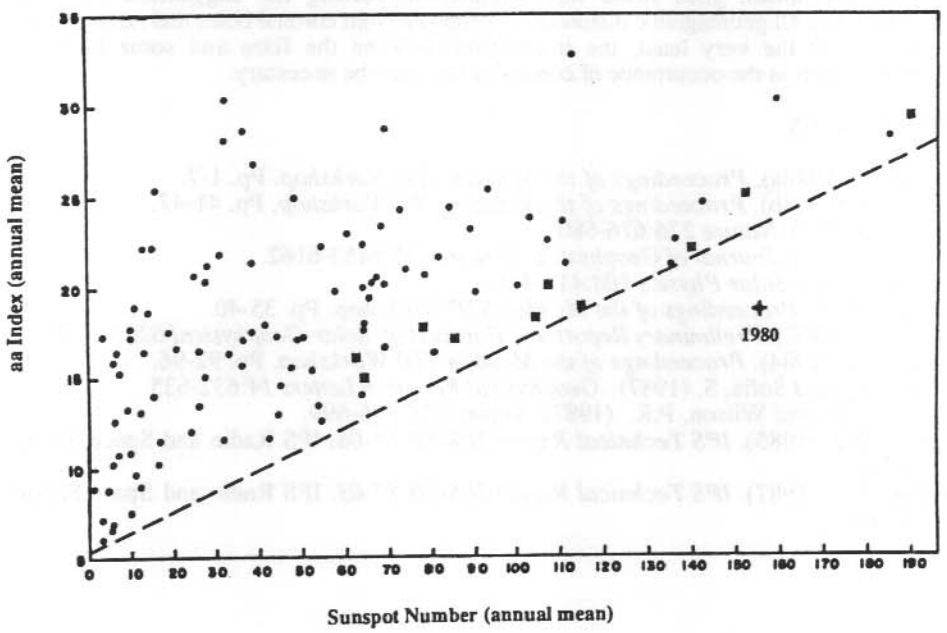

Figure 4. The yearly-averaged value of the aa index plotted against the yearly-averaged sunspot number for 1869 to 1975. The diagram is adapted from Feynman (1982). The cross indicates the position in the diagram of the year 1980.

Geomagnetic activity around the maximum of a solar cycle is usually attributed to the effects of solar flares and filament disappearances. The suggestion that geomagnetic activity near maximum can be inhibited by the coming cycle implies that either flare and filament disappearances were less frequent or else that they were less geoeffective. Table 3 suggests that the latter situation seems to have applied during 1980. The table lists the number of 'X' class X-ray flares in each year since 1976 and the number of these which were followed by a geomagnetically disturbed day on day 2 after the flare. For comparison, the background level of disturbed days is also tabulated, this being derived from the average of 100 days prior to and 100 days after the flare. The table illustrates that, for years other than 1980, there is a larger than background chance that a disturbance would follow an X class flare. The year 1980 is a striking exception. Of the 18 X class flares in that year not one was followed by a disturbed day.

Whilst 1980 might represent an extreme example of the suppression of magnetic disturbances prior to the onset of precursor geomagnetic activity, there are indications of other possible cases in Figure 3. For example, cycle 18 had a pronounced dip in geomagnetic activity near its maximum sunspot number. This preceded the onset of strong geomagnetic activity which was the precursor to the record cycle 19. Another dip occurred prior to precursor geomagnetic activity in the declining phases of cycles 18 and 20. Cycle 19 illustrates an opposite situation where the level of geomagnetic activity tracked the sunspot number quite well. In this case, the cycle was followed by a weaker cycle (number 20) for which there was little precursor geomagnetic activity.

The extraordinarily low level of geomagnetic disturbance in 1980 and the low geoeffectiveness of solar flares in 1980 have considerable implications for current ideas on the forecasting of geomagnetic disturbances from solar flare activity. Table 3 illustrates that during 1980 the chance that a geomagnetic disturbance would follow a solar flare depended on some global property of the Sun as well as the individual properties of the flare (such as location and flare energy). This notion goes some way towards supporting the suggestion by Hewish (unpublished) that all geomagnetic disturbances originate from coronal holes and none arise from solar flares. At the very least, the interaction between the flare and some large scale phenomenon (such as the occurrence of coronal holes) may be necessary.

3.5 REFERENCES

Brown, G.M. (1984a). *Proceedings of the Meudon STP Workshop*. Pp. 1-7.
Brown, G.M. (1984b). *Proceedings of the Meudon STP Workshop*. Pp. 41-47.
Dicke, R.H. (1978). *Nature 276*:676-680.
Feynman, J. (1982). *Journal of Geophysical Research 87*:6153-6162.
Kane, R.P. (1987). *Solar Physics 108*:415-416.
Kataja, E. (1984). *Proceedings of the Meudon STP Workshop*. Pp. 35-40.
Sargent, H.H. (1987). *Preliminary Report and Forecast of Solar-Geophysical 626*:12-14.
Schatten, K.H. (1984). *Proceedings of the Meudon STP Workshop*. Pp. 92-96.
Schatten, K.H. *and* Sofia, S. (1987). *Geophysical Research Letters 14*:632-635
Snodgrass, H.B. *and* Wilson, P.R. (1987). *Nature 328*:696-699.
Thompson, R.J. (1985). *IPS Technical Report IPS-TR-85-06*, IPS Radio and Space Services, Sydney.
Thompson, R.J. (1987). *IPS Technical Report IPS-TR-87-03*. IPS Radio and Space Services, Sydney.

4. RECURRENT GEOMAGNETIC STORMS

P.J. Wilkinson
IPS Radio and Space Services
PO Box 1548
Chatswood NSW 2057
Australia

ABSTRACT

Recurrent geomagnetic disturbance behaviour is readily recognised. The general properties are sufficiently well known that when a recurrent pattern has become established, its return every 27 days can be anticipated with some confidence. Identification of a solar source for recurrent activity was only achieved in the last decade, but now it is generally accepted that long-lived coronal holes are the solar source. Since this identification, modelling, theory and observations have clarified many of the properties of both the source regions and how they affect the earth.

However, it is still not possible to predict the onset times, duration and intensity of a recurrent disturbed period or the first occurrence of the period. Retrospective studies can make solar source identifications, but we still have no predictive models for these events.

The general properties of coronal holes, their interaction with the solar wind and the resultant geomagnetic activity will be reviewed to highlight the problems that must be solved before these events are fully understood.

4.1 DISCUSSION

Once a pattern has been recognised, it can usually be assumed that the source of the pattern will soon be identified. Chapman and Bartels (1940) attribute the first published description of 27 day patterns in the recurrence of geomagnetic activity to Broun, in 1858. However, at that time, the recurring nature of magnetic activity was not clear and the phenomenon did not receive much attention. Later, Maunder (1907) re-established recurrent geomagnetic activity as a geophysical feature and Chree and Stagg, using an epoch analysis method, showed both disturbed and quiet magnetic conditions repeated, in a statistical sense, every 27 days.

The Sun rotates once every 25 days. However, because of the Earth's orbital motion, the apparent rotation period observed from the Earth is 27 days. That is, it takes 27 days for a point on the solar surface at central meridian - a line joining the solar north and south poles and intersecting a line joining the centres of the Sun and the Earth - to return to this position. Bartels' charts are drawn to accentuate the 27-day observed solar rotation by stacking successive 27-day periods one below the other. When magnetic activity is summarised using the Bartels' Kp charts, repeated increases in magnetic activity every 27 days are often easy to find.

Clearly, if geomagnetic activity at the Earth recurs every 27 days, then the source of the activity probably has a solar origin. However, no reasonable solar source could be identified and Bartels (1932) was led to coin the term M-region, or mystery region, to describe the solar source of the recurrent disturbances.

Over 40 years later a likely solar source was finally identified as the M-region. The first conclusive evidence came from X-ray pictures of the Sun taken from Skylab. These full-disk solar pictures revealed immense regions of reduced X-ray flux in the solar corona and were given the name 'coronal holes.' Later studies of radio emissions from the Sun showed that depressions in radio-wave intensities, which persisted for several days, could be associated with the passage of a coronal hole across solar central meridian.

Coronal holes have many interesting properties. Most important, observationally, is their low x-ray emissions, which allowed them to be identified in the first place. However, their most important physical property is that coronal holes are associated with open magnetic field lines connecting the corona to the solar wind. Some authors consider coronal holes could be the major source for solar wind particles and, by association, the interplanetary magnetic field (IMF).

A simplistic picture of the solar wind structure can be obtained by imagining that the surface of the Sun is covered by solar wind 'sources'. A parcel of solar wind from any one source, if tracked, would travel out radially from the solar surface with a speed of about 300 km/sec. If all the parcels from a single source were joined then, because of solar rotation, they would form a spiral. This spiral form is called the Parker spiral after Parker, who first studied in detail this model for the solar wind. The IMF is frozen into the solar wind plasma and therefore also has a spiral structure. The picture is simplistic partly because we don't know with certainty what a solar wind source looks like and partly because we don't know how important interactions are within the solar wind. However, we do know that the IMF follows the Parker spiral shape closely.

Returning to coronal holes, these open magnetic field line regions are now closely associated with the emission of high speed solar wind streams that expand into the solar wind, compressing slower solar wind plasma ahead of the stream and leaving a rarefied region behind. The compression results from the presence of the IMF which prevents solar wind parcels with different velocities from passing through one another.

Coronal holes are now known to be present in the solar polar regions for most of the solar cycle. However, for high speed streams emanating from coronal holes to be of importance at the Earth, the hole must extend to low solar latitudes, typically less than 30° from the solar equator. During the declining phase of the solar cycle, coronal holes are more likely to extend into the solar equatorial region. A typical pattern develops; after solar maximum, two equatorial coronal holes develop, survive for many solar rotations until, as solar minimum approaches, one hole retracts to the pole before the structure breaks down completely. Such descriptions are phenomenological, but they offer a feel for the gross processes occurring. Knowledge of the coronal structure and, in particular, the effects at the Earth appears to be a useful precursor for solar activity prediction (Thompson 1988). The resulting high speed solar wind streams emanating from equatorial coronal holes will reach the ecliptic and will therefore interact with the Earth.

These streams are long-lived and possibly the biggest organised structures that the Earth encounters on a regular basis. They also impose order on the solar wind, a fact that can have important implications for many statistical studies.

As a first order approximation, the larger the solar wind velocity at the Earth the larger the extent of global magnetic activity. This simple statistical relationship has been established many times. Using this relationship, some reasonable conclusions can be drawn about geomagnetic storms caused by the coronal hole high speed wind streams. For instance, slower streams, which produce less compression of the solar wind, will be associated with more gradual storm onsets than storms caused by faster streams which will probably start more rapidly. Furthermore, while storm start times are roughly recurrent, they can drift from being exactly 27 days reflecting dynamic changes in the stream source.

However, the solar wind velocity association is incomplete if the effects of the IMF are ignored. The IMF can change in direction from pointing towards the Earth to pointing away from the Earth. The transition region has been called a sector boundary and the period when the IMF points predominantly in one direction is called a sector. Initially sector boundaries were interpreted as a mapping of the neutral line of the photospheric magnetic field into the solar wind. However, it is now known that the IMF is linked to the corona, not the photosphere, so the coronal emissions will carry the signature of the coronal fields. These, in turn, may be linked to

the photospheric field with the corona possibly acting as a low pass filter for the photospheric magnetic fields.

The signature of the coronal fields is carried away from the Sun by the high speed solar wind streams. A summary of stream properties is really a summary of stream interaction regions that are created by the co-rotating high speed solar wind streams. As already discussed, faster streams will compress the slower solar wind producing a collisionless interaction region dominated by magnetic fields that prevent the streams from passing through one another. This is called a co-rotating interaction region, or CIR. At the leading edge of a region there is a build-up of plasma and an associated increase in the plasma number density. At the trailing edge, the hot plasma leaves behind it a rarefied region of reduced number density.

Because the solar plasma is compressed as it interacts, the IMF sector structure will remain intact but will also be compressed.

Coronal holes are found to be located within a single magnetic sector in the corona. The resultant solar wind streams therefore carry the field signature of the coronal hole and hence of the common sector. There is no apparent physical relationship between the coronal hole and either the sector or the sector boundary.

However, as the solar wind moves away from the Sun, the faster wind stream overtakes the slower solar wind and the embedded sector boundary, so that the sector boundary and the stream interface approach one another. At the Earth, the sector boundary precedes the stream interface by, typically, a few hours to a day. The smaller the time difference, the faster the stream velocity probably is and therefore the more disturbed the magnetic field is likely to be.

The sector structure is actually associated with a current sheet that lies roughly around the solar equator. The IMF points towards the Sun on one side of the sheet and away on the other. The ecliptic is offset with respect to the equatorial current sheet so the Earth will pass through the current sheet twice each solar rotation. Passages through the current sheet equal passages through sector boundaries. They are the same thing.

We do not know what shape the current sheet has in the corona - it may be flat, or it may be warped because of the underlying photospheric magnetic fields. Either way, solar rotation exaggerates the warps and fast solar wind streams compact warps that exist to the front of them. Even if the current sheet is flat within the corona, the stream interactions will produce warps by the time the region reaches the Earth's orbit.

The dynamics of the solar wind cause sectors, sector boundaries or, more accurately the current sheet to become linked at the Earth's orbit. However, there is still one more link to consider. Why is there geomagnetic activity and why doesn't the largest solar wind velocity necessarily cause the greatest magnetic activity?

Geomagnetic activity is linked to substorm activity that, in turn, is closely related to changes in the IMF, not so much at sector boundaries which produce IMF changes perpendicular to the Earth's field, but IMF changes parallel to the earth's field. In particular, when the IMF has a component opposed to the Earth's field, usually called B_Z negative, substorms are more likely to occur. Solar wind measurements show that the larger the solar wind velocity, the larger the spectrum of fluctuations present. It now seems likely that just as the current sheet becomes compressed, so will smaller fluctuations. It is these fluctuations that produce the variations in B_Z associated with substorms and hence geomagnetic activity. Thus, by analogy, high solar wind velocity bears the same relationship to geomagnetic activity as the sunspot number does to solar activity. While being good predictors of activity, neither gives much help in understanding what happens physically.

4.2 SUMMARY

This short review has emphasised the general features of the solar wind source for recurrent geomagnetic activity. Physical concepts, based on spacecraft measurements of the Sun and solar wind, consolidate most of the known statistical properties of recurrent geomagnetic activity. However, the picture is probably still incomplete. Not all coronal holes within 30° of the solar equator produce magnetic disturbances and conversely not all fast solar wind streams necessarily originate within coronal holes. Most important, interactions between streams within the solar wind may be a more potent source for geomagnetic activity than an isolated stream involving no stream interactions. This has led some scientists to regard the co-rotating high speed solar wind stream as the natural solar wind co-ordinate system and all other solar events should map into this system.

4.3 REFERENCES

Bartels, J. (1932). Terrestrial-magnetic activity and its relations to solar phenomena. *Terrestrial Magnetism and Atmospheric Electricity 19*:1.

Broun, J.A. (1858). On certain results of magnetical observations. *Philos. Magazine 16*:81-99. In: S. Chapman and J. Bartels (Eds). *Geomagnetism*. Claredon Press.

Chapman, S. *and* Bartels, J. (1940). *Geomagnetism*. Claredon Press.

Chree, C. *and* Stagg, J. M. (1927). Recurrence phenomena in terrestrial magnetism. *Phil. Trans. London (A) 227*:21-62. In: S. Chapman and J. Bartels (Eds). *Geomagnetism*. Claredon Press.

Maunder, A.S.D. (1907). Catalogue of recurrent groups of sunspots, 1874-1906. *Greenwich Photoheliographic Results for 1907, Appendix*. In: S. Chapman and J. Bartel (Eds). *Geomagnetism*. Claredon Press.

Thompson, R.J. (1989). The amplitude of solar cycle number 22. *ANARE Research Notes* (this volume).

5. A REVIEW: REMOTE SENSING OF THE IONOSPHERE WITH ADVANCED SOUNDERS

B.L. Tedd
Department of Physics
La Trobe University
Bundoora Vic 3083
Australia

ABSTRACT

Advanced ionospheric sounders are the latest generation of instruments that sound the ionosphere by means of the coherent reflection of HF radiowaves. The Digisonde and Dynasonde are the most sophisticated of these instruments as they provide a complete description of the received ionospheric echo. These instruments and two other advanced sounders are described in this paper. Particular attention is made of their role in current ionospheric research, which includes detailed observations of ionospheric structures and motions in the polar cap.

5.1 INTRODUCTION

The conventional ionosonde has existed for over 50 years (Villard 1976) and still proves its worth in ionospheric research. The instrument provides virtual height information as a function of frequency in addition to limited amplitude and HF wave polarisation information. The design of the conventional ionosonde has improved over the years culminating in the sounders produced by the Ionospheric Prediction Service (IPS) and KEL Aerospace. These latter sounders have advanced features such as microprocessor control and high accuracy digital records.

In the 1960s researchers began to investigate how more information about the received ionospheric echo could be determined. The phase ionosonde (Whitehead and Kantarizis 1967) is able to measure the change in phase of an ionospheric echo as a function of frequency. The HF CW Doppler sounder (Watts and Davies 1960) provides information about vertical ionospheric motions by measuring the Doppler shift of the ionospheric echo. The Rinesonde (Wright and Fedor 1969) provides information about horizontal ionospheric motions by measuring complex amplitudes at spaced antennas. These developments have led to the modern advanced ionospheric sounder which is able to describe fully the ionospheric echo.

The Digisonde and Dynasonde are the two most sophisticated sounders currently deployed. These instruments provide the range, amplitude, HF phase, wave polarisation, angles of arrival and Doppler shifts of the received ionospheric echo. The features in common between the Digisonde and Dynasonde are (Reinisch 1986) a) all transmitted signals are phase coherent to allow phase measurements, b) the receiver output signal is digitised to allow the application of advanced data processing techniques, the multiplexing of data, remote data output and computer archiving of data, and c) a receiving antenna array is deployed to measure angles of arrival and polarisation.

In addition to these two instruments, other sounders with advanced capabilities exist, such as the HF radar and Disonde. This review will briefly discuss what information can be obtained from these instruments and their role in current research.

5.2 THE DIGISONDE

The Digisonde 256 (Bibl et al. 1981) was developed at the University of Lowell, USA. Instruments are currently operating at thirteen sites around the world, including one run by La Trobe University at Beveridge, near Melbourne. A worldwide network of some forty sounders is planned for the near future and will provide new inputs to the modelling of the global ionosphere.

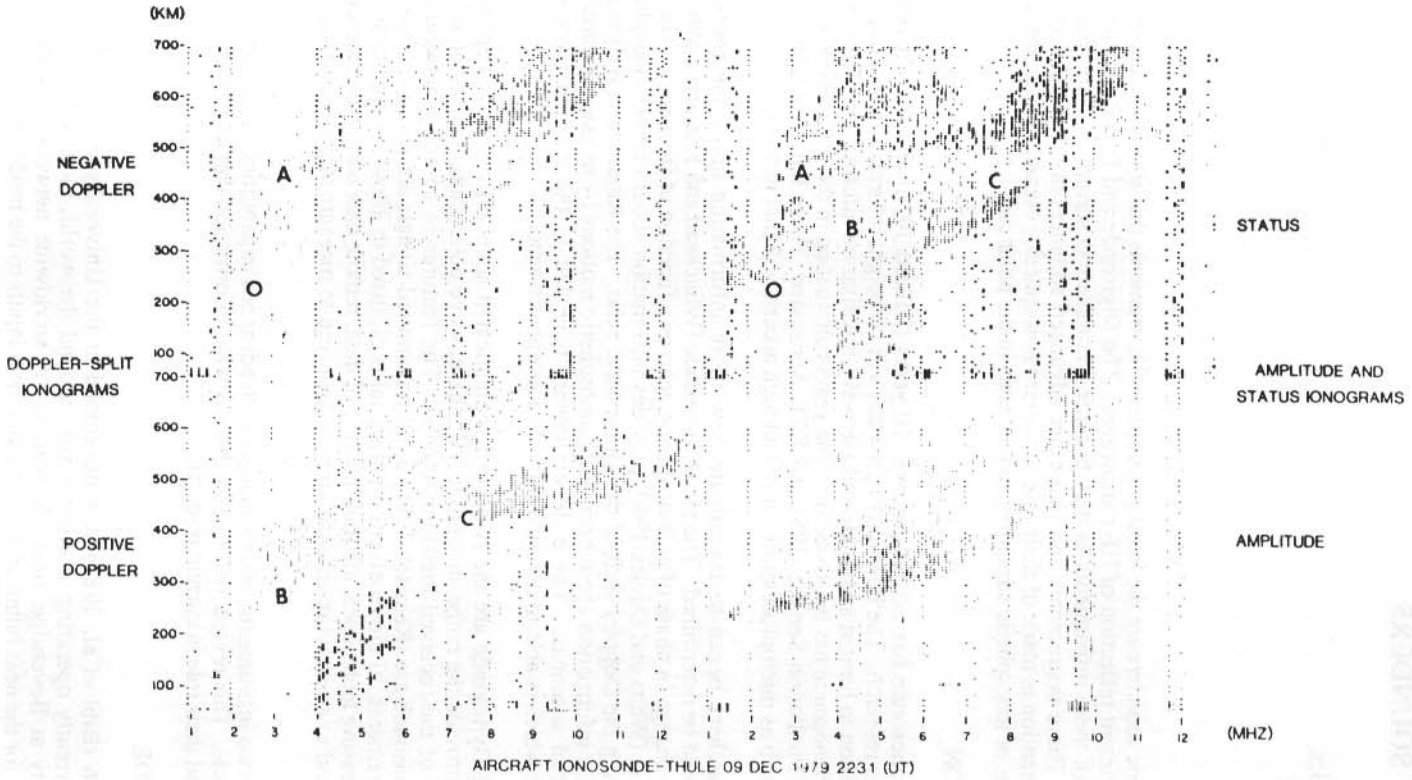

Figure 1. Typical digital amplitude ionogram for a period of steady arc drift (from Buchau et al. 1983).

The Digisonde can be operated in ionogram, Doppler-drift or fixed frequency modes. The mode, or combination of modes, is chosen to suit the ionospheric information required. The ionogram mode provides a complete description of the received ionospheric echo as a function of frequency. Ordinary and extra-ordinary wave polarisations can be distinguished as can vertical and off vertical echoes, and positive and negative Doppler shifts. Figure 1 presents ionogram mode data which represent a period of steady arc drift across the polar observing station (Buchau et al. 1983). The lower right panel is an amplitude ionogram which is printed out using an optically-weighted font which preserves digital information while providing the appearance of a standard analog ionogram. A colour-coded presentation is also available at La Trobe and has the advantage that an inexperienced eye can discern important features of the ionogram at a glance. The ionogram shows the overhead ionosphere under strong spread *F* conditions. The upper right panel is a 'status' ionogram corresponding to the amplitude ionogram below. The Doppler frequency measured in each frequency-range bin is printed. Doppler numbers 1 to 7 indicate positive Doppler, and 8 to 15 negative Doppler, both increasing with increasing numerical value. This Doppler information can be separated into negative and positive ionograms as shown in the top left and top right panels, respectively. The feature labelled O represents the overhead ionosphere, while features labelled A, B and C are patches of localised irregularities either approaching (B,C) or receding (A) from the station. The status ionogram can also provide azimuth of arrival information if some Doppler resolution is sacrificed. A very useful feature, particularly for the routine monitoring of the ionosphere, is the automatic calculation of electron density profiles from the digital ionograms (Reinisch and Huang 1983). It has been demonstrated that automatic scaling of ionograms is possible with high reliability, even under severe spread *F* conditions.

The Doppler-drift mode of the Digisonde has recently been improved and automated. Spectral analysis of the complex amplitudes of echoes received at a number of spaced antennae reveals the number and extent of simultaneously-existing reflection areas in the ionosphere. This allows the tracking of ionospheric movements or drifts. Figure 2 shows the median *F* region drift over a 24 hour period in the polar ionosphere (Reinisch 1986). The direction of the horizontal drift exhibits good agreement with the predicted antisunward direction. Drift measurements are currently being made by a chain of Arctic Digisondes operated by the Air Force Geophysics Laboratory, USA. These time-continuous measurements of the high-latitude convection are an important compliment to sporadic satellite and incoherent scatter radar measurements.

At La Trobe University work is also in progress employing the ionogram and drift modes of the Digisonde. In addition, the university's Digisonde has a fixed frequency mode which allows the phase of the returned ionospheric echo to be monitored for up to four different frequencies. Highly accurate virtual height measurements are possible by monitoring the phase of two closely-spaced frequencies and using the stationary phase principal (Whitehead and Kantarizis 1967). Further, monitoring the rate of change of phase with time for a particular frequency provides Doppler information of high accuracy and high temporal resolution. A project is currently underway to relate Doppler variations observed at each of four well-spaced frequencies with geomagnetic pulsations (periods 10 to 100 s) observed with an induction magnetometer. Both sets of variations are believed to arise from the propagation of hydromagnetic waves through the ionosphere.

5.3 THE DYNASONDE

The Dynasonde (or Advanced Ionospheric Sounder) was developed by the Space Environment Laboratory of the National Oceanic and Atmospheric Administration (NOAA) in Boulder, Colorado (Grubb 1979). These instruments have been built and deployed around the world. The Dynasonde has various operating modes which differ from the Digisonde by their statistical sampling quantities in the time and frequency domains (Wright and Pitteway 1979). One of the major users of the Dynasonde is the British Antarctic Survey in their studies of the Antarctic ionosphere (Dudeney et al. 1982). Features of the mid-latitude trough are identified in the left-

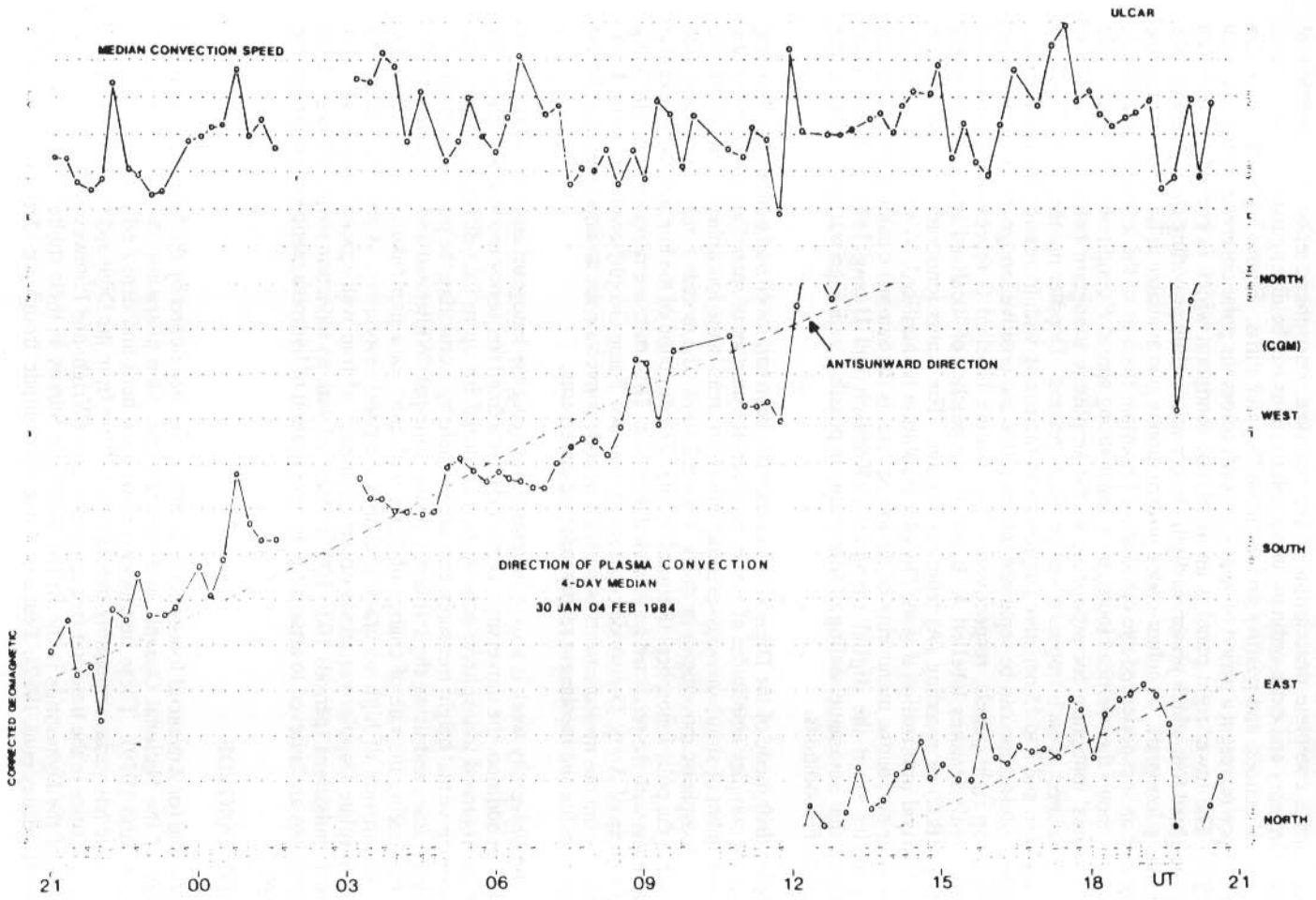

Figure 2. Plasma convection at Thule, Greenland. Four -day median shows consistent antisunward plasma flow (from Reinisch 1986).

hand panels of the ionograms of Figure 3 (Dudeney et al. 1983). The unique ability of the instrument to locate the echoing region is illustrated in the right-hand panels. Powerful insights into the structure, dynamics and formation of various phenomena in the Antarctic ionosphere are being gained by coordinating the operation of the advanced sounders with other experiments such as in situ langmuir probes (e.g. Rodger et al. 1986). At equatorial latitudes, the dynasonde has also been employed to study the detailed structure of spread *F* (Argo and Kelley 1986) and of sporadic *E* (Wright 1982). Finally, the concept of a global real-time ionospheric monitoring network has been furthered by the work of Wright and Kressman (1983). Identical dynasondes, some 864 km apart, were synchronised for bistatic sounding.

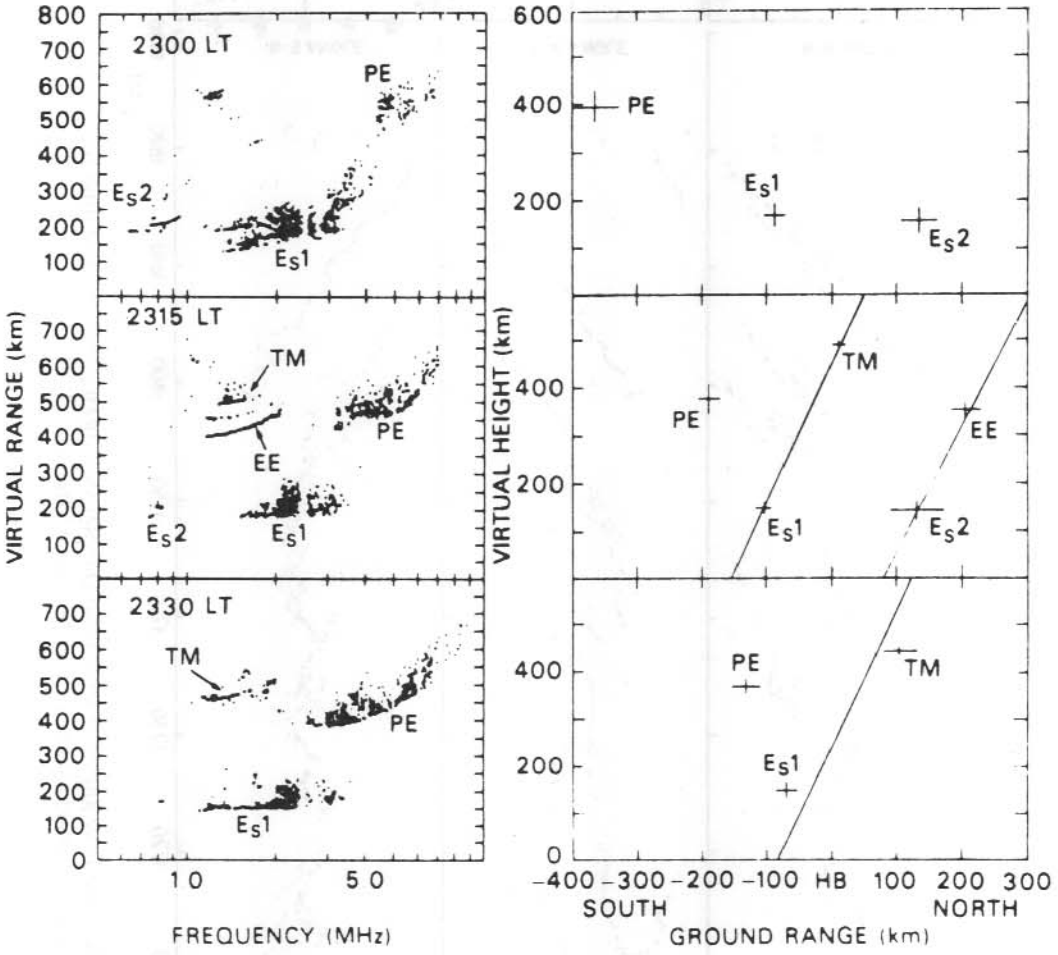

Figure 3. Left-hand panel: ionograms from Halley Bay, recorded by the advanced ionospheric sounder on 26 August, 1981, with the echoing regions of the main ionospheric trough indicated as: PE ≡ poleward edge, TM ≡ trough minimum and EE ≡ equatorial edge. Right-hand panel: the corresponding virtual heights and locations of the echoing regions in a north-south geographic plane. The sloping lines indicate the direction of the geomagnetic field in this plane (from Dudeney et al. 1983).

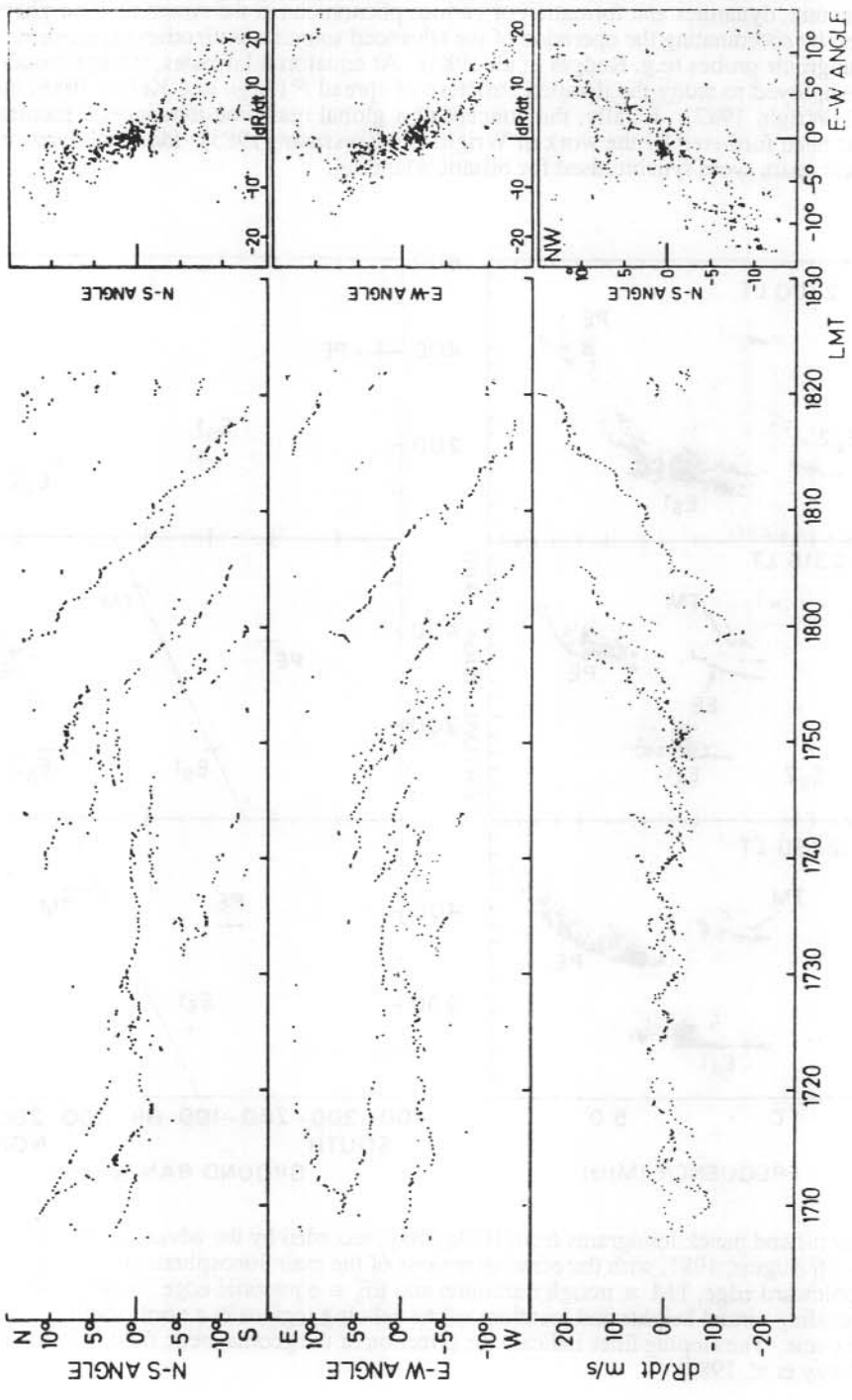

Figure 4. Plot of N-S and E-W angles of arrival and Doppler shift dR/dt as functions of time and each other for a sporadic *E* cloud structure (from From and Whitehead 1986).

5.4 OTHER ADVANCED SOUNDERS

Other sounders are less sophisticated than the Digisonde or Dynasonde but are proving very useful tools in ionospheric research. An HF radar located at Bribie Island in Queensland is operated by the University of Queensland (From and Whitehead 1984). The sounder employs crossed-fan beams produced by crossed linear transmitter and receiver arrays to simulate a steerable pencil beam at three operating frequencies. Complex amplitude information at the spaced antennas provides very high resolution angle of arrival and Doppler shift data. Figure 4 presents evidence to show that partially-reflecting sporadic *E* takes the form of successive clouds of ionisation moving across the field of view of the radar (From and Whitehead 1986). This instrument continues to be employed for sporadic *E* studies. In particular, a coordinated experiment is planned with a mobile VHF radar to investigate small scale plasma waves associated with sporadic *E*.

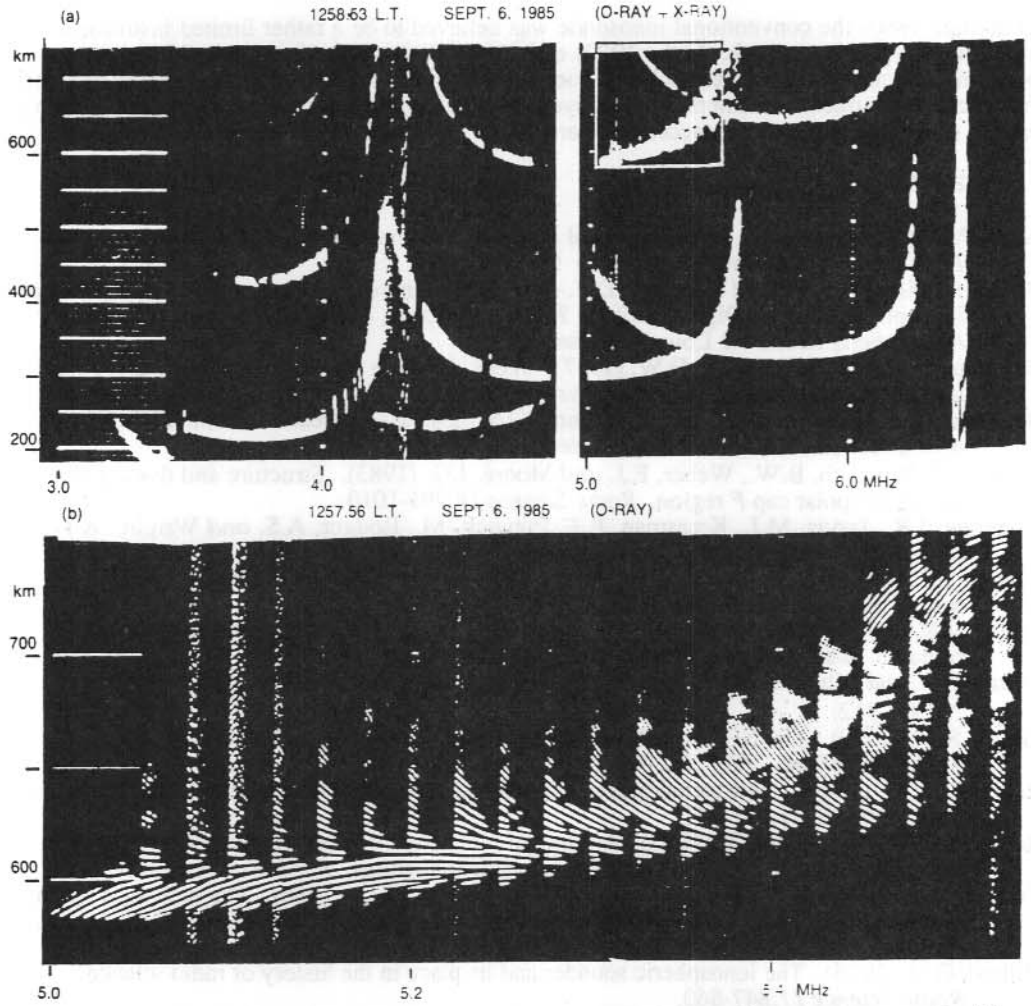

Figure 5(a). Full-range ionogram with rectangle showing height and frequency ranges for (b); (b) ionogram recorded 57 s before (a) showing main-trace and cross-over traces (swept gain 60 dB every 0.5 s). (from Bowman and Hainsworth 1987).

The Disonde is a directional ionosonde which is also located at Bribie Island and operated by the University of Queensland. It is intentionally a low budget instrument and photographic recording methods are employed (Bowman et al. 1986). Figure 5 is an example of recordings which illustrate several of the features of the Disonde. The bottom panel is a limited frequency and height range ionogram (Bowman and Hainsworth 1987). Fine structure in a spread *F* trace, which is barely detectable on the full-scale ionogram (top panel), can be studied. Swept-gain recordings allow comparative signal strengths of ionospheric echoes to be determined. The small-scale interference fringes are produced by phase modulation and allow phase-coherent signals to be identified. This feature is useful in determining whether the spread *F* arises from specularly-reflected or from scattered ionospheric returns. The Disonde has significantly advanced our knowledge and understanding of the spread *F* phenomenon.

5.5 CONCLUSIONS

In the late 1960s the conventional ionosonde was believed to be a rather limited instrument for modern ionospheric research. In the 1970s and 1980s the ionospheric sounder has regained its position as a much respected research tool due to the advanced features of the modern instrument. Advanced ionospheric sounders are deployed worldwide and are currently yielding exciting results, especially in the more inaccessible parts of the globe such as the Arctic and Antarctic.

5.6 REFERENCES

Argo, P.E. *and* Kelley, M.C. (1986). Digital ionosonde observations during equatorial spread *F*. *Journal of Geophysical Research 91*:5539-5555.

Bibl, K., Reinisch, B.W. *and* Kitrosser, D.F. (1981). General description of the compact digital ionospheric sounder Digisonde 256. *Technical Report, University of Lowell Centre for Atmospheric Research.* Lowell, Massachusetts.

Bowman, G.G. *and* Hainsworth, D.W. (1987). Weak day-time spread-F signals from the mid latitude ionosphere. *Annales Geophysicae 5A*:127-132.

Bowman, G.G., Hainsworth, D.W. *and* Dunne, G.S. (1987). A research-oriented ionosonde with direction capabilities. *Radio Science 21*:297-303.

Buchau, J., Reinisch, B.W., Weber, E.J. *and* Moore, J.G. (1983). Structure and dynamics of the winter polar cap *F* region. *Radio Science 18*:995-1010.

Dudeney, J.R., Jarvis, M.J., Kressman, R.I., Pinnock, M., Rodger, A.S. *and* Wright, K.H. (1982). Ionospheric troughs in Antarctica. *Nature 295*:307-308.

Dudeney, J.R., Rodger, A.S. *and* Jarvis, M.J. (1983). Radio studies of the main *F* region trough in Antarctica. *Radio Science 18*:927-936.

From, W.R. *and* Whitehead, J.D. (1984). The calibration of an HF radar used for ionospheric research. *Radio Science 19*:423-428.

From, W.R. *and* Whitehead, J.D. (1986). E_S structure using an HF radar. *Radio Science 21*:309-312.

Grubb, R.N. (1979). The NOAA SEL HF radar system (ionospheric sounder). *NOAA Technical Memo. ERL SEL-55*. 18 pp.

Reinisch, B.W. (1986). New techniques in ground-based ionospheric sounding and studies. *Radio Science 21*:331-341.

Reinisch, B.W. *and* Huang, X. (1983). Automatic calculation of electron density profiles from digital ionograms. 3. Processing of bottomside ionograms. *Radio Science 18*:477-492.

Rodger, A.S., Brace, L.H., Hoegy, W.R. *and* Winningham, J.D. (1986). The poleward edge of the mid-latitude trough - its formation, orientation and dynamics. *Journal of Atmospheric and Terrestrial Physics 48*:715-728.

Villard, O.G. (1976). The ionospheric sounder and its place in the history of radio science. *Radio Science 11*:847-860.

Watts, J.M. *and* Davies, K. (1960). Rapid frequency analysis of fading radio signals. *Journal of Geophysical Research 65*:2295-2301.

Whitehead, J.D. *and* Kantarizis, E. (1967). Errors in the measurement of virtual height using a phase ionosonde. *Journal of Atmospheric and Terrestrial Physics 29*:1483-1488.

Wright, J.W. (1982). The application of dopplionograms to an understanding of sporadic *E*. *Journal of Geophysical Research 87*:1723-1726.

Wright, J.W. *and* Fedor, L.S. (1969). The interpretation of ionospheric radio drift measurements. II. Kinesonde observations of microstructure and vertical motion in sporadic *E*. *Journal of Atmospheric and Terrestrial Physics 31*:925-942.

Wright, J.W. *and* Kressman R.I. (1983). First bistatic oblique-incidence ionograms between digital ionograms. *Radio Science 18*:608-614.

Wright, J.W. *and* Pitteway, M.L.V. (1979). Real-time data acquisition and interpretation capabilities of the Dynasonde. 1. Data acquisition and real-time display. *Radio Science 14*:815-825.

6. THE IPS FIFTH GENERATION IONOSPHERIC MONITORING SYSTEM

Bruce Paterson and Craig Bevins
IPS Radio and Space Services
PO Box 702
Darlinghurst NSW 2010
Australia

ABSTRACT

The new (A model) IPS series five ionosonde network incorporates several major developments in hardware and software enabling substantial improvements in ionospheric monitoring and predictions. The transmitter can generate a variety of pulse shapes to optimally match requirements. The receiver measures signal strength so that absorption can be estimated and the threshold can be dynamically determined. An agile frequency synthesiser facilitates efficient frequency selection. The transmitter and receiver can also be controlled independently and this enables oblique ionograms, beacon monitoring and channel occupancy statistical calculations to be made. The 'B' model will add o-x separation and pulse coding which will improve signal identification. Each ionosonde incorporates a general purpose UNIX based microcomputer system for control, data analysis, reduction and storage, communications, remote fault diagnosis and status monitoring. The ionosonde communicates with the central IPS computer using the ACSNET network software via the public switched telephone network, X.25 or other suitable data carrier, enabling ready integration with the worldwide ionospheric, geophysical and solar monitoring network. The system software is modular in design and may be remotely maintained and updated, enabling the system to rapidly respond to changing conditions and requirements. Although local autoscaling is planned for the ionosonde, raw ionograms will initially be transmitted to the Ionospheric Prediction Service in NSW for computer assisted manual scaling.

6.1 INTRODUCTION

Ionospheric science has a constant demand for increased quantity and quality of data. Each new generation of ionosondes was improved and developed until the next generation became inevitable. First generation fixed frequency devices became multifrequency. Second generation tuneable sondes became easier to use and ionograms as we know them appeared. Third generation sondes were all valves, cams and motors and required daily attention. Some solid state additions were made. Fourth generation sondes are almost completely solid state, with electronic tuning and film that lasts a week. Additions have enabled them to be remotely controlled and return data in real time. Now the need and the technology exist for a major leap forward - the fifth generation - and this paper is about some of the technology being implemented by the IPS, and the enhancement of the prediction system this will make possible.

A fifth generation ionosonde is built with a general purpose computer controlling the associated transmitter and receiver and with electronic linkage with the rest of the prediction system. The transmitter and receiver have some flexibility of their operation parameters and this makes it possible for the computer to optimise the sonde dynamically. The computer can use data from the control system, data gathered earlier and data recently gathered to decide what is needed and then to suitably configure the transmitter and receiver.

6.2 HARDWARE

6.2.1 *The transmitter's pulse shape*

Previous transmitter designs have used a simple keying circuit for a modulator. Fourier Transform theory shows that such pulses have substantial sidelobes in the frequency domain, i.e.

they cause interference to many channels near to the one being sounded. If the receiver bandwidth is wide enough to pass most of these sidelobes then the receiver will suffer severe interference. If the receiver filter is designed to only pass the central lobe frequency components then the resultant pulse will show severe ringing with resultant poor height resolution. Improving the pulse shape is desirable, but ideal shapes such as raised cosine, Gaussian, Kaiser etc. have been difficult to generate. Suitable complementary receiver filters have been even more difficult to construct.

The 5A uses a new approach. The desired pulse is stored in ROM. When a 'START' pulse occurs, the ROM is quickly read into a D to A converter, which then modulates 30 MHz. The modulator is balanced and the analogue signal can go either side of zero. By adding a second identical ROM A to D modulator chain whose output is added to the first, but in which the 30 MHz signal is phase shifted by 90° with respect to the first, then any modulation is possible by a suitable choice of data in the two ROMs. The authors have chosen to transmit a Gaussian pulse (to better than 1% accuracy).

The receiver filter is a minimum phase design that is easy to construct (a cascade of three third order Butterworths), but this would cause some ringing problems. However, by convolving the Gaussian pulse with the complex conjugate of the phase response of the receiver filter, the resultant transmitted pulse still has the power spectrum of a Gaussian pulse (unchanged) but the pulse that emerges from the receiver filter is now that which would emerge if a standard Gaussian pulse is fed into a filter with the same amplitude response as the present design, but with a perfectly linear phase response. This produces a significant reduction in ringing without any extra component cost. Further, the 'linear' power amplifier in the transmitter is not perfectly linear, and by characterising its nonlinearity a compensating nonlinearity can be incorporated in the ROM data so that the transmitted signal is exactly as desired. Finally, such a modulator makes it easy to add phase encoding to the modulation in the future.

6.2.2 *The detector*

The receiver is designed for high dynamic range and the gain can be set by the computer. The detector is a logarithmic amplitude amplifier and detector combination having excellent logarithmic linearity over more than 60 dB dynamic range. This drives an 8 bit A to D converter so the system amplitude resolution is 1/4 dB. The simplest form of subsequent processing is echo detection by threshold, but now thresholds may be set after a channel is sampled and thus can use the results of that sounding in determining the threshold. More advanced processing methods can use the amplitude data directly to give improved results. It is also easy to determine absorption at any frequency.

6.2.3 *Transmitter and receiver independence*

The transmitter and receiver can be independently controlled. By using the receiver only it is easy to compile channel use statistics and in particular, to monitor specific beacons and broadcast stations for strength and fading. When precision time references are added to these ionosondes it will also be possible for one sonde to listen for another, i.e. do oblique soundings. Though separate control might seem a small step, from the viewpoint of ionospheric predictions it may be the most far reaching of all since it enables conditions between sonde sites to be determined and more specifically, enables propagation predictions to be tested in a routine objective manner.

6.2.4 *The frequency synthesiser*

Separate frequency synthesisers giving 5 kHz steps between 1 MHz and 21.475 MHz (4096 channels) are used in the transmitter and receiver, but they are referenced to the same 1 MHz standard. In order to achieve the best receiver performance, notably, the maximum dynamic range, it is necessary to avoid reciprocal mixing desensitisation. That is, the synthesiser must be as clean as possible. Close sideband noise has been kept low by minimising additional noise

from the control circuitry and maintaining high gain with a pole at the origin in the low pass filter (so phase noise performance is second order). Mid frequency sideband noise has been kept low since the closed loop frequency response has negligible gain rise and the reference sidebands are suppressed by transmission zeros (first harmonic) and circuit balance. Wideband oscillator noise is extremely low by design. The oscillator is a low noise level stabilised linear amplifier with high Q feedback. This has the additional advantage of very low harmonic output, and with the addition of a simple filter the synthesiser has no detectable spurious or harmonic output (to at least 70 dB below carrier).

The high attenuation at high frequencies normally needed to give good reference sideband rejection normally leads to a sluggish loop. Here, the loop has been very carefully (but not critically) designed and the resultant circuit has eight poles including two that are complex and three zeros, including a purely complex pair. The resultant closed loop response is an excellent approximation to linear phase and the step response when changing channels is critically damped (no visible ringing). Channel changing is very fast (for the channel spacing) with band end to band end settling time less than 50 ms, being less to nearby channels.

6.2.5 *Maintenance*

The new ionosonde is being designed with highly standardised and modularised construction and with some self test and remote diagnostic facilities. Since operation is unattended and often remote, reliability is a significant design consideration but in the event of a fault, on site fault location and repair should be rapidly performed.

6.2.6 *Future*

It is planned to upgrade the 5A to a 5B after the first batch of 5As is deployed. The 5B will have two delta aerials – with one for transmission and the other for reception. The transmitters will be able to transmit circular or linear polarisation. The receiver will have a second receiver channel installed (motherboard provision already available - the three extra modules can just slot in) so that one will permanently monitor 'o' mode and one will monitor 'x' mode. The transmitter can selectively excite either and this will greatly facilitate echo detection and autoscaling.

The other big difference will be the use of a high resolution (14 bit planned) digital signal processor in the detector, which will operate on the signal directly rather than on its amplitude (as in the 5A). By simply adding new ROMs to the transmitter modulator, pulse stretching, phase encoding and correlation detection become possible with a resultant huge increase in signal to noise ratio. Pulse shapes can easily be changed to suit the part of the ionogram being sounded. When sounding flat parts of the ionogram, frequency resolution can be poor but height accuracy can be good by using heavily phase encoded signals. When near a cusp, height resolution is not so important but frequency resolution is more important. The ideal pulse is now the longest possible pure Gaussian. Other pulses may be selected for other applications. Still further choices are possible in receive only mode.

6.3 SOFTWARE

6.3.1 *Introduction*

The IPS Series V ionosonde network consists of an arbitrary number of subordinate data-gathering sites configured in star topology about a central control computer.

As previously discussed, each ionosonde consists of a general purpose control and communication microcomputer, and custom designed peripheral hardware.

The Series V software subsystem is resident on the microcomputer and based on the UNIX operating system (Ritchie and Thompson 1978). This operating system was decided upon over the more conventional MS-DOS for the following reasons:

a. compatibility with the central network control and development computer which is also UNIX-based
b. its multi-user, multi-tasking orientation
c. its support of modular design techniques
d. its rich set of development and debugging tools
e. easy portability to other computer architectures

At the present time the ionosonde is based on an IBM PC/AT or compatible computer, although by virtue of the portability of the UNIX system and the techniques used in the implementation of the software subsystem this is by no means mandated in perpetuity. Indeed, the ionosonde software is readily portable to any computer system running UNIX System V, which presently encompasses a range of processors from the ubiquitous IBM PC through the DEC VAX to the IBM 370 and Cray supercomputer. This independence from any one hardware vendor allows well placed responses in a timely fashion to either changing user demands or new computing technology.

The primary goals in the development of the system were:

a. remote stations should operate automatically and, in the absence of catastrophic failure, require no routine intervention
b. a flexible and reliable network communications system
c. the construction of the system in a highly modular form, using a 'building-block' approach to aid ease of maintenance and modification
d. the minimisation of data transmission costs
e. compatibility with the IPS central computer systems
f. with the exception of the custom components, be based largely upon 'off-the-shelf' components

All of these goals are either met or facilitated by a combination of the functions provided by UNIX and the ACSnet network software developed at the University of Sydney (Lauder et al. 1984). UNIX provides access control, process scheduling and resource allocation services traditionally associated with the operating system while ACSnet provides a reliable virtual circuit protocol package upon which various control, remote execution and file transfer facilities are based (Lauder 1984). The communications carrier presently being used is simple PSTN dialup, although facilities are provided for X.25 packet network, CSIRONET and Ethernet communications. Any future protocol may be readily supported simply by the addition of an appropriate software module.

Functionally, then, the system consists of three major components: the operating system (UNIX), the communications software (ACSnet) and the ionosonde software itself, each of which are in turn composed of a number of sub-components or modules.

6.3.2 *Implementation*

Discounting the purely mechanical processes of installing and configuring the operating system and networking software, implementation consisted of first developing the low-level device interface software, and subsequently, the high-level control software.

The interface software, or 'driver', is system-level software and actually forms an integral component of the operating system 'kernel'. It contains all of the device-specific code required to manipulate the controller at the level of its electrical connection with the computer and its purpose is to localise and hide I/O operations of a specialised nature behind a more general model of

device control at the applications level. In terms of implementation, it is the single most complicated element of the entire system as it must not only drive the device with which it is concerned but also take care to minimise its impact on completely independent tasks which may require urgent CPU attention. The driver is the only truly non-portable component of the entire ionosonde system software.

The modular approach has been adopted in the construction of the ionosonde control software itself, employing the UNIX 'tool-box' and 'pipe-fitting' concepts of building a software system from a number of discrete program components or blocks, each designed to optimally perform some single function with the assumption that the output of one program will form the input to another. This naturally promotes both a 'bottom-up' approach to implementation, enabling a prototypical system to be produced as early as possible and later incrementally modified until the system is complete, and significantly reduces the effort required to subsequently maintain and modify the system.

6.4 OPERATION

There are three basic steps to the production of an ionogram which correspond to processes which we will designate 'sounder', and 'despatcher'. The main process is sounder, which performs soundings according to specified parameters including the range of channels to be sounded, the number of pulses per channel, pulse shape, receive filter selection, transmitter power and attenuation. Sounder produces a 'raw' ionogram which is then passed for further processing to the reducer process. Reducer in its turn passes the processed data to despatcher for delivery to its destination.

The system has two modes of operation - daemon* and special. It normally operates in daemon mode whereby it performs soundings at regular intervals according to parameters sourced from a standard configuration file. In daemon mode, the default reducer process currently consists of the application of simple shrink and grow noise reduction (Webster 1985) and data compression (Welch 1984) algorithms to the data. The default despatcher passes these data to the network spooler to be transmitted to the central control computer for archival and analyst interpretation. Research is currently in progress to replace the rather simple-minded reducer with autoscaling software whereby the despatcher will automatically insert the scaled values into a database on the central computer.

Special mode, as its name might imply, is used for one-off or non-routine soundings probably in response to an analyst or client requesting real-time interrogation of the ionospheric sounding network. In this mode, operating parameters may be altered and the reducer process redefined to permit non-standard processing of the ionogram. The data in this case are returned to the requesting user or process rather than being archived on the central computer.

Management of the network is conducted remotely from the central control computer. The term management here encompasses a broad range of tasks from the routine alteration of the standard operating and scheduling parameters at the remote sites to the maintenance and installation of system software.

All operations may be directed to the network as a whole or to individual sites. Additionally, via the 'domain' (Kummerfeld et al. 1984, Mockapetris 1983) or sub-net mechanism supported by ACSnet, certain subsets of the network may be configured to belong to subdomains according to arbitrary criteria. By way of example, the network could well be subdivided into high-, mid- and low-latitude stations with the relevant operating parameters of the sub-domains being independently managed.

*From Greek mythology, meaning an attendant or in-dwelling spirit or supernatural being.

6.5 REFERENCES

Kummerfeld, R. *and* Lauder, P.R. (1984). *Domain addressing in SUNIII*. Sydney University Basser Department of Computer Science.

Lauder, P. R. (1984). *A reliable virtual circuit protocol package*. Sydney University Basser Department of Computer Science.

Lauder, P. R., Kummerfeld, R. J. *and* Elz, R. (1984). ACSnet - The Australian alternative to UUCP. *The Australian UNIX System Users' Group Newsletter 5(4)*.

Mockapetris. (1983). *Domain names - concepts and facilities*. U.S. Department of Defence Advanced Research Projects Agency, RFC-882.

Ritchie, D.M. *and* Thompson, K. (1978). The UNIX time-sharing system. *The Bell System Technical Journal 57*:1-25.

Webster, G.K. (1985). *Applications of modern computing techniques to ionospheric sounding*. Macquarie University School of Mathematics and Physics.

Welch, T.A. (1984). A technique for high-performance data compression. *IEEE Computer 17*:8-19.

7. DETECTING IONOSPHERIC STRUCTURES AND MOTION USING THE DIGISONDE-256

D.L. Johnston and P.L. Dyson
Department of Physics
La Trobe University
Bundoora Vic 3083
Australia

ABSTRACT

Spectral analysis of the complex signal of ionospheric radio echoes received at spaced antennae identifies simultaneously existing reflection areas. The radial velocity component of each ionospheric reflector can be determined from Doppler analysis and assuming a constant velocity field, a resultant 3-D velocity vector can be calculated. Initial results using simulated data and data collected using the Doppler drift mode of the Digisonde-256 are presented.

7.1 INTRODUCTION

All ionospheric surfaces of adequate electron density that fulfil the perpendicularity condition will reflect a radiowave. When an echo is reflected from a moving isodensity surface, a Doppler shift is imposed on the reflected wave (Pfister 1971). The Doppler shift is determined by the velocity **V** of the reflecting surface and the radiowave vector **K**

$$\Delta f = \frac{1}{\pi} \mathbf{V} \cdot \mathbf{K}$$

By using a spectral analysis technique on the phase and amplitude recordings of the reflected signals received at spaced antennae the different reflection areas can be located (Pfister and Bibl 1972). A Doppler analysis on the data produced from such a technique can be used to determine the movement of the reflecting ionisation.

The Digisonde-256, an advanced digital ionosonde developed by the University of Lowell, has an operational mode included in its design to provide data for this type of analysis. A possible spatial resolution of 1.5 km between reflection surfaces at an altitude of 200 km can be achieved with Doppler frequency shift of 0.03 Hz (Bibl and Reinisch 1978). The usefulness of this mode as a tool for monitoring ionospheric motion, particularly in polar regions, is seen in Figure 1 (Reinisch 1986) which shows the median plasma convection over a 24-hour period during four days at Thule, Greenland.

By way of initiating a regular mid-latitude drift monitoring routine using the La Trobe University Digisonde-256 located at Beveridge, Victoria, an evaluation has been made of a Doppler drift technique developed at the University of Lowell (Dozois 1981) for an earlier model digisonde. The original method has been modified for the Digisonde-256.

7.2 METHOD

The Doppler drift mode of the digisonde is run alternatively with the normal ionogram mode. To produce full Doppler and angle of arrival resolution, the Doppler drift mode samples 1, 2 or 4 selectable frequencies at their corresponding echo ranges using a 5 km window. The Doppler-shifted echoes are received at an array of 1, 2, 4 or 7 antennae. In-phase and quadrature components of the signal at each antenna are input in real time into a hardware processor which performs a discrete Fourier transform. One drift measurement consists of amplitude and time-independent phase of the Doppler spectral components of the signal received at each antenna.

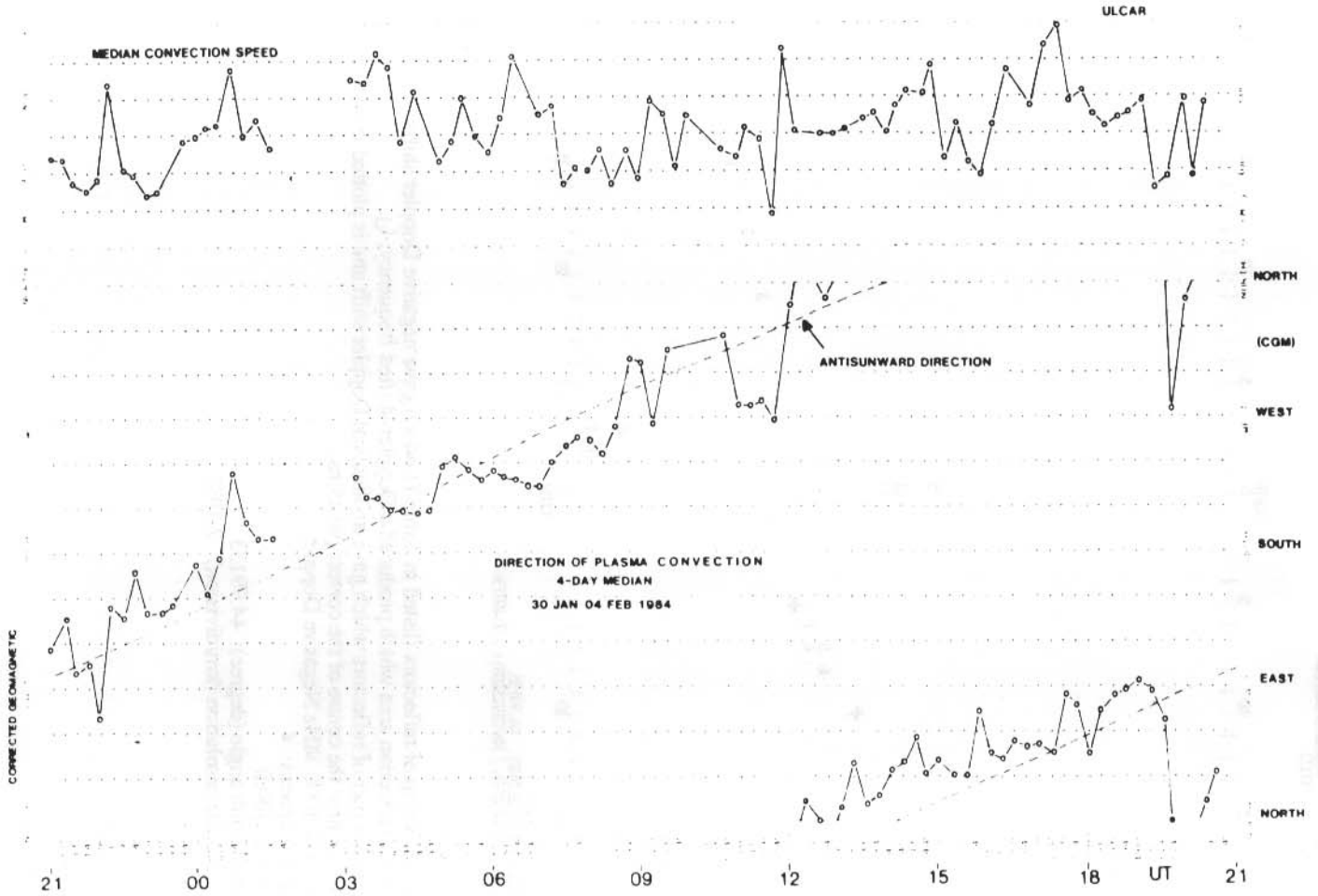

Figure 1. Plasma convection at Thule, Greenland. Four-day median shows consistent antisunward plasma flow (from Reinisch 1986).

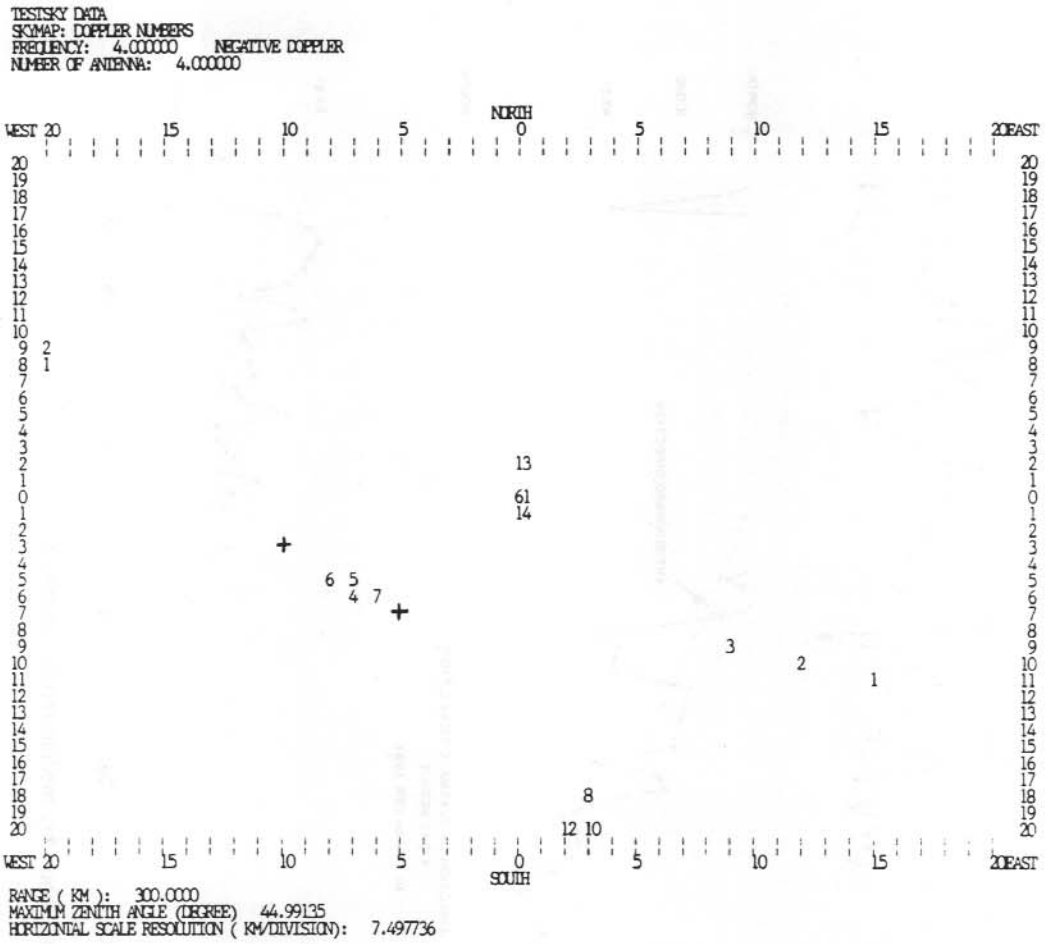

Figure 2. Skymap of reflectors (listed in Table 1) which gave negative Doppler shifts.
d - Indicates reflection area which produced a Doppler-shifted frequency, f_d.
x - Indicates a pair of reflectors which gave an identical Doppler shift and is plotted as one reflector near the centre of the correct positions.
Frequency: 4.0000 MHz Negative Doppler
Number of antennas: 4
Range (km): 300.0
Maximum zenith angle (degree): 44.99133
Horizontal scale resolution (km/division): 7.4977

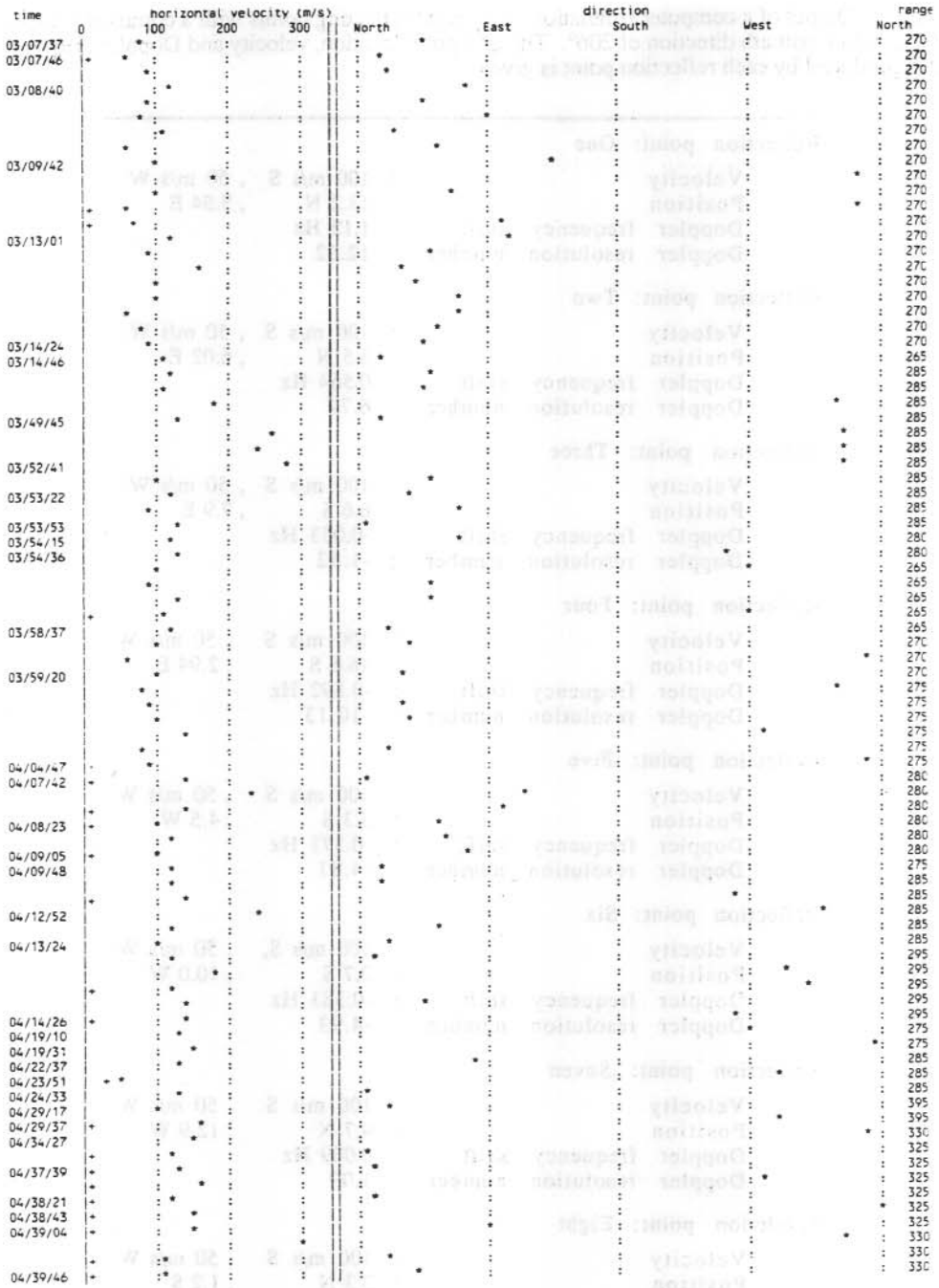

Figure 3. Results of ninety minutes of test measurements with the Digisonde-256 using four antennas and four frequencies, each with a single 5 km height range window.

Table 1. Output of a computer simulation using eight reflecting points with a common velocity of 112 m/s and azimuth direction of 206°. The grid point location, velocity and Doppler frequency shift produced by each reflection point is given.

Reflection point: One		
Velocity	: 100 m/s S	, 50 m/s W
Position	: 13.2 N	, 3.54 E
Doppler frequency shift	: 1.12 Hz	
Doppler resolution number	: 12.52	
Reflection point: Two		
Velocity	: 100 m/s S	, 50 m/s W
Position	: 3.5 N	, 6.02 E
Doppler frequency shift	: 0.564 Hz	
Doppler resolution number	: 6.77	
Reflection point: Three		
Velocity	: 100 m/s S	, 50 m/s W
Position	: 6.6 S	, 7.9 E
Doppler frequency shift	: -0.053 Hz	
Doppler resolution number	: -1.52	
Reflection point: Four		
Velocity	: 100 m/s S	, 50 m/s W
Position	: 16.6 S	, 2.94 E
Doppler frequency shift	: -0.892 Hz	
Doppler resolution number	: -10.13	
Reflection point: Five		
Velocity	: 100 m/s S	, 50 m/s W
Position	: 5.3 S	, 4.5 W
Doppler frequency shift	: -0.373 Hz	
Doppler resolution number	: -4.81	
Reflection point: Six		
Velocity	: 100 m/s S,	, 50 m/s W
Position	: 2.7 S	, 10.0 W
Doppler frequency shift	: -0.383 Hz	
Doppler resolution number:	: -4.93	
Reflection point: Seven		
Velocity	: 100 m/s S	, 50 m/s W
Position	: 4.7 N	, 12.9 W
Doppler frequency shift	: 0.009 Hz	
Doppler resolution number	: 1.09	
Refelction point: Eight		
Velocity	: 100 m/s S	, 50 m/s W
Position	: 3.3 N	, 1.2 S
Doppler frequency shift	: 0.312 Hz	
Doppler resolution number	: 4.19	

These data can be used to generate a picture of the ionosphere's structures and motions during the time of measurement. The area above the sounder is divided into a 41 x 41 grid to form a skymap. The angular spectra is produced by calculating the frequency-wave number power density (FWPD)

$$P(d,j) = \sum_{j} \sum_{j'} F(j,d) F^{*}(j',d) exp\left[-i\left(\mathbf{k} \cdot \left(\mathbf{a}_{j} - \mathbf{a}_{j'}\right)\right)\right]$$

where F(j,i) = the spectrum for antenna j
a = the antenna j position vector
k = a scanning vector of constant magnitude 2 and varying direction.

The scanning vector specifies the angle of arrival for each point on the grid of the skymap. The power density is calculated for each of the 1681 points on the skymap for each Doppler component. The location of the reflecting surface is indicated by the position of the maximum power density. If more than one Doppler component is found at the same location, the one with the largest amplitude is selected.

Data from the skymap are used to determine a three-dimensional velocity vector for each time window. The Doppler equation gives only the radial component of the velocity, to obtain a general three-dimensional velocity for each time window it is necessary to use more than one of the Doppler spectral components in the velocity calculation. It is assumed that during the time of the measurement all reflecting surfaces have the same velocity, and a least squares method, with weighting factors equal to the antenna amplitude, is used to calculate the velocity. Tests, using simulated data, indicated that to produce a reliable three-dimensional velocity at least 5 of the 256 Doppler spectral components calculated in a given measurement should be used in the least squares velocity calculation. Any measurement which did not achieve this requirement is considered not valid. The median velocity vector for each minute is then plotted.

7.3 RESULTS

It is possible for more than one reflecting surface to produce the same Doppler shift. Computer simulated data using eight reflecting points with a common velocity of 112 m/s and azimuth direction of 206°. The grid point location, velocity and Doppler frequency shift produced by each reflection point is given in Table 1.

Reflection points 5 and 6 produce the same Doppler shift within the resolution for this test (-0.388 Hz, Doppler resolution number -5). Figure 2 shows the skymap of reflectors which gave negative Doppler shifts. The location of the reflection area which produced a Doppler-shifted frequency f_d, is indicated by Doppler resolution number **d**. The pair of reflectors which gave the identical Doppler shift is seen as one reflector near the centre of the correct positions (indicated by an 'x'). The velocity calculated from this skymap data was 121 m/s at 203° azimuth.

A series of test measurements were taken during July 1987, using four antennas and four frequencies, each with a single 5 km height range window. Each ten second measurement produced a spectra of 128 Doppler shifted components. Figure 3 shows the results of ninety minutes of data. The recordings were not continuous as the Doppler drift mode was run alternately with normal ionograms. No recorded result indicates there was an insufficient number of Doppler components for the least squares fit velocity calculation.

7.4 DISCUSSION/CONCLUSION

No independent confirmation of these results was possible. The limited Doppler and angle of arrival information available on the ionograms taken concurrently with the drift measurements

indicated a general northeast flow towards the station and a second velocity west to northwest was also detected. Both indicate more than one structure being present, the Doppler drift technique in its present form determines the velocity of whichever echo dominates the range window during the time of measurement.

A further investigation into the velocity calculations of some of the measurements in which there were insufficient reliable velocity calculations for the least-squared fit showed indications of the velocities of both structures. This suggests that while the technique is providing at least consistent results, the assumption that during the time of measurement, all the reflecting surfaces have the same velocity, is not always valid and further refinements to the present technique are necessary.

With further development, this technique will be even more useful and, as demonstrated by Reinisch (1986), it gives a reliable means of monitoring motions of the polar ionosphere. Consequently installation of an ionosonde with these capabilities at an ANARE station in Antarctica would greatly enhance Australia's upper atmosphere physics research program in the region.

7.5 REFERENCES

Bibl, K. *and* Reinisch, B. (1978). The universal digital ionosonde. *Radio Science 13*:519-530.

Dozois, C. (1981). *A high frequency radio technique for measuring plasma drifts in the ionosphere*. Masters Thesis, University of Lowell.

Pfister, W. (1971). The wave-like nature of inhomogenieties in the E-region. *Journal of Atmospheric and Terrestrial Physics 33*:999-1025.

Pfister, W. *and* Bibl, K. (1972). A modernised technique for ionospheric drifts with spectral analysis. *Space Research 12*:975-982.

Reinisch, B. (1986). New techniques in ground-based ionospheric soundings and studies. *Radio Science 21*:331-341.

8. DIURNAL, SEASONAL, AND STORM-TIME VARIABILITY OF THE TOTAL ELECTRON CONTENT OF THE IONOSPHERE NORTH OF MACQUARIE ISLAND

M. Craven[1], E.A. Essex[2] and I. Platt[2]

[1]Antarctic Division
Kingston Tas 7050
Australia

[2]Department of Physics
La Trobe University
Bundoora Vic 3083
Australia

ABSTRACT

Measurements taken near solar minimum of the total electron content (TEC) of the ionosphere equatorward of Macquarie Island (54.5°S, 158.9°E), using the Faraday rotation technique, indicate that the peak in day-time TEC maximises around late autumn, progressively decreases through winter to spring and gradually recovers with the onset of summer. The morning post-sunrise build up phase of TEC becomes progressively less uniform from winter through summer, whilst the post-sunset TEC decay phase is often disrupted, during all seasons, by the onset of auroral sub-storms and/or the passage of the ionospheric trough, even during this near solar minimum observation period. Comparisons of the experimental results are made with the IRI model ionosphere. Magnetic storm events are often accompanied by a large increase in TEC lasting several hours, with increased sub-storm activity on successive evenings, and a general reduction of day-time TEC levels during the storm recovery phase of 2-3 days. The large enhancements in TEC generally occur around the time of the minimum value of the Dst index.

8.1 INTRODUCTION

When highly accurate measurements for ranging, VLBI or precise time comparisons are made using propagation through the ionosphere, it is necessary to eliminate or correct ionospheric TEC effects. Obviously corrections made using real time observations are desirable. If observed values are not available, estimated values from an ionospheric model have to be used.

In this paper, observations of the TEC obtained by the Faraday rotation method during 1984 to 1985 are presented. The results of the comparisons of these observed values with the IRI model are then presented.

8.2 OBSERVATIONS

Two hundred and forty-seven days absolute TEC data were determined covering the period May 1984 to January 1985, yielding a seasonal coverage extending from late autumn to mid-summer. The TEC observations were made at Macquarie Island (54.5°S, 158.9°E geographic) corresponding to an invariant latitude of 65°S using the 136 MHz transmissions from the geostationary satellites ATS-1 and ETS-2 (Lambert et al. 1986). The sub-ionospheric points in geographic co-ordinates for the two satellites were located at 152.9°E, 48.45°S for ETS-2 and at 160° ±0.8°E, 48° ±2.6°S for ATS-1. The elevations to the satellites were 23° for ETS-2 and 28° for ATS-1. The sub-ionospheric points correspond to an invariant latitude of around 60°S. Further details may be found in Craven and Essex (1987).

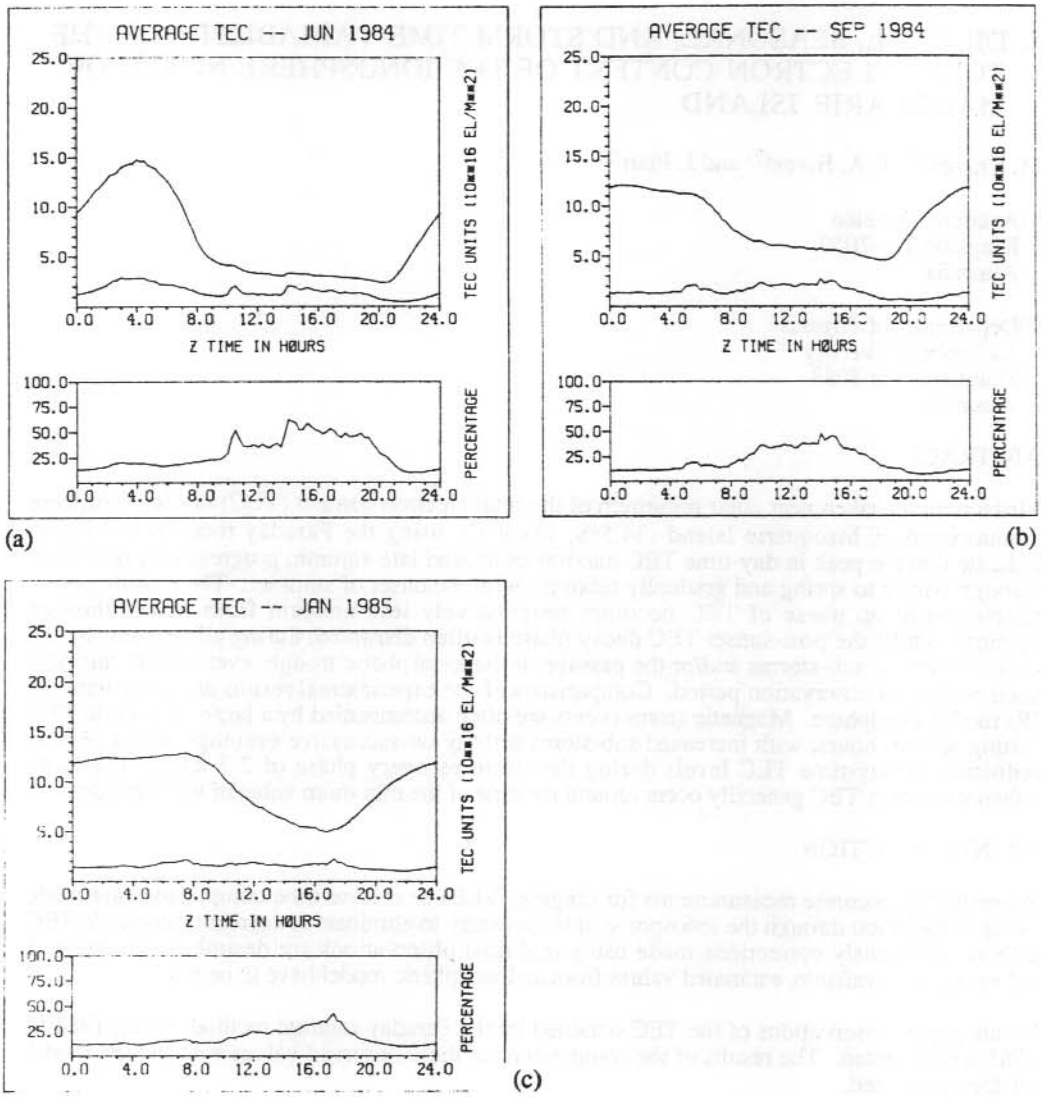

Figure 1. Monthly averages, standard deviations and percentage variation of the standard deviation from the monthly average for (a) June 1984, (b) September 1984 and (c) January 1985.

8.2.1 *Monthly averages*

Features of the data at these latitudes include the night-time (0800-1600 UT) disturbance activity and the onset of the mid-latitude trough appearing around 0700 UT during winter. These features have been discussed by Lambert and Cohen (1986).

Monthly averages, and their corresponding standard deviations, were calculated at 15 minute intervals. As a measure of the day-to-day variability of the TEC, the percentage ratio of the standard deviation to the average TEC was calculated. Figure 1 shows the results for June and September 1984 and January 1985. It is observed that the percentage variation can exceed 50% during night-time disturbances. The day-time TEC peak is a maximum in June at around 15 TEC units. The maximum value of the TEC then decreases through July and August to an October (spring) minimum near 10 TEC units, then gradually recovers by December-January (mid-summer) to levels around 12.5 TEC units.

For the northern hemispheric study of TEC from Anchorage, Alaska, for the year 1976-77, Soicher (1986) reported that the average monthly TEC values were always below 15 TEC units. The L shell value of the SIP was 3.35 compared with our SIP point value of around L=4. He found a seasonal variability wherein the maximum day-time peak occurred in April (spring) with progressively lower values through August (late summer), October (autumn) to December (winter). Soicher's (1986) results were obtained over a period of 10-18 months following the March 1976 solar minimum (between cycles 20-21) whilst the results presented here were gathered some 10-20 months prior to the September 1986 solar minimum. In agreement with Soicher (1986), the authors found that the day-time day-to-day variability, as measured by the ratio of the standard deviation to the average TEC values, shows no significant seasonal variation. This ratio is always less then 25% during the day, and is usually greater than 25% (often exceeding 50%) during the night.

8.2.2 *Comparisons with the IRI 1986 model*

As the TEC data discussed here are the first comprehensive set obtained at that higher latitude in the Southern Hemisphere, a comparison was made between them and the IRI model (Lincoln and Conkright 1981), the 1986 updated version being used. The smoothed sunspot number R12 was used in the calculations. Figure 2 shows a comparison between the median observed data values, the IRI(CCIR) model and the Bent topside model for 3 months. The Ching-Chiu model was also calculated but found to show large variations from the observed data points and hence is not included here. Also included in Figure 2 is the percentage difference between the observed values and the IRI (CCIR) model. For June 1984, the percentage error is largest around sunset and just before sunrise. However, the error does not exceed 50%. For September 1984, however, the day-time fit of the model gives percentage errors less than 25% for 12 hours. For night-time, however, the errors can exceed 150% due to auroral activity. For December 1984, the model tends to overestimate the TEC values by from 10% up to 30% for the whole day. It appears that one of the main factors affecting the estimate of TEC is the occurrence of the auroral activity. An auroral activity index needs to be incorporated into the model to produce a more realistic value of the TEC. Previous comparisons of the IRI model with TEC observed values in the Southern Hemisphere at 31°S have shown discrepancies usually less than 20% (McNamara and Wilkinson 1983).

8.2.3 *Magnetic storm effects*

Despite extensive studies of the storm time behaviour of the ionosphere using both experimental and modelling techniques, the underlying causes of the positive phase and negative phase of ionospheric storms are still not well understood. Previous studies have shown that there are marked longitudinal, seasonal and latitudinal variations in the ionospheric response to a magnetic storm (Essex 1986). Jones (1971) defines an 'S-event' in terms of the geomagnetic storm-time disturbance parameter, the equatorial Dst (H) index. An S-event is said to occur when Dst changes from a positive value through zero to a negative value of less than 20 nT within a few hours. The S-event starts when the Dst goes through zero, and ends when it reaches its most negative value. Jones (1971) found that, for mid-latitudes, increases in TEC during storms were always associated with S-events, predominantly toward the end of the event, provided the S-event partly included the period 0800-1200 LT.

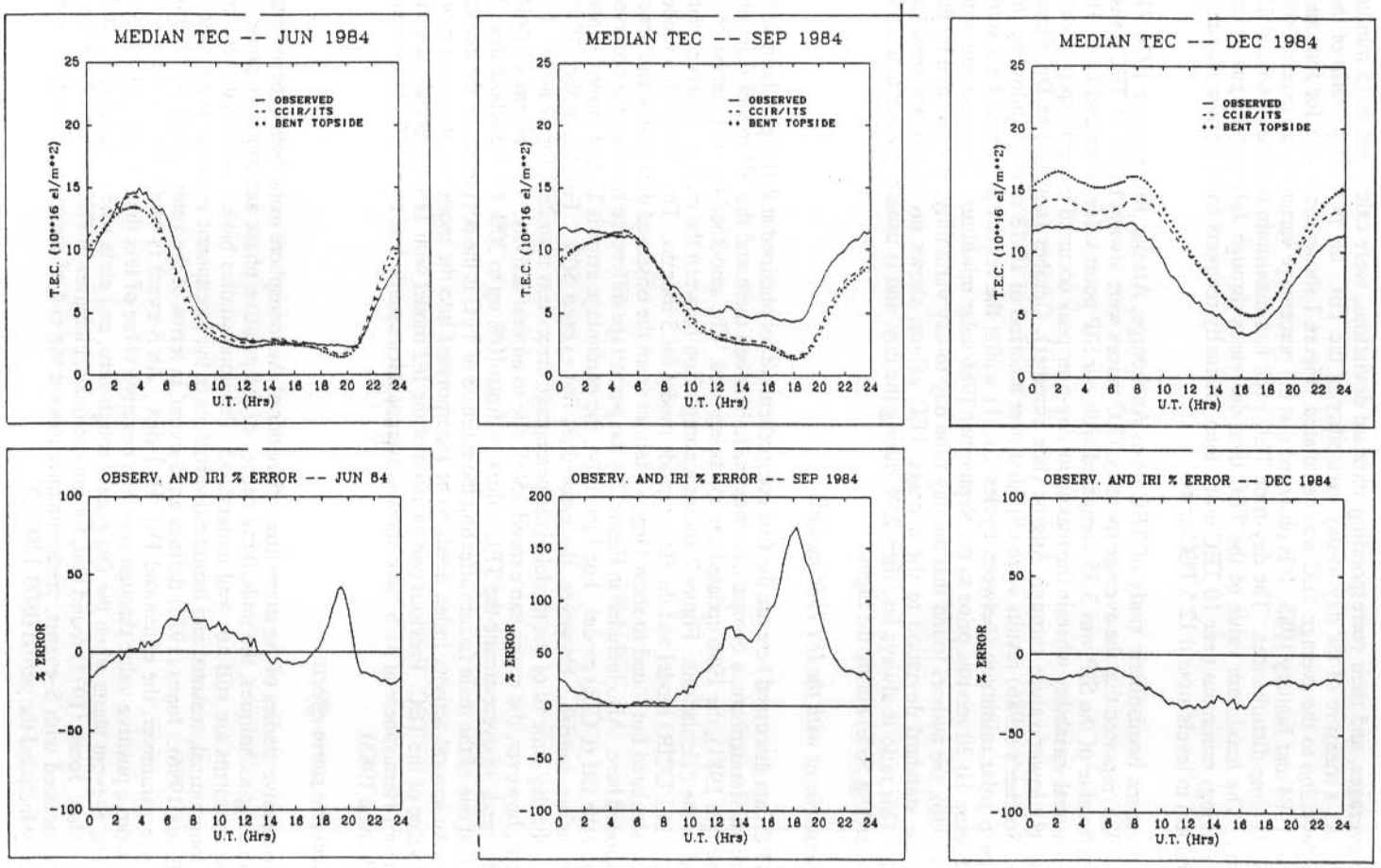

Figure 2. Comparison of the TEC observations with the IRI(CCIR) model for (a) June 1984, (b) September 1984 and (c) December 1984.

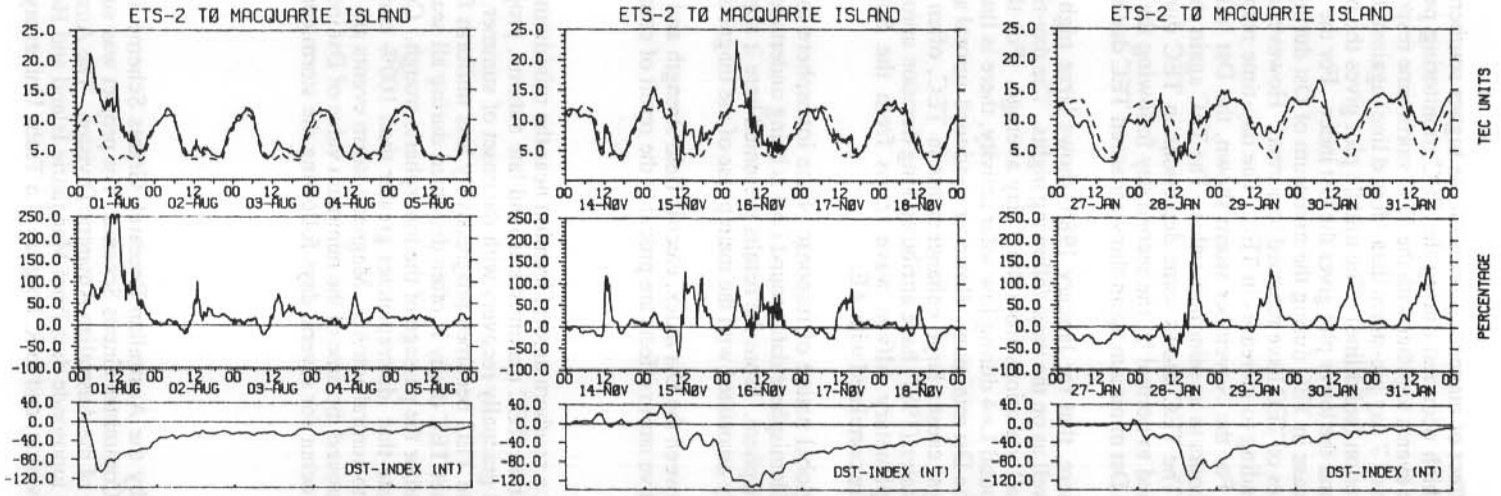

Figure 3. Comparison of the storm time behaviour of the TEC for three storms with the 7 day mean preceding the storm commencement. Also shown are percentage variation of the storm time TEC from the 7 day average and the Dst index.

In order to investigate the effect of magnetic storms on the higher southern latitudes using the TEC data, nine S-events which occurred during the TEC monitoring period were selected. Figure 3 shows three of these events together with the TEC storm time response. The top plot in each figure gives the average of 7 day pre-storm data (dotted line) against the TEC value for the succeeding 5 days of observation (solid line). The middle plot gives the percentage change in TEC throughout the period, and the lower plot gives the Dst index. For the August storm shown (winter) there is a large increase in TEC during the minimum of Dst during the evening hours. The following day-time values of TEC have returned to normal. However at night-time there is continued auroral activity leading to increases in TEC. The day-time response is typical for a mid-latitude winter storm. For the November storm shown, the Dst index shows a gradual decrease over more than 24 hours to its minimum value. The TEC again shows a large increase around the minimum Dst. The TEC shows some depletions in TEC during day-time of the following day but has returned to normal by the second day following the minimum Dst. The first two nights following the Dst minimum again show enhanced TEC due to auroral activity.

The third example shown here, that for January 1985, shows large night-time enhancement during the Dst minimum as well as on the three following nights. The day-time values following the minimum Dst show small variations from the 7 day average. For the magnetic storms' effects on the ionosphere around L=4 during low solar activity, there is little effect on the day-time TEC values following the Dst minimum. However continued auroral activity at night-time, often lasting for several days, causes large enhancements in TEC, often greater than 100%. Recently Tsurutani and Gonzalez (1987) have attributed long duration auroral activity events to outward propagating interplanetary Alfven wave trains from the Sun. The southward components of these waves are correlated with AE.

In order to understand the global nature of response of the ionosphere to magnetic storms, a comparison of our Southern Hemisphere data around L=4 is being undertaken with simultaneous data from the Northern Hemisphere. From the results presented here it appears that storm time increases in TEC are generally associated with the main phase of the magnetic Dst index.

However, the association between the Dst index, electric field strength and thermospheric wind requires further study. Negative storm effects are probably the result of composition changes.

8.3 CONCLUSION

The behaviour of the TEC at a southern auroral location near the minimum of the solar cycle is presented. The peak in day-time TEC maximises around late autumn, progressively decreases through winter to spring and gradually recovers with the onset of summer. The morning post-sunrise build up phase of the TEC becomes progressively less uniform from winter through summer, whilst the post sunset TEC decay is often disrupted during all seasons by the onset of geomagnetic disturbances and/or the passage of the ionospheric trough. Comparisons with the IRI model ionosphere indicate that discrepancies greater than 100% can occur between the observations and model due to auroral activity. Magnetic storm events are generally associated with large increases in TEC around the time of the minimum value of Dst index. Large increases in the night-time TEC often occur for several days following the storm commencement due to auroral activity.

ACKNOWLEDGMENTS

This research is supported by the Australian Research Grants Scheme and by the Australian Antarctic Science Advisory Committee Grants Scheme. The project was supported by the Upper Atmosphere Physics Section of the Australian Antarctic Division. The Australian IPS Radio and Space Services provided the ionosonde data from Macquarie Island and Hobart. Special thanks to Dr G. Burns (Antarctic Division) and to R. Polglase (La Trobe University).

8.4 REFERENCES

Craven, M. *and* Essex, E.A. (1987). Diurnal, seasonal and storm time variability of thetotal electron content of the ionosphere north of Macquarie Island. *ANARE Research Notes Number 56*. Antarctic Division, Kingston.

Essex, E.A. (1986). The effect of magnetic storms on the ionosphere during 1978.*Proceedings of the Beacon Satellite Symposium 1*:187-200. Oulu, Finland.

Jones, K.L. (1971). Storm time variation of the F2 layer electron concentration. *Journal of Atmospheric and Terrestrial Physics 33*:379-389.

Lambert, M. *and* Cohen, E.A. (1986). Monitoring ionospheric irregularities in the southern auroral region by means of a satellite beacon. *Radio Science 21*:347-350.

Lambert, M., Jacklyn, P. *and* Cohen, E.A. (1986). Total electron content of the ionosphere north of Macquarie Island. *ANARE Research Notes Number 34*. Antarctic Division, Kingston.

Lincoln, J.V. *and* Conkright, R.O. (1981). International Reference Ionosphere IRI 79. *World Data Centre - A for Solar Terrestrial Physics, Report UAG 82*. Boulder, Colorado.

McNamara L.F. *and* Wilkinson, P.J. (1983). Prediction of total electron content using theInternational Reference Ionosphere. *Journal of Atmospheric and Terrestrial Physics 45*:169-174.

Soicher, H. (1986). Variability of transionospheric signal time delay at subauroral latitudes. *IEEE Transactions on Antennas and Propagation AP-34*(110):1313-1319.

Tsurutani, B.T. *and* Gonzalez, W.D. (1987). The cause of high intensity long duration continuous AE activity (HILDCAAS): Interplanetary Alfven Wave trains. *Planetary and Space Science 35*:405-412.

9. AN INVESTIGATION INTO THE SOUTHERN HEMISPHERE MID-LATITUDE IONOSPHERIC TROUGH

Michael Mallis
Department of Physics
La Trobe University
Bundoora Vic 3083
Australia

ABSTRACT

Preliminary satellite beacon observations are presented as part of a long-term monitoring study into the latitudinal variation of the *F* region electron content with special emphasis on the Southern Hemisphere mid-latitude ionospheric trough. Of particular interest in this study is the location and storm-time response of the trough as observed from mid- and auroral-latitude sites.

9.1 INTRODUCTION

The mid-latitude (ML) or main trough is a well defined feature of the ionosphere. It can simply be described as a depression in the nocturnal *F* layer electron and total positive ion densities. The ML trough was first reported by Muldrew (1965) and Sharp (1966) from ionograms obtained from the topside sounding satellite Alouette 1. It has been found that the ML trough has a mean position of L ~ 4 and is in the order of 10° latitude wide. The trough minimum is found at about an invariant latitude (Λ) of 65° in the evening hours decreasing to < 60° at later hours local time. It is found to be a persistent night-time feature in both hemispheres with about a 95% occurrence frequency (Ahmed et al. 1979).

The trough is identified as a sharp decrease in the ionisation density with steep poleward and equatorward walls. Although the trough is a night-time phenomena it has been observed in the pre-dusk, dawn and noon-time sectors (Pinnock 1985).

The primary aim of this research is to initially identify the ML trough and then over the course of at least twelve months produce a morphological description of the trough. The differential-Doppler technique used is very well suited for this study as it can provide very high resolution and accurate measurements. In particular it is planned to investigate how the trough responds to storm-time events.

9.2 EXPERIMENT

The experiment essentially consists of monitoring and recording two continuous radio transmissions from the TRANSIT series satellites. These satellites are low altitude (~ 1100 km) polar orbiting beacons with an orbital period of about 107 minutes and are visible for up to 20 minutes to a ground observer. By receiving and later processing these transmissions it is possible to determine the vertical columnar total electron content (TEC) below the satellite. Because the satellite traverses the sky it is possible to construct TEC maps of the sky as a function of latitude spanning up to 15° in latitude either side of the receiver site.

The equipment consists of a modified commercial JMR-1 satellite survey receiver which is interfaced to a desk-top computer. Data are logged onto a 130 mm floppy disk as well as monitored on a thermal chart printer. Three identical sets of equipment have been constructed. Sets are installed at Beveridge (37.3°S, 144.6°E), Victoria, and at Macquarie Island (54.5°S, 159.0°E). A third set is being kept in reserve. The equipment has been fully operational since December 1987. Processing of data is performed at La Trobe University.

Computer programs run at La Trobe University every 3 weeks provide satellite prediction times for those satellites that are to be tracked. These times are manually inputted to the computer which automatically monitors and records satellite transmissions. In the case of Macquarie Island these prediction times are faxed via ANARESAT every 3 weeks. Typically about ten passes can be expected on any one day lasting anywhere from 14 to 18 minutes of recording time. The equipment operates with minimal intervention apart from routine pass-time inputs and disk changes.

Data are logged at 10 Hz (variable from 1 to 20 Hz) for up to 20 minutes per pass which can generate enough data to fill a disk in 5 days at Beveridge and 4 days at Macquarie Island. The main selection criteria for Beveridge is that the maximum local elevation angle of the satellite must rise 45° and above 50° for Macquarie Island, before the whole pass is recorded.

9.3 RESULTS

The result presented here is representative of the sort of data that is being collected at Macquarie Island and Beveridge. The example is the first satellite pass recorded and analysed from Macquarie Island after the experiment was established in December 1987. Figure 1 depicts the sub-ionospheric point trace for a pass of Transit satellite 15362 on day number 341 1987 starting at 0328 UT. Note that the ionospheric height is taken to be at 400 km. The satellite travelled in a southward direction.

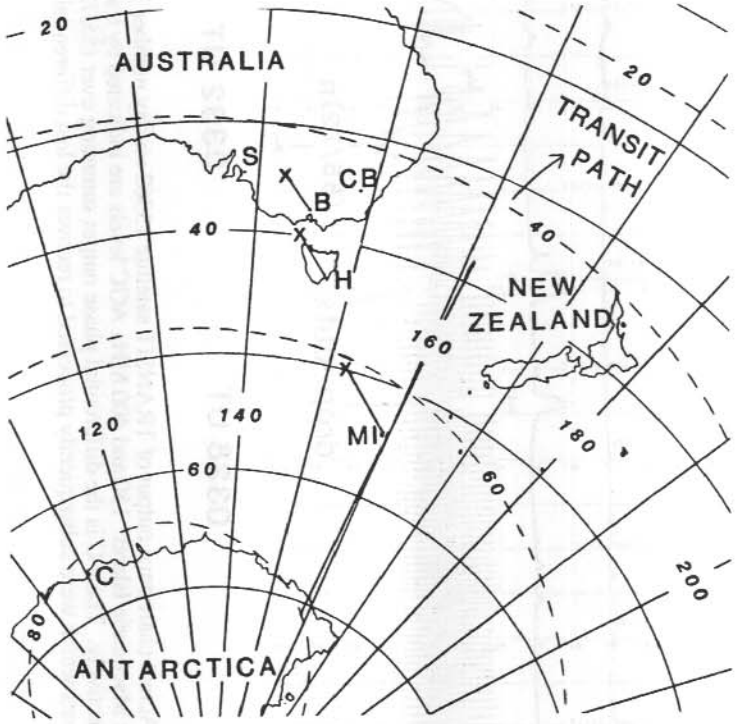

Figure 1. Sub-ionospheric point race for TRANSIT satellite 15362 on day number 341 1987. Also shown are the sub-ionospheric points for the three Faraday Rotation receiver experiments (marked by an X) installed at Beveridge (B), Hobart (H) and Macquarie Island (MI). Dashed lines depict invariant latitude.

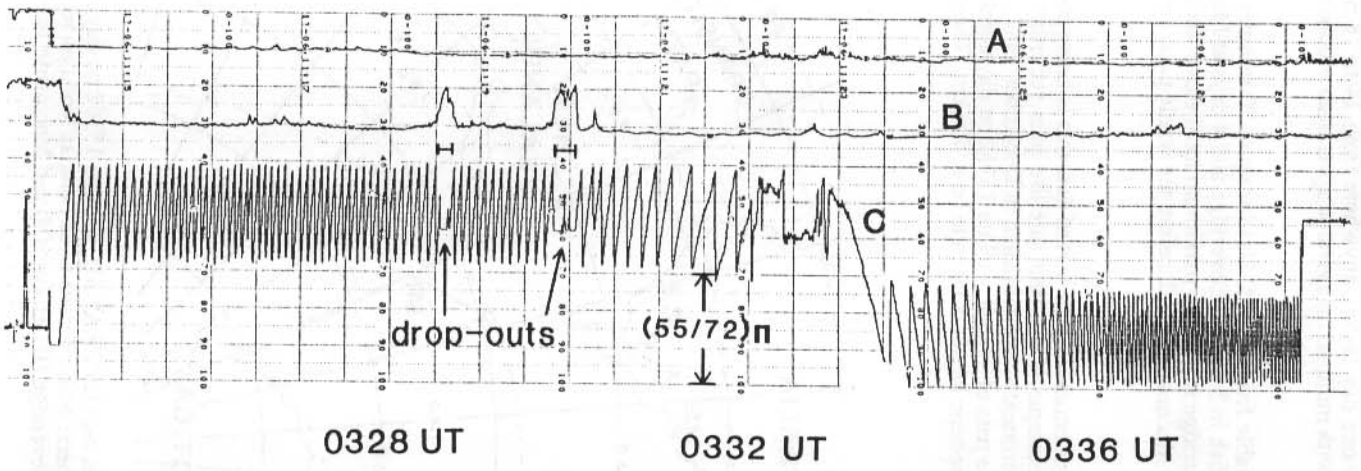

Figure 2. Actual chart trace output of TRANSIT satellite 15362 on day number 341 1987 recorded at Macquarie Island. 150 and 400 MHz AGC levels are indicated by traces labelled B and A respectively. Trace C is the differential phase output summing over $(55/72)\pi$. Note the two drop-outs which were subsequently processed to recover the lost differential phase trace.

Figure 2 shows the output chart trace for this pass. Traces A and B depict the 150 MHz and 400 MHz AGC outputs of the satellite receiver and are used to identify periods of poor signal reception of drop-outs. Two such drop-outs are depicted. Trace C is the differential phase output between the 150 MHz and 400 MHz signals. To recover columnar TEC this trace is merely multiplied by a scaling factor and various constants. Note that only data from a satellite achieving an elevation angle of 30°or more relative to the receiver are analysed and plotted. This is due to unavoidable mathematical and physical constraints that start to introduce errors that cannot be accurately compensated.

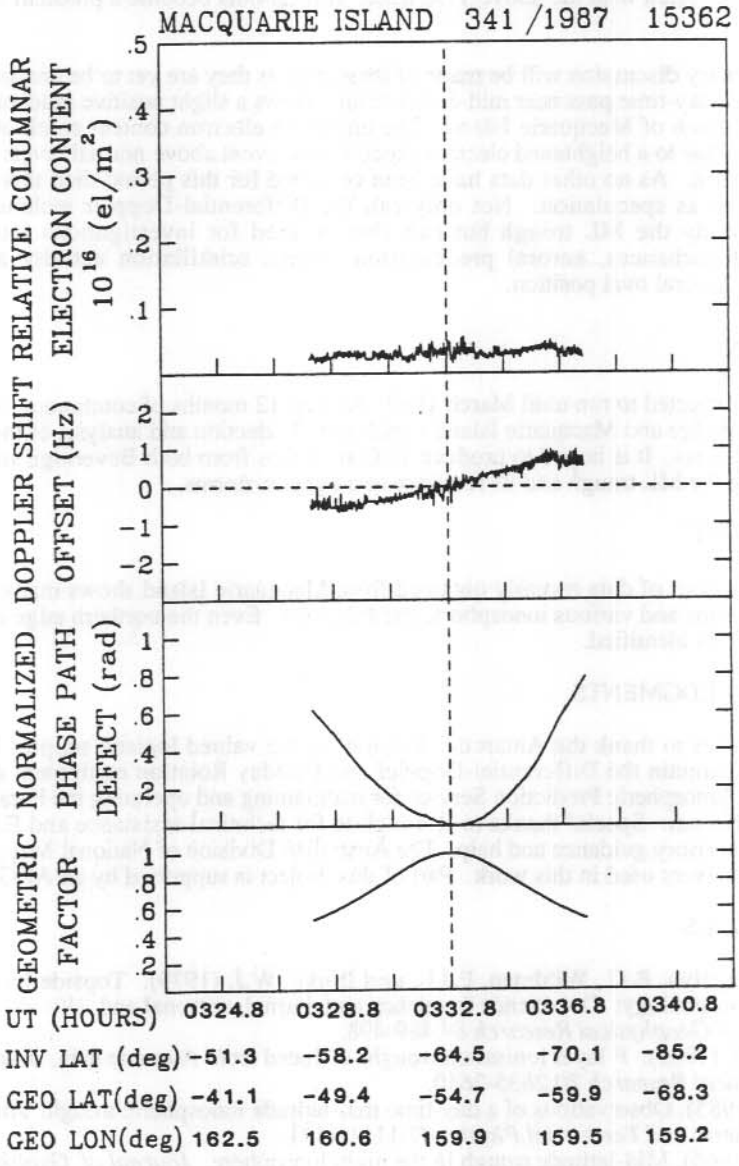

Figure 3. Final analysis of satellite pass showing relative columnar TEC in top panel.

Figure 3 shows the same satellite pass reduced to yield relative columnar TEC (top panel), normalised phase path defect (this is actually trace C of Figure 2 reconstructed and inverted to yield a continuous trace; third panel from top), Doppler shift offset (this is the first time differential of the phase path defect; second panel from top) and the geometric factor (varies as a function of satellite position relative to observer; bottom panel). These traces are plotted as functions of time (UT), invariant latitude, geographic latitude and longitude. The plots of Figure 3 have been put through a 2 Hz filter so that the integrity and veracity of the trace can be preserved. If drop-out periods do not exceed about 10 seconds and are not numerous during the course of a pass then the reconstructed TEC curve is simply 'filled-in' by linear interpolation techniques as occurred with the above TEC trace. If drop-outs become a problem then the pass is rejected.

Only a preliminary discussion will be made of these data as they are yet to be analysed in detail. Figure 3 is for a day-time pass near mid-Summer and shows a slight positive gradient in electron content to the south of Macquarie Island. The enhanced electron content south of Macquarie Island could be due to a heightened electron precipitation event above normal levels perhaps due to magnetic storm. As no other data have been collected for this period then this explanation should be taken as speculation. Not only can the Differential-Doppler technique be used primarily to study the ML trough but can also be used for investigations into travelling ionospheric disturbances, auroral precipitation events, scintillation activity and even in identifying the auroral oval position.

9.4 OUTLOOK

The project is expected to run until March 1989. At least 12 months of continuous data collection from both Beveridge and Macquarie Island is planned. Reduction and analysis of the data will be an on-going process. It is hoped to produce TEC sky maps from both Beveridge and Macquarie Island showing the ML trough and its response to magnetic-storms.

9.5 POSTSCRIPT

Preliminary analysis of data recently obtained from Macquarie Island shows many examples of TIDs, scintillations and various ionospheric irregularities. Even the northern edge of the auroral oval can be clearly identified.

9.6 ACKNOWLEDGMENTS

The author wishes to thank the Antarctic Division for the valued logistic support in helping to establish and maintain the Differential-Doppler and Faraday Rotation equipment at Macquarie Island, and the Ionospheric Prediction Service for maintaining and operating the Faraday Rotation equipment in Hobart. Special thanks to R. Polglase for technical assistance and E.A. Essex for her valued supervisory guidance and help. The Australian Division of National Mapping supplied the geodetic receivers used in this work. Part of this project is supported by an ARGS grant.

9.7 REFERENCES

Ahmed, M., Sagalyn, R.C., Wildman, P.J.L. *and* Burke, W.J. (1979). Topside ionospheric trough morphology: Occurrence frequency and diurnal, seasonal and altitude variations. *Journal of Geophysical Research 84*:489-498.

Muldrew, D. B. (1965). *F* layer ionisation troughs deduced from Alouette data. *Journal of Geophysical Research 70*:2635-2650.

Pinnock, M. (1985). Observations of a day-time mid-latitude ionospheric trough. *Journal of Atmospheric and Terrestrial Physics 47*:1111-1121.

Sharp, G.W. (1966). Mid-latitude trough in the night ionosphere. *Journal of Geophysical Research 71*:1345-1356.

10. THE STUDY OF TRAVELLING IONOSPHERIC DISTURBANCES OVER MACQUARIE ISLAND USING AN OBLIQUE CW SOUNDER

H.M. Beggs[1] and E.C. Butcher[2]

[1]Antarctic Division
Kingston Tas 7050
Australia

[2]Physics Department
La Trobe University
Bundoora Vic 3083
Australia

ABSTRACT

From April to October 1987 an oblique (4° off vertical) HF ionospheric sounder was deployed on Macquarie Island (geographic coordinates 54.5°S, and 159.0°E; invariant coordinates 64.5°S, 177.7°E; L=5.25) in order to study *F* region travelling ionospheric disturbances (TIDs) in the southern auroral region. The amplitude and change in phase path of the received 3.399 MHz continuous signal were recorded digitally, and dynamic power spectra were produced using the maximum entropy method. The periods and occurrence of medium-scale and large-scale travelling ionospheric disturbances were measured from these dynamic power spectra and compared with results from a similar experiment performed in Melbourne, Australia.

Interesting results for day-time travelling ionospheric disturbances for May to August 1987 have been obtained. Many data records illustrate a strong correlation between oscillations in the phase path and the received amplitude of the sounding signal. A minimum in the occurrence of fluctuations in the phase path with periods near 30 minutes has been observed. The day-time signal strength exhibited an apparent cut-off for medium-scale travelling ionospheric disturbances at around 30 minutes. This 'cut-off' was investigated using a ray-tracing program developed by Peter Dyson and John Bennett, which indicated that for constant TID phase speeds the peak-to-peak variation of the amplitude of a radio echo, induced by the passage of a TID, decreases much faster with TID period than does the peak-to-peak variation of the change in phase path.

10.1 INTRODUCTION

Atmospheric gravity waves (AGWs) in the neutral atmosphere manifest themselves as quasi-periodic electron density perturbations when they reach ionospheric heights (Hines 1960). These perturbations are termed travelling ionospheric disturbances (TIDs) and propagate horizontally outwards from the source region. The properties of TIDs (periods, velocities, sources and direction of travel) have been studied extensively, particularly at mid-latitudes (Hunsucker 1982).

TIDs are usually classified as large- or medium-scale, depending on their periodicity, wavelength and horizontal velocity. Both classes of TID are able to propagate horizontally for thousands of kilometres (Francis 1973). Large-scale travelling ionospheric disturbances (LSTIDs) have periods of 50 min to 3 hours, horizontal phase speeds of > 500 m/s (Hunsucker 1987), and originate in the auroral regions, especially during magnetic storms (e.g. Hunsucker 1982, 1987; Davis 1971; Crowley and Williams 1987). They can travel distances up to 1000 km without much attenuation or change in the shape of the wave train (Evans et al. 1983). There has been considerable success in linking individual auroral events to large-scale TIDs observed as they propagated from high- to mid-latitudes (e.g. Hunsucker 1982, Crowley and Williams 1987, Hajkowicz 1983, Francis 1975).

Medium-scale travelling ionospheric disturbances (MSTIDs) have periods of 20-45 minutes and phase speeds of 80-450 m/s (Hunsucker 1987). They are far more commonly observed than LSTIDs, appearing 30-50% of the time in the everyday ionosphere (Titheridge 1968). Sources of MSTIDs may be separated into two classes: (i) tropospheric (meteorological) sources, and (ii) ionospheric sources related to magnetic substorms (Waldock and Jones 1987).

Francis (1975) concluded from early experiments that MSTIDs are more frequent at higher latitudes, consistent with their generation by auroral sources, and can be linked to local magnetic activity. However, Crowley et al. (1987) observed short period TIDs over the Antarctic Peninsula that during magnetically active periods were caused solely by particle precipitation at mid-latitudes, and none of their year's data showed any link between small period TIDs and auroral region sources. This same lack of correlation between the occurrence of MSTIDs and geomagnetic activity has been observed in Finland (Turunen and Nygren 1978) and at Syowa Station, Antarctica (Ogawa et al. 1987). MSTIDs cannot propagate for distances over about 1000 km before dissipative processes dominate (Francis 1975), so Waldock and Jones (1987) proposed that tropospheric sources such as the meteorological jet stream, frontal systems and penetrative convection were more important sources for MSTIDs observed at mid-latitudes. Hunsucker (1982) estimated that 10-20% of medium-scale mid-latitude TIDs may be linked to high-latitude sources. Distributions of wave periods have been obtained for TIDs occurring at mid-latitudes (Joyner and Butcher 1980, Setty et al. 1973, Reddi and Rao 1971, Toman 1976), but very little is known about the TID spectrum in the auroral regions.

Macquarie Island is in a unique situation to study the relationship between TIDs observed in high- and mid-latitudes, as it may be inside or outside the auroral oval depending on the time of day and degree of magnetic activity. Measurements of the period and frequency of occurrence of TIDs have been made on Macquarie Island during 1987 and complement digisonde and phase path sounder data of the same nature obtained in Melbourne, Australia (Joyner and Butcher 1980).

The changing distortions in the isoionic surfaces due to the TIDs can be observed as increases and decreases in phase path of continuous radio waves reflected obliquely from these distorted isoionic surfaces. The phase path technique is a very sensitive means of measuring variations in height, and it is possible to detect perturbations causing even small distortions in the isoionic surface (Reddi and Rao 1971). In 1987 this phase path method was employed in the measurement of the periods and time dependence of TIDs over Macquarie Island, in conjunction with the neglected technique of searching for TID-induced quasi-periodic fluctuations in the amplitude of the obliquely reflected radio signal.

10.2 EXPERIMENT

A continuous double-sideband modulated signal, reflected obliquely from the ionosphere, was chosen in order to monitor TIDs (Baulch et al. 1984). A 30 watt AM transmitter, installed at Hurd Point at the southern end of Macquarie Island, transmitted a 3.399 MHz signal having 2 kHz modulation via a single half wavelength dipole. In order to reduce effects due to ground wave the transmitting dipole antenna was located at the base of a 200 m cliff and oriented towards the receiver. The signal was received at the ANARE station 28 km to the north using crossed delta antennae which were shared with the IPS ionosonde. An o-x separator was used to select for the required ordinary wave. The receiver contained tracking phase-lock loops to track the changes in frequency of the carrier and sidebands. The signals were divided down to 2 kHz and digitally phase detected. The amplitude of the carrier and variations in the phase of the carrier and sidebands were logged to disk every 10 seconds, via a Z80 microprocessor using a Forth routine.

Data were also collected from an IPS ionosonde, a standard riometer, magnetometer and meteorological balloon flights on Macquarie Island with the intention of correlating them with the TID data.

10.3 RESULTS AND DISCUSSION

From May to the end of August 1987 the transmitter at Hurd Point was switched on daily at 2200 UT (0800 AEST) and off at 0400 UT (1400 AEST). During these times the foF2 of the ionosphere above Macquarie Island was above the carrier frequency of 3.399 MHz on 38 of the days and the signal strength was sufficient for the phase-lock loops in the receiver to lock onto the signal. Using ionosonde records obtained at Macquarie Island foE values were determined for these 38 days and found to be all well below 3.399 MHz, hence the signal was received via *F* region reflection mode for these data records. Periodic variations in the change in phase path were observed in 36 days of data. The standard riometer records (showing the degree of absorption of cosmic noise by the ionosphere) were very quiet on all 38 days of data used for analysis. Figure 1(a) gives an example of a record of the change of the phase path per minute, ΔP/min, of the received 3.399 MHz signal for the morning of 26 July 1987. For clearness the one minute data have been smoothed using a running average over 5 minutes. Between 2200 UT and 2300 UT of 25 July 1987, the signal strength was too weak for the receiver to remain in lock. After 2300 UT a quasi-periodic variation, assumed to be the ionospheric signature of an MSTID, with a period of around 18 minutes is evident in the data. Figure 1(b) shows the corresponding signal strength of the carrier averaged over 1 minute.

The unfiltered data sets were input to a maximum entropy program developed by Reid (1979). A window of 120 minutes was chosen, incremented every 5 minutes, with one data point every minute. The optimum order for a window of 120 points was determined to be 30 (25% of the window) by plotting dynamic power spectra over a range of orders and examining for spectral 'splitting'. Figure 2(a) gives the dynamic power spectra of the unsmoothed ΔP/min data over the period 2300 UT to 0400 UT corresponding to the data shown in Figure 1(a). Figure 2(b) gives the dynamic power spectra of the signal strength data shown in Figure 1(b) for the period 2300 UT to 0400 UT. Power is given in dB above sample variance of the data record. There is a noticeable coincidence between the ionospheric disturbance of period approximately 18 minutes in the phase path spectra and a periodic variation in the signal strength spectra. This type of coincidence was evident when studying dynamic power spectra in 24 cases from a total of 88 periodic variations in the ΔP/min data, and 39 quasi-periodic fluctuations in the signal strength data. However, several very strong spectral peaks in the signal strength dynamic power spectra would not be discernible at all in the ΔP/min spectra and vice versa. This is evident, for example, in the strong spectral peak of 11 minutes period in the change in phase path (Figure 2(a)) and the lack of spectral power of the same period in the signal strength (Figure 2(b)).

The observed variations in the amplitude were the effect of the focusing-defocusing of the periodic compressions and rarefactions of the electron density on the transmitted rays, whereas the variations in the change in phase path were caused by a combination of variations in the electron density below the reflection point and fluctuations in the height of reflection.

Both ΔP/min and amplitude data sets were band-pass filtered in the frequency domain in order to study the correlation between the two at the times when, from a study of the dynamic power spectra, TIDs appear to be present. The results of this analysis are presented in Beggs and Butcher (in press).

Histograms were plotted for the frequency of occurrence of a particular periodic variation in the ΔP/min and signal strength records against the total range of periods of the variation (Figures 3(a) and (b) respectively). Thirty-eight days of data were used in the analysis for (a) and 33 for (b). The spectral peaks chosen to be included in these histograms had to fulfil the criteria that their strength was at least 10 dB above the sample variance of the file and that they persisted for longer than two cycles in the dynamic power spectra. Hence, for example, the shaded area in Figure 2(a) would have been included in the analysis for Figure 3(a), and the entire period range included. Dynamic power spectra with data windows of both 120 and 360 minutes were used in this analysis, enabling TIDs with periods up to 180 minutes to be prominent in the dynamic

(a)

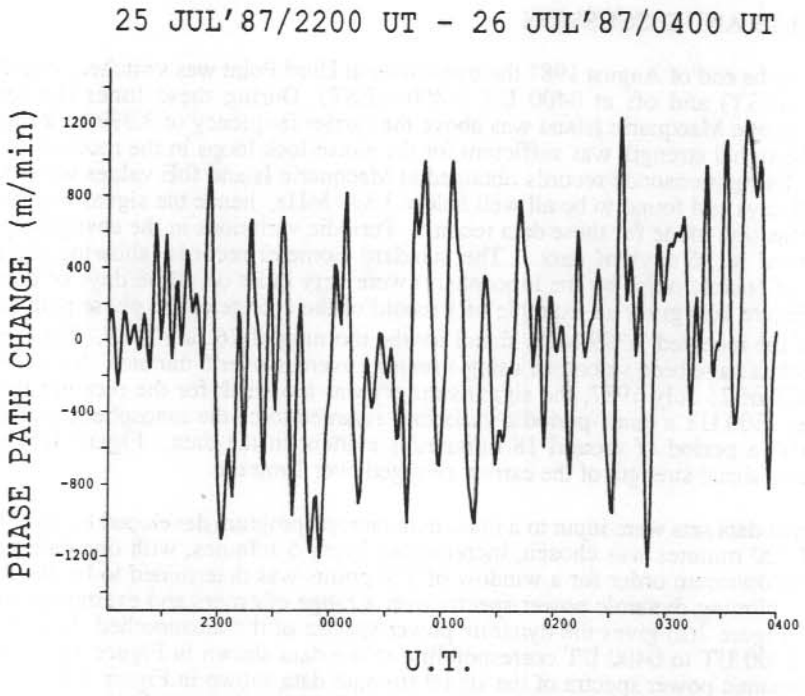

(b)

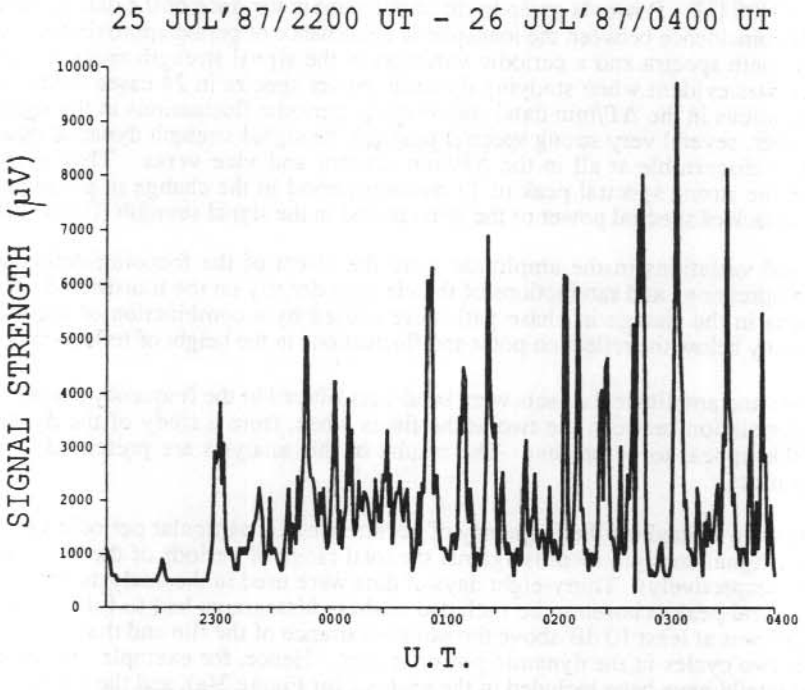

Figure 1(a). The change in phase path per minute band-pass filtered over 5 to 360 minutes for the morning of 26 July 1987. (b). Signal strength variations for the morning of 26 July 1987.

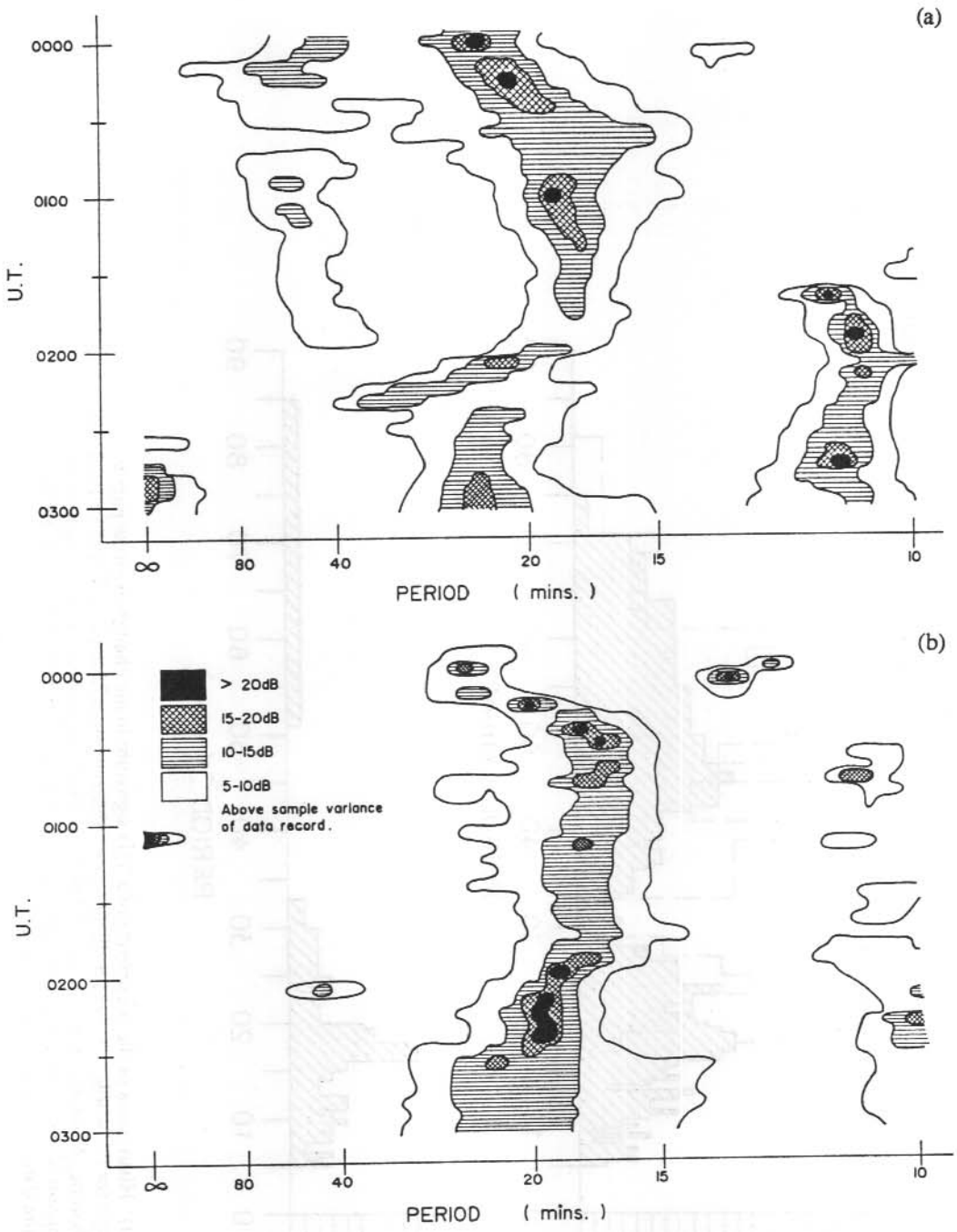

Figure 2(a). Dynamic power spectra of the change in phase path per minute for the data shown in Figure 1(a). (b). Dynamic power spectra of the signal strength for the data shown in Figure 1(b).

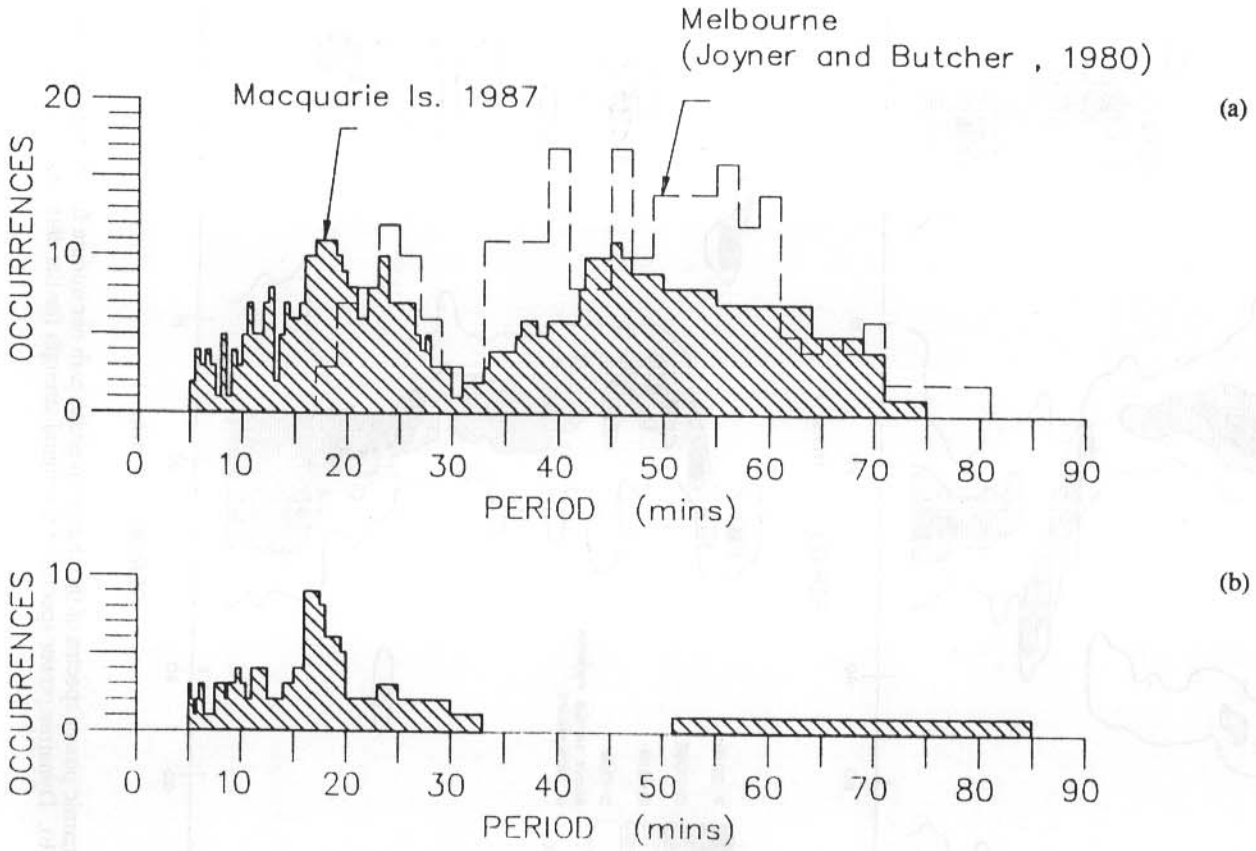

Figure 3(a). Histograms of the occurrence of a TID signature in the change in phase path v. period range for the whole data set for disturbances observed over Macquarie Island in 1987, and over Melbourne, Australia, during July 1973 to April 1974, both using the phase path method. (b). Histogram of the occurrence of periodic variations in the signal strength versus period range for the entire data set from Macquarie Island.

power spectra. However, there appears to be a cut-off, possibly due to the data analysis, from 75 to 85 minutes. The low period cut-off due to the method of analysis was at 5 minutes.

Included in Figure 3(a) is the histogram of the occurrence of a given TID wave period versus period for the change in phase path on a 4.5 MHz CW signal obliquely propagated on 69 nights from July 1973 to April 1974 over Melbourne, Australia (Joyner and Butcher 1980). The extraordinary rather than the ordinary ray, night rather than day, and power spectra rather than dynamic power spectra were used in Joyner and Butcher's analysis. However, it is possible to make a comparison between the two histograms as both give the period *range* of a TID 'wave packet' rather than its *mean* period. Rather different distributions were obtained for the Macquarie Island data when ΔP/min and the signal strength were plotted against the *mean* period of the TID wave packet (Beggs and Butcher, in press). The distributions in Figure 3(a) exhibit a minimum in the occurrence of TIDs with periods of around 30 minutes. Joyner and Butcher interpreted their distribution as being due to two sets of TIDs, one of short period with an upper cut-off near 30 minutes, and the other of longer period with a lower cut-off near 30 minutes. The power contained in those periods > 30 minutes increased with the K-sum for Macquarie Island, about 2200 km south-east of Melbourne, and were assumed to be associated with magnetic activity in the southern auroral region. For periods < 30 minutes there was no correlation between the power in the periods and the K-sum for Macquarie Island and they were assumed to be associated with sources closer to Melbourne. There was no difference in the distribution of the periods of the TIDs over Melbourne for high and low local magnetic activity, implying there was no difference in the source on both occasions. Joyner (1975) did not extend his analysis below 12 minutes, as TIDs below this period were lost in noise.

It is possible that as the Macquarie Island data were collected during the day-time the large-scale TIDs observed in the 1987 data originated to the south of Macquarie Island in the day-time auroral regions. However, an investigation of K-indices from Macquarie Island and Dumont d'Urville revealed no relationship between the magnetic activity in the vicinity, and to the south, of Macquarie Island and the incidence of TIDs observed over Macquarie Island (Beggs and Butcher, in press). This lack of correlation may possibly be linked to the inablility of the experiment to monitor a steady, obliquely propagated signal during magnetically moderate to active periods (i.e. K-index > 2). Good reception was not possible at times when strong magnetic activity occurred and ionospheric sources were most likely to be present.

The histogram in Figure 3(b) is derived from counting the number of periodic perturbations in the signal strength of the received 3.399 MHz signal during the time 2200 UT to 0400 UT on 33 days, using the same criteria as was used to derive the Macquarie Island histogram in Figure 3(a). In this case there appears to be a virtual maximum cut-off at 33 minutes, with only one strong quasi-periodic variation ('wave packet') appearing in the dynamic power spectra at a much larger period. It was suspected that this lack of periodic variation in the signal strength having periods above 33 minutes may have been linked to the ratio of wave perturbation amplitude to wavelength, which, along with their periods, are critical in terms of the magnitude of radio propagation effects (Toman 1976). This was investigated using a ray-tracing program written by Peter Dyson and John Bennett (Bennett and Dyson 1984).

The following parameters were used in the program:

(i) one TID in the F region travelling parallel to the TX-RX baseline
(ii) f_oF2 = critical frequency of Chapman layer = 5 MHz (typical of the quiet day-time ionosphere over Macquarie Island)
(iii) scale height of Chapman layer = 50 km
(iv) no background winds
(v) ground distance between transmitter and receiver = 30 km ~ 0.3° latitude
(vi) radio wave frequency = 3.4 MHz
(vii) no E layer present

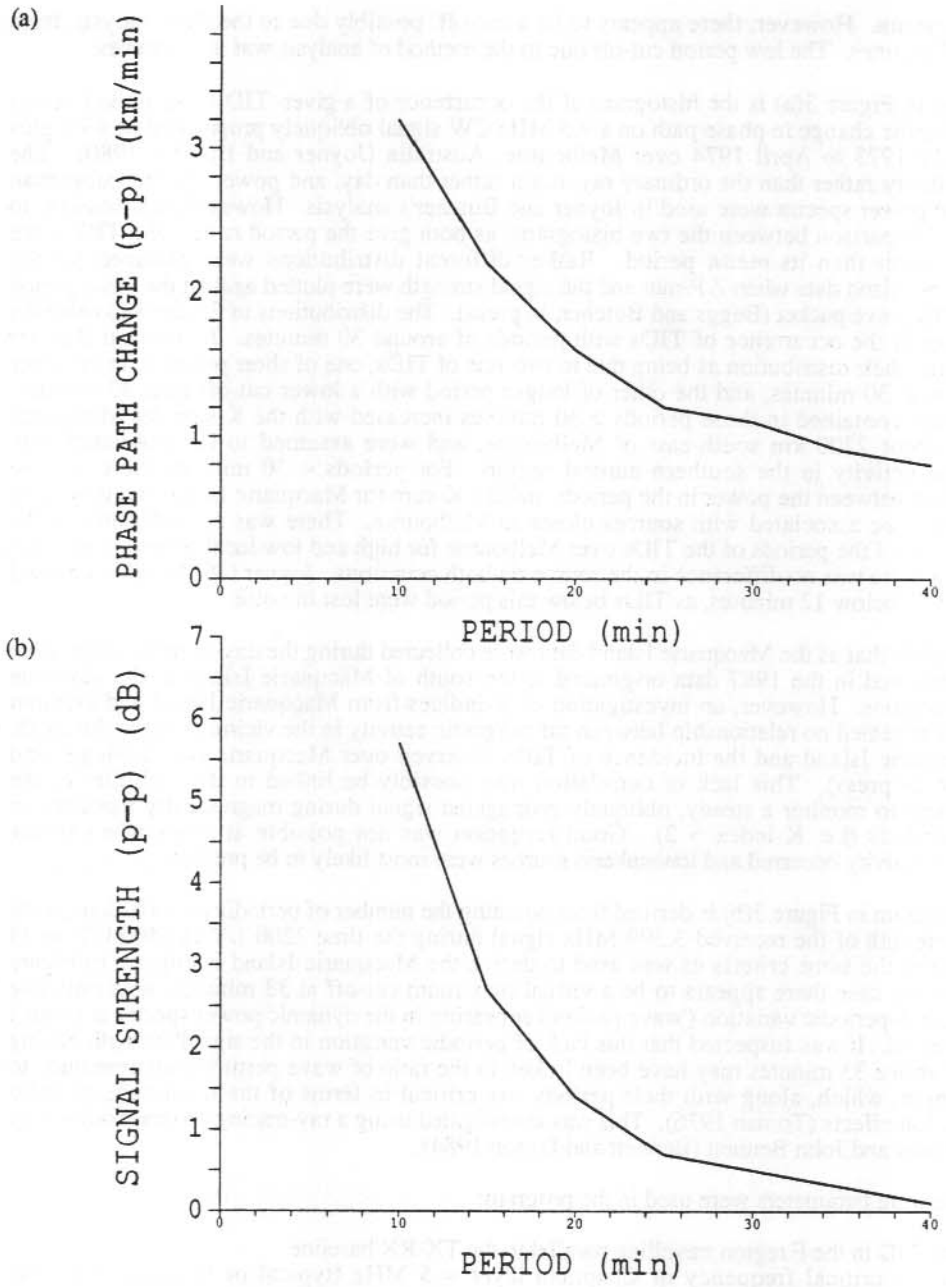

Figure 4. Results of ray-tracing the reflection of a radio wave of frequency 3.4 MHz from the *F* region at an altitude of 182 km, with a variation in reflection height of ±2 km. The horizontal phase speed of the modelled TID was 200 m/s. (a). Magnitude of variations in the change in phase path of the obliquely reflected radio wave with respect to the period of the TID. (b). Magnitude of variations in the divergent power of the radio wave (signal strength) with respect to the period of the TID.

The TID amplitude was input into the ray-tracing programs in terms of percentage change in electron concentration. It was found that the ratio of the TID wavelength (in km) to TID amplitude (in percentage of background electron concentration), λ / α, determined the number of rays reaching the receiver. For $\lambda / \alpha < 12$ (in km/%) there was more than one ray received. The observed peak-to-peak variation in phase path, P_{p-p}, of the day-time Macquarie Island signal did not exceed 10 km on those days used for analysis. Using ray-tracing it was found that $P_{p-p} = 10$ km corresponded to a value of $\alpha = 10\%$ and a peak-to-peak variation in reflection height of about 7.5 km in this case. For medium-scale TIDs the phase speed lies in the range 80 m/s < V < 450 m/s (Hunsucker 1987) and the range of periods is 10 minutes < τ < 60 minutes (Waldock and Jones 1987), implying that 48 km < λ < 1620 km. Hence, in the case of the day-time Macquarie Island oblique propagation experiment, for interference to occur λ must be less than 120 km when α is at its maximum value of 10%. For typical values of $\alpha = 5\%$, λ would have to be less than 60 km in order that more than one reflected ray be received. Such low wavelengths for MSTIDs are extremely unlikely, and so it was considered that the Macquarie Island day-time data suffered very little, if any, interference from multiple reflections.

Ray-tracing results indicated that:

(i) TID-induced fluctuations in the phase path, P, and divergent power at the receiver (signal strength) were in phase with variations in the reflection height, and were of the same period. As was evident in the Macquarie Island data, the ray-tracing programs showed that variation in ΔP/min leads the variation in signal strength by 90°.

(ii) The magnitude of the variations in the phase path, P_{p-p}, induced by a TID is proportional to the percentage variation in electron concentration at the height of reflection, but is independent of wavelength, period or phase speed of the TID.

(iii) The magnitude of the variations in the change in phase path with time, $(\Delta P/\Delta t)_{p-p}$, increases with increasing TID amplitude, and decreases inversely with increasing TID period. $(\Delta P/\Delta t)_{p-p}$ is independent of the TID phase speed or wavelength. In fact, $(\Delta P/\Delta t)_{p-p} = k_1/\tau = 1/(3\tau)$ (km/min) (see Figure 4(a)).

(iv) The magnitude of the variations in the signal strength, A_{p-p}, increases with increasing TID amplitude (in percentage of background electron concentration), and decreases approximately inversely with TID wavelength. A_{p-p} is independent of TID phase speed or period. However, if the TID phase speed, V, remains constant then A_{p-p} is approximately inversely proportional to the period, $A_{p-p} \equiv k_2/\tau$ (km/min) (see Figure 4(b)).

From a comparison of Figures 4(a) and (b) it may readily be seen that the variations in the signal strength, A_{p-p}, induced by the passage of a TID at the height of reflection, decrease much faster with TID period than do the variations in $(\Delta P/\Delta t)_{p-p}$, i.e. $k_2 < k_1$. This may have been the cause of the apparent 'cut off' in the signal strength variations above periods of 33 minutes. Unfortunately, due to the difficulty in comparing theoretical and actual antennae and receiver gains between the ray-tracing program and the experiment, it was not possible to determine by means of ray-tracing the phase speed of the TIDs observed over Macquarie Island.

10.4 ACKNOWLEDGMENTS

The observations were carried out at the Australian National Antarctic Research Expedition's station at Macquarie Island. The authors thank the Director, Antarctic Division, Department of the Arts, Sport, the Environment, Tourism and Territories for logistic support. This work was supported by the Australian Research Grants Scheme. Many people contributed to the success of this experiment. Our thanks go to Bill Cercone, Robert Polglase, Peter Hammer of La Trobe University; Mark Loveridge, Dave Barrett and Howard Burton of Antarctic Division; and Darryel Binns of National Parks and Wildlife Service. The authors would like to acknowledge the generous advice and assistance of Dr John Reid of CSIRO in Hobart, George Goldstone of IPS, and Drs Peter Dyson and John Bennett for the use of their ray-tracing program. K-indices were supplied by Stewart Dennis of the Bureau of Mineral Resources. Drafting of figures was performed by John Cox of the Antarctic Division.

10.5 REFERENCES

Baulch, R.N.E., Butcher, E.C., Devlin, J.C. *and* Hammer, P.R. (1984). A simple sounder to measure the properties of ionospherically reflected radio waves. *Journal of Atmospheric and Terrestrial Physics 46*:895-903.

Beggs, H.M. *and* Butcher, E.C. (in press). A study of travelling ionospheric disturbances over Macquarie Island using an oblique cw sounder. *Planetary and Space Science.*

Crowley, G., Jones, T.B. and Dudeney, J.R. (1987). Comparison of short period T.I.D. morphologies in Antarctica during geomagnetically quiet and active intervals. *Journal of Atmospheric and Terrestrial Physics 49*:1155-1162.

Crowley, G. *and* Williams, P. J. S. (1987). Observations of the source and propagation of atmospheric gravity waves. *Nature 328*:231-233.

Davis, M.J. (1971). On polar substorms as the source of large-scale travelling ionospheric disturbances. *Journal of Geophysical Research 76*:4525-4533.

Bennett, J.A *and* Dyson, P.L. (1984). New ray tracing techniques and their application to the study of ionospheric irregularities. In: *Proceedings of the Australian Institute of Physics, Sixth National Congress, August 1984, Griffith University 81*:27-31.

Evans, J.V., Holt, J.M. *and* Wand, R.H. (1983). A differential-Doppler study of travelling ionospheric disturbances from Millstone Hill. *Radio Science 18*:435- 451.

Francis, S.H. (1973). Lower-atmospheric gravity modes and their relation to medium- scale travelling ionospheric disturbances. *Journal of Geophysical Research 78*:8289-8295.

Francis, S.H. (1975). Global propagation of atmospheric gravity waves: a review. *Journal of Atmospheric and Terrestrial Physics 37*:1011-1054.

Hajkowicz, L.A. (1983). Auroral riometer absorptions and the *F* region disturbances observed over a wide range of latitudes. *Journal of Atmospheric and Terrestrial Physics 45*:175 179.

Hines, C.O. (1960). Internal atmospheric gravity waves at ionospheric heights. *Canadian Journal of Physics 38*:1441-1481.

Hunsucker, R. D. (1982). Atmospheric gravity waves generated in the high-latitude ionosphere: a review. *Reviews of Geophysical and Space Physics 20*:293-315.

Hunsucker, R.D. (1987). The sources of gravity waves. *Nature 328*:204-205.

Joyner, K.H. *and* Butcher, E.C. (1980). Gravity wave effects in the night time F region. *Journal of Atmospheric and Terrestrial Physics 42*:455-459.

Ogawa, T., Igarashi, K., Aikyo, K. *and* Maeno, H. (1987). NNSS satellite observations of medium-scale traveling ionospheric disturbances at southern high-latitudes. *Journal of Geomagnetism and Geoelectricity 39*:709-721.

Reddi, C.R. *and* Rao, B.R. (1971). Characteristics of travelling ionospheric perturbations over Waltair using phase path technique. *Journal of Atmospheric and Terrestrial Physics 33*:251-266.

Reid, J.S. (1979). Confidence limits and maximum entropy spectra. *Journal of Geophysical Research 84*:5289-5301.

Setty, C.S. G.K., Gupta, A.B. *and* Nagpal, O.P. (1973). Ionospheric response to internal gravity waves observed at Delhi. *Journal of Atmospheric and Terrestrial Physics 35*:1351-1361.

Titheridge, J.E. (1968). Periodic disturbances in the ionosphere. *Journal of Geophysical Research 73*:243-252.

Toman, K. (1976). On wavelike perturbations in the *F* region. *Radio Science 11*:107- 119.

Turunen, Y. *and* Nygren, T. (1978). Observation of gravity waves in the high-latitude *F* layer by using fixed frequency sounding. *Journal of Atmospheric and Terrestrial Physics 40*:1303-1308.

Waldock, J.A. *and* Jones, T.B. (1987). Source regions of medium scale travelling ionospheric disturbances observed at mid-latitudes. *Journal of Atmospheric and Terrestrial Physics 49*:105-114.

11. Pi(b) AND Pi2 GEOMAGNETIC PULSATIONS ASSOCIATED WITH SUBSTORM ONSET

I.F. Grant[1,2], G.B. Burns[1] and K.D. Cole[2]

[1]Antarctic Division
Kingston Tas 7050
Australia

[2]Physics Department
La Trobe University
Bundoora Vic 3083
Australia

ABSTRACT

Observations of Pi(b) and Pi2 geomagnetic pulsations and of the associated auroral intensity variations made from Macquarie Island are presented. For Pi(b) the induction magnetometer signal correlated better with the time derivative of the auroral intensity variations than with the intensity itself. The optical and magnetic variations were simultaneous to within 10 seconds, supporting a precipitation-driven ionospheric source for Pi(b). A simple model of a circular patch of enhanced *E* region conductivity is able to produce some of the observed features of the magnetic pulsations, notably the abrupt reversals in rotation direction of the horizontal polarisation vector. Pi2 which have the polarisation rotation sustained in one direction for several cycles cannot be explained easily by the model.

11.1 INTRODUCTION

The Pi(b) and Pi2 classes of geomagnetic pulsations are closely associated with the onset of auroral substorms. Both types have an impulsive wave of a few minutes duration. Pi2 are trains of damped sinusoidal oscillations with period 40-150 seconds. Pi(b) have an irregular waveform and have a broad spectrum which can extend from Pi2 frequencies up to 10 Hz. Pi(b) are seen only near the auroral zone close to magnetic midnight. Pi2, while strongest at auroral latitudes at night, are not as localised in either latitude or time as are Pi(b). In fact Pi2 are observed at low latitudes and in the day-time (Saito 1969). At any particular station, there are intermediate events covering the full range of appearances between the Pi(b) and Pi2 just described. Figure 1 shows a variety of event types.

The generation mechanisms of both classes of magnetic disturbance are still uncertain. There is much evidence of a close association of Pi(b) with the precipitation of energetic electrons (Heacock and Hunsucker 1981). Pi(b) occur only at the brightening or distortion of active auroral arcs which is typical of substorm break-up and expansion. Pi(b) have been observed associated with fluctuations of ionospheric electron density observed by riometer (Heacock and Hunsucker 1977, Lanzerotti et al. 1978, Haldoupis et al. 1982) or radar (Haldoupis and Nielsen 1983). Auroral precipitation varies the *E* region electron density and hence the *E* region conductivity. The fluctuating *E* region currents which might result are a possible explanation for the associated magnetic pulsations. Hydromagnetic waves originating in the magnetosphere have also been proposed to explain Pi(b) (e.g. Bosinger and Wedeken 1987).

The most common explanation for auroral Pi2 is that it is a field-line resonance (Baumjohann and Glassmeier 1984). It is generally believed that at the onset of a substorm, part of the current flowing across the magnetotail in the equatorial plane is diverted through the ionosphere via field-aligned currents (FACs) (McPherron et al. 1973). This reconfiguration of the magnetospheric current system is expected to produce a transient hydromagnetic wave on a closed field line, successively reflecting from conjugate ionospheres. The hydromagnetic wave would be

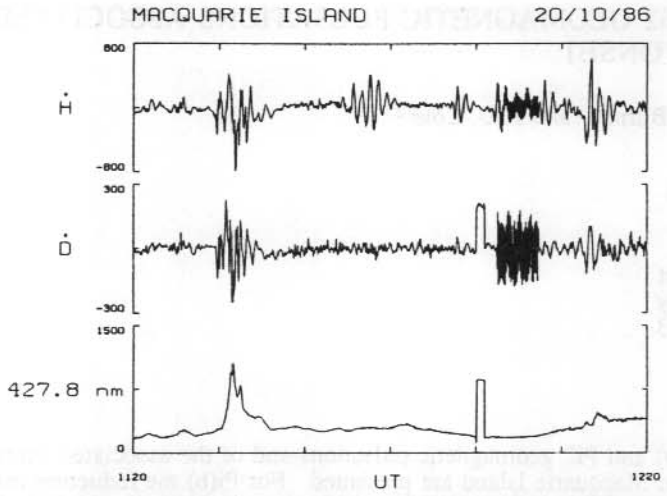

Figure 1. A 60 minute length of digital data from Macquarie Island containing several Pi(b) and Pi2 events. The vertical scales are arbitrary and the H and D pulsation scales are equal to within 10%.

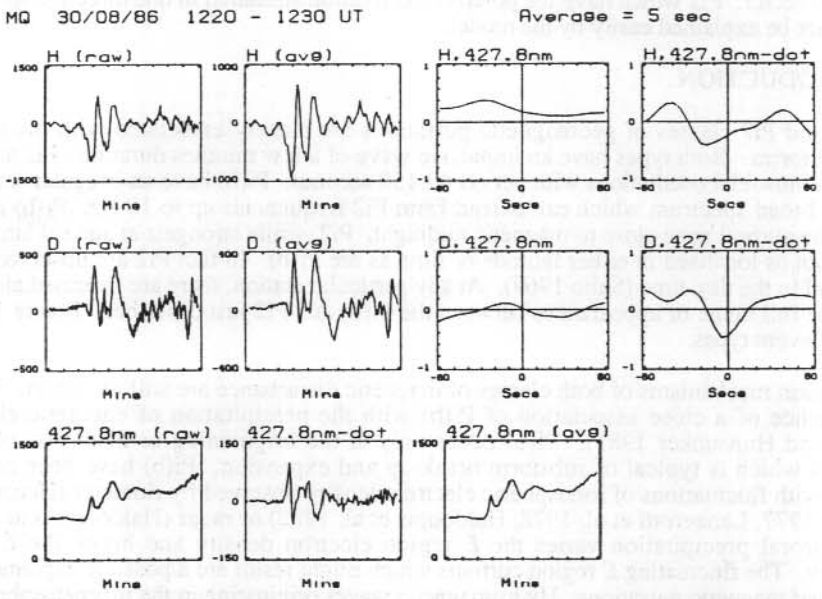

Figure 2. Data and cross-correlations for a 10 minute data block. The plots in the first column show the raw data from the H and D induction magnetometers and the 427.8 nm photometer. The scales are as in Figure 1. The second column shows the H and D signals after smoothing by averaging, and the photometer signal after smoothing and differentiation. The smoothed but undifferentiated photometer trace is at the bottom of the third column. The remaining four plots in the top-right corner are the cross-correlation functions of each of the H and D smoothed magnetic signals with the undifferentiated (4278A) and differentiated (4278A-dot) smoothed photometer signal. The magnetic pulsation signal leads the optical for a positive lag.

accompanied by an oscillating FAC. The Pi2 observed on the ground might be due to ionospheric currents induced by the hydromagnetic wave (Samson and Rostoker 1983) or by its accompanying FAC (Pashin et al. 1982), or might be the direct magnetic field of the FAC (Tamao 1986). Pi2 have been observed to be correlated with modulation of electron precipitation (Stuart et al. 1977) and with auroral intensity fluctuations (Namgaladze et al. 1967, Fukunishi and Hirasawa 1970). This suggests that precipitation-modulation of ionospheric currents should also be examined for Pi2.

In this paper the authors investigate precipitation-modulated ionospheric currents as a possible mechanism for the generation of Pi(b) and Pi2. They compare the magnetic fluctuations with auroral intensity variations and examine a simple model of a patch of enhanced *E* region conductivity to determine the type of magnetic signatures which can result from this mechanism.

11.2 OBSERVATIONS

The data discussed here were collected at the ANARE station at Macquarie Island (geographic coordinates 54.5°S, 159.0°E; geomagnetic coordinates 64.5°S, 177.7°E) between April and December 1986. Induction magnetometers monitored the three orthogonal components of the geomagnetic field, although only the H (north-south) and D (east-west) components are used here. A zenith-oriented photometer with a 60° field of view measured auroral emission at 427.8 nm at night. During each night the three magnetic signals and the optical signal were digitised five times per second and stored in 10 minute blocks. Those blocks containing Pi(b) or Pi2 activity were retained after each night. An all-sky camera was operated at one frame per minute when the sky was expected to be clear.

11.3 CROSS-CORRELATION ANALYSIS

Grant et al. (1988) have found that Pi(b) are usually accompanied by variations in auroral optical intensity while Pi2 are usually not. To see how closely Pi(b) are associated with auroral electron precipitation, the optical and magnetic signals were compared by cross-correlation. Cross-correlation has been very successfully used to support precipitation-modulated *E* region conductivity as the mechanism for the PiC magnetic pulsations associated with pulsating aurora (Oguti et al. 1984, Oguti and Hayashi 1984, Burns and Cole 1985, Burns and Craven (in press)).

The authors have measured the auroral intensity I and the time derivative of the geomagnetic field dB/dt as functions of time. For the 427.8 nm emission, I is essentially proportional to the ionisation rate Q with negligible time delay. For a fixed electric field, the size of the magnetic perturbation ΔB due to any modification of the *E* region current system will be roughly proportional to the current fluctuation, and hence to the change in *E* region conductivity, and thus to the electron density n. Hence dB/dt will be roughly proportional to dn/dt. The ionospheric rate equation is

$$\frac{dn}{dt} = Q - \alpha n^2$$

where α is the recombination coefficient. Interpreting Jones and Rees' (1973) theoretical results, the characteristic response time for the ionisation of the night-time auroral *E* region is 5 to 20 seconds. The auroral luminosity variations examined here are on a time scale of about 1 minute and so are slower than the ionospheric response. Under these conditions the rate equation is approximately $n \sim Q^{1/2}$. Thus we expect the induction magnetometer signal dB/dt to correlate better with dI/dt than with I. This contrasts with PiC which have a 5 to 10 second period, for which case the rate equation becomes $dn/dt \sim Q$ and the correlation is found to be better with I.

The data were processed in the 10 minute lengths in which they were recorded. The H, D and optical signals were each averaged to one point every 5 seconds. Then each of H and D was

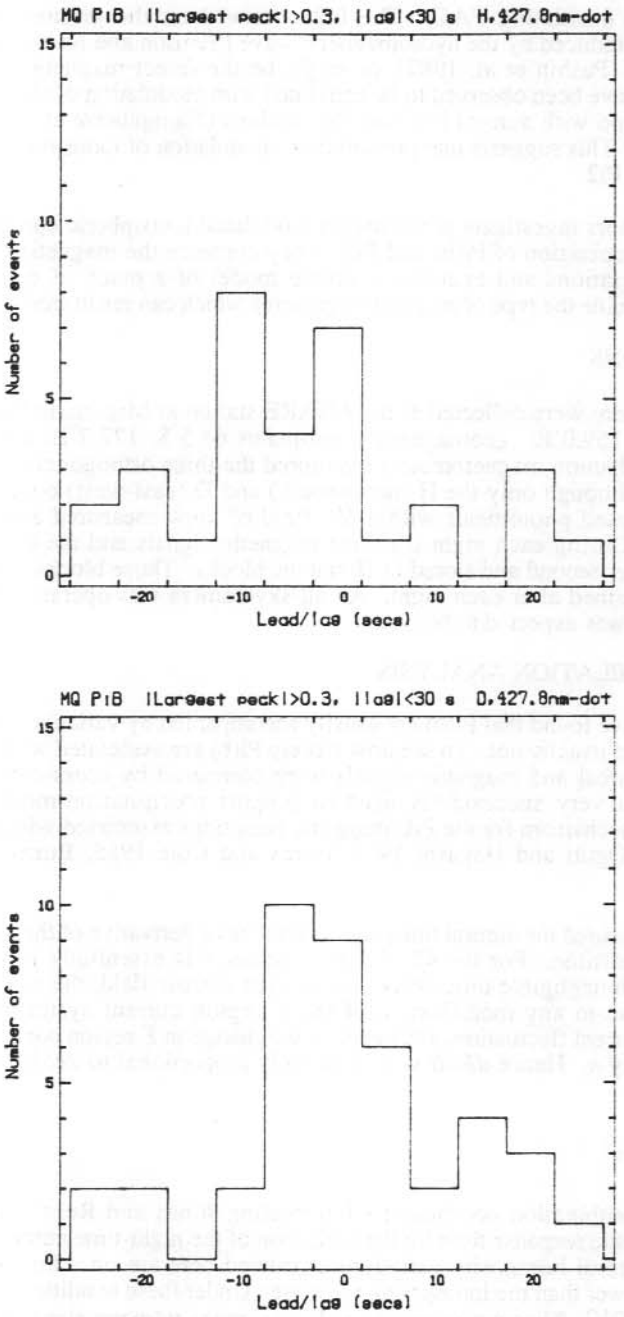

Figure 3. Histogram of lags of the cross-correlation function peak which has the largest absolute value of correlation coefficient of the peaks lying less than 30 seconds from zero. The cross-correlations are for the derivative of the optical signal with the H (top) and D (bottom) magnetic pulsation signal.

correlated with the optical signal and with its derivative. Figure 2 is a typical example. The *dI/dt* cross-correlation functions show the peaks expected from a notable correlation, while the cross-correlations with *I* are flatter, indicating a poorer correlation.

If Pi(b) are driven by precipitation, the cross-correlations should have a peak near zero lag. Most of the *dI/dt* correlations do have a peak near zero lag but often other, sometimes stronger peaks are present also, due to periodicities in the signals. Thus for each cross-correlation we measured the location of the peak within 30 seconds of zero lag with the largest absolute value of correlation coefficient. Figure 3 shows the distribution of lags. It is clear that the lags cluster near zero, showing that the Pi(b) magnetic fluctuations are coincident with the precipitation variations to within 10 seconds.

11.4 CURRENT SYSTEM MODEL

To see what magnetic signatures might be produced by a patch of enhanced *E* region conductivity, the authors used the existing model developed by Oguti and Hayashi (1984) to study PiC.

The model considers the conducting region of the ionosphere as a two-dimensional horizontal distribution of height-integrated conductivities which may be visualised as a sheet ionosphere. The ambient geomagnetic field is taken as vertical. The height-integrated Hall and Pedersen conductivities are greater inside a circular patch of the sheet than outside and uniform in both regions. The ambient convection electric field is imposed in the plane of the sheet, causing polarisation charges to appear at the patch boundary and a consequent modification of the electric field near the patch. Charge build-up is balanced by discharge by Pedersen currents inside and outside the patch and by FACs terminating only on the patch boundary. The percentage of the discharge current which is field-aligned is fixed to be P% at all points on the boundary. The arrangement of charges and currents is assumed to be at equilibrium and static. The two-dimensional Laplace's equation is solved to give the modified electric field which together with the assumed conductivity distribution yields the modified current system. Subtracting the ambient current system (i.e. that with no conductivity enhancement) leaves the modified current system introduced by enhancing the circular patch's conductivity (e.g. Figure 4(a)). Using the Biot-Savart Law, the magnetic field due to the modified current system may be calculated analytically for a point under the centre of the patch, or numerically for a general point on the ground (Figure 4(b)).

For the simplest Pi(b) events, the auroral intensity is a simple peak - monotonically increasing, then decreasing. Such peaks typically last one or two minutes. An attempt was made to model these events. It was presumed that the optical peak is produced either by the steady rise and then fall of the conductivity of a region within the field of view, or by a patch of constant, enhanced conductivity passing into and then out of the field. The 1 minute resolution of the available all-sky camera film did not allow a determination of which process was responsible for any particular brightness peak. Thus the model was used to determine the predicted magnetic perturbation for each process.

For the conductivities outside and inside the patch, the values for quiet and disturbed midnight conditions were used respectively, as reported by Brekke et al. (1974) and Baumjohann et al. (1981). The ambient electric field was taken as westward, since the field is near that direction at the time of break-up or Pi(b) onset (Brekke et al. 1974, Baumjohann et al. 1981).

To determine the effect of varying conductivity, the conductivity peak was modelled by one cycle of an offset sine wave. At a series of times, the magnetic perturbation under the centre of the patch (corresponding to a patch stationary overhead) was determined for the instantaneous conductivity, and successive values were differenced to estimate the time derivative of the magnetic field for comparison with the induction magnetometer output. Figure 5(a) shows the typical behaviour of the resulting horizontal polarisation vector. During the conductivity rise, the

(a)

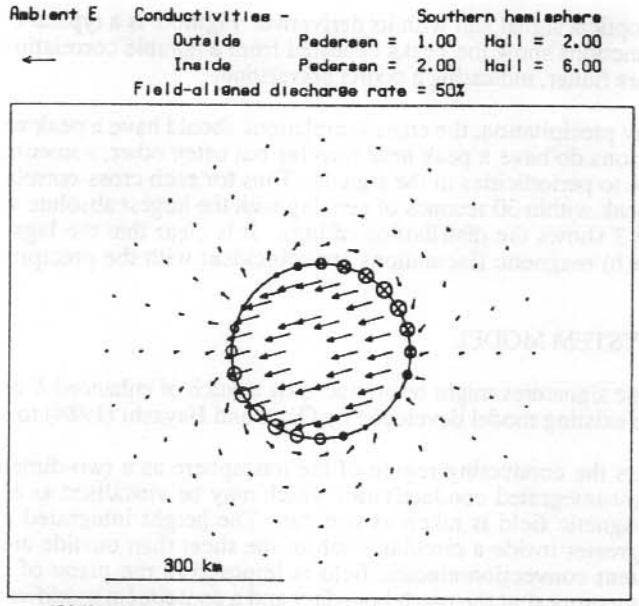

MODIFICATION CURRENTS

(b)

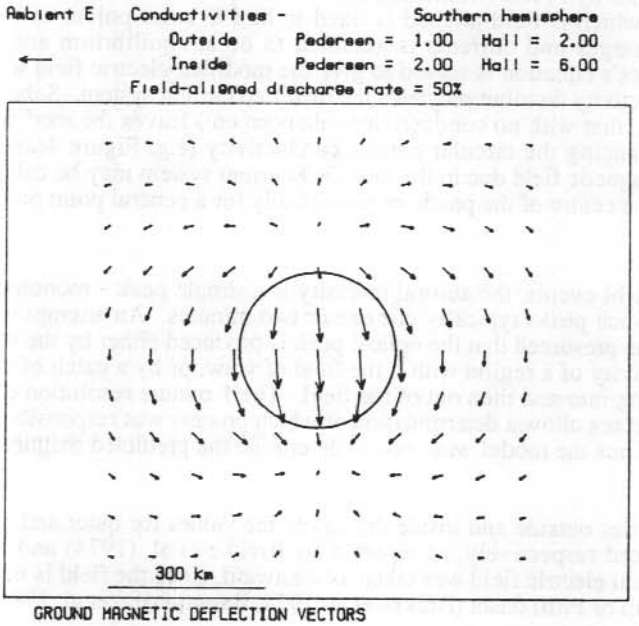

GROUND MAGNETIC DEFLECTION VECTORS

Figure 4(a). The pattern of additional electric currents in and around a circular patch of enhanced *E* region conductivity as predicted by the Oguti and Hayashi (1984) model. The vectors into and out of the page on the boundary of the patch are downward and upward directed field-aligned currents respectively. The other vectors are in the plane of the ionosphere. The height-integrated conductivities are in siemens. (b). The resulting pattern of magnetic perturbation vectors on the ground under the patch.

vector rotates in first one sense then the other. It then flips 180° and executes the reverse sequence of rotations during the fall in conductivity. Repeated reversals of rotation sense have been reported for Pi(b) (Haldoupis et al. 1982) and for auroral Pi2 (Pashin et al. 1982).

To predict the effects of motion of the patch, fixed values for the model parameters were used. The magnetic field was evaluated at points along a line on the ground and successive values differenced to again give the induction magnetometer response (Figure 5(b)). The behaviour of the polarisation vector for a moving patch can be similar to that for a conductivity peak. If the patch passes to one side of the observer, the magnitude of the vector passes through a non-zero minimum at the time of closest approach, and the direction of rotation may reverse before or after this point.

In comparing these predictions with the data collected for this study, it must be remembered that conductivity variations will lag 5-10 seconds behind auroral luminosity variations because of the ionisation response.

On examining those recorded events with essentially simple single peaks in luminosity, one finds that while very few match either type of prediction in all respects, many events show some corresponding features. Figure 6(a) shows one of the best matches to the behaviour of the polarisation vector expected from a changing conductivity (cf. Figure 5(a)). The reversals in rotation sense and the 180° flip in direction are as described above. The vector passes through zero about 20 seconds after the last luminosity maximum. This is at the long end of the expected range of delays. However, the initial deflection is predominantly northward rather than southward as the model predicts for a westward ambient electric field. In other cases the initial rotation sense is wrong.

Some Pi2 clearly do not fit the model. Figure 6(b) shows a Pi2 for which the polarisation vector rotates three cycles, whereas little more than 360° can be produced by the model for either a conductivity peak or a moving patch.

11.5 CONCLUSIONS

We have shown that Pi(b) magnetic fluctuations are correlated with auroral particle precipitation with a time difference of less than 10 seconds. This supports a precipitation-controlled source in the *E* region for Pi(b). We have found that a very simple model of enhanced *E* region conductivity can produce magnetic perturbations on the ground with some of the features of Pi(b) and Pi2 pulsations, in particular the rotation reversals of the horizontal polarisation vector.

To take this modelling further, a more realistic geometry should be used, better matching the shape of the patch to an auroral arc. To allow stringent comparison of theory with observation, a fast auroral imaging system - TV with video, for example - is needed to follow the intensity changes and motion of auroral forms during the dynamic break-up phase of the substorm.

ACKNOWLEDGMENTS

The induction magnetometers used in this study were provided by the Geophysical Institute, University of Alaska. ANARE expeditioners at Macquarie Island in 1986, particularly S. Jongens, helped with the data collection.

11.6 REFERENCES

Baumjohann, W. *and* Glassmeier, K.-H. (1984). The transient response mechanism and Pi2 pulsations at substorm onset - Review and outlook. *Planetary and Space Science* 32:1361-1370.

(a)

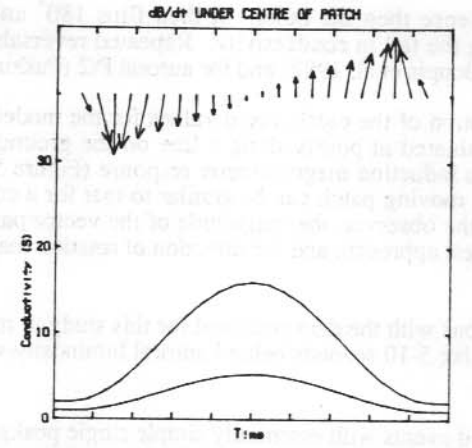

Conductivities - Southern hemisphere
Minimum Pedersen = 1.00 Hall = 2.00
Maximum Pedersen = 5.30 Hall = 16.00
Field-aligned discharge rate = 50%
Patch radius = 150 km
E azimuth = 270 degs

(b)

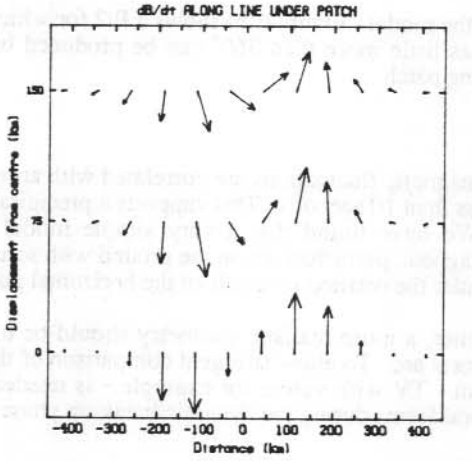

Conductivities - Southern hemisphere
Outside Pedersen = 1.00 Hall = 2.00
Inside Pedersen = 5.30 Hall = 16.00
Field-aligned discharge rate = 50%
Patch radius = 150 km
E azimuth = 270 degs Line azimuth = 0 degs

Figure 5. Examples of the predicted behaviour of the induction magnetometer horizontal polarisation vector. North (positive H) is up and east (positive D) is right for the polarisation vector. (a). The behaviour expected from a peak in the conductivity of an overhead patch. (b). The behaviour expected for a patch of fixed conductivity moving southward and passing to the west of the observer.

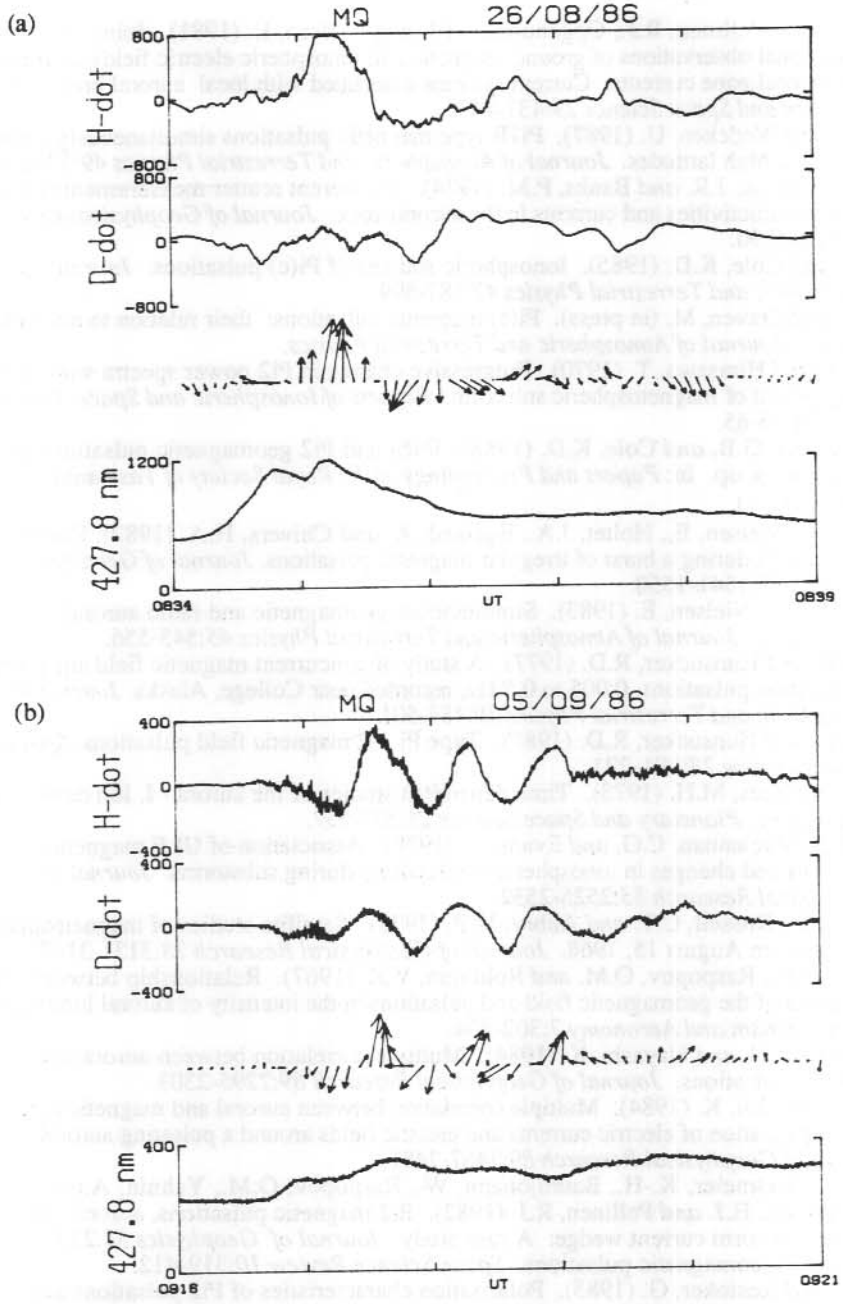

Figure 6. Raw data and induction magnetometer horizontal polarisation vectors for events with simple auroral luminosity peaks observed at Macquarie Island. The vector directions are as for Figure 5. The H and D scales are nearly equal. (a). A good match to the model prediction for a peak in conductivity. (b). A Pi2 which does not fit the model.

Baumjohann, W., Pellinen, R.J., Opgenoorth, H.J. *and* Nielsen, E. (1981). Joint two-dimensional observations of ground magnetic and ionospheric electric fields associated with auroral zone currents: Current systems associated with local auroral break-ups. *Planetary and Space Science 29*:431-447.

Bosinger, T. *and* Wedeken, U. (1987). Pi1B type magnetic pulsations simultaneously observed at mid and high latitudes. *Journal of Atmospheric and Terrestrial Physics 49*:573-598.

Brekke, A., Doupnik, J.R. *and* Banks, P.M. (1974). Incoherent scatter measurements of *E* region conductivities and currents in the auroral zone. *Journal of Geophysical Research 79*:3773-3790.

Burns, G.B. *and* Cole, K.D. (1985). Ionospheric sources of Pi(c) pulsations. *Journal of Atmospheric and Terrestrial Physics 47*:587-599.

Burns, G.B. *and* Craven, M. (in press). Pi(c) magnetic pulsations: their relation to ionospheric currents. *Journal of Atmospheric and Terrestrial Physics*.

Fukunishi, H. *and* Hirasawa, T. (1970). Progressive change in Pi2 power spectra with the development of magnetospheric substorm. *Reports of Ionospheric and Space Research Japan 24*:45-65.

Grant, I.F., Burns, G.B. *and* Cole, K.D. (1988). Pi(b) and Pi2 geomagnetic pulsations at auroral break-up. In: *Papers and Proceedings of the Royal Society of Tasmania 22(1)*:303-311.

Haldoupis, C.I., Nielsen, E., Holtet, J.A., Egeland, A. *and* Chivers, H.A. (1982). Radar auroral observations during a burst of irregular magnetic pulsations. *Journal of Geophysical Research 87*:1541-1550.

Haldoupis, C.I. *and* Nielsen, E. (1983). Simultaneous geomagnetic and radio auroral observations. *Journal of Atmospheric and Terrestrial Physics 45*:543-556.

Heacock, R.R. *and* Hunsucker, R.D. (1977). A study of concurrent magnetic field and particle precipitation pulsations, 0.005 to 0.5 Hz, recorded near College, Alaska. *Journal of Atmospheric and Terrestrial Physics 39*:487-501.

Heacock, R.R. *and* Hunsucker, R.D. (1981). Type Pi 1-2 magnetic field pulsations. *Space Science Review 28*:191-221.

Jones, R.A. *and* Rees, M.H. (1973). Time dependent studies of the aurora - I. Ion density and composition. *Planetary and Space Science 21*:537-557.

Lanzerotti, L.J. Maclennan, C.G. *and* Evans, C. (1978). Association of ULF magnetic variations and changes in ionospheric conductivity during substorms. *Journal of Geophysical Research 83*:2525-2532.

McPherron, R.L., Russell, C.T. *and* Aubry, M.P. (1973). Satellite studies of magnetospheric substorms on August 15, 1968. *Journal of Geophysical Research 78*:3131-3149.

Namgaladze, A.N., Raspopov, O.M. *and* Roldugin, V.K. (1967). Relationship between Pi2 pulsations of the geomagnetic field and pulsations in the intensity of auroral luminescence. *Geomagnetism and Aeronomy 7*:302-304.

Oguti, T., Meek, J.H. *and* Hayashi, K. (1984). Multiple correlation between auroral and magnetic pulsations. *Journal of Geophysical Research 89*:2295-2303.

Oguti, T. *and* Hayashi, K. (1984). Multiple correlation between auroral and magnetic pulsations 2. Determination of electric currents and electric fields around a pulsating auroral patch. *Journal of Geophysical Research 89*:7467-7481.

Pashin, A.B., Glassmeier, K.-H., Baumjohann, W., Raspopov, O.M., Yahnin, A.G., Opgenoorth, H.J. *and* Pellinen, R.J. (1982). Pi2 magnetic pulsations, auroral break-ups, and the substorm current wedge: A case study. *Journal of Geophysics 51*:223-233.

Saito, T. (1969). Geomagnetic pulsations. *Space Science Review 10*:319-412.

Samson, J.C. *and* Rostoker, G. (1983). Polarisation characteristics of Pi2 pulsations and implications for their source mechanisms: Influence of the westward travelling surge. *Planetary and Space Science 31*:435-458.

Stuart, W.F., Green, C.A. *and* Harris, T.J. (1977). Correlation between modulation of the intensity of precipitating electrons in the auroral zone and a coincident Pi2. *Journal of Atmospheric and Terrestrial Physics 39*:631-635.

Tamao, T. (1986). Direct contribution of oblique field-aligned currents to ground magnetic fields. *Journal of Geophysical Research 91*:183-189.

12. TIME DIFFERENCES BETWEEN H AND D COMPONENT Pi(c) PULSATIONS

G.B. Burns and M. Craven
Antarctic Division
Kingston Tas 7050
Australia

ABSTRACT

Burns and Craven (in press) present results implying a time difference in the ground measured magnetic signatures of Hall and Pedersen current fluctuations during pulsating aurora. In this paper, one month's data of measured delays between H and D component Pi(c) pulsations and the N_2^+1NG(0,1) band emission at 427.8 nm are compared with riometer absorption and f_0E ionospheric measurements for evidence of the delay mechanism. While not conclusive, it is established experimentally that the propagation delay time of a ULF wave through the ionosphere increases by 0.1 seconds for each increment of ~0.45 x 10^{11} el/m^3 in the ionospheric *E* region electron concentration.

12.1 INTRODUCTION

The close peak-to-peak correspondence between optical auroral pulsations and magnetic Pi(c) pulsation events has led to the general acceptance that the Pi(c) magnetic pulsations result from electron precipitation induced conductivity enhancements of existing *E* region current systems (Arnoldy et al. 1982, Burns 1983, Engebretson et al. 1983, Oguti and Hayashi 1984, Craven 1984, Burns and Cole 1985, Engebretson et al. 1986). Burns and Cole (1985) found that generally the H component of the Pi(c) pulsations led the D component by 0.4 seconds.

The general morphology of the Pi(c) pulsations correlations with the optical fluctuations is well explained by the enhanced conductivity patch model of Oguti and Hayashi (1984). With an assumed equatorward *E* region electric field, typical of the post-midnight auroral region where pulsating aurora and Pi(c) pulsations are colocated, the Oguti and Hayashi model implies that the D component Pi(c) pulsations result from a 'strong' sum of the magnetic signatures of Hall and Pedersen current fluctuations while the H component is a 'weaker' difference of the magnetic signatures of the two fluctuating currents. This theoretically models the generally negative nature of the correlation between the optical pulsations and both the H and D magnetic pulsation components, and the stronger D component/optical fluctuation cross-correlations compared with the H component/optical fluctuation cross-correlations which are found experimentally (Arnoldy et al. 1982, Burns and Cole 1985). The rare positive correlations between either or both magnetic pulsation components and the optical fluctuations can be explained by variations in the direction of the applied *E* region electric field.

Burns and Craven (in press) found that where one of the magnetic pulsation components (either H or D) was positively correlated with the optical pulsations and the other component was negatively correlated, then the D component pulsations led the H component pulsations. This is the opposite of the general case. When both pulsation components are positively correlated with the optical fluctuations, then the H component pulsations again led the D component pulsations. Consideration of the effect of the rotation of the applied *E* region electric field in the Oguti and Hayashi model implied that this variation in the polarisation of the Pi(c) pulsations resulted from the ground recorded signature of the Hall current fluctuations leading the ground recorded signature of the Pedersen current fluctuations (Burns and Craven, in press). Such a result is likely to be related to the respective altitude deference of the two current systems. The Hall current peaks around 105 km and the Pedersen current around 120 km for general auroral conditions (Brekke et al. 1974). A further fact is required to understand the possible mechanisms proposed to explain the time difference, which is of the order of half a second. This is that at the

altitude at which the respective currents flow, both the Hall and Pedersen conductivity are proportional to the electron concentration.

Burns and Craven (in press) proposed the following three possible mechanisms for the ground recorded signature of the Hall current fluctuations leading the associated signature of the Pedersen current fluctuations during pulsating aurora Pi(c) events.

1. Measurement of the 'velocity dispersion' of electrons arriving at the auroral ionosphere and associated with pulsating aurora have led to the acceptance of a geomagnetic equatorial source for the precipitating fluxes (Bryant et al. 1975, Yau et al. 1981). The highest energy electrons associated with the modulated electron burst reach the auroral ionosphere earlier, and deposit their energy at a lower altitude, than their less energetic associates. The Hall current fluctuation may thus precede the Pedersen current fluctuation.

2. The magnetic fluctuation recorded at the ground is delayed by the propagation of the associated ultra-low frequency (ULF) electromagnetic wave through the ionosphere (Francis and Karplus 1960, Campbell 1970). The extra propagation delay of the ULF wave from the higher Pedersen current altitude may account for the measured delay.

3. Jones and Rees (1973) note that the speed with which the increase in electron density in the *E* region follows the ionisation pulse depends principally on the electron concentration itself. The higher the electron concentration, the more rapidly the electron density increases following an ionisation pulse. During pulsating aurora, the electron density is likely to reach higher concentrations at Hall current heights than at Pedersen current heights. The rate at which the Hall conductivity increases may, by this mechanism, exceed the rate at which the Pedersen conductivity increases.

12.2 THE ENERGY OF THE PRECIPITATING ELECTRONS

In this section the authors consider the implications on the proposed mechanisms of increasing the energy of the incident auroral electrons. The incident pulsating auroral electrons modulate the conductivity in the Hall and Pedersen current systems by modulating the ionisation rate and thus the electron density at the height of the respective current systems. It is assumed that the Hall and Pedersen current systems remain at the same altitude and that there is no variation in the incident flux as the energy of the incident electrons vary. In discussing the effects of energy variations in the incident flux on the proposed mechanisms, consideration will be given to the implied variation in the time difference between the H and D component pulsations and between the individual magnetic pulsation components and the optical fluctuations for the general equatorward *E* region electric field case.

The altitude of the Pedersen current is assumed to be of the order of 120 km which is the altitude maximally ionised by 3 keV electrons. The Hall current is assumed to be at 105 km which is maximally ionised by 10 keV electrons (Rees 1963, Stenbaek-Nielsen and Hallinan 1979). A further difficulty with this consideration is: what is the typical energy range of pulsating auroral fluxes? Direct rocket measurements (e.g. McEwen et al. 1981) tend to indicate energies of the order of 2-4 keV while lower border altitude measurements (Stenbaek-Nielsen and Hallinan 1979) imply energies of the order of 10 keV or higher.

12.2.1 *Velocity dispersion*

Following the assumptions already made, if the distance from the geomagnetic equator to the ionosphere is not systematically dependent on the average energy of the precipitating electrons, the dispersal time of the 10 keV and 3 kV electrons responsible for the ionisation at the Hall and Pedersen current altitudes will remain constant. Thus the velocity dispersion mechanism implies that the time difference between the ground recorded signatures of the Hall and Pedersen current

fluctuations will remain essentially constant as the average energy of the incident electrons increases.

The Oguti and Hayashi model with an equatorward *E* region electric field implies that the D component pulsations result from a sum of Hall and Pedersen fluctuations while the H component pulsations are a subtraction. As the e-folding energy of the incident electrons increases from 3 keV to 10 keV then the Hall current fluctuations will have an increasing influence on both magnetic pulsation components. This should bring both the D and H component pulsations closer to the Hall current signature. The implication of the model is that the H component pulsations should lead the D component pulsations at all times for the assumptions made, but if velocity dispersion is the dominant control mechanism, then as the average energy of the incident fluxes increases in the range 3 to 10 keV, the time difference should decrease. The time difference between the D component pulsations and the optical pulsations should decrease and the time difference between the H component pulsations and the optical pulsations should increase.

12.2.2 *ULF propagation through the ionosphere*

As the e-folding energy of the incident electrons increases in the range from 3 to 10 keV, for constant flux, the electron density between the heights of the Pedersen and Hall currents will increase. The electron density below the Hall current altitude will also increase. Thus if the delay of a ULF wave propagating from the Pedersen current height to the Hall current height is controlling the time delay between the ground received signatures of the respective current fluctuations, this delay will increase as the e-folding energy of the incident electrons increases in the range from 3 to 10 keV. Note that the delay of both Hall and Pedersen associated ULF signals with respect to the optical fluctuations will increase as the energy increases, but that the delay of the Pedersen associated signal increases by a larger amount.

Considering the Oguti and Hayashi model implications for an equatorward E region electric field, the situation between the H component and D component pulsations for this mechanism is complicated. The increased energy alone tends to bring both the D and H components closer to the Hall fluctuation delay as discussed in the last section. With the Pedersen current fluctuation magnetic signature being delayed even more than the Hall current fluctuation magnetic signature, then both the D component and H component pulsations should be delayed with respect to the optical pulsations. More detailed modelling is needed to determine whether the delay between the H and the D component varies. Any variation between the H and D component time delays will be less dramatic than between the individual components and the optical pulsations as the energy of the incident electrons varies.

12.2.3 *Rate of conductivity increase*

If the controlling factor for the time delay between the Hall and Pedersen current fluctuation magnetic signatures is the rate at which the respective conductivities increase following the ionisation burst, then the time difference should increase as the e-folding energy of the incident auroral electrons increases from 3 to 10 keV. The speed with which the electron density and thus the conductivity follows the ionisation depends principally on the initial electron density (Jones and Rees 1973). As the e-folding energy of the incident electrons increases above 3 keV for a constant incident flux, the electron density at the Pedersen current heights will decrease while at the Hall current height it will increase. This situation will hold until the e-folding energy of the incident electrons exceeds the peak ionisation energy of the Hall current altitude, which is approximately 10 keV. If this mechanism controls the time difference between the Hall and Pedersen fluctuating current magnetic signals, then the time difference between the optical and Hall signal fluctuations should decrease, and between the optical and the Pedersen signal it should increase.

Consider again the implications of the model which has the D component pulsations as the sum of Hall and Pedersen effects and the H component pulsations as being a difference. The D

component pulsations situation is complicated, but should result in the time difference with respect to the optical pulsations decreasing, perhaps even resulting in a splitting of the D component magnetic pulsation peak as the Hall and Pedersen contributions move apart. The H component should strongly decrease in delay with respect to the optical pulsations if this mechanism is dominant.

12.3 THE FLUX OF THE PRECIPITATING ELECTRONS

In this section the implications on the proposed mechanisms of increasing the flux of the incident auroral electrons while maintaining a constant energy distribution are considered.

12.3.1 *Velocity dispersion*

The time difference between 3 keV and 10 keV electrons propagating from the geomagnetic equator is independent of the flux, therefore this mechanism implies that the time difference between the various signals is independent of the particle flux.

12.3.2 *ULF propagation through the ionosphere*

As the incident flux increases, the ionisation at all levels will increase. If the time of propagation of a ULF wave between Pedersen and Hall current altitudes is the principal influence on the measured delay then an increased flux will result in both Hall and Pedersen magnetic signatures being delayed with respect to the optical fluctuations, the Pedersen more so.

The Oguti and Hayashi model implies that both the H and D component magnetic pulsations should be delayed with respect to the optical pulsations as the flux increases. Any variation in the time delay between the H and D components is difficult to predict, but will not be as dramatic as the variations in the time delay between the individual components and the optical pulsations.

12.3.*3 Rate of conductivity increase*

As above, as the incident flux increases, the ionisation at all levels will increase. As the rate of conductivity increase is proportional to the ionisation level, then the conductivity should increase more rapidly at both Hall and Pedersen current heights. This will decrease the time delays between the magnetic signatures of the Hall and Pedersen current fluctuations and the optical variations.

The Oguti and Hayashi model implies that the H and D component pulsations will be more closely coincident with the optical pulsations as the flux increases. Any time variation between the H and D component pulsations will not be as dramatic as between the individual components and the optical pulsations.

12.4 THE DATA, ANALYSIS AND RESULTS

Observations made at the Australian National Antarctic Research Expedition Station of Macquarie Island (invariant latitude 64.5S) in the one month period, 6 September to 7 October 1985, are considered in this analysis.

Magnetic D and H component induction magnetometer data and optical intensities of the N_2^+1NG(0,1) band at 427.8 nm recorded by a wide angle (30° half-angle), zenith-oriented photometer were collected digitally at a rate of 10 Hz. Cross-correlations, of 5 minute data blocks, between the optical and magnetic components were evaluated for periods of pulsating aurora to determine the delay between the respective components (Burns and Cole 1985). Ninety-seven data files yielding good correlations between the optical pulsations and the D component pulsations, and twenty-nine data files yielding good correlations between the optical pulsations and the H component pulsations, were found in the sample period. The delay between the

magnetic components and the optical components was determined from the location of the peak of the cross-correlation function to an accuracy of 0.1 seconds. The time difference between the individual magnetic pulsation components refers to the difference between the individual component delays with respect to the optical pulsations (Burns and Craven, in press).

A riometer, operating at 30 MHz monitored the level of cosmic noise absorption on chart at 10 cm/hr. The absorption, accurate to an estimated 0.02 dB, was calculated at the beginning and end of each 5 minute period for which good correlations between the magnetic pulsation components and optical pulsations were obtained.

Ionosonde data, photographically recorded at 15 minute intervals using an Australian type 4B ionosonde were available. For this study f_0E values were scaled, wherever possible, for sounding times encompassing the correlation times. When absorption did not render the ionograms useless, an accuracy of 0.1 MHz was generally obtainable.

In Figure 1 the D component delay with respect to the optical pulsations for the ninety-seven correlations obtained, is plotted against riometer absorption at times encompassing the correlation period. A slight liberty is taken in presenting the data in this and other figures to ensure that data points do not overlap.

The bars in Figure 1 indicate the range covered by the riometer absorption values evaluated at the beginning and end of the 5 minute correlation period for which the delay was determined. A trend of increasing delays between the optical and D component pulsations as the riometer absorption level increases is shown.

Figure 2 shows the H component delays with respect to the optical pulsations, for the twenty-nine correlations obtained, plotted against riometer absorption, as per Figure 1. No correlation is discernible for this limited data set.

A plot of the time difference between the H and D component pulsations against riometer absorption showed no discernible trend and is not presented here.

The f_0E value squared is linearly related to the maximum electron concentration of the E layer (Ratcliffe and Weekes 1960). In Figure 3, the D component delay with respect to the optical pulsations is plotted against f_0E squared. The bar indicates the range covered by the f_0E squared values for the ionosonde soundings surrounding the 5 minute period of the cross-correlation analysis. Due to absorption, f_0E values could only be determined for thirty of the ninety-seven good D component correlations. At the top of Figure 3 are listed, for each delay time, the number of good correlations for which absorption prevented a valid data point being obtained. A best line fit to Figure 3 implies that the propagation delay of a ULF wave through the ionosphere increases by 0.1 seconds for each increment of 0.45×10^{11} el/m^3 in the ionosphere E region electron concentration.

12.5 DISCUSSION

Table 1 summarises the conclusions of Sections 12.2 and 12.3.

Riometer absorption increases if the flux of incident electrons increases, but it is more sensitive to increases in the energy of the incident particles. The f_0E squared value should increase linearly as the flux increases but it has a more complicated, and perhaps less sensitive, relation to the energy of the precipitating flux. That the time delay of the D component with respect to the optical pulsations increases as both the riometer absorption levels and f_0E values increase can be seen from Table 1 to be consistent only with the mechanism of the delay of a ULF wave by the ionosphere.

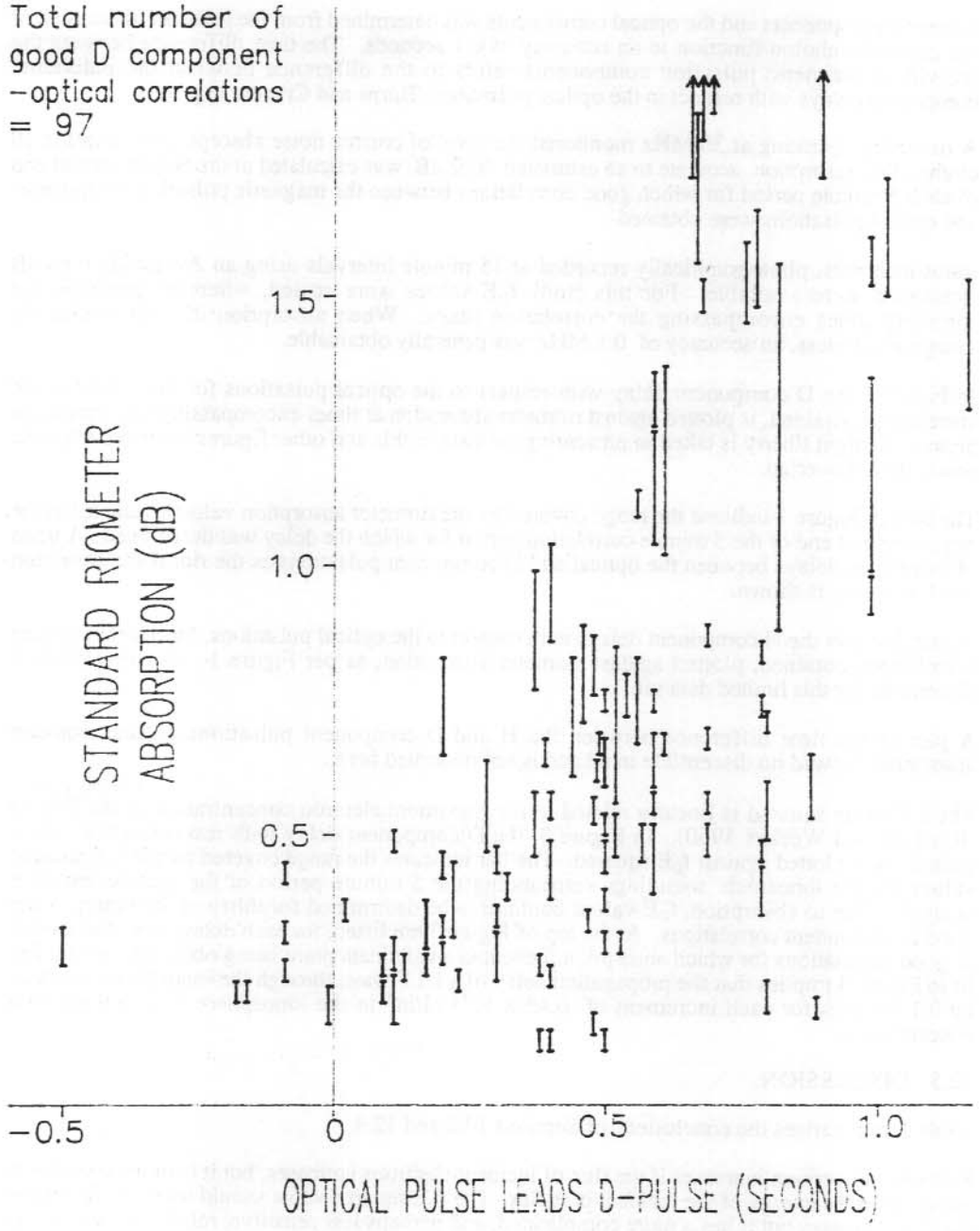

Figure 1. The delay between the optical pulsations and the D component magnetic pulsations plotted against the riometer absorption. The bars indicate the range covered by the riometer absorption values evaluated at the beginning and end of the 5 minute correlation period for which the delay was determined.

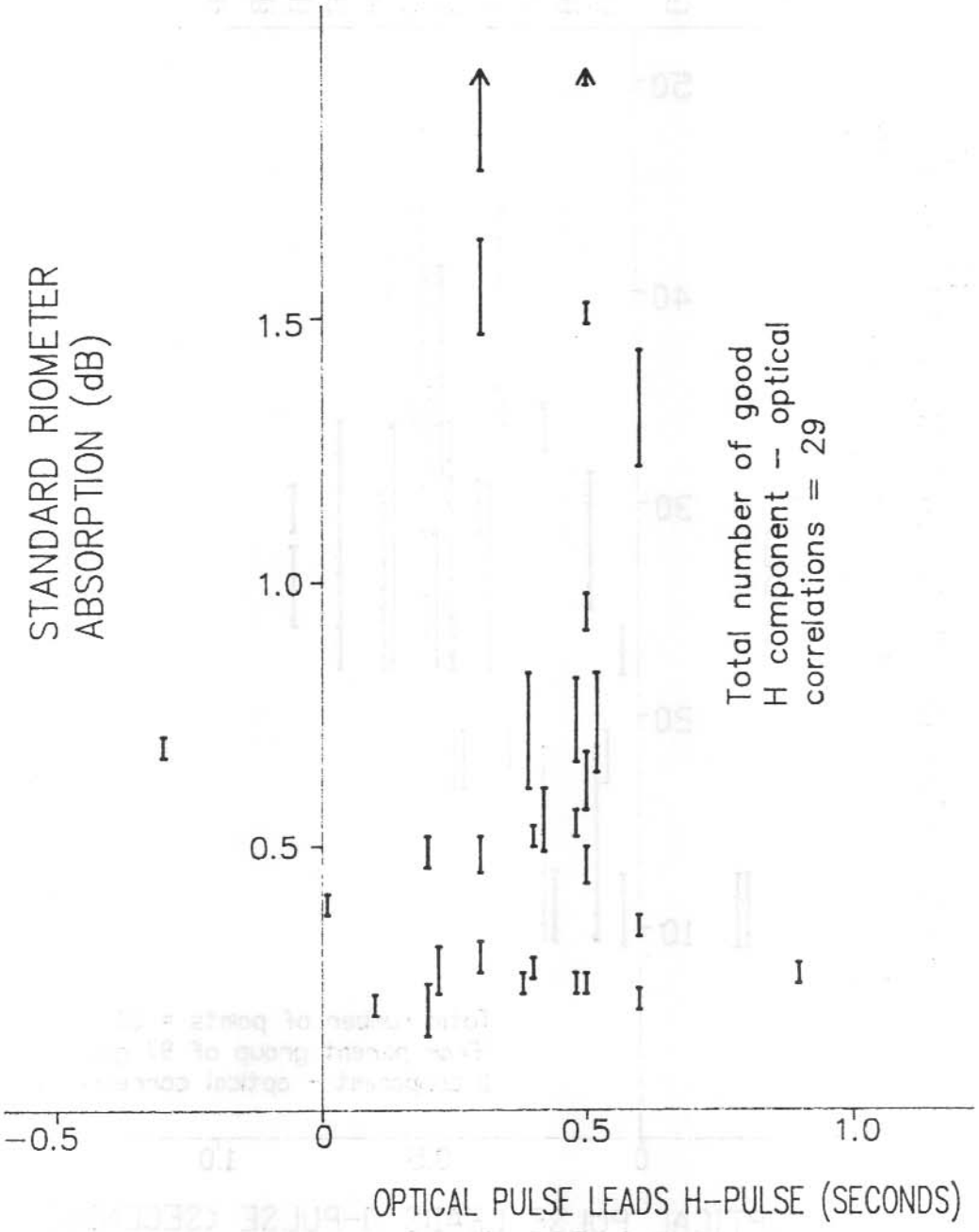

Figure 2. The delay between the optical pulsations and the H component magnetic pulsations plotted against the riometer absorption. As per Figure 1.

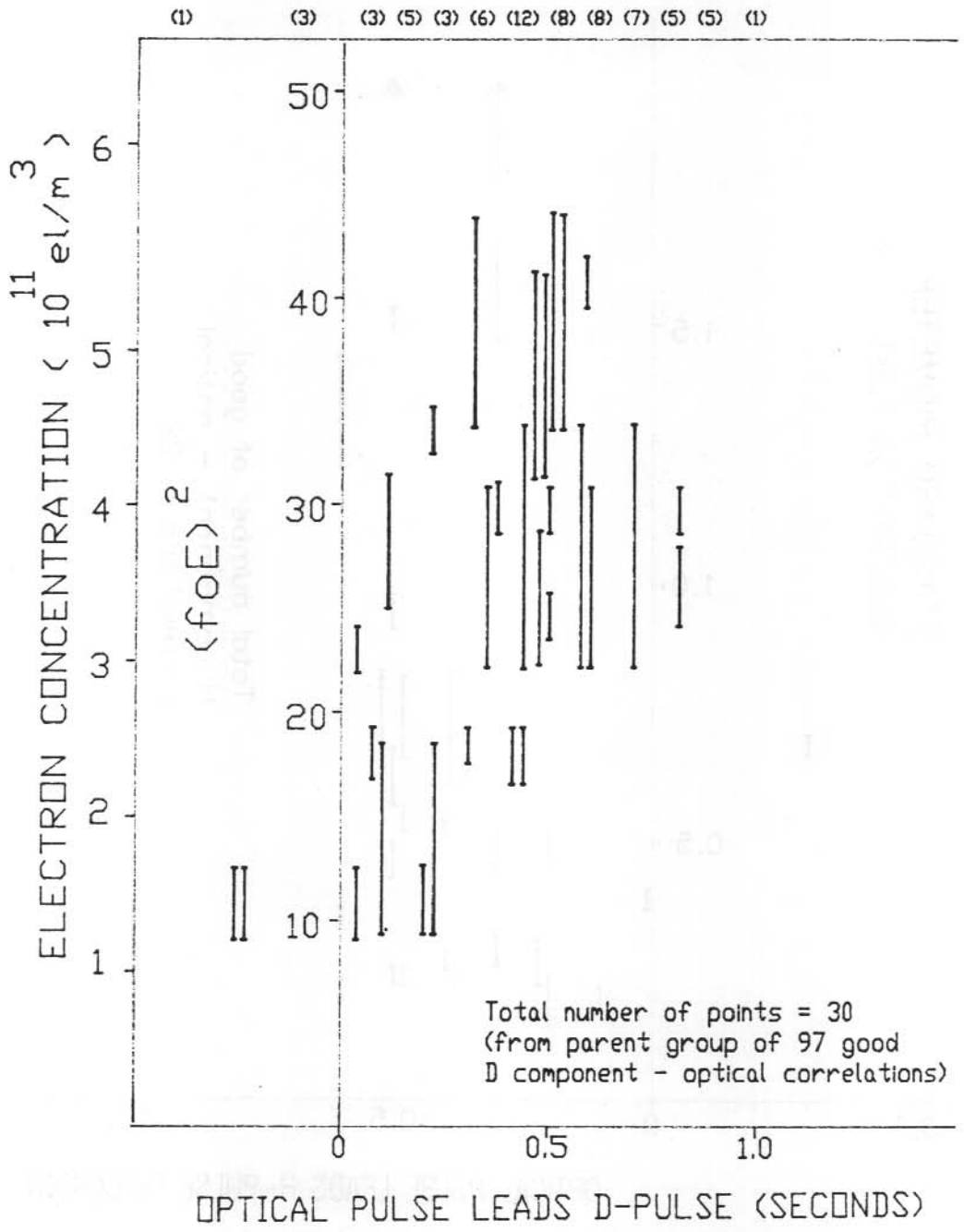

Figure 3. The D component delay with respect to the optical pulsations plotted against f_0E squared. The bar indicates the range covered by the f_0E squared values for the ionosonde soundings surrounding the period of the cross-correlation analysis. At the top of the plot, the number of good correlations for which absorption prevented an f_0E determination are listed.

Table 1. Showing the variation in the delay expected between various components as the energy of the incident electrons increases, and as the flux of the incident electrons increases, by the mechanisms proposed.

	Energy Increases (↑)	Flux Increases(↑)
mech1:		
Opt vs D	$\Delta t\downarrow$	$\Delta t\rightarrow$
Opt vs H	$\Delta t\uparrow$	$\Delta t\rightarrow$
H vs D	$\Delta t\downarrow$	$\Delta t\rightarrow$
mech2:		
Opt vs D	$\Delta t\uparrow$	$\Delta t\uparrow$
Opt vs H	$\Delta t\uparrow$	$\Delta t\uparrow$
H vs D	$\Delta t\rightarrow$	$\Delta t\rightarrow$
mech3:		
Opt vs D	$\Delta t\downarrow$	$\Delta t\downarrow$
Opt vs H	$\Delta t\downarrow$	$\Delta t\downarrow$
H vs D	$\Delta t\uparrow$	$\Delta t\rightarrow$

For conclusive proof, it must be shown that the measured delay can amount to the 0.5 second delay inferred between the magnetic signature of the Hall and Pedersen current fluctuations. It would also be appropriate to model the delays discussed in Sections 12.2 and 12.3 so as to put the conclusions on a firmer footing, and to establish the relationship between the H component and optical pulsation delays to the energy and flux of the incident electrons by use of a larger data set.

ACKNOWLEDGMENTS

The induction coils used in this experiment were made available by the Geophysical Institute, University of Alaska. The ionogram records were supplied by IPS Radio and Space Services, Sydney. ANARE expeditioners at Macquarie Island in 1985 assisted with the data collection and the staff of the Antarctic Division assisted in the preparation of this report.

REFERENCES

Arnoldy, R.L., Dragoon, K., Cahill, L.J., Mende, S.B. *and* Rosenberg, T.J. (1982). Detailed correlations of magnetic field and riometer observations at L=4.2 with pulsating aurora. *Journal of Geophysical Research 87*:10449-10456.

Brekke, A., Doupnik, J.R. *and* Banks, P.M. (1974). Incoherent scatter measurements of E region conductivities and currents in the auroral zone. *Journal of Geophysical Research 79*:3773-3790.

Bryant, D.A., Smith, M.F. *and* Courtier, G.M. (1975). Distant modulation of electron intensity during the expansion phase of an auroral substorm. *Planetary and Space Science 23*:867-878.

Burns, G.B. (1983). *Pulsating aurora: photometer, riometer and micropulsation coil observations*. PhD thesis, La Trobe University.

Burns, G.B. *and* Cole, K.D. (1985). Ionospheric sources of Pi(c) pulsations. *Journal of Atmospheric and Terrestrial Physics 47*:587-599.

Burns, G.B. *and* Craven, M. (in press). Pi(c) magnetic pulsations: their relation to ionospheric currents. *Journal of Atmospheric and Terrestrial Physics*.

Campbell, W.H. (1970). Rapid auroral luminosity fluctuations and geomagnetic field pulsations. *Journal of Geophysical Research 75*:6182-6208.

Craven, M. (1984). *Pulsating auroral and magnetic Pi(c) pulsations*. MSc thesis, University of Tasmania.

Engebretson, M.J., Cahill, L.J., Arnoldy, R.L., Mende, S.B. *and* Rosenberg, T.J. (1983). Correlated irregular magnetic pulsations and optical emissions observed at Siple station, Antarctica. *Journal of Geophysical Research 88*:4841-4852.

Engebretson, M.J., Cahill, L.J., Winningham, J.D., Rosenberg, T.J., Arnoldy, R.L. Maynard, N.C., Suguira, M. *and* Doolittle, J.H. (1986). Relations between morning sector Pi1 pulsation activity and particle and field characteristics observed by the DE2 satellite. *Journal of Geophysical Research 91*:1535-1547.

Francis, W.E. *and* Karplus, R. (1960). Hydromagnetic waves in the ionosphere. *Journal of Geophysical Research 65*:3593-3600.

Jones, R.A. *and* Rees, M.H. (1973). Time dependent studies of aurora. I. Ion density and composition. *Planetary and Space Science 21*:537-557.

McEwen, D.J., Yee, E., Whalen, B.A. *and* Yau, A.W. (1981). Auroral electron energies: comparisons of in situ measurements with spectroscopically inferred energies. *Canadian Journal of Physics 59*:1106-1115.

Oguti T. *and* Hayashi K. (1984). Multiple correlation between auroral and magnetic pulsations 2. Determination of electric currents and electric fields around a pulsating auroral patch. *Journal of Geophysical Research 89*:7467-7481.

Ratcliffe, J.A. *and* Weekes, K. (1960). The ionosphere. In: J.A. Ratcliffe (Ed.) *Physics of the Upper Atmosphere*. N.Y. Academic Press.

Rees, M.H. (1963). Auroral ionisation and excitation of incident electrons. *Planetary and Space Science 11*:1209-1218.

Stenbaek-Nielsen, H.C. *and* Hallinan, T.J. (1979). Pulsating auroras: evidence for non-collisional thermalisation of precipitating electrons. *Journal of Geophysical Research 84*:3257-3271.

Yau, A.W., Whalen, B.A. *and* McEwen, D.J. (1981). Rocket-borne measurements of particle pulsation in pulsating aurora. *Journal of Geophysical Research 86*:5673- 5681.

13. PENETRATION OF ELECTRIC FIELD IN HIGH LATITUDE IONOSPHERE

D.Y. Zhang and K.D. Cole
Physics Department
La Trobe University
Bundoora Vic 3083
Australia

ABSTRACT

The mapping of the spectra of the electrostatic field below 300 km altitude is theoretically calculated for a horizontally stratified auroral ionosphere. Perpendicular electric fields of large scale size are the same for different altitudes of the ionosphere. However, electric fields of small scale size vary with altitude and decrease drastically when the scale size is smaller than a certain value which depends on altitude. These results are similar to those observed by satellites above 300 km altitude. The 'smoothing' of the electric field when penetrating a horizontally stratified ionosphere is demonstrated. The possible smallest scale of parallel electric field structure within the ionosphere is found. Presented also is a method of finding the smallest horizontal length with which the electric field can penetrate the ionosphere with little distortion. For an average conductivity model, this length is found to be about 1 km. Finally, the mapping of packets of electric field to the ground are constructed.

13.1 INTRODUCTION

Because of the great parallel conductivity along the geomagnetic field lines in the upper region of the auroral ionosphere, the convection electric field of the magnetosphere can be mapped into the ionosphere. To study the mapping of electrostatic field in the lower ionosphere where collisions dominate, it is always convenient to first decompose the packet of electrostatic field into a number of Fourier components each of which has its particular scale size.

13.2 FORMULATION

The starting point for the analysis of this electric field mapping is that the electric current j is continuous everywhere in the atmosphere, that is,

$$\nabla \cdot \mathbf{J} = 0 \tag{1}$$

The current is driven by an electrostatic or quasi-electrostatic field E which must satisfy the Maxwell equation.

$$\nabla \times \mathbf{E} = 0 \tag{2}$$

Electric field is related to the current by

$$\mathbf{J} = \sigma_0 \mathbf{E}_{||} + \sigma_1 \mathbf{E}_{\perp} + \sigma_2 \mathbf{b} \times \mathbf{E} \tag{3}$$

where $\mathbf{E}_{||}$ and $\mathbf{E}_{\perp}$ are respectively the components of $\mathbf{E}$ parallel and perpendicular to the magnetic field whose direction is $\mathbf{b}$ which is assumed to be identical with the z direction. The symbols σ_0, σ_2 and σ_1 are parallel, Cowling and Pedersen conductivities respectively. The atmosphere and ionosphere are considered to be horizontally stratified and the magnetic field lines are vertical, viz., σ_0, σ_1 and σ_2 are functions of z only. Equation (2) is satisfied by a potential field such that

$$\mathbf{E} = -\nabla\Psi \tag{4}$$

Equations (1), (2), (3) and (4) combine to give

$$\frac{\partial}{\partial z}\left(\sigma_0 \frac{\partial \Psi}{\partial z}\right) + \sigma_1 \nabla_\perp^2 \Psi = 0 \tag{5}$$

The expression of operator $\nabla_\perp{}^2$ depends on the coordinate system used. We examine a two-dimensional situation in which x is the magnetic east direction and $\partial Y/\partial x = 0$. The potential function is then governed by

$$\frac{\partial}{\partial z}\left(\sigma_0 \frac{\partial \Psi}{\partial z}\right) + \sigma_1 \frac{\partial^2 \Psi}{\partial y^2} = 0 \tag{6}$$

where y is identified with the north-south direction. For a general packet of ionospheric electrostatic fields the solution of (6) can be written as

$$\Psi(y, z) = \int_{-\infty}^{\infty} F(k) e^{iky} \psi_k(z)\, dk \tag{7}$$

where $F(k)$ is the Fourier transform of the packet of electric potential, and therefore the spectral function of the packet of electric potential. Note that the spectral function here means the magnitude, not the square of the magnitude, as is conventionally the case. The reciprocal of k is the scale size. The function $\psi_k(z)$ is governed by the following equation.

$$\frac{d}{dz}\left(\sigma_0 \frac{d\psi_k}{dz}\right) - \sigma_1 k^2 \psi_k(z) = 0 \tag{8}$$

The function $\psi_k(z)$ determines the relationship between upper and lower altitudes for a given scale size. In addition, $\psi_k(z)$ could be considered as representing the relationship between different scale sizes for a particular altitude, i.e., the spectrum.

13.3 RESULTS AND INTERPRETATION

13.3.1 *General*

The basic equation is elliptic, so it is sufficient to simply specify the boundary values. The bottom side is the electrical 'ground' of the earth at which the potential is zero, viz., $\Psi(y, 0) = 0$. On the top side of the auroral ionosphere, at 300 km altitude, either the potential or the electric field can be specified. For this particular analysis the authors have chosen to specify the electric field. It is possible to specify either the parallel or the perpendicular component of the electric field. In equation (7), the product $F(k)\psi_k(z)$ as a function of k gives the spectra of the electric field potential at various altitudes. The function $F(k)$ is independent of altitude z, and therefore could be interpreted as the top side spectral function of the packet of electric field component that is parallel or perpendicular to the geomagnetic field lines, depending on which component is specified on the top side boundary.

Accordingly, if the parallel component of a packet of electric field on the top side boundary is specified, $\psi'_k(300) = 1$. The prime denotes a derivative with respect to z. Thus $F(k)\psi'_k(z)$ as a function of k gives the spectra of the parallel component for different altitudes, and $F(k)k\psi_k(z)$ as a function of k gives the spectra of the perpendicular component. Because function $F(k)$

could be arbitrary we first study the functions $\psi'_k(z)$ and $k\psi_k(z)$. They are shown in Figure 1 and Figure 2 and represent the spectra of parallel and perpendicular electric field respectively for different altitudes when the parallel component of the electric field at the top side boundary is a delta function $\delta(y)$. Chiu's (1974) conductivity profile has been used representing an average ionosphere and atmosphere between the ground and 400 km altitude.

Similarly, the perpendicular component of a packet of electric field on the top side can be specified, $k\psi_k(300) = 0$. Then $F(k)k\psi_k(z)$ as a function of k gives the spectra of the perpendicular component for different altitudes, and $F(k)\psi'_k(z)$ gives the spectra of the parallel component. $k\psi_k(z)$ and $\psi'_k(z)$ are the spectral functions of the perpendicular and parallel components of an electrostatic field for different altitudes for which the perpendicular component of the electric field on the top side boundary is a delta function $\delta(y)$. They are shown in Figure 3 and Figure 4 respectively.

Figure 1 and Figure 2 are normalised to the top side parallel component and Figure 3 and Figure 4 are normalised to the top side perpendicular component. At a glance, the values shown are prohibitively large. However, the electric field specified on the top side boundary is normalised to 1 V/m which is unrealistically large especially for parallel electric field. For example, the parallel electric current on the top side boundary is around 1 $\mu A/m^2$, and the parallel electric field corresponding to this current is of order 10^{-9}V/m. Because the equation is linear one can scale the solution by appropriate factors. Secondly, when synthesising from a real spectral function of the electric field in space, all components including the very small will contribute. This will be shown later in the paper.

Figures 1 - 4 reveal a number of features of electric field mapping in the ionosphere. As has been pointed out by Chiu (1974), electric fields of large scale size can penetrate the ionosphere much more readily than those of smaller scale size. From Figures 1 - 4, it can be seen that both parallel and perpendicular electric field components decrease for larger k, i.e., for smaller scale size as they penetrate. From Figures 2 and 3, it is concluded that large scale perpendicular electric fields are identical for different altitudes in the ionosphere. However, small scale electric fields differ, and for cases when the scale size is smaller than a certain value they drop drastically as they penetrate. Satellite data above 300 km altitude also show this phenomenon.

13.3.2 *Penetration of a general field to lower altitudes*

From Figures 1 - 4 it can be seen that intrinsically the ionosphere at lower altitudes contains less small scale size components when an electrostatic field is penetrating from above. This effect leads to smoothing of the electric field at lower altitudes relative to the higher altitudes. As is shown in Figure 5, the simultaneous measurement by satellites DE-1 and DE-2 (Weimer et al. 1985) at different altitudes shows that this phenomenon also occurs in the system above 300 km altitude.

In the convectional electric field in the magnetosphere, there are regions in which $\nabla \cdot \mathbf{E} \neq 0$. In other words there may be regions where the electric field is changing on short spatial scales, therefore the field has the appearance of a discontinuity, viewed on a large scale. From the point of view of the spectrum, this means the small scale size components are of large amplitude. So long as the ratio of perpendicular and parallel conductivities is non-zero, the small scale components will be weakened in penetrating into the ionosphere. Therefore the discontinuity will be smoothed in the ionosphere. An illustrative calculation given by Lyons (1980) clearly shows this. Let us now examine two restricted electric field packets. Their parallel components on the top side boundary are as follows:

$$f_1(y) = e^{-ay^2} \tag{9}$$

$$f_2(y) = \sqrt{2ae}\, y\, e^{-ay^2} \tag{10}$$

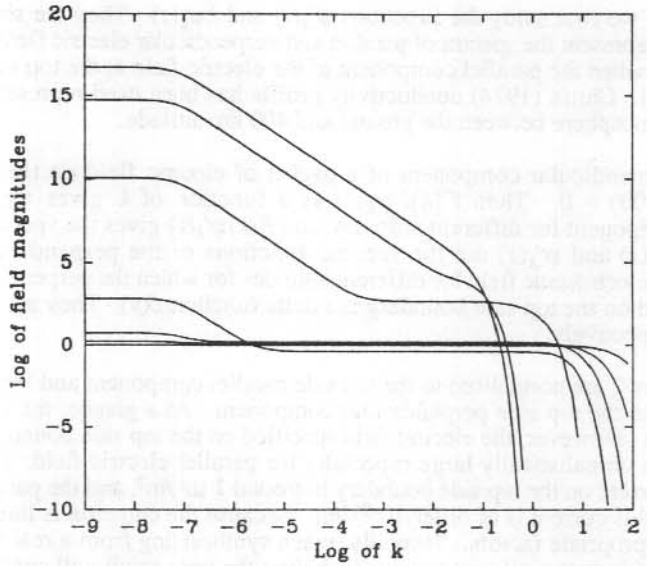

Figure 1. Log of parallel electric field magnitude versus log of reciprocal of scale size. The curves are calculated from equation (8) with $\psi_k(0) = 0$, $\psi'_k(300) = 1$. The parallel electric field magnitude is normalised to the top side parallel electric field, $\psi'_k(z)/\psi'_k(300)$. From top to bottom, the curves correspond to the altitudes of 0, 27, 73, 118, 178, 224 and 270 km respectively.

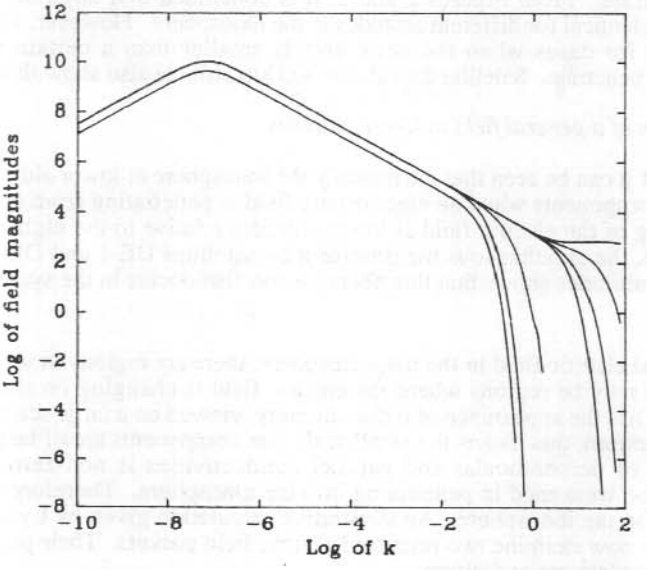

Figure 2. Log of perpendicular electric field magnitude versus log of reciprocal of scale size. The curves are calculated from equation (8) with $\psi_k(0) = 0$, $\psi'_k(300) = 1$. The perpendicular electric field magnitude is normalised to the top side parallel electric field, $k\psi_k(z)/\psi'_k(300)$. From top to bottom, the curves correspond to the altitudes of 300, 240, 179, 118, 57, 27 and 6 km, respectively.

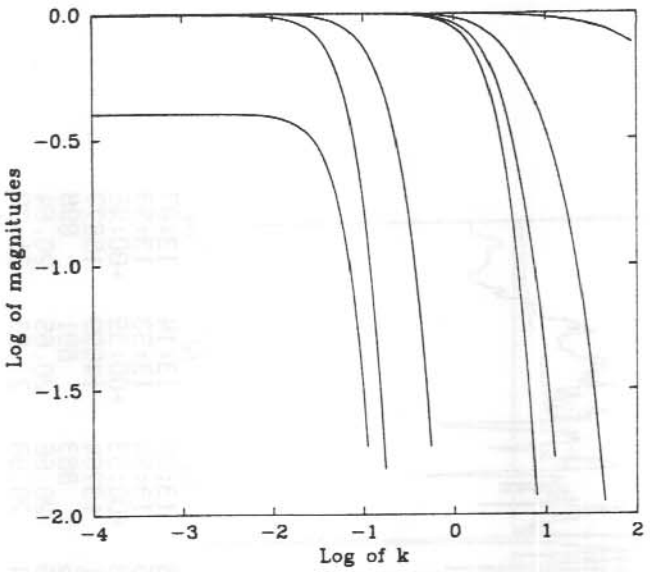

Figure 3. Log of perpendicular electric field magnitude versus log of reciprocal of scale size. The curves are calculated from equation (8) with $\psi_k(0) = 0$, $k\psi_k(300) = 1$. The perpendicular electric field magnitude is normalised to the top side perpendicular electric field, $\psi_k(z)/\psi_k(300)$. From top to bottom, the curves correspond to the altitudes of 297, 239, 179, 118, 57, 27 and 3 km, respectively.

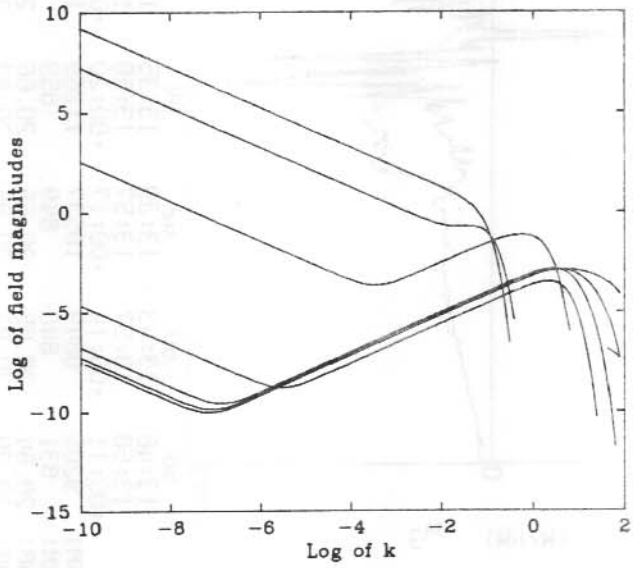

Figure 4. Log of parallel electric field magnitude versus log of the reciprocal of scale size. The curves are calculated from equation (8) with $\psi_k(0) = 0$, $k\psi_k(300) = 1$. The parallel electric field magnitude is normalised to the top side perpendicular electric field, $\psi'_k(z)/k\psi_k(300)$. From top to bottom, the curves correspond to the altitudes of 0, 27, 73, 118, 178, 224 and 270 km, respectively.

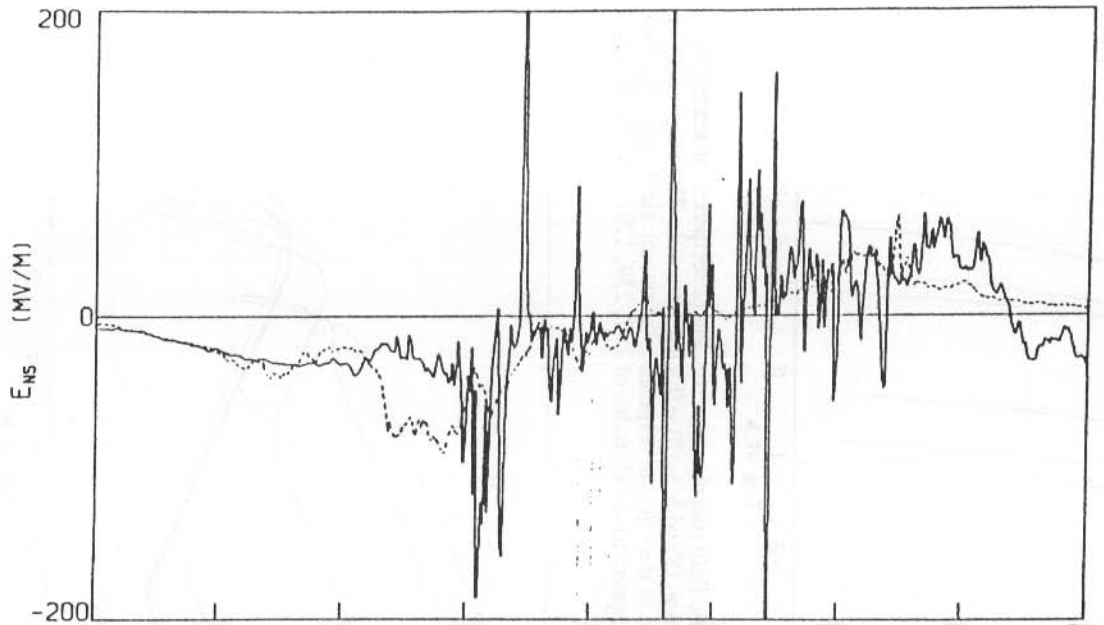

INV LAT	58	60	62	64	66	68	70	72	74
UT.DE-1	13:46	13:43	13:39	13:35	13:31	13:26	13:20	13:14	13:07
UT.DE-2	13:58	13:57	13:57	13:56	13:55	13:55	13:54	13:53	13:53
ΔT	+00:11	+00:14	+00:17	+00:20	+00:24	+00:28	+00:33	+00:39	+00:45
ALT.DE-1(KM)	9205	9849	10537	11269	12050	12881	13764	14699	15677
ALT.DE-2(KM)	831	840	849	859	867	875	883	891	898
MLT.DE-1(HR)	20.64	20.65	20.65	20.66	20.66	20.66	20.66	20.65	20.64
MLT.DE-2(HR)	20.79	20.82	20.84	20.87	20.90	20.94	20.98	21.03	21.09

Figure 5. Electric fields measured by DE-1 and DE-2 on day 303 (30 October 1981). The electric field data are collected along the orbit of the satellites and are projected to a common radial distance of 1 Earth radius. The solid line shows the measurement by DE-1 whose perigee is at 675 km altitude and apogee at 23250 km. The dashed line shows the electric field from DE-2 whose perigee is at 305 km and apogee at 1000 km (from Weimer et al. 1985).

Their spectrums are respectively (as in Figures 6 and 7):

$$F_1(k) = \frac{1}{\sqrt{a\pi}} e^{-k^2/(4a)} \tag{11}$$

$$F_2(k) = \sqrt{\frac{e}{2\pi}}\, k\, e^{-k^2/(4a)} \tag{12}$$

where a is a parameter that determines the horizontal scale length of the electric field packets. The second case corresponds to that in which there is a return current. The spectra for altitudes lower than 300 km is the product of the mapping function $\psi_k(z)$ and the spectral function of the electrostatic field packet on the top side boundary. Thus when the parameter $a \leq 1.0$, the spectra between 120 km and 300 km are mainly controlled by the spectral function of the electric field at 300 km altitude. This means that an electric field packet with a horizontal size larger than 1 km can penetrate the ionosphere to 120 km altitude with little distortion. The length of 1 km is the order of thickness of an auroral arc or ray (Alfven 1981). When the horizontal scale of the electric packet is too small, the small scale size components will be significant, and therefore the field will encounter distortions. An example is shown in Figure 8 in which the parallel component of electric field at 300 km altitude is a delta function $\delta(y)$. This is the smallest horizontal length possible, and in penetrating, it is heavily reduced and distorted. In addition, Figure 8 could be considered as the smallest possible structure of electric field mapped from above 300 km altitude. On the ground, the parallel electric field is 0.3 V/m if the electric field on the top side boundary is $\delta(y)$ 10^{-9} V/m.

13.3.3 *Integrated electric field and current zero*

When the integral of parallel electric field across the top side boundary is zero, the current flowing into the ionosphere equals the current flowing out of the ionosphere at the top side boundary. From the theory of signal analysis, we know that the large scale components will be decreased more or less as is shown in Figure 7. From Figure 1, it is expected that the parallel electric field mapped to the lower region is less than that when there is net current flowing through the top side boundary. As an example, the electric field on the ground is represented by Figure 10 for the case when the parallel component on the top side boundary is expressed by equation (10) (as is shown in Figure 9) and the currents flowing into and out of the ionosphere are balanced.

As is mentioned in the last section, when there is a net parallel component of electric field on the top side boundary, the electric field on the ground is about 0.3 V/m which is much larger than when there is no net current flowing through the top side boundary. The significance of this effect is that whenever the detected electric field on the ground is drastically increased, a net current flowing into or out of the ionosphere will be one of the causes.

From Figures 9 and 10 it may be seen that larger horizontal scale length results in a larger amplitude of electric field on the ground. The magnitude of electric field on the ground is dependent not only on the amplitude of the electric field on the top side boundary, but also on its horizontal scale length. A similar conclusion is also obtained by Chiu (1974).

13.3.4 *Mapping of arbitrary electric field*

Let us perform the mapping of an arbitrary electric field from 300 km altitude to the ground. For any packet of electric field $f(y)$ on the top side boundary of which the spectral function is $F(k)$, the electric field on the ground is the inverse Fourier transform of $F(k)\psi_k(0)$. Suppose the inverse Fourier transform of $\psi_k(0)$ is $\Phi(y)$, the mapping on the ground is

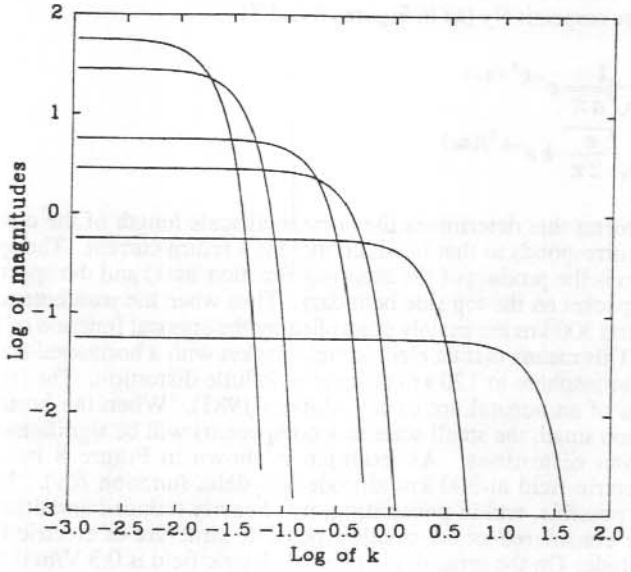

Figure 6. Spectra calculated from formula (11) in the text. From top to bottom or left to right, the parameter a is chosen as: 10^{-4}, 4 x 10^{-4}, 10^{-2}, 4 x 10^{-2}, 10^{0} and 10^{2}.

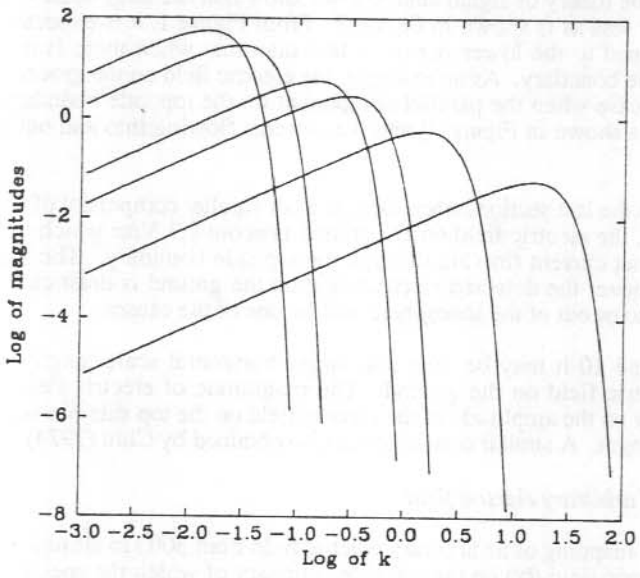

Figure 7. Spectra calculated from formula (12) in the text. From top to bottom or left to right, the parameter a is chosen as: 10^{-4}, 4 x 10^{-4}, 10^{-2}, 4 x 10^{-2}, 10^{0} and 10^{2}.

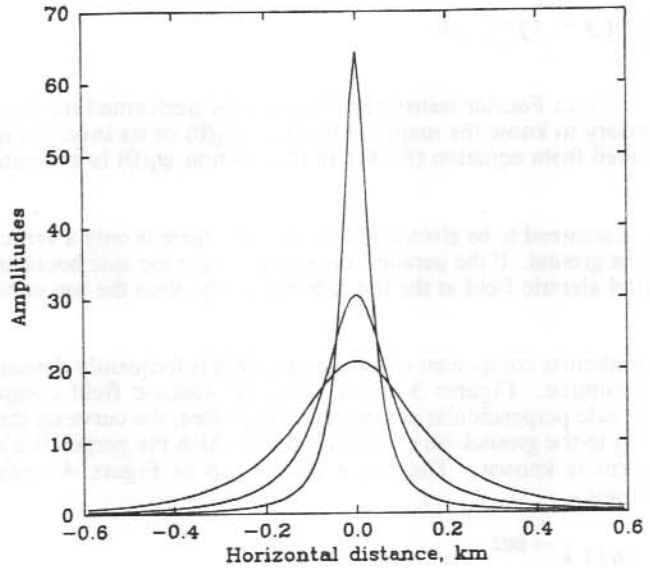

Figure 8. The calculated parallel electric field at altitudes of 270 km (the curve with a large peak), 239 km (the curve with a medium peak) and 210 km (the curve with a small peak), when parallel electric field on the top side boundary is a delta function $\delta(y)$.

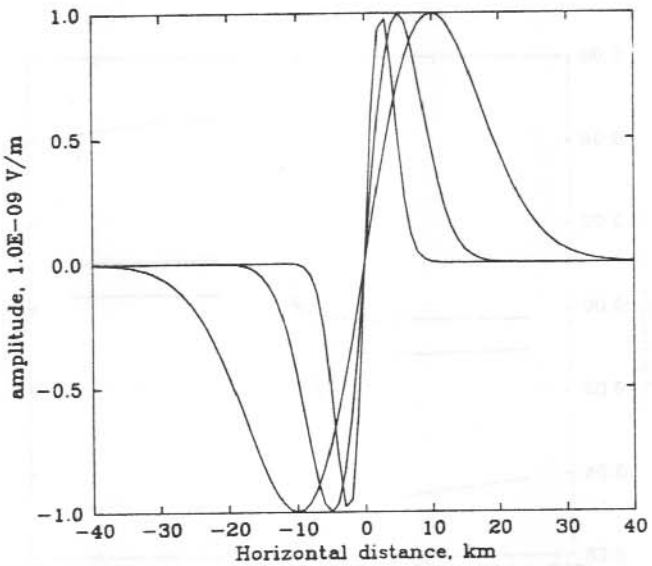

Figure 9. The parallel electric field distribution on the top side boundary calculated from equation (10). The parameter a is chosen as the following (from right to left in the positive plane): 5×10^3, 2×10^{-2} and $7.4 \times 10^{-2}/km^2$.

$$E(y) = \int_0^\infty f(y - t)\,\Phi(t)dt \tag{13}$$

Or alternatively, the direct Fourier transform (7) could be performed numerically. For both situations it is necessary to know the mapping function $\psi_k(0)$ or its inverse Fourier transform. They could be obtained from equation (8), but in this section $\psi_k(0)$ is estimated by piecewise approximation.

Because the ground is assumed to be electrically conducting, there is only a vertical component of the electric field on the ground. If the parallel component on the top side boundary is known, that is if $f(y)$ is the parallel electric field at the top side boundary, then the top curve of Figure 1 is used as $\psi_k(0)$.

In practice, the perpendicular component of the electric field is frequently detected because of its relatively larger magnitude. Figures 3 and 4 show the electric field components that are normalised to the top side perpendicular component. Therefore, the curve on the top of Figure 4 is used when mapping to the ground the electric field for which the perpendicular component at an altitude of 300 km is known. The curve on the top of Figure 4 could be piecewise approximated as follows:

$$\psi_k(0) = \begin{cases} 0.1624\,k^{-1.002} & 0 < k \le 0.01 \\ 5.09 \times 10^{-13} k^{-11.42} & k > 0.01 \end{cases} \tag{14}$$

The inverse Fourier transform of $\psi_k(0)$, $\Phi(y)$ could then be obtained. Therefore, any electric field on the top side boundary, whose perpendicular component is $f(y)$, could be obtained from either equations (13) or (7).

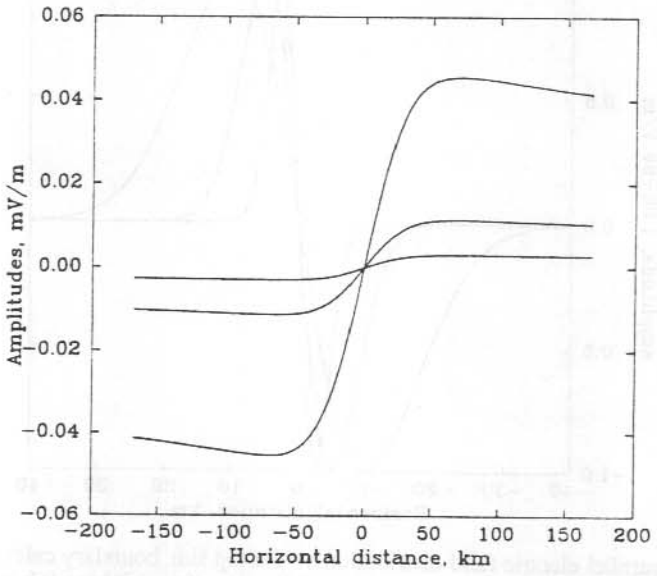

Figure 10. The electric field distribution on the ground for a parallel electric field on the top side boundary as in equation (10) or Figure 9. The parameter a chosen as the following (from top to bottom on the right): 5×10^{-3}, 2×10^{-2}, $7.4 \times 10^{-2}/km^2$.

13.4 REFERENCES

Alfven, H. (1981). *Cosmic Plasma Physics*. D. Reidel Publishing Company, Netherlands.

Chiu, Y.T. (1974). Self-consistent electrostatic field mapping in the high latitude ionosphere. *Journal of Geophysical Research 79*:2790.

Lyons, L.R. (1980). Generation of large-scale regions of auroral currents, electric potentials, and precipitation by the divergence of the convection electric field. *Journal of Geophysical Research 85*:17.

Weimer, D.R., Goertz, C.K., Gurnett, D.A., Maynard, N.C. *and* Burch, J.L.(1985). Auroral zone electric fields from DE-1 and DE-2 at magnetic conjugations. *Journal of Geophysical Research 90*:7479.

14. PROPAGATION STUDIES AT 244 MHz AND 1.5 GHz AT HIGH SOUTHERN LATITUDES

E.A. Essex[1] and D. Rasch[2]

[1]La Trobe University
Bundoora Vic 3083
Australia

[2]Antarctic Division
Kingston Tas 7050
Australia

ABSTRACT

During 1987, measurements of the signal strength variations of a FLTSATCOM beacon on 244 MHz and a 1.5 GHz beacon from INTELSAT V-F5 were undertaken at the Australian Antarctic station Davis. Four distinct types of scintillation events have been recorded: weak fading events (1.5 GHz only) which are assumed to be of tropospheric origin, events with durations of the order of hours, 'burst' events of 1-10 minutes duration, and quasi-periodic or 'spike' signal oscillations. Examples of scintillation indices, power spectra and the direction of motion of the irregularities are presented. Possible sources of these scintillation disturbances are discussed. The authors' observations may have implications for the future design of L band communications systems at southern mid-latitudes.

14.1 INTRODUCTION

A radio wave traversing the upper and lower atmosphere of the Earth is subject to distortions of phase, amplitude and angle of arrival. These are referred to as scintillations. When the radio wave traverses drifting ionospheric irregularities, it experiences scintillations which vary widely with the frequency of the radio wave, magnetic and solar activity, time of day, season and latitude. Even at frequencies above 1 GHz large signal level fluctuations are likely to occur, particularly during years with high solar activity. On a global scale there are three major regions of scintillation, all with a pronounced night-time maximum in occurrence. The equatorial region, within $\pm 20^{\circ}$ of the magnetic equator, records the greatest depth of scintillation fading. The high-latitude region, here defined as including the auroral oval and regions poleward of this (generally following Aarons (1982)), has the next greatest depth. The remaining region, the middle latitudes, has the least.

In the region poleward of Australia very few studies of scintillation activity have been carried out, especially at frequencies above 1 GHz. In the Southern Hemisphere the separation of the geomagnetic and geographic poles is much larger than in the Northern Hemisphere. Hence the region south of Australia presents a unique environment for study. In order to study ionospheric irregularities and their effect on satellite transmissions at high southern latitudes, observations were undertaken from Davis during 1987. In this study a quantitative evaluation of the effects of ionospheric scintillations at 244 MHz and 1.5 GHz was made.

14.2 OUTLINE OF THE EXPERIMENT

Figure 1 shows Davis in Australian Antarctic Territory. It is located at 68.6°S, 78.0°E (geographic), 74.6°S (invariant). In this study the transmissions of the geostationary satellites Fleetsat (244 MHz) and Inmarsat (1.5 GHz) were monitored. Fleetsat is located at 73°E and Inmarsat at 63°E. The sub-ionospheric points for an altitude of 120 km (*E* region) are 64.6°S, 77.1°E for Fleetsat and 64.5°S, 75.3°E for Inmarsat. The corresponding sub-ionospheric points for an altitude of 350 km (*F* region) are 59.0°S, 76.2°E and 58.9°S, 72.7°E. The elevation angle

to both satellites is 13° Separation between the sub–ionospheric points for the two satellites is around 90 km for the *E* region and 215 km for the *F* region. Magnetic midnight corresponds to 20.7 UT for *F* region and 21.2 UT for *E* region sub-ionospheric points. Transmissions from both satellites are circularly polarised and therefore received signal strengths are not affected by Faraday rotation.

The Fleetsat signals (244 MHz) were received on a dedicated system consisting of a nine element Yagi antenna, a masthead preamplifier and a receiver located 30 m away in the Davis laboratory. The Inmarsat signals (1.5 GHz) were received by a satellite ground station used for telephone communications from Davis. Equipment of this type is generally operated from ships, and has an auto tracking facility to accommodate a moving platform. This facility was disabled for the duration of the study. The Inmarsat signal was monitored via a 10.5 MHz IF test point prior to any automatic gain control in the ground station. The systems were regularly calibrated and amplitude data from both receivers logged at 20 samples per second on an LSI 11/23 computer.

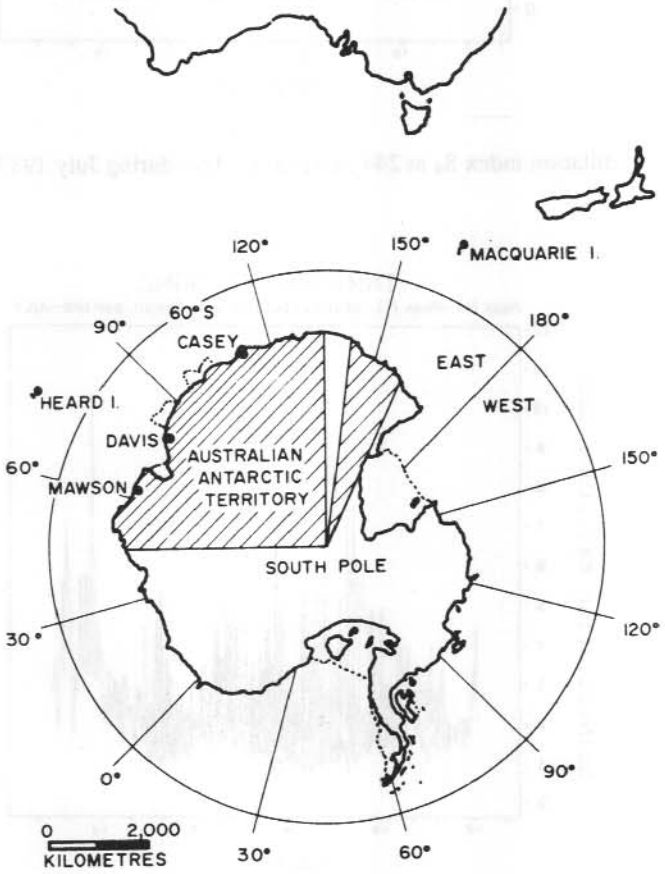

Figure 1. A map of Antarctica showing the location of Davis.

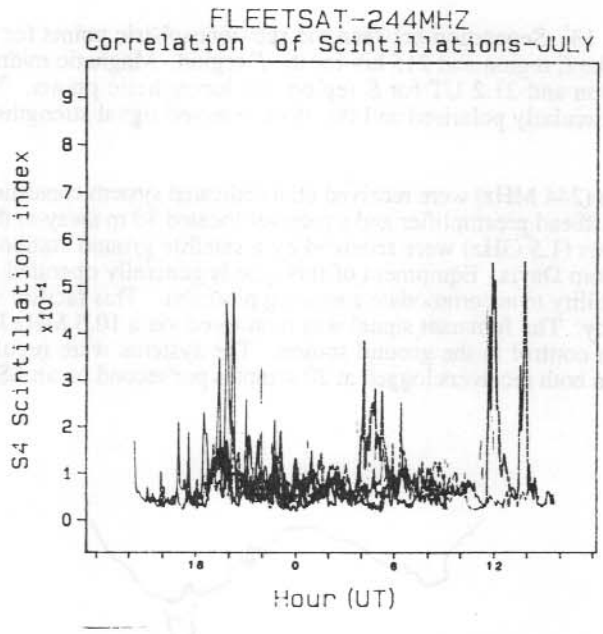

Figure 2. The scintillation index S_4 at 244 MHz on 11 days during July 1987.

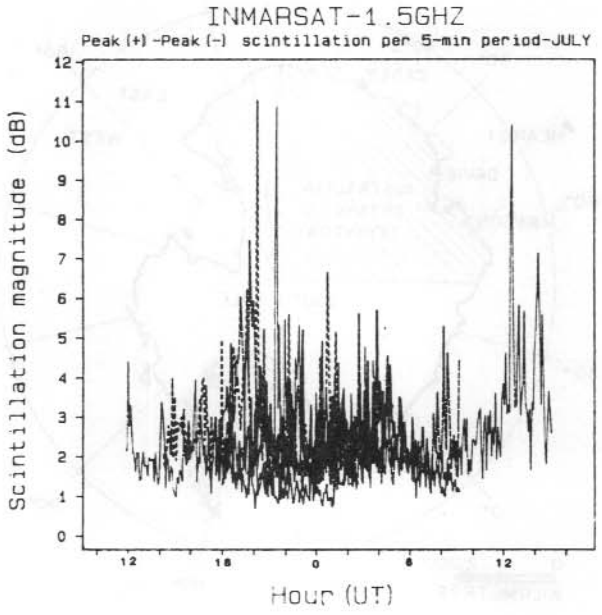

Figure 3. The scintillation magnitude for Inmarsat on 8 days during July 1987.

14.3 EXPERIMENTAL RESULTS AND DISCUSSION

14.3.1 *Types of scintillation*

The scintillation events recorded in 1987 could be classified into four types:

(1) Weak (1-6 dB) 1.5 GHz fading, with a duration of the order of 1-10 minutes, which is presumed to be of tropospheric rather than ionospheric origin. This type of event will not be discussed in this paper.

(2) Scintillation events with durations of the order of hours. The amplitude variation and the duration of these events are consistent with previous high-latitude studies (Aarons 1982, and references therein).

(3) Short duration events (1-10 minute 'bursts'), of larger amplitude than the type 2 events, which were often superimposed on these type 2 events.

(4) Quasi-periodic signal oscillations with a central fade a common feature. There is often a good correlation between satellites for events of types 2 and 3. Although type 2 events generally correlate best with time delays of 10-40 minutes, type 3 events often appear to occur simultaneously on both satellites. While type 4 events occur at both 244 MHz and 1.5 GHz, correlations between the two frequencies for this type of event cannot be established with the authors' data.

Figure 2 shows the scintillation index S_4, for 244 MHz, for 11 days during July 1987. The S_4 index, a measure of the scintillation strength, is defined as the square root of the variance of the received power divided by the mean value of the received power for a chosen time interval (Briggs and Parkin 1963). The S_4 index presented in Figure 2 is evaluated over 5 minute intervals.

An example of the magnitude of scintillation activity on 1.5 GHz for eight days in July is shown in Figure 3. The magnitude, in dB, is determined from the difference between the highest and lowest amplitude recorded in each 5 minute interval. Figures 2 and 3 show peaks in scintillation activity around 20 UT (23 MLT). These peaks may correspond to auroral activity in the midnight sector at the sub-ionospheric point. The 244 MHz scintillation activity (Figure 2) shows two other peaks, one around 05 UT (08 MLT) and another near 13 UT (16 MLT). Scintillation activity at these times may correspond to the passage of the auroral oval over the sub-ionospheric point before and after magnetic noon. The 1.5 GHz scintillation activity (Figure 3) shows similar peaks but also shows some activity around 09 UT (12 MLT). The 244 MHz scintillation activity (Figure 2) is a minimum at this time. It is important to note that Figures 2 and 3 correspond to activity recorded over only a few days and thus may not be typical of long term averages. It should also be noted that the S_4 index emphasises 'average activity' of the 5 minute interval, while the 'scintillation magnitude' emphasises the maximum excursion over this period. Either of these factors may account for the discrepancy around 09 UT.

14.3.2 *Plasma drift speeds*

Observations by satellite have shown the existence of a two cell magnetospherically induced ionospheric convection pattern in the polar *F* region when the interplanetary magnetic field (IMF) has a southward component (Heelis et al. 1982) (Figure 4). This pattern results in an anti-sunward drift at high latitudes and a sunward drift at lower latitudes, except on the noon-midnight meridian, in the auroral zone. When the IMF has a northward component, the plasma flow pattern is more irregular and less predictable. Kilometre-scale irregularities responsible for VHF and UHF scintillations are often present within *F* region plasma, and drift with the plasma for many hours before diffusing. Type 2 scintillation events can thus be studied to determine movements of the background plasma.

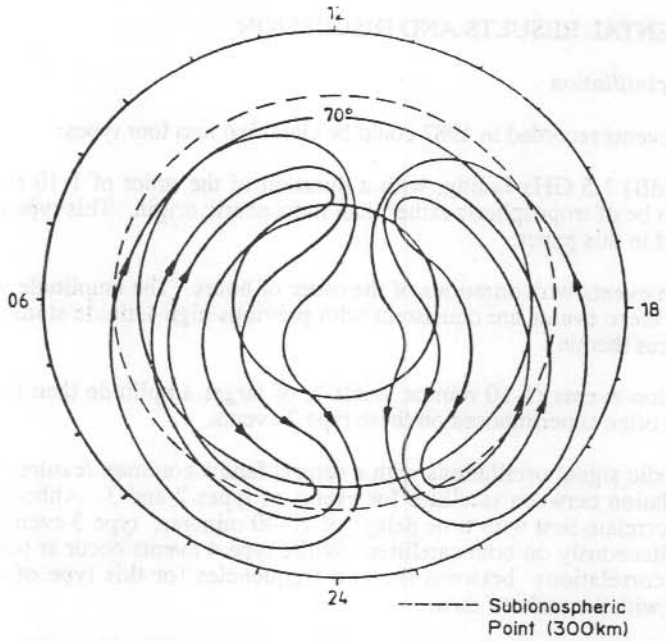

Figure 4. The polar plasma flow in magnetic local time (MLT) and invariant latitude coordinates (from Heelis et.al. 1982).

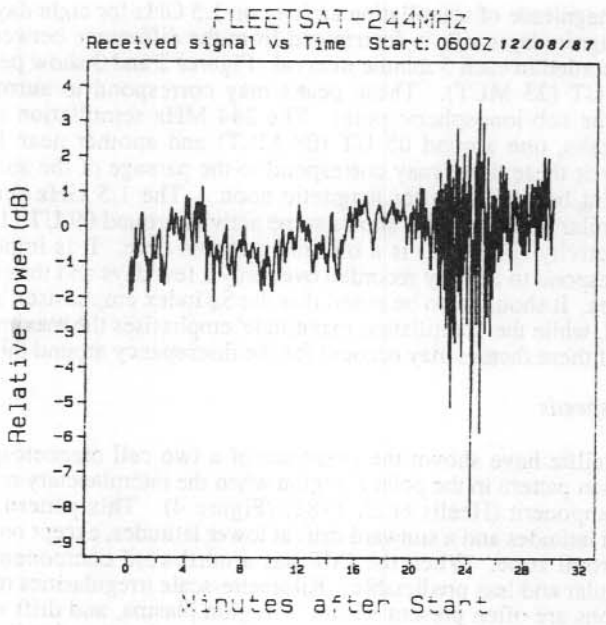

Figure 5. Type 2 scintillation activity followed by a type 3 event.

In order to study the plasma drift three techniques were used:

(i) *Power spectral analysis*

When the power spectrum for a scintillation event is plotted in dB versus log (frequency), the spectrum can generally be approximated by two straight lines with different slopes. The frequency corresponding to the intersection of the two lines is termed the Fresnel frequency. Contributions at the Fresnel frequency to amplitude scintillations are due to irregularities with a spatial scale size equal to the Fresnel size. For observations utilising a geostationary satellite the Fresnel size is $(\pi\lambda z)^{1/2}$, where λ is the signal wavelength (in metres) and z is the oblique range between the irregularity and the receiver (in metres).

For this experiment, the Fresnel sizes for the F region are 2070 m and 840 m for 244 MHz and 1.5 GHz respectively. At E region heights the Fresnel sizes are 1330 m and 540 m respectively. Thus this experiment is concerned with irregularities with a spatial scale size in the range 500 m to 2 km approximately.

For frequencies above the Fresnel frequency the power spectrum has a negative gradient, given by (Rufenach 1972)

$$m = -10\,(p - 1)$$

in dB/decade, where p is the spectral index .

The spectral index is generally 4 ± 1 for scintillation events observed over a wide range of latitudes (Yeh and Liu 1982, and references therein).

Figure 6 shows two spectra computed for 10 minute intervals corresponding to the period just prior, and just subsequent to, the onset of the type 3 event. The rolloff slopes of the spectra both yield a value of $p = 3.7$ which is in close agreement with previous results. The extent to which the signal is diffracted by irregularities with scale sizes larger then the Fresnel size decreases as the scale size of the irregularities increases. Thus the power spectrum has a reduced gradient at frequencies below the Fresnel frequency.

If a height for the irregularities is assumed, it is possible to calculate the oblique range z from the system geometry. Then, having measured the Fresnel frequency from the power spectrum, the transverse component of the irregularity velocity can be computed from the relationship (Singleton 1974)

$$V_e = F_f\,(\pi\lambda\, z)^{1/2}.$$

Difficulties in determining the Fresnel frequency from the power spectrum, and the uncertainty in the assumed height of the irregularities, may contribute significantly to uncertainties in the calculated transverse component of the plasma velocity.

An irregularity height of 350 km was chosen for the weak long-duration type 2 scintillation event in Figure 5. This is a reasonable assumption since the long duration of this type of event (at Davis they have been observed on occasion to persist for in excess of 24 hours) is more consistent with recombination times in the F region than the E region. For this assumed height a transverse velocity of less than 30 m/sec was calculated. If the type 3 burst superimposed on this type 2 event (Figure 5) also results from irregularities at a height of 350 km, a transverse velocity in excess of 200 m/sec is obtained. The spectral index p depends on the distribution of irregularity scale sizes drifting through the raypath. The similar spectral indices ($p = 3.7$) for the type 2 and 3 events may be taken to indicate that the irregularites responsible for the two event types are located in the same region of the ionosphere. However, several features of the type 3 event suggest an E region origin. These are:

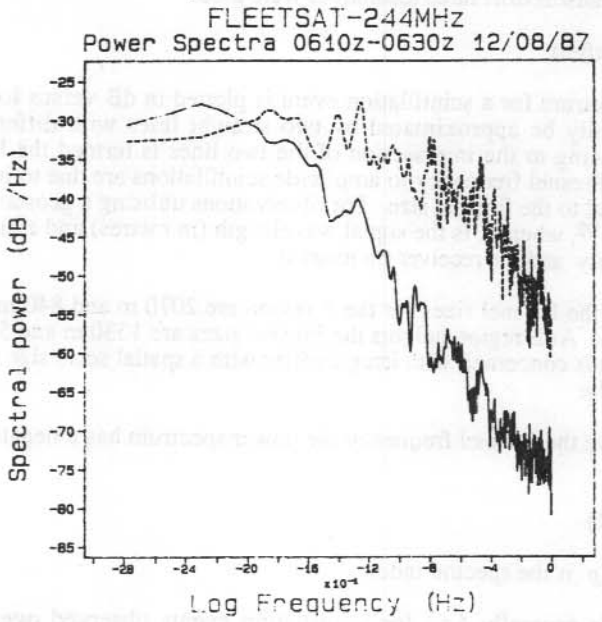

Figure 6. Power spectra for the type 2 and type 3 events shown in Figure 5.

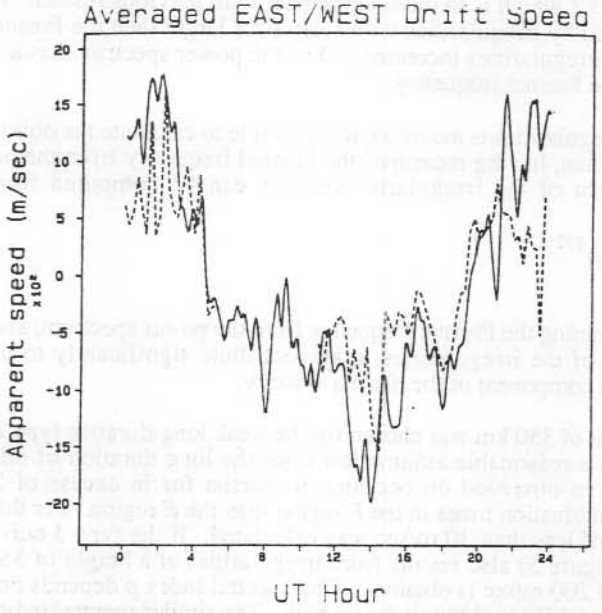

Figure 7. The averaged east-west drift speed (with east positive) for 6 days of data in September 1987 (—) determined using the spaced antenna method, and the transverse velocity component obtained from power spectral analysis for 10 September 1987 (- - -).

(1) a sudden onset within 1 minute
(2) a typical duration of less than 10 minutes
(3) a dramatic increase in plasma velocity during the event, and
(4) often simultaneous bursts on both satellite signals, even though their sub-ionospheric points are separated by 90 km (*E* region, 120 km) or 215 km (*F* region, 350 km).

These features are consistent with particle precipitation associated with substorm activity. Auroral heating effects, or possibly electric fields associated with irregular precipitation in the *E* region, may drive streams of plasma at high velocity. Under these circumstances, we might expect irregularity formation to occur rapidly via gradient drift or two-stream instability processes. The often apparent simultaneity between events seen at points at least 90km apart may indicate the east-west extent of the precipitation event.

(ii) *Spaced antenna method*

The second method used to measure the drift speed of ionospheric irregularities involved placing two Yagi antennas 130 m apart in the magnetic east-west direction and simultaneously monitoring 244 MHz signals on both. For type 2 scintillations, the time delay ΔT yielding best cross-correlation between the two signals was computed to the nearest 0.05 seconds. An 'apparent' velocity was computed by dividing the antenna separation by ΔT. This will yield the true velocity of the irregularities if they are drifting parallel to the base-line connecting the two antennas. If the drift is not exactly parallel to the baseline then an overestimate of the true velocity will be computed by this method. Conversely, the spectral analysis method discussed in the previous section, being sensitive only to the transverse component of velocity, will always yield a velocity less than or equal to the true velocity. Thus the two methods can be used to give an upper and lower limit to the true plasma velocity.

Figure 7 shows a six day average of the east-west drift speed obtained by the spaced antenna method and an overlapping day of power spectrum results. Only one day of power spectrum results were analysed because of the limited digital data storage facilities at Davis. The direction of the plasma drift determined using the spectral analysis method is assumed to be the same as that measured simultaneously by the spaced antenna method. Considering that the two methods should yield identical velocities only under ideal conditions, and that one is a six day average while the other presents results for a single day only, the curves are strikingly similar. This may result from the fact that the days analysed were chosen on the basis of almost continuous scintillation activity. These results therefore respresent plasma velocities for a disturbed ionosphere only.

The results show that the plasma has a westward drift component from 05 UT (08 MLT) until 19 UT (22 MLT), and an eastward component from around 21 UT (0 MLT) to 04 UT (07 MLT). The drift direction reverses abruptly just prior to magnetic midnight, and again between 04 UT (07 MLT) and 05 UT (08 MLT). Good agreement between the two plots around 12 UT (15 MLT) to 19 UT (22 MLT) indicates a predominantly westward flow while disagreement between the plots around 22 UT - 02 UT (01 MLT - 05 MLT) suggests the flow may have a substantial drift component parallel to the raypath. To summarise, the results obtained for the 6 days in September suggest an afternoon convection cell which is larger than the morning cell, in contrast to Figure 4. More information (e.g. IMF/data) for the period is required to interpret these results further.

(iii) *Spaced sub-ionospheric points*

The third method used to determine the east-west velocities was that of identifying similar type 2 scintillation events on 244 MHz and 1.5 GHz, and calculating the time shift for maximum correlation of the signals. Figure 8 shows an example of scintillation on two frequencies, the 1.5 GHz signal having been detrended by a 10 second high pass filter. The velocity calculated from the delay of 25 minutes for a height of 350 km is 145 m sec^{-1} which is in good agreement

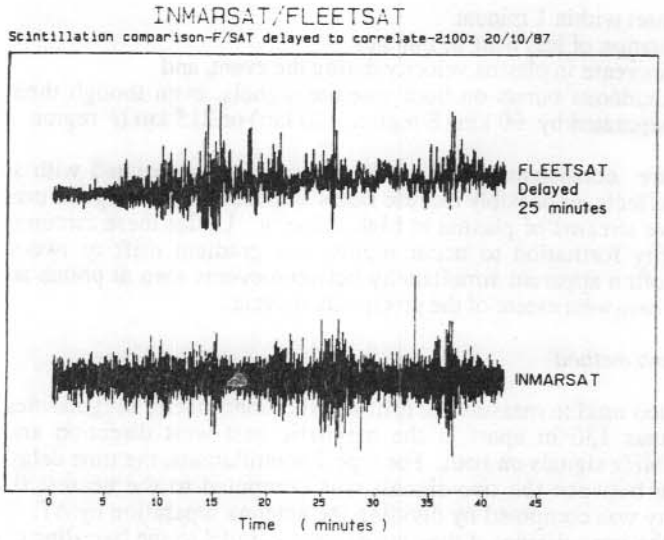

Figure 8. An example showing correlation between scintillation events on 244 MHz and 1.5 GHz

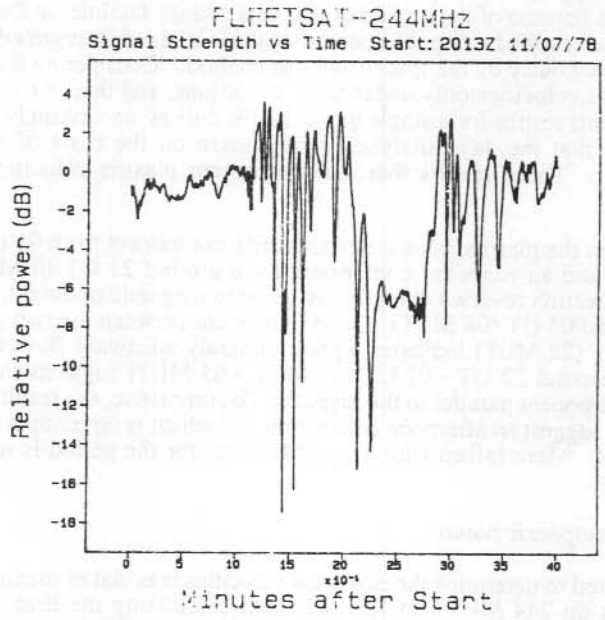

Figure 9. A quasiperiodic (type 4) event on 244 MHz showing an extended central fade.

with the 165 m sec^{-1} obtained from the Fresnel frequency computed during this time. Large errors can be associated with this method due to the assumption that the plasma is drifting in a direction which will intersect both satellite raypaths. Maximum accuracy should be obtained around 0600 MLT and 1800 MLT when plasma drift is predominantly east-west (see Figure 4).

Yeh and Liu (1982) have shown that for a power-law irregularity spectrum, the frequency dependence of the S_4 index is $S_4 = f^{-n}$ where $n = (p+2)/4$.

Using a value of $p = 3.7$ obtained for the spectra in Figure 6, a type 2 scintillation event on 244 MHz which has a scintillation index S_4 of 0.25 should produce a corresponding event on 1.5 GHz with a scintillation index of 0.022. An event with a scintillation index of 0.022 would be near the limit that could be identified above the contribution due to atmospheric scattering at 1.5 GHz. Thus this method of obtaining drift velocity can only be used for reasonably strong 244 MHz scintillation events.

14.3.3 *Quasi-periodic scintillations or spikes*

Quasi-periodic or 'spike' scintillations (type 4 events) were consistently recorded at Davis on both frequencies. Quasi-periodic events have been reported for thirty years (Hajkowicz 1977) and references therein, Karasawa (1987) and references therein), on both satellite and radio star signals. Interpretations as to their cause have included diffraction through drifting *E* or *F* region lenses, interference effects related to reflection from sporadic-E layers or *F* region travelling ionospheric disturbances (TIDs). Figures 9, 10 and 11 show examples of type 4 events recorded at Davis on 244 MHz or 1.5 GHz. The occurrence statistics of the quasiperiodic scintillations on 244 MHz and 1.5 GHz are shown in Figures 12 and 13. Scintillations at both frequencies show a peak in occurrence around 18 UT (21 MLT). Figure 9 is of particular interest because it shows a 6 dB signal fade at the centre of a 244 MHz event for approximately 30 seconds. Similar extended central fading has not been seen on 1.5 GHz.

Correlation between events on 244 MHz and 1.5 GHz was difficult to establish with the Davis data. Occasionally there was an event which appeared simultaneously on both frequencies, suggesting an auroral origin similar to type 3 events. At auroral latitudes, conditions should be ideal for the formation of field-aligned columns of ionisation as modelled by Davies and Whitehead (1977). At other times, no relationship between type 4 events at the two different frequencies could be seen.

Another interesting result from the 1.5 GHz statistics is an apparent spread in occurrences during the winter months. This may indicate the presence of an additional phenomenon which operates in the absence of daylight. The absence of similar events on 244 MHz may relate to the scale size of the phenomenon. The authors hypothesise that these winter events may result from columns of ionisation depletion rather than enhancement, relating to the influx of small comets into the Earth's atmosphere (Frank et al. 1986). Frank et al. interpreted depletions of the Earth's dayglow emissions at ultraviolet wavelengths as being due to the influx of these small comets. The Davis observations may indicate the night-time deep penetration of the comets into the ionosphere causing severe depletions of ionisation.

On 1.5 GHz, the Davis data shows that quasiperiodic scintillations have been responsible for the greatest decrease in signal levels, and may be dominant in determining communication link failures at this frequency.

14.4 CONCLUSION

This paper has presented the results of a preliminary study of propagation at 244 MHz and 1.5 GHz at high latitudes in the Southern Hemisphere. Studies of the convection pattern using scintillations may result in an inexpensive and reliable technique for determining the direction of

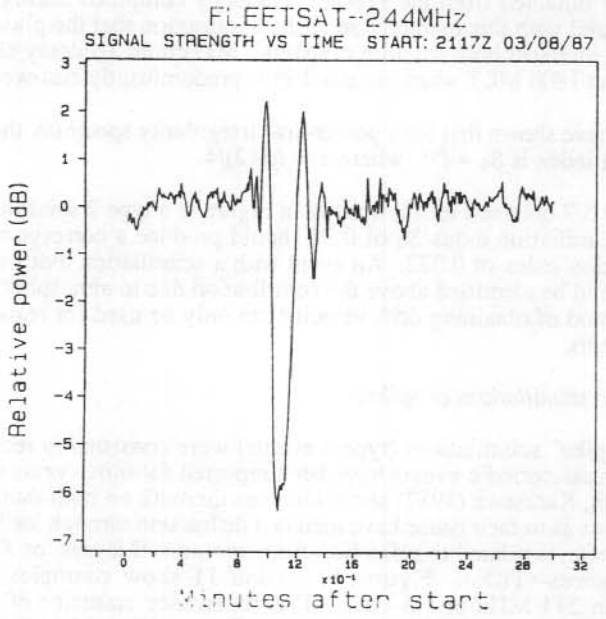

Figure 10. A quasiperiodic 'spike' on 244 MHz.

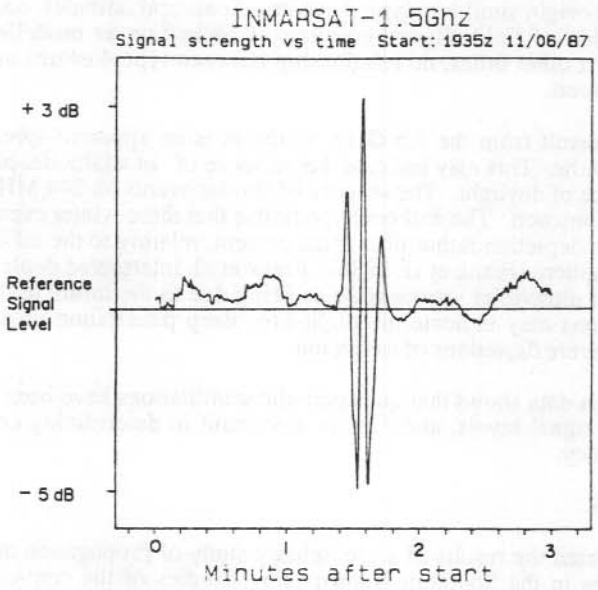

Figure 11. A quasiperiodic 'spike' on 1.5 GHz showing a similar form to Figure 10.

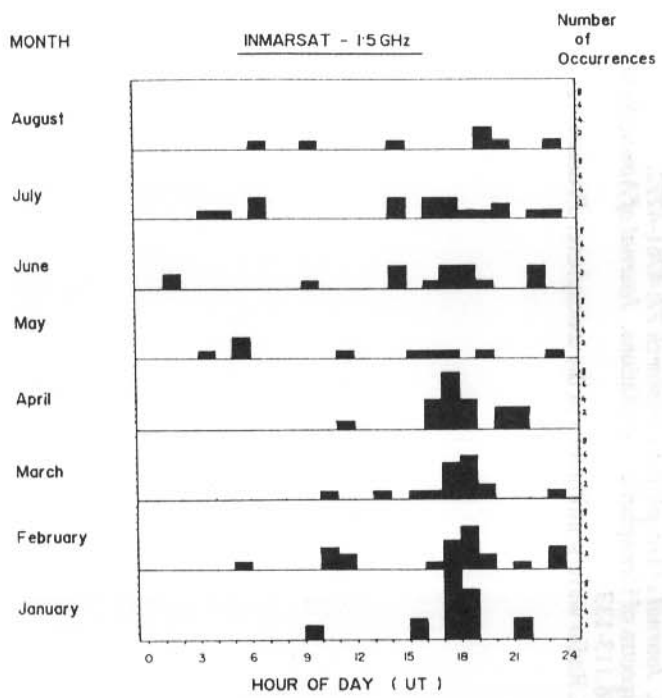

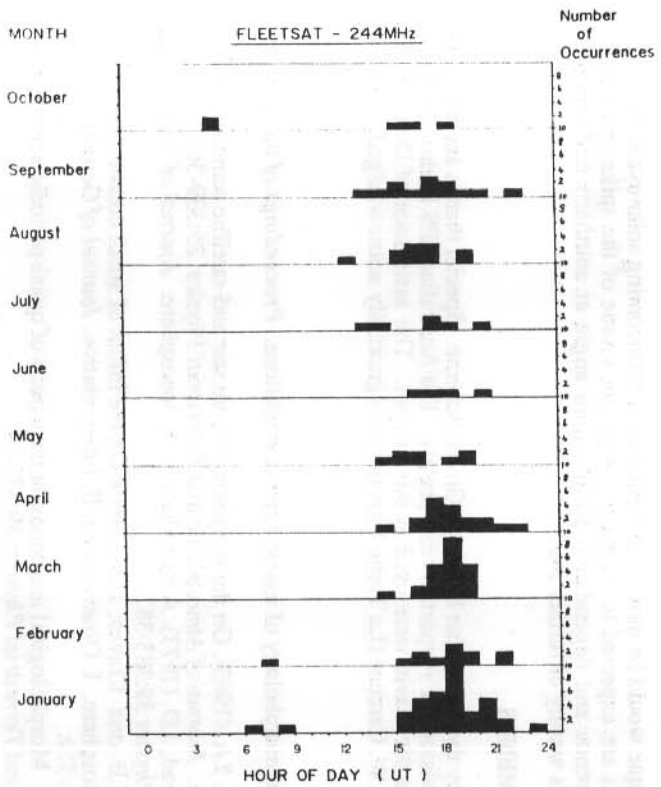

(left)
Figure 12. The diurnal/seasonal distribution of quasiperiodic scintillations with well defined central minima or maxima on 244 MHz.

(right)
Figure 13. The diurnal/seasonal distribution of 'spike' scintillations on 1.5 GHz.

the IMF. Such a technique would be most useful during the forthcoming solar cycle maximum when scintillation levels are expected to increase. Also, the source of the spike scintillation events and their occurrence and dependence on elevation angle at southern mid-latitudes, especially at 1.5 GHz, is worthy of further study.

14.5 ACKNOWLEDGMENTS

This work is supported by the Australian Research Grants Scheme. Special thanks are due to the Australian Antarctic Division for support for this project. The Australian IPS Radio and Space Services ionosonde data for Davis were used in this project. The assistance of Dr G. Burns (Antarctic Division) and W. Cercone (La Trobe University) is gratefully acknowledged.

14.6 REFERENCES

Aarons, J. (1982). Global morphology of ionospheric scintillations. *Proceedings of the IEEE 70(4)*:360-378.

Briggs, B.H. *and* Parkin, I.A. (1963). On the variation of radio star and satellite scintillations with zenith angle. *Journal of Atmospheric and Terrestrial Physics 25*:339-365.

Davies, K. *and* Whitehead, J.D. (1977). A radio lens in the ionosphere. *Journal of Atmospheric and Terrestrial Physics 39*:383-387.

Frank, L.A., Sigwarth, J.B. *and* Craven, J.D. (1986). On the influx of small comets into the earth's upper atmosphere. I. Observations, II. Interpretation. *Journal of Geophysical Research 13*:303-310.

Hajkowicz, L.A. (1977). Morphological and ionospheric aspects of quasi-periodic scintillations. *Journal of Atmospheric and Terrestrial Physics 39*:833-841.

Karasawa, Y. (1987). Interpretation of quasi-periodic scintillation at frequencies above 1GHz. *The Transactions of the IEICE 70* :768-774.

Heelis, R.A., Lowell, J.K. *and* Spiro, R.W. (1982). A model of the high-latitude ionospheric convection pattern. *Journal of Geophysical Research 87*: 6339-6345.

Rufenach, C.L. (1972). Power law wave number spectrum deduced from ionospheric scintillation observations. *Journal of Geophysical Research 77*: 4761-4772.

Singleton, D.G. (1974). Power spectra of ionospheric scintillations. *Journal of Atmospheric and Terrestrial Physics 36*:113-133.

Yeh, K.C. *and* Liu, C-H. (1982). Radio wave scintillations in the ionosphere. *Proceedings of IEEE* 70(4):324-360.

15. SCANNING SPECTROPHOTOMETER OBSERVATIONS OF HYDROXYL EMISSIONS AT DAVIS, ANTARCTICA

P.F.B. Williams
Antarctic Division
Kingston Tas 7050
Australia

ABSTRACT

A scanning spectrophotometer was used to measure spectra of the (8-3) Meinel emission of hydroxyl during the 1987 winter at Davis station (geographic coordinates 68.6°S, 78.0°E), Antarctica. This was accompanied by a 6-channel photometer tuned to four OH (8-3) P_1 branch lines. Consideration is given to the difficulties inherent in determining the temperature of the emission region. Preliminary results and temperature estimates are presented.

15.1 INTRODUCTION

Observations of hydroxyl airglow, principally in the (8-3) Meinel band, were made from Davis through late autumn to early spring, 1987. Two of the broad aims were to establish typical temperatures (or temperature ranges) near the mesopause, and learn more of auroral and other forms of "contamination" in this spectral region, and their effects on rotational temperature estimates. This paper presents some spectra obtained, with examples of contamination, and preliminary estimates of temperatures from late August to early October.

15.2 THEORY

It is reasonably well established that the OH emissions maximise around 86 ± 1 km, with a layer thickness of 6 to 10 km (e.g. Lopez-Moreno 1984, Battaner and Sanchez-Saavedra 1984, Vallance Jones 1985, von Zahn et al. 1987).

An important reason for estimation of OH rotational temperatures is to deduce neutral temperatures at the mesopause. For many years the mesopause was considered to be close to 85 km., conveniently within the OH emissions layer. However, recent studies have shown that, at least in high northern latitude winter atmospheres, the temperature minimum, while possessing short-term variability (hours to minutes), occurs close to 100 km, 13 to 14 km above the OH peak (Philbrick et al. 1985, von Zahn 1987, von Zahn and Neuber 1987). Thus it may be that the OH rotational temperatures measured at Davis throughout winter may be greater than the mesopause temperature to the order of 20°K (von Zahn and Neuber 1987).

To reduce emission intensities to temperatures it is assumed the rotational states are thermalised, and thus populated according to a Boltzmann distribution. For a given branch, the emission intensity versus quantum number, J, relationship may be resolved uniquely for any temperature from the relative intensities of any two lines, via equation (1),

$$T_{n,m} = \frac{E_{v'}(J'_m) - E_{v'}(J'_n)}{k \ln\left\{\frac{I_n}{I_m} \cdot \frac{A(J''_{m+i}, v'' \leftarrow J'_m, v')}{A(J''_{n+i}, v'' \leftarrow J'_n, v')} \cdot \frac{2J'_m + 1}{2J'_n + 1}\right\}} \qquad (1)$$

where $T_{n,m}$ is the rotational temperature estimated from intensities, I, of two lines from rotational levels J'_n, J'_m in the upper vibrational level v', and J''_{n+i}, J''_{m+i} in the lower vibrational level v"; $E_v(J)$ is the energy of level J, v; and $A(J'', v'' \leftarrow J', v')$ is the Einstein coefficient for

transition from J', v' to J",v". For the P branch of OH(8-3), v" = 8, v' = 3 and i = +1. (The above equation was adapted from Mies 1974.) Lambda type doubling is ignored.

Estimation of relative intensities is complicated by:

a. instrument response
b. baseline estimation (i.e. removing background continuum and dark noise)
c. removal of contamination
d. allowance for temporal variations between observations of individual lines

Within experimental accuracy, instrumental response may usually be ignored. Baseline estimates are mentioned later. Removal of auroral contamination is difficult, and only qualitative evaluation of its effect is attempted. Temporal variations are best removed by time averaging or interpolation.

Temperatures were usually obtained from equation (1) using all possible intensity rations, I_n/I_m, from the lines measured. Theoretically, these should all result in an identical temperature (assuming thermalisation). In reality there is some variance between the estimates, and a measure of this spread (e.g. standard deviation) is an indication of how well the measured intensities fitted the Boltzmann distribution. It may be used as a measurement of confidence in the temperature estimate. A large spread may arise from:

a. contamination
b. low signal to noise ratio
c. non-thermalisation
d. non-homogeneous thermal distribution within the field of view

15.3 INSTRUMENTATION

Instrumentation comprised principally a scanning spectrometer and a six-channel photometer. The 1.26 m Czerny-Turner spectrometer was used primarily for spectral scans.

The photometer employed a 6-position rotating filter wheel. Channels were tuned to the $P_1(2)$, $P_1(3)$, $P_1(4)$ and $P_1(5)$ lines of OH(8-3), as well as 7350 Å for monitoring the 'background continuum'. The sixth channel was unfiltered, and served both for calibration/test purposes and as a monitor of general photometric conditions.

Because of the weakness of the airglow, combined with the poor photomultiplier response in the near infrared, both instruments were oriented, via front silvered mirrors, to an elevation of approximately 30° above the S-E horizon, to benefit from the increased column volume at the emitting layer, compared to the zenith orientation. Photon counting was employed, using a cooled photomultiplier tube. The choice of the S-E horizon had the advantage that much less of the visible auroral activity is observed to the south than the north.

The two instruments were linked to a single micro-computer for overall control and data storage.

A wide-angle twin-channel photometer, zenith oriented, served as an auroral monitor at 5577 and 4278 Å.

Also operating as regular observatory instruments were an all-sky-camera, fluxgate and induction magnetometers, and a standard riometer (30.1 MHz).

15.4 SPECTRA

Some typical spectra are included in Figure 1. These are for 27 August and cover the range 7220 to 7530 Å (including OH(8-3) R, Q and P branches). The upper spectrum has only weak auroral

contamination, mainly in the R and Q branches. The later (lower) spectrum exhibits clearly an auroral contribution affecting most of the spectrum. The strong peak between approximately 7400 and 7500 Å is probably due to very intense activity varying rapidly within the time of a scan, and should not be interpreted as a reliable spectrum of the aurora.

The auroral contaminants of concern are shown in the sequence of spectra in Figure 2. The strong auroral couplets of OII are commonly present, varying in degree from negligible to several times stronger than the OH(8-3) P branch lines. The lower couplet, at 7318.6 and 7319.4 Å, is to the higher wavelength side of $P_1(2)$ (7316.4 Å). It appears as a slight bulge on the side of the $P_1(2)$ line in the 26 July spectrum, and as the major peak in the 22 July spectrum. The higher couplet, at 7329.9 and 7330.7 Å, is not resolved from the $P_2(3)$ line (7330.0 Å), and is seen as an apparent strengthening of that line compared to the rest of the branch, as on 26 July. Again, on 22 July, it is seen as a major peak.

N_2 IP(5-3) and IP(4-2) bands appear to be present at very low levels normally, and become strong only during active aurorae. The (5-3) band (bandhead at 7387.2 Å) effectively covers the $P_1(4)$ line of OH(8-3). It also has a significant line within the region covered by the 'background' (7350 Å) filter of the 6-channel photometer. The (4-2) band, headed at 7504.7 Å, covers the weak OH(8-3) $P_1(7)$ line, but can be expected to have little effect on the $P_1(6)$ line at 7346.1 Å. The $P_1(5)$ line should be immune to auroral activity.

The spectrum for 22 July shows that, even with strong contamination from OII, the N_2 bands may still be relatively weak.

The Meinel (5-2) band of N_2 occurs within the R branch of OH(8-3), but is not easily resolved and its contribution is difficult to assess.

The OI auroral line at 7254.4 Å, whose existence is generally considered uncertain (Chamberlain 1961), may contribute to apparent variability in the small peak near the R branch.

$N_2$1P(6-4) emissions may interfere with the Q branch spectrum, but cannot be specifically identified from our spectra, and must be assumed weak compared to the Q branch.

15.5 TEMPERATURES

Figure 3 presents two OH(8-3) region spectra (R to $P_1(5)$ branches), for 24 August. These reasonably contamination free spectra are representative of spectra from which the temperature estimates of Table 1 were determined. The temperatures include all estimates for the last month and a half of observations.

In most instances, two or more methods were employed for deciding on the base levels of the spectral lines. For each method the standard deviation, σ_t, for the temperatures derived from each pair of lines (as outlined in Section 15.2) was calculated, and for the method with the lowest σ_t the average of the estimates, along with the standard deviation, were included in the table. The grand average of these temperatures is 217°K, with a standard deviation of 36°K.

Inspection of the table shows a tendency for the 'high deviation' estimates to be significantly above average. If only those with $\sigma_t < 100$°K are averaged, the result is 205°K with a standard deviation of 14°K. (Further limiting the allowed σ_t lowers the average temperature slightly, with little change in the resulting deviation.) As a preliminary estimate, it would appear the OH rotational temperature near Davis in late winter to early spring is in the range 198 to 220°K. This is significantly higher than the range 160 to 170°K estimated by Stubbs et al. (1983) from Mawson station during winter 1979.

Figure 4 shows an example of photometer data for 20 September, a clear, moonless night. Counts were made on each channel (except the unfiltered channel) for 30 seconds, a complete

Day	U.T.	Span (min.)	Temp. (K)	Dev. (K)	Pl(3) / Bkgnd.	Pl(3) / Noise	Cloud	Aurora	Moon
237	1811	89	226	42			O/CAST	NIL(?)	N+(DN)
	1954	89	203	24			O/CAST	NIL(?)	N+(DN)
	2139	89	192	14			O/CAST	NIL(?)	N+(DN)
	2324(?)	89	213	12			O/CAST	NIL(?)	N+(DN)
238	1857	64	228	40			PART	NIL(?)	N+(DN)
	2013	63	275	133			PART	STRONG	N+(DN)
239	1841	163	226	40			NIL	MOD-STR	N+(DN)
240	2240	63	193	36			O/CAST	MOD(?)	1/4-(DN)
242	2044	64	268	137			NIL	WEAK(?)	1/4(UP)
245	1402	63	185	6	.6	8	NIL	NIL(?)	1/4(UP)
	2327	63	199	36	.3	6	NIL	NIL(?)	1/4(UP)
246	1402	62	178	9			O/CAST	?	1/4+(UP)
	1515	63	185	29			O/CAST	?	1/4+(UP)
	1629	63	280	115			O/CAST	?	1/4+(UP)
	1743	63	209	62			O/CAST	?	1/4+(UP)
	1857	64	311	172			O/CAST	?	1/4+(UP)
	2010	63	211	85			O/CAST	?	1/4+(UP)
	2124	63	349	305			O/CAST	?	1/4+(UP)
	2238	63	218	18			O/CAST	?	1/4+(UP)
255	1932	162	203	15	1.6		NIL	STRONG	3/4-(DN)
256	1628	84	212	20	1.2		NIL	MOD	3/4-(DN)
257	1432	63	194	2	1.2	10	LITTLE	V.WEAK	3/4(DN)
	1839	88	198	26	1.4	12	NIL	STRONG	3/4(DN)
258	1616	163	203	13	1.4	9	CL-BRKN	WEAK	3/4+(DN)
	1936	162	233	31	1.3	9	CLEAR	WEAK	3/4+(DN)
260	2151	63	197	23	1.2		LITTLE	MOD	3/4+(DN)
261	1605	63	199	31	1.6		NIL	WEAK	3/4+(DN)
	2146	62	198	4	.9		NIL	NIL	3/4+(DN)
262	1817	64	210	5	1.3		NIL	NIL	N-(DN)
272	1617	63	198	10	1.0	11	NIL	WEAK	1/4-(UP)
273	1532	63	216	46	.7	14	V.THIN	NIL	1/4(UP)
	2059	64	227	38	.6	9	THIN		1/4(UP)
274	1902	63	207	8	1.3	13	V.THIN	WEAK	1/4+(UP)
275	1658	162	206	8	.9	14	THIN	NIL	1/4+(UP)
276	1641	88	194	14	.6	13	V.THIN	NIL	F-(UP)
	1821	88	187	14	.7	12	V.THIN	NIL	F-(UP)
	2001	88	220	34	.3	10	THIN	NIL	F-(UP)
280	1738	88	201	31	.8	11	NIL	NIL	F(UP)
	1919	88	196	34	.7	12	SLIGHT	NIL	F(UP)
	2032	35	177	6	.5	6.5	BROKEN	NIL	F(UP)
283	1943	88	204	21	.8	7.7	NIL	MOD	F+(DN)
285	1728	88	187	12	.5	5	H.O/CST	NIL	3/4-(DN)
	1915	88	196	26	.5	5	O/CAST	NIL	3/4-(DN)

Table 1. Contamination 'free' temperature estimates from 25 August to 12 October, as explained in the text. 'Span' indicates the duration over which each spectrum was accumulated.

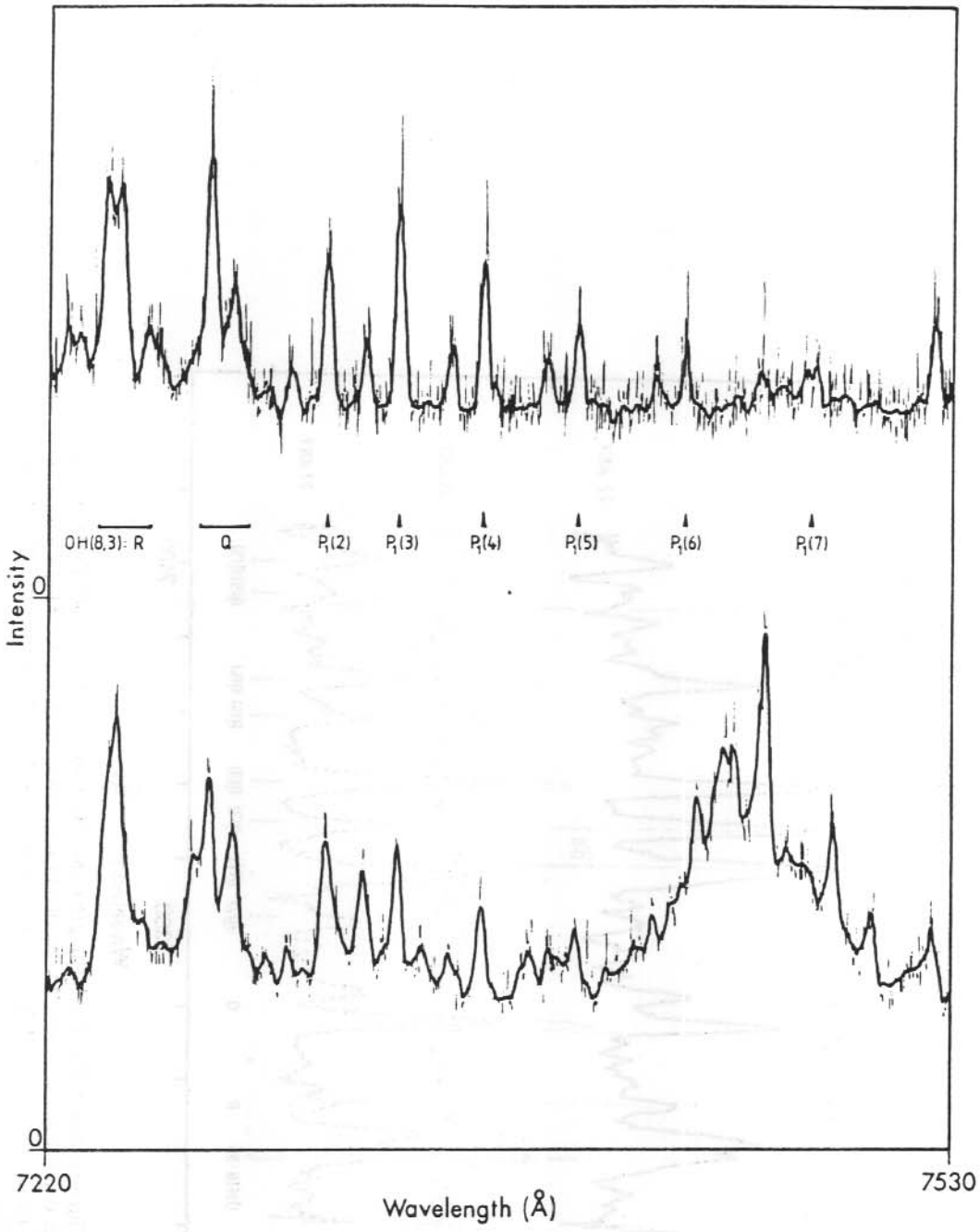

Figure 1. Two spectra of OH(8-3) region from 27 August 1987 (day 239). The lower spectrum shows effects of active aurorae. Each spectrum was the accumulation of five consecutive scans, taking a total of 163 minutes.

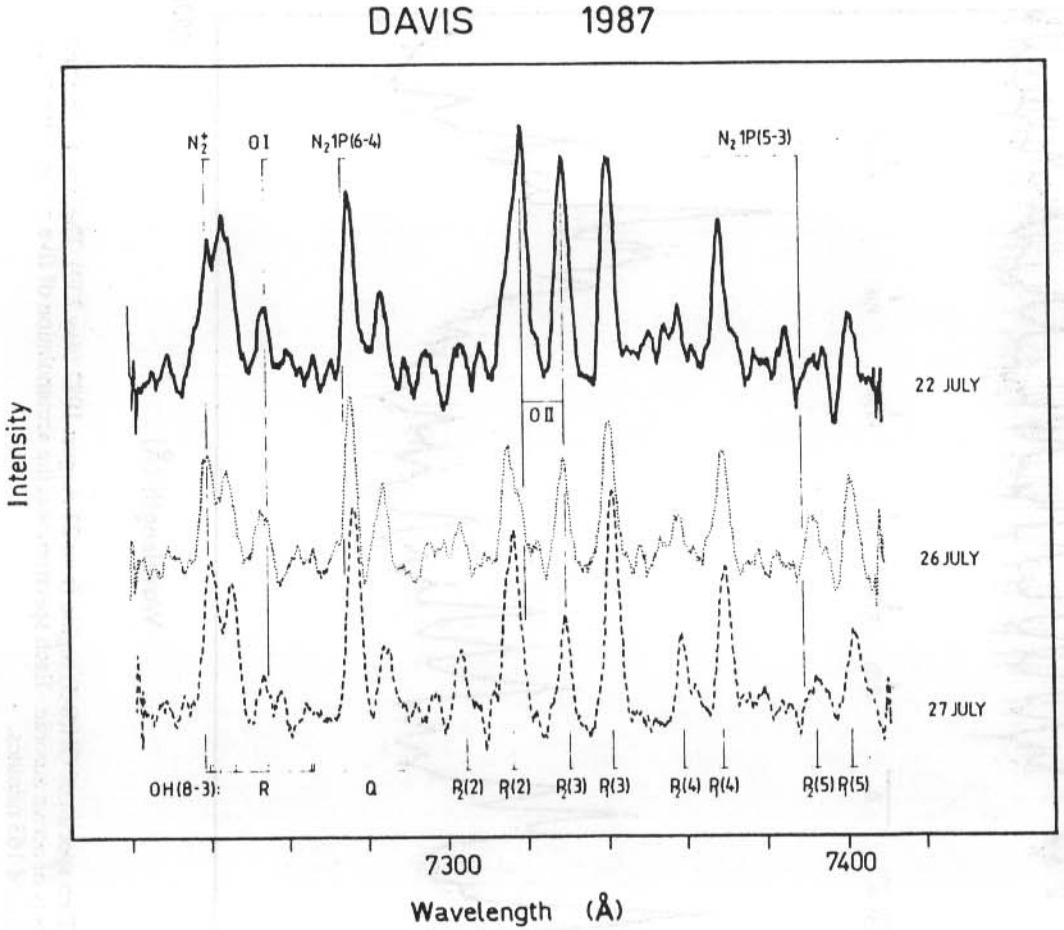

Figure 2. Three spectra of the OH(8-3) region, showing various auroral contaminations. Each of the lower two spectra was the accumulation of five consecutive scans, taking a total of 89 minutes. The spectrum for 22 July was the accumulation of twenty scans over approximately 100 minutes.

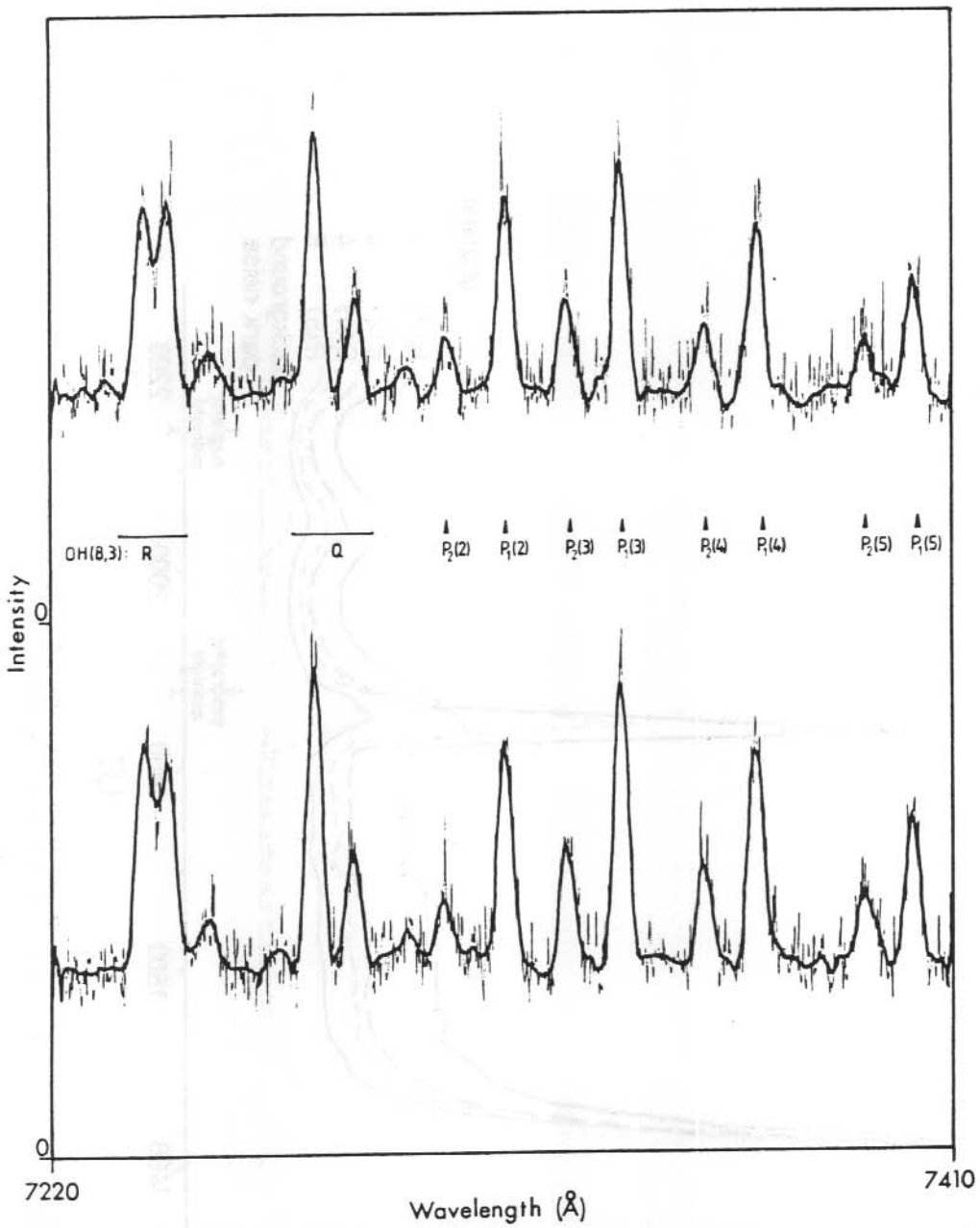

Figure 3. Two spectra of OH(8-3) region from 24 August 1987 (day 236). These are typical of the good quality spectra recorded and from which the higher confidence temperature estimates, as in Table 1, were obtained. Each spectrum is the accumulation of five scans, taking a total time of 89 minutes.

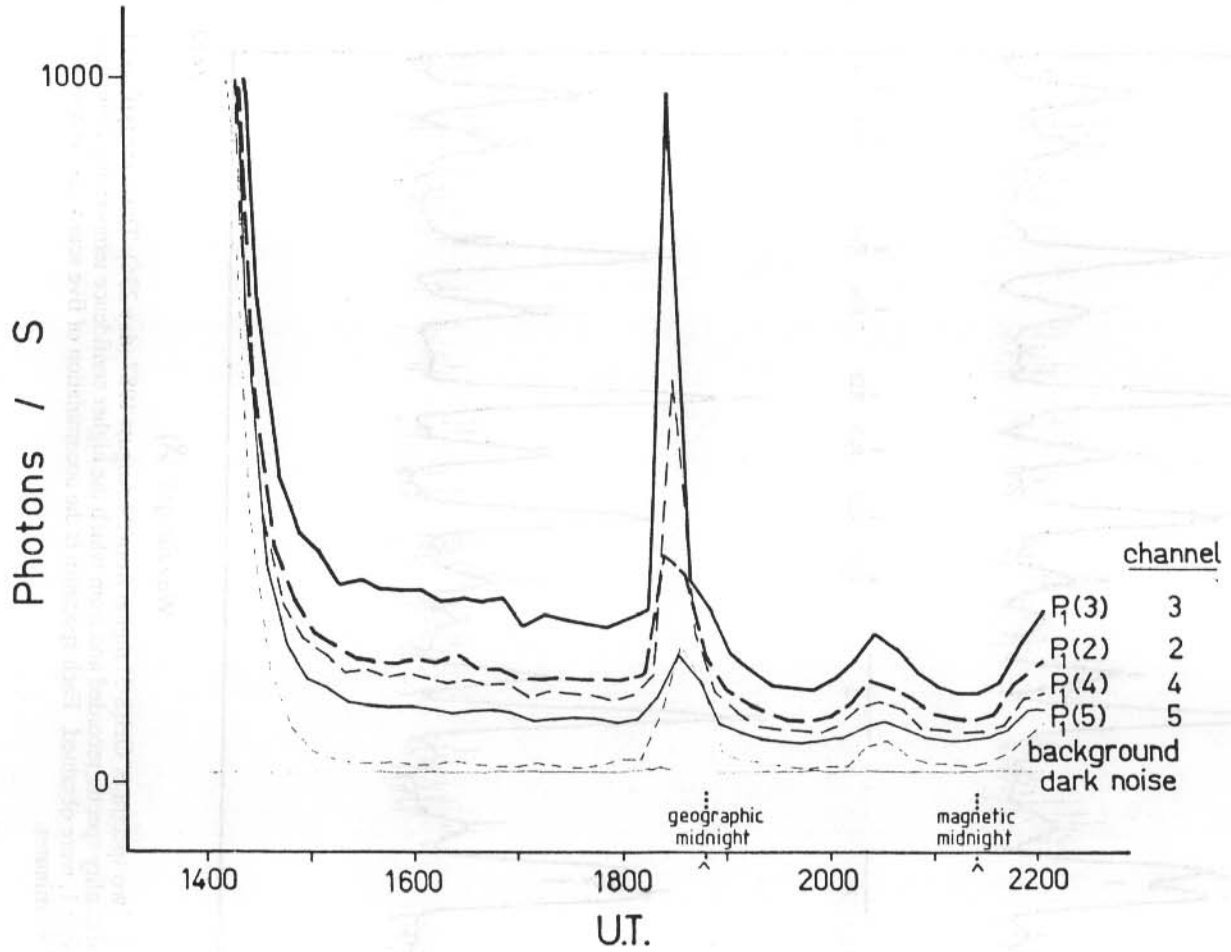

Figure 4. Raw data for the 6-channel photometer for 20 September 1987 (day 263). Counts were taken over 30 seconds on each channel, with a cycle completed in approximately 10 minutes.

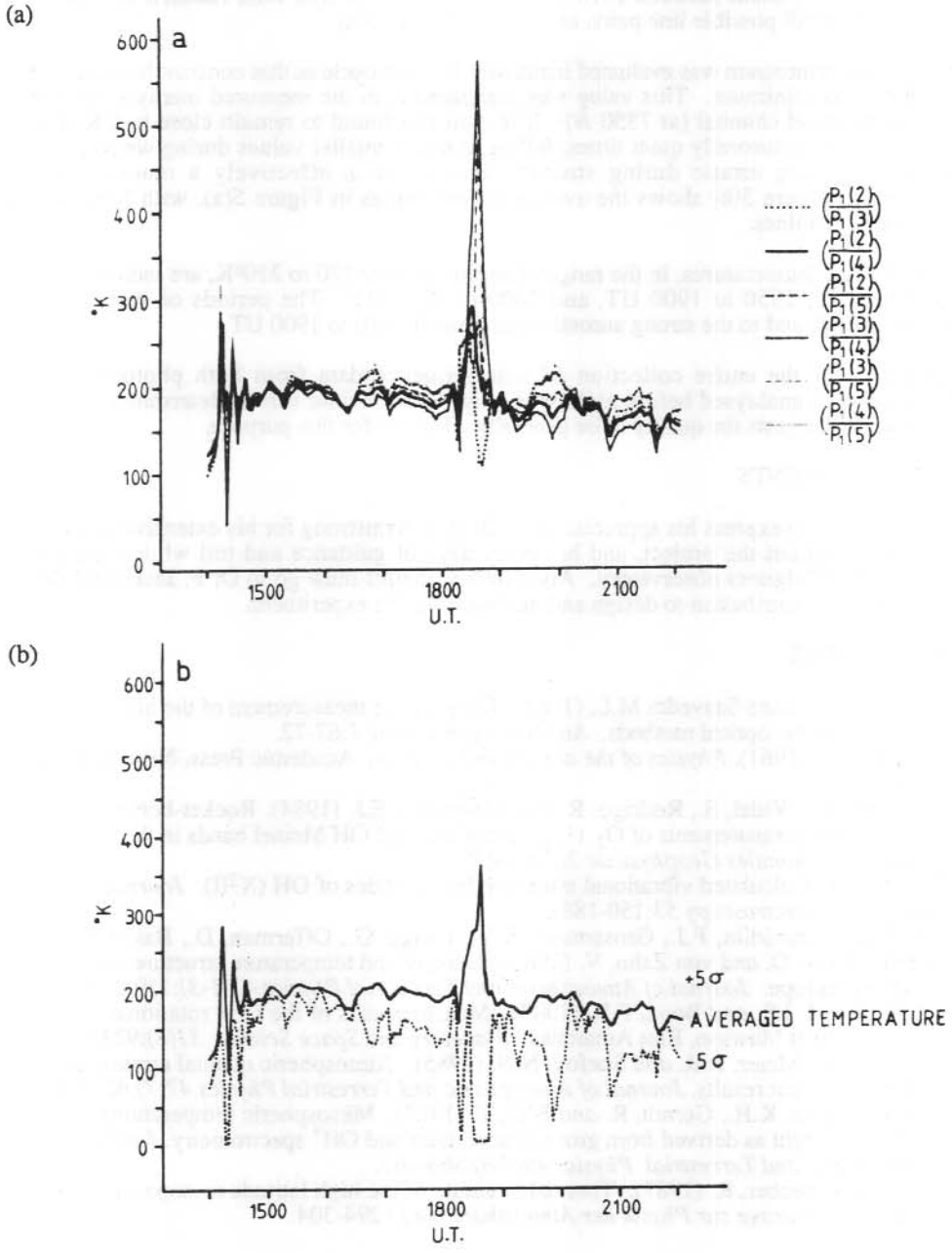

Figure 5. Temperatures reduced from the photometer data of 20 September (Figure 4): (a) for each possible ratio of P_1 branch lines, (b) averaged over all ratios.

cycle taking approximately 12 minutes. A period of moderately strong auroral activity within the field of view is prominent between 1810 and 1900 UT. These data were reduced to rotational temperatures from all possible line pairs, as shown in Figure 5(a).

The background continuum was evaluated iteratively for each cycle as that constant baseline value for which σ_t was minimum. This value was compared with the measured intensity from the nominal background channel (at 7350 Å). It is typically found to remain close to 0.8 of that measurement during aurorally quiet times, falling to much smaller values during weakly active times and becoming erratic during stronger events. It is effectively a monitor of N_2 contamination. Figure 5(b) shows the average of the curves in Figure 5(a), with $\pm 5\sigma_t$ limits given by the dotted lines.

'High confidence' temperatures, in the range of approximately 170 to 210°K, are indicated from 1440 to 1630 UT, 1850 to 1900 UT, and 2000 to 2040 UT. The periods of very high σ_t correspond to dusk and to the strong auroral event around 1810 to 1900 UT.

It is essential for the entire collection of time sequence data from both photometer and spectrometer to be analaysed before nightly or seasonal behaviour can be determined, but that processed so far suggests the quality to be generally adequate for this purpose.

ACKNOWLEDGMENTS

The author wishes to express his appreciation to Dr E.B. Armstrong for his extensive assistance and advice throughout the project, and his many days of guidance and toil while testing the equipment at the Culgoora observatory. Also, sincere thanks must go to Dr F. Jacka and Dr P. L. Dyson for their contribution to design and hardware for the experiment.

15.6 REFERENCES

Battaner, E. *and* Sanchez-Saavedra M.L. (1984). Temperature measurement of the high atmosphere by optical methods. *Annales Geophysicae 1*:67-72.

Chamberlain, J.W. (1961). *Physics of the aurora and airglow*. Academic Press, New York and London.

Lopez-Moreno, J.J., Vidal, S., Rodrigo, R. *and* Llewellyn, E.J. (1984). Rocket-borne photometric measurements of O_2 ($^1\Delta_g$), green line and OH Meinel bands in the nightglow. *Annales Geophysicae 2(1)*:61-66.

Mies, F.H. (1974). Calculated vibrational transition probabilities of OH ($X^2\Pi$). *Journal of Molecular Spectroscopy 53*:150-188.

Philbrick, G.R., Schmidlin, F.J., Grossmann, K.V., Lange, G., Offerman, D., Baker, K.D., Krankowsky, D. *and* von Zahn, V. (1985). Density and temperature structure over northern Europe. *Journal of Atmospheric and Terrestrial Physics 47(1-3)*:159-172.

Stubbs, L.C., Boyd, J.S. *and* Bond, F.R. (1983). Measurements of the O-H rotational temperature at Mawson, East Antarctica. *Planetary and Space Science 31(8)*:923-932.

Vallance Jones, A., Meier, R.R. *and* Shefov, N.N. (1985). Atmospheric quantal emissions: a review of recent results. *Journal of Atmospheric and Terrestrial Physics 47(7)*:623-642.

von Zahn, V., Fricke, K.H., Gerndt, R. *and* Blix, T. (1987). Mesospheric temperatures and the OH layer height as derived from ground-based lidar and OH^* spectrometry. *Journal of Atmospheric and Terrestrial Physics 49(7-8)*:863-869.

von Zahn, U. *and* Neuber, R. (1987). Thermal structure of the high latitude mesopause region in winter. *Beitrage zur Physik der Atmosphare 60(3)*:294-304.

16. ANALYSIS OF DAY-TIME OBSERVATIONS OF THE λ 630 nm THERMOSPHERIC EMISSION OVER MAWSON, ANTARCTICA

M. Conde[1,2] and F. Jacka[1]

[1]The Mawson Institute for Antarctic Research
University of Adelaide
Adelaide SA 5000
Australia

[2]Antarctic Division
Kingston Tas 7050
Australia

ABSTRACT

A dual etalon scanning Fabry-Perot spectrometer was used at Mawson, Antarctica, for day-time observation of the λ 630 nm oxygen O(1D) emission, originating in the thermosphere at 200-300 km altitude. An outline is presented of the data reduction employed to isolate the emission from the considerably more intense background of scattered sunlight. Model profiles were fitted to the spectra obtained, yielding estimates of the intensity and Doppler broadening of the emission feature. Estimates of the intensity of the Ring component, a broad bandwidth, unpolarised component of skylight, were also obtained.

Data were compared from two separate years, 1982 and 1986, corresponding to solar maximum and minimum periods respectively. The average temperature from all 1982 profiles was 1250°K, whereas the 1986 average was 900°K. The range of the diurnal temperature variation was approximately 500°K in both cases. The 1986 intensity distribution peaked around local midday. The base of the 1982 intensity distribution also peaked around local midday, although there were many occurrences of higher intensities in the afternoon and evening. Greater intensities were seen in the data from 1982, the period of higher solar and magnetic activity. Similar Ring component intensities were observed in 1982 and 1986. This component of sky light is attributed to a ground reflection mechanism.

16.1 INTRODUCTION

Scanning Fabry-Perot spectrometer observations of Doppler shifts and broadening of various atmospheric optical emissions have been used for over two decades to measure neutral winds and temperatures within the emitting regions. However, the use of this technique has been almost entirely limited to night-time and twilight observing conditions. To extend these measurements into daylight hours, the authors have observed the λ 630 nm O(1D) line of atomic oxygen, a conspicuous feature of the airglow at all latitudes, which maximises in intensity around local noon. At high latitudes this emission is also a conspicuous feature of the spectrum of the aurora, which is in general more intense than the airglow. Because of the diurnal variation of the geographic latitude of the auroral oval (at any given longitude), the aurora typically maximises at Mawson around local geomagnetic noon. At all times the λ 630 nm emission intensity is low compared with that of day-time scattered sunlight, and contributes typically only a few percent of the total intensity at its peak wavelength (Noxon 1964, 1968 Bens et al. 1965; Barmore 1977; Cocks and Jacka 1979; Cocks 1983).

The scattered solar component of skylight exhibits the same Fraunhofer absorption lines as direct sunlight. However, both the direct and scattered solar spectra are displaced in wavelength by gravitational red shift, and Doppler shift due to the relative motion of the observer and the Sun. The Doppler component of the shift is due mainly to the rotation of the Earth. Hence, during daylight, thermospheric optical emissions are usually seen superimposed on a Fraunhofer

absorption feature, although at a slightly different wavelength, the displacement varying with solar zenith angle. In addition to the scattered solar contribution, there is a weak, broad band, unpolarised contribution to sky brightness, known as the Ring component, first observed by Grainger and Ring (1962). The presence of the Ring component makes Fraunhofer absorption lines appear less deep relative to the continuum level in skylight than they appear in sunlight.

16.2 INSTRUMENTATION AND OBSERVATIONS

Day-time spectroscopic observations of atmospheric emissions ideally require an instrument with a single wavelength passband, or at least one with very good sideband rejection. This is to prevent leakage of power from the adjacent continuum, and of spectral structure from nearby atmospheric absorption features. The present observations were taken with a dual Fabry-Perot spectrometer consisting of two etalons in series with a 0.3 nm bandwidth interference filter. The instrument, described by Jacka (1984), was an improved version of the one described by Cocks et al. (1980). Functionally, the main difference between these two spectrometers was that in the Mawson instrument both etalons were servo controlled both in separation and parallelism, whereas in the earlier instrument only the high resolution etalon was so controlled.

The instrument was scanned in wavelength by varying the etalon plate separations in 128 steps, covering a total wavelength range of 45 picometres (pm) in six seconds. Spectra were obtained by performing a series of scans, and summing the observed intensities separately for each of the 128 different wavelengths. In order that the scattered solar component could be accounted for in subsequent analysis, scans of the pure Sun spectrum (taken through a separate solar telescope) were intercalated with the sky scans, and separately summed. This approach allowed effectively simultaneous Sun and sky spectra to be obtained, avoiding the need to correct the Sun spectrum for variation of Doppler shift with solar zenith angle. Typical acquisition times for a 128 channel sky-Sun spectral pair were around 1 hour. Observations were taken during the austral spring, summer and autumn periods in the years 1982-1986. Figures 1 and 2 illustrate some typical Sun and sky spectra. The emission feature was always more prominent in the 1982 spectra than in the 1986 spectra.

16.3 ANALYSIS

16.3.1 *The chi-squared goodness of fit parameter*

It is assumed that the observed sky spectrum can be represented as the sum of the Sun spectrum plus an emission feature plus a constant Ring component. Matching the directly observed Sun spectrum to the scattered solar component of the sky spectrum requires the inclusion of a normalisation term, $\eta(\lambda)$. That is

$$\text{sky}(\lambda) = \eta(\lambda)\ \text{sun}(\lambda) + w(\lambda).(E(\lambda) + R) \qquad (1)$$

where
$E(\lambda)$ = sky emission feature
$\eta(\lambda)$ = normalisation function
R = ring component
$w(\lambda)$ = spectrometer white light response, normalised to an average value of 1.

The spectrometer white light response is included in (1) above because roll off of the filter envelope and lack of perfect wavelength scan synchronism between the two Fabry-Perot etalons results in a spectral response that is not perfectly flat. $w(\lambda)$ was obtained prior to each sky-Sun observation by recording the spectrum of a laboratory white light source. The normalisation, $\eta(\lambda)$, is allowed to vary with wavelength, to account for variation in scattering efficiency with wavelength, changing solar zenith angle during the data acquisition, and spectral distortions due to (say) cloud drifting through either the Sun or sky fields of view. The simplest way to represent $n(\lambda)$ is with a polynomial

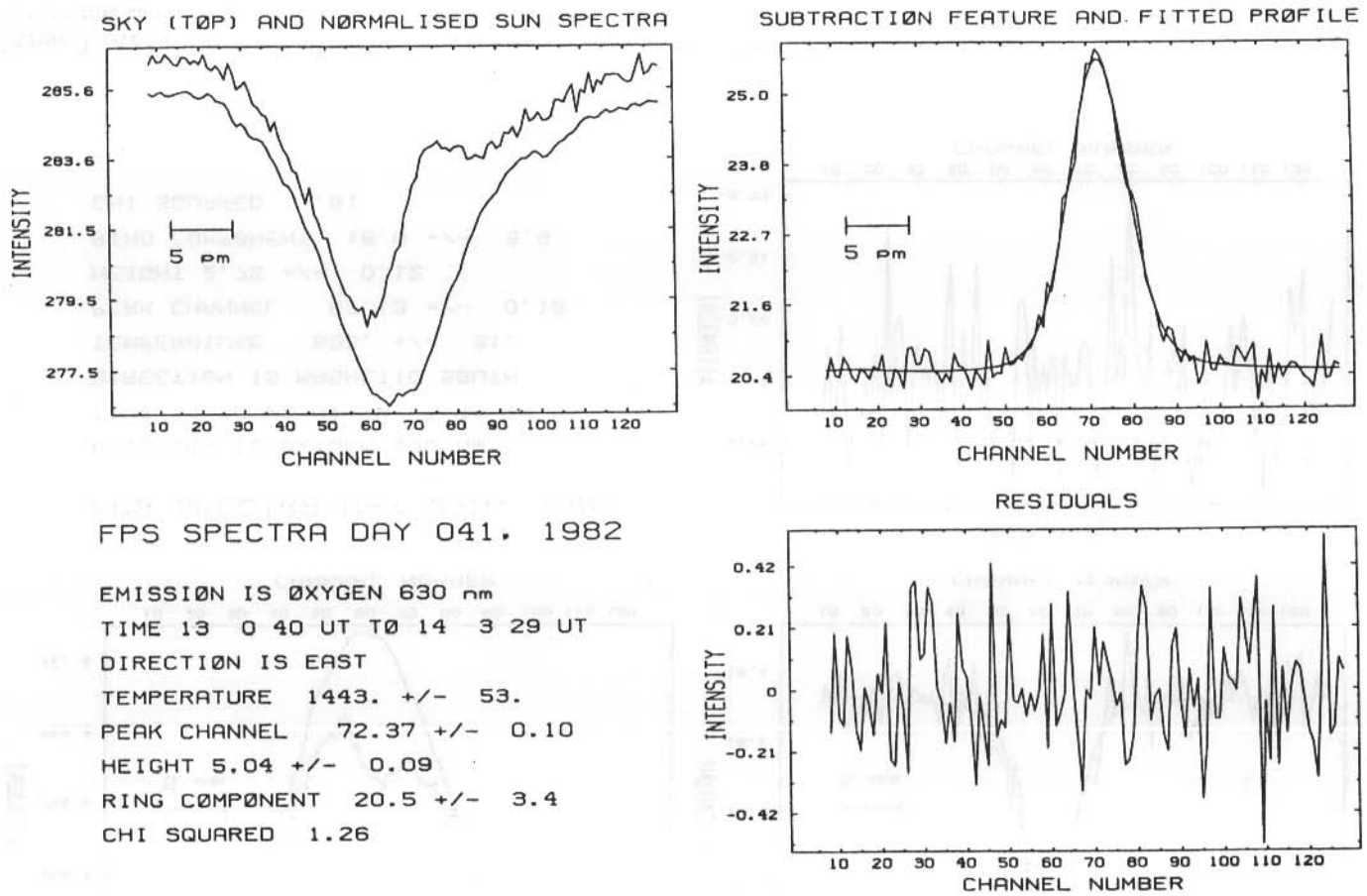

Figure 1. Results of analysis of a pair of sky and Sun spectra recorded on day 041 1982. The intensity scale used, although arbitrary, is the same in each panel, enabling direct comparisons. The horizontal bar of 5 picometres indicates the wavelength scale.

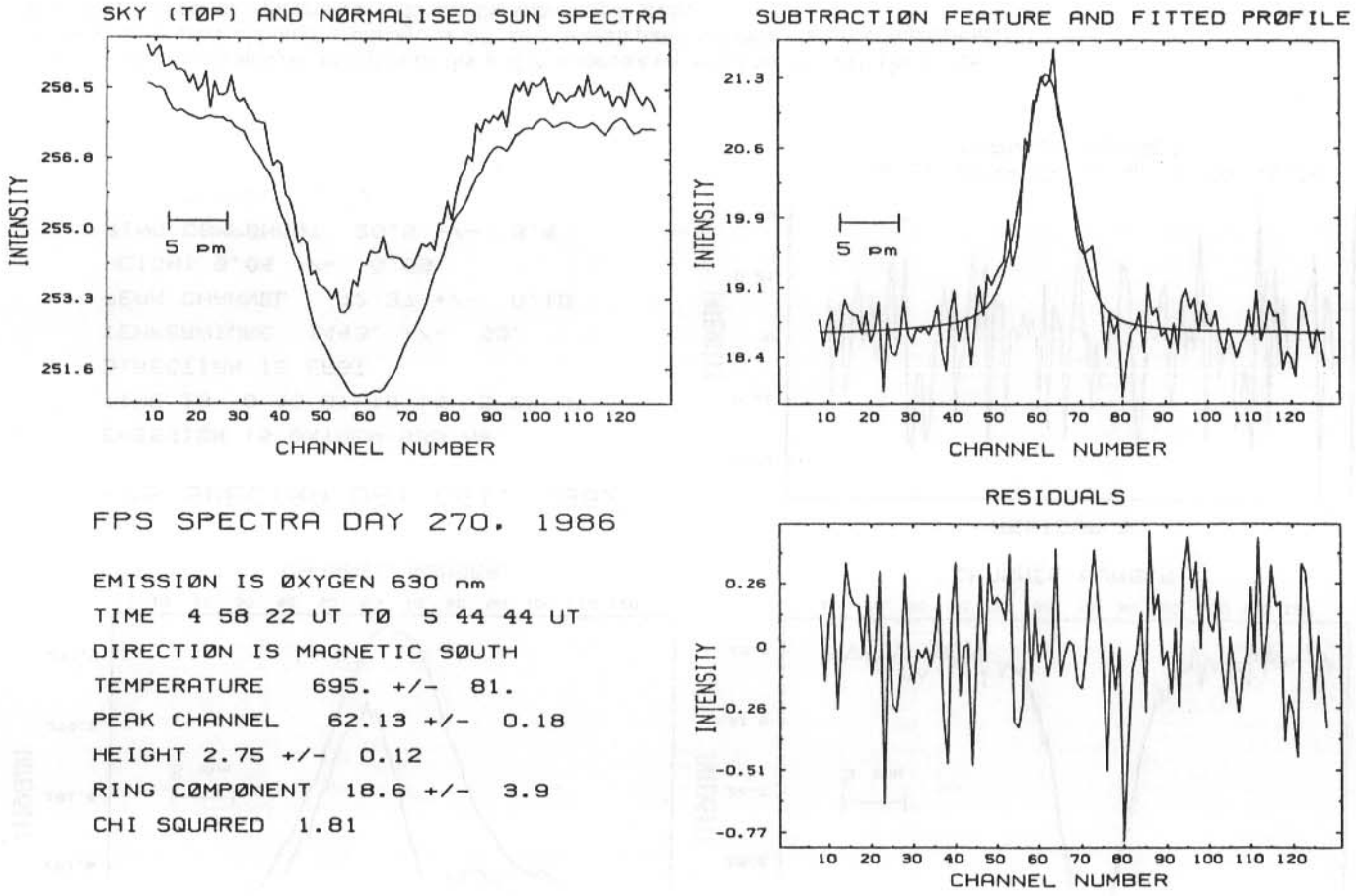

Figure 2. As for Figure 1, but the spectra were recorded on day 270, 1986. The intensity scale is the same as for Figure 1.

$$\eta(\lambda) = a_1 + a_2\lambda + a_3\lambda^2 + a_4\lambda^3 + \ldots + a_n\lambda^{n-1} \qquad (2)$$

Writing $R = a_0$, and substituting (2) into (1) gives

$$sky(\lambda) = a_0 w(\lambda) + a_1 sun(\lambda) + a_2\lambda sun(\lambda) + a_3\lambda^2 sun(\lambda) + \ldots + w(\lambda).E(\lambda) \qquad (3)$$

Providing the coefficients a_2 in equation (3) are small, and $w(\lambda)$ is flat to within a few percent, plotting the sky spectrum against the Sun spectrum yields a straight line, except for points in the region of the emission wavelength, which are displaced above the line (Figure 3). In practice n was limited to 2 (the linear term), as higher order terms can distort the shape of the normalised Sun spectrum, and are hard to justify physically. However, the analysis is formulated allowing n to be any integer.

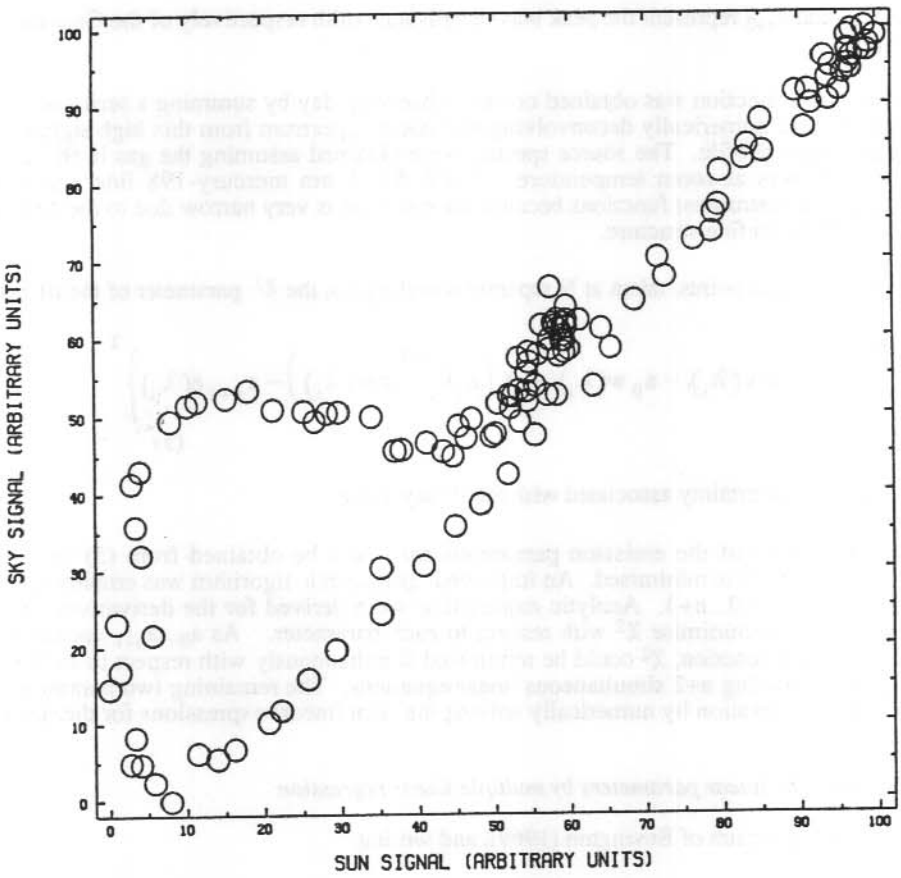

Figure 3. Sky signal at succesive wavelengths (channel numbers) plotted against Sun signal from figure 1. The majority of points lie along a straight line, indicating the linear relation between sky and sun spectra. Points are displaced above the line by the presence of the emission feature in the sky spectrum. The signals have each been scaled to lie in the range 0 to 100, and their values may not be compared with those in Figure 1.

Determination of the the peak position, width and intensity of the emission feature requires that an explicit expression containing these parameters be included for the term $w(\lambda)E(\lambda)$. As the emission is a narrow bandwidth feature, and $w(\lambda)$ only varies by a few percent over the entire scan range, its effect on the recorded emission spectrum may be neglected. With this simplification, the recorded emission spectrum is represented as the convolution of a Gaussian curve (the actual emission spectrum), and the spectrometer instrument function. The latter function is simply the recorded spectrum that would be obtained from observing a source with an 'ideal' delta function emission spectrum. Thus using $I(\lambda)$ to represent the instrument function, and an asterisk to denote the convolution operation, $E(\lambda)$ may be written as

$$E(\lambda) = a_{n+1}e(\lambda)$$

where a_{n+1} represents the emission intensity, and $e(\lambda)$ is given by

$$e(\lambda) = I(\lambda) * \exp -\{(\lambda - a_{n+2})/a_{n+3}\}^2 \qquad (4)$$

where a_{n+2} and a_{n+3} represent the peak wavelength and width respectively of the Gaussian source spectrum.

The instrument function was obtained on each observing day by summing a series of mercury-198 spectra, and numerically deconvolving the source spectrum from this high signal to noise ratio cumulative profile. The source spectra were obtained assuming the gas in the (very low power) lamp was at room temperature. The λ 546.1 nm mercury-198 line was used for generating the instrument functions because the emission is very narrow due to the high atomic mass, and it has no fine structure.

For N sky-Sun data points, taken at N separate wavelengths, the χ^2 parameter of the fit becomes

$$\chi^2 = \sum_{i=1}^{N} \frac{1}{\sigma_i^2} \left\{ \mathrm{sky}(\lambda_i) - a_0\, w(\lambda_i) - \sum_{j=1}^{n} \left(a_j \lambda_i^{\,j-1}\, \mathrm{sun}(\lambda_i) \right) - a_{n+1} e(\lambda_i) \right\}^2 \qquad (5)$$

where σ_i is the uncertainty associated with the i^{th} sky value.

The best estimates of the emission parameters may now be obtained from (5) by choosing $a_0 \ldots a_{n+3}$ such that χ^2 is minimised. An improved grid search algorithm was employed to solve $\partial\chi^2/\partial a_j = 0$, for $j = 0 \ldots n+3$. Analytic expressions were derived for the derivatives, and were used to iteratively minimise χ^2 with respect to each parameter. As $a_0 \ldots a_{n+1}$ appear linearly within the fitting function, χ^2 could be minimised simultaneously with respect to each of these parameters by solving n+2 simultaneous linear equations. The remaining two parameters were updated at each iteration by numerically solving the (non linear) expressions for the derivatives independently.

16.3.2 *Solving for linear parameters by multiple linear regression*

Following the approach of Bevington (1969), and writing

$$X_0 = w(\lambda)$$
$$X_1 = sun(\lambda)$$
$$X_2 = \lambda sun(\lambda)$$
$$X_3 = \lambda^2 sun(\lambda)$$
$$\vdots$$
$$X_n = \lambda^{n-1} sun(\lambda)$$
$$X_{n+1} = e(\lambda)$$

then $a_0 \ldots a_{n+1}$ may be obtained by minimising the χ^2 parameter by solving

$$\frac{\partial}{\partial a_k}\left(\sum_{i=1}^{N}\left\{\frac{1}{\sigma_i^2}\left[sky(\lambda_i) - \sum_{j=0}^{n+1} a_j X_j(\lambda_i)\right]\right\}^2\right) = 0 \qquad (6)$$

which gives n+2 simultaneous linear equations in n+2 unknowns. These may be expressed in matrix form as

$$\underline{\beta} = \alpha\, \underline{a} \qquad (7)$$

where $\underline{\beta}$ is a column matrix of order n+2 defined by

$$\beta_k = \sum_{i=1}^{N} \frac{1}{\sigma_i^2} sky(\lambda_i) X_k(\lambda_i)$$

and α is a square matrix of order n+2 defined by

$$\alpha_{jk} = \sum_{i=1}^{N} \frac{1}{\sigma_i^2} X_j(\lambda_i) X_k(\lambda_i)$$

Equation (6) may be solved by numerically inverting the curvature matrix, α, to give

$$\underline{a} = \varepsilon\, \underline{\beta} \qquad (8)$$

where $\varepsilon = \alpha^{-1}$

or explicitly

$$a_j = \sum_{k=0}^{n+1}\left\{\varepsilon_{jk} \sum_{i=1}^{N} \frac{1}{\sigma_i^2} sky(\lambda_i) X_k(\lambda_i)\right\} \qquad (9)$$

and the error in determining the j^{th} coefficient is given by

$$(\sigma_{a_j})^2 = \varepsilon_{jj} \qquad (10)$$

16.3.3 *Solving for the non linear parameters by Newton-Raphson iteration*

The derivatives with respect to the two non linear parameters were found from

$$\frac{\partial \chi^2}{\partial a_{n+2}} = \frac{\partial \chi^2}{\partial e(\lambda)} \frac{\partial e(\lambda)}{\partial a_{n+2}}$$

$$= -2\sum_{i=1}^{N} \frac{1}{\sigma_i^2} \left(r(\lambda_i) a_{n+1} g(\lambda_i) \right) \qquad (11)$$

where

$$r(\lambda) = sky(\lambda) - \sum_{j=0}^{n+1} a_j X_j(\lambda)$$

$$g(\lambda) = \frac{\partial e(\lambda)}{\partial a_{n+2}}$$

and $g(\lambda)$ was obtained by numerically differentiating $e(\lambda)$ with respect to a_{n+2}, at each λ_i.

Similarly

$$\frac{\partial \chi^2}{\partial a_{n+3}} = \frac{\partial \chi^2}{\partial e(\lambda)} \frac{\partial e(\lambda)}{\partial a_{n+3}}$$

$$= -2\sum_{i=1}^{N} \frac{1}{\sigma_i^2} \left(r(\lambda_i) a_{n+1} h(\lambda_i) \right) \qquad (12)$$

where

$$h(\lambda) = \frac{\partial e(\lambda)}{\partial a_{n+3}}$$

$h(\lambda)$ also being obtained by numerical differentiation.

So for a given choice of all the other parameters, χ^2 may be minimised with respect to a_{n+2} by setting (11) above equal to zero, and similarly setting (12) to zero minimises χ^2 with respect to a_{n+3}. However, as neither (11) nor (12) could be solved for zero analytically, a Newton-Raphson iteration scheme was employed. Thus (11) was set to zero numerically by generating a sequence of estimates $\{a_{n+2}\}_k$ from the relation

$$(a_{n+2})_k = (a_{n+2})_{k-1} - \frac{\partial \chi^2 / \partial (a_{n+2})_{k-1}}{\partial^2 \chi^2 / \partial \left[(a_{n+2})_{k-1} \right]^2} \qquad (13)$$

until succesive estimates for a_{n+2} were within a chosen tolerance (0.01 channels) of each other. The second partial derivative was computed by numerically differentiating (11) once with respect to a_{n+2}. A similar approach was used to obtain a_{n+3}, from the sequence

$$(a_{n+3})_k = (a_{n+3})_{k-1} - \frac{\partial \chi^2 / \partial (a_{n+3})_{k-1}}{\partial^2 \chi^2 / \partial [(a_{n+3})_{k-1}]^2} \qquad (14)$$

where the stopping criterion chosen was to iterate until succesive peak width estimates differed by an amount corresponding to a difference in temperature estimate of less than two degrees kelvin.

From the analysis of Bevington (1969), the errors in the two parameters solved independently are given by

$$\frac{1}{\sigma^2 a_{n+2}} = \frac{1}{2} \frac{\partial^2 \chi^2}{\partial (a_{n+2})^2} \qquad (15)$$

and

$$\frac{1}{\sigma^2 a_{n+3}} = \frac{1}{2} \frac{\partial^2 \chi^2}{\partial (a_{n+3})^2} \qquad (16)$$

and these derivatives are already computed within the Newton-Raphson scheme.

16.3.4 *The complete grid search procedure*

The grid search procedure used for solving for all parameters $a_0 \ldots a_{n+3}$ may be summarised as follows:

(1) generate initial estimates for a_{n+2}, a_{n+3}
(2) minimise χ^2 with respect to $a_0 \ldots a_{n+1}$ by multiple linear regression
(3) minimise χ^2 with respect to a_{n+2} by Newton-Raphson iteration
(4) minimise χ^2 with respect to a_{n+3} by Newton-Raphson iteration
(5) go back to (2) until succesive temperature estimates are within 2°K

The σ_i were assumed to be constant across the sky spectrum, the value being determined by high pass filtering the spectra, and then evaluating the mean deviation from zero. The Sun spectra were smoothed by numerical convolution with a Gaussian curve of 1/e half width of between one and two channels, as the least squares regression process assumes a noise free abcissa.

The a_0 term computed above gave a direct estimate of the Ring component. The fitted Gaussian curve widths (the a_{n+3} term) gave estimates of the emission temperature, and the peak position (the a_{n+2} term) relative to the Hg-198 profiles gave the Doppler shift due to the line of sight wind.

The intensity of the laboratory white light source spectrum was used to scale the areas under the fitted curves. This provided a measure of the relative emission intensities.

To test the dayglow extraction procedure, a routine was developed to synthesise sky-Sun spectral pairs containing an emission feature of known parameters in the sky profile. Actual observed Sun

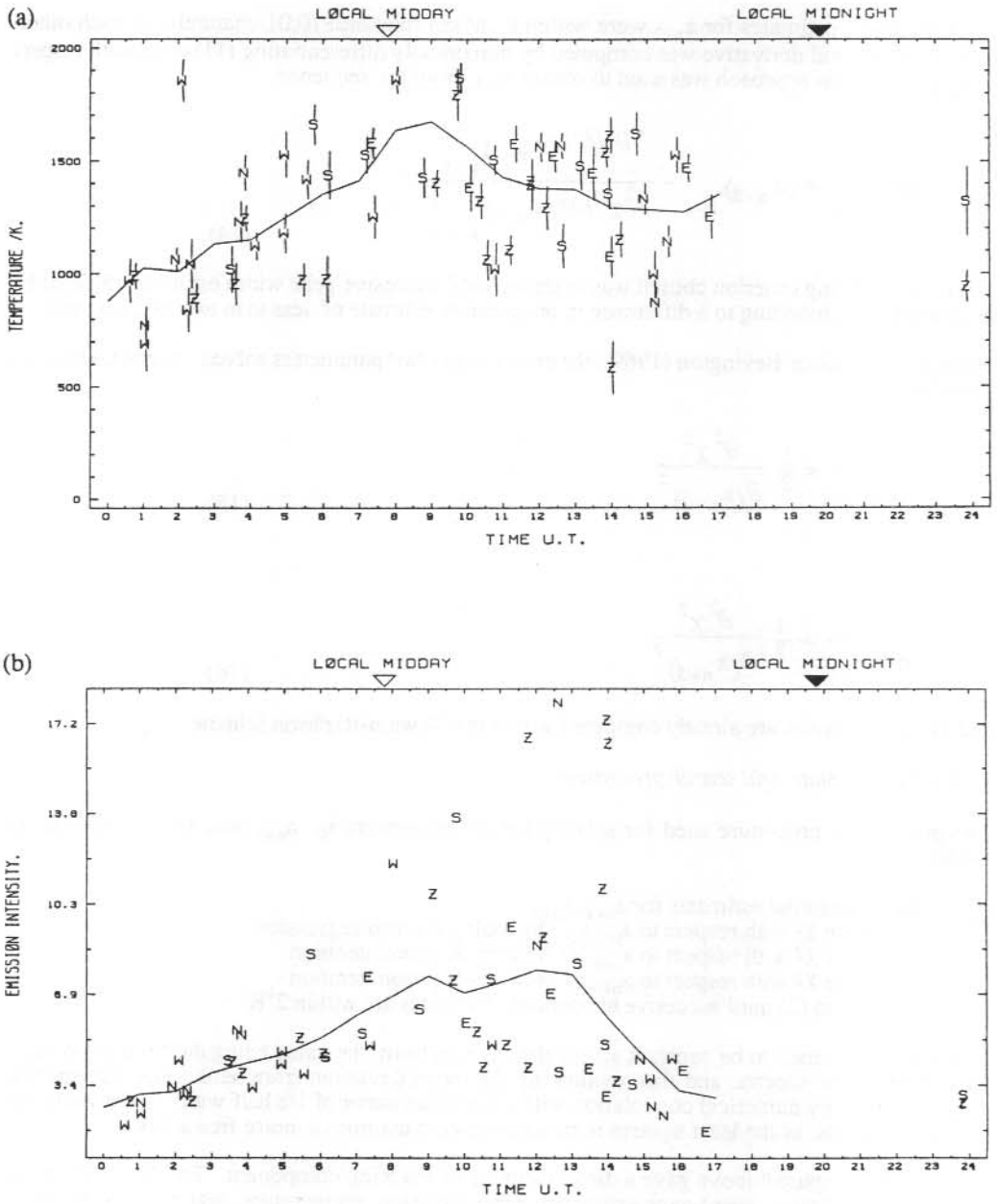

Figure 4(a). Plot of temperature vs universal time for all 1982 results. (b). Plot of emission intensity (in arbitrary units) vs universal time for all 1982 results. The solid curves are three hourly weighted running means plotted at hourly intervals. No attempt has been made to sort data according to magnetic activity or 10.7 cm solar flux. The times of local midday and midnight are indicated.

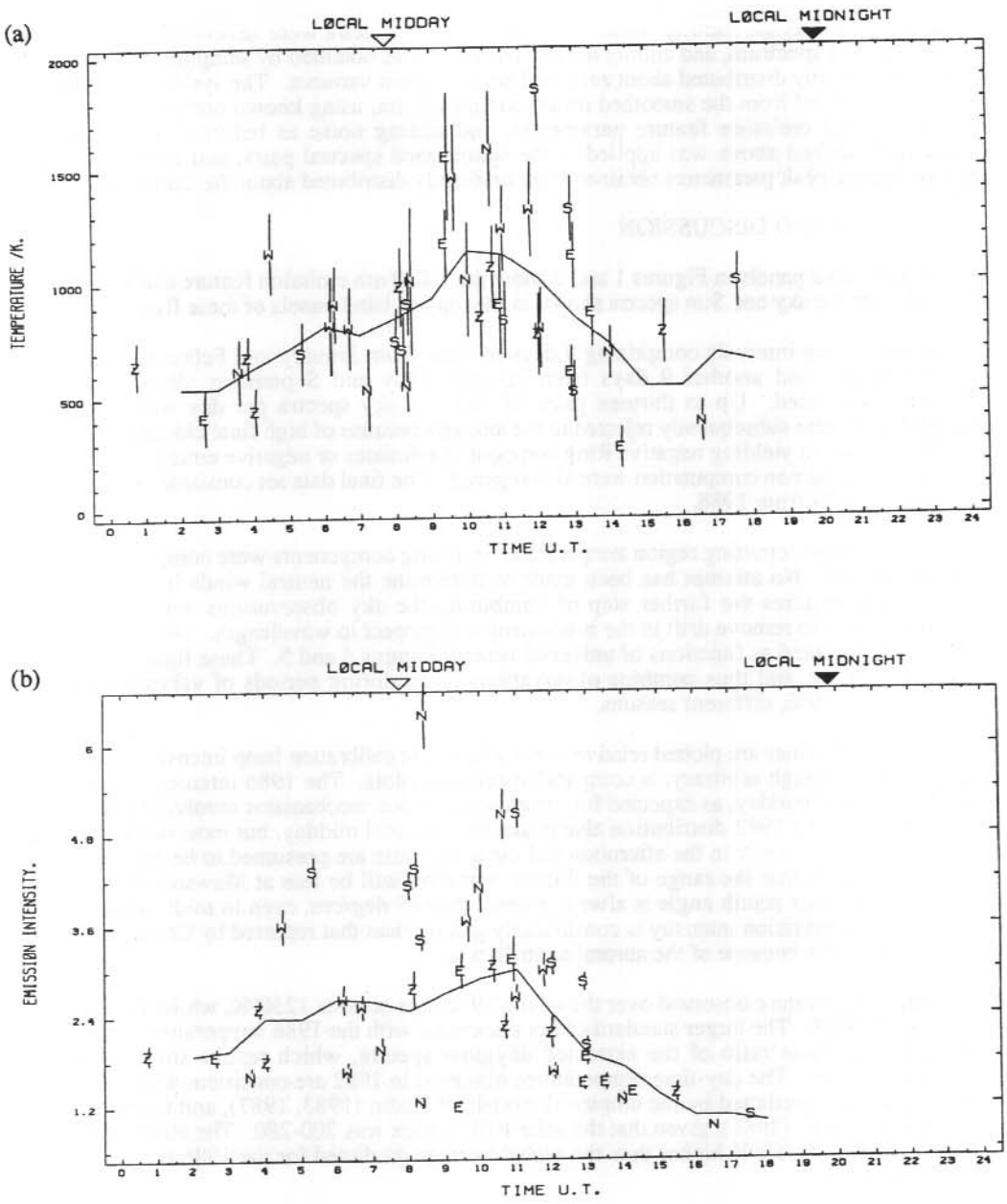

Figure 5(a). Plot of temperature vs universal time for all 1986 results. (b). Plot of emission intensity (in the same units as for figure 4) vs universal time for all 1986 results. The solid curves are three hourly weighted running means plotted at hourly intervals. No attempt has been made to sort data according to magnetic activity or 10.7 cm solar flux. The times of local midday and midnight are indicated.

spectra were used as the starting point. The synthetic sun spectra were generated by smoothing an observed Sun spectrum, and adding noise. The noise was obtained by sampling from a parent population normally distributed about zero, and with a known variance. The synthetic sky spectra were also generated from the smoothed observed Sun spectra, using known normalisations, Ring components and emission feature parameters, and adding noise as before. The extraction procedure described above was applied to the synthesised spectral pairs, and as expected, the emission feature peak parameters obtained were uniformly distributed about the correct values.

16.4 RESULTS AND DISCUSSION

The top right hand panels in Figures 1 and 2 show the λ 630 nm emission feature and fitted curve extracted from the sky and Sun spectra shown in the top left hand panels of these figures.

For this study, two intervals comprising 9 days of data from January and February 1982, near solar maximum, and another 9 days from January, May and September 1986, near solar minimum, were used. Up to thirteen pairs of Sun and sky spectra per day were recorded, although many were subsequently rejected in the analysis because of high final chi-squared values for the fits. Spectra yielding negative Ring component estimates or negative emission intensities in the the normalisation computation were also rejected. The final data set consisted of 62 profiles from 1982, and 39 from 1986.

Emission intensities, emitting region temperatures and Ring components were computed from the extracted spectra. No attempt has been made to determine the neutral winds in the emission region as this requires the further step of combining the sky observations with wavelength calibration results to remove drift in the instrument with respect to wavelength. The results of the analysis are presented as functions of universal time in Figures 4 and 5. These figures represent the whole data set, and thus combine observations taken during periods of varying magnetic activity and, for 1986, different seasons.

The emission intensities are plotted relative to the white light calibration lamp intensity resulting in a scale which although arbitrary, is comparable between plots. The 1986 intensity distribution peaks around local midday, as expected for dayglow excitation mechanisms involving solar EUV. The base level of the 1982 distribution also peaks around local midday, but most occurrences of enhanced intensities occur in the afternoon and evening; these are presumed to be due to aurora. It is to be expected that the range of the diurnal variation will be less at Mawson than at mid-latitudes, as the solar zenith angle is always greater than 45 degrees, even in midsummer. The variability of the emission intensity is considerably greater than that reported by Cocks and Jacka (1979), presumably because of the auroral contribution.

The average temperature observed over the whole 1982 data set was 1250°K, whilst for 1986 the average was 900°K. The larger standard errors associated with the 1986 temperatures reflect the lower signal to noise ratio of the extracted dayglow spectra, which results from the lower emission intensities. The day-time temperatures observed in 1982 are consistent with the global average behaviour predicted by the empirical models of Hedin (1983, 1987), and the theoretical model of Roble et al. (1987), given that the solar F10.7 index was 200-280. The observed values were approximately 150°K higher than the global average predicted for the 1986 period with an F10.7 index of 70.

Both the 1982 and 1986 aggregate temperature plots indicate that the median temperature increases during the morning hours, and decreases in the afternoon. The magnitude of the diurnal variation for both the 1982 and 1986 data sets is around 500°K, considerably greater than that predicted by the global thermospheric general circulation models of Fuller-Rowell et al. (1980) and Dickinson et al. (1981), and the empirical models of Thuillier et al. (1977) and Hedin (1983, 1987). All of these models predict diurnal variations at Mawson in the range 100°K to 200°K, depending on solar activity and season. The mid-latitude dayglow temperature measurements of Cocks and Jacka (1979) showed an average diurnal variation of 400°K, again significantly greater than

model predictions. As Mawson is an auroral zone station, the diurnal thermospheric temperature variation observed there should be further modulated by the passage of the observatory through different regimes of Joule heating and particle precipitation, as the station moves under the auroral oval. The time lag between local midday and the passage of the temperature maximum for both the years examined here, and for the Cocks and Jacka results, was approximately 4 hours, whereas the models predict the temperature maximum should occur around 4 hours after local midday.

The 1982 and 1986 Ring component intensities were highly variable. Expressed as a percentage of the total sky signal, the Ring component varied from less than 1%, up to as high as 10% or even occasionally 15%. Values observed by Barmore (1975) and by Cocks (1983) were typically about 2% of the sky signal. The observed large Ring component at Mawson supports the ground reflection mechanism proposed by Hunten (1970), as the albedo of the surrounding snow and ice cover is very high. The aerosol fluorescence mechanism of Barmore (1975) is not supported, as the atmospheric aerosol content of Antarctic air is extremely small.

16.5 CONCLUSION

A satisfactory method has been developed for the analysis of day-time observations of the λ 630 nm oxygen emission from the thermosphere. This permits determination of thermospheric temperature and emission intensity, and the intensity of the Ring component.

Two sets of observations have been examined, corresponding to periods of very high and very low solar activity. Higher emission intensities were seen to occur more frequently around local midday. The 1982 observations gave an average day-time temperature of 1250°K, whereas the 1986 average was 900°K. For both periods the magnitude of the diurnal variation was two to three times greater than predicted by thermospheric models, and the phase of the variation was advanced by 2 hours relative to model predictions. Ring component intensities observed were considerably greater than reported by mid-latitude observers, and support a ground reflection generation mechanism.

It is hoped that analysis of 1983 and 1984 dayglow data, as well as continued observations in the summer of 1988-89, will increase the set of reliable dayglow profiles, and thus clarify some of the trends seen in this preliminary study.

16.6 ACKNOWLEDGMENTS

The 1982 data were recorded by Norman Jones. This work was assisted by the Australian Research Grants Scheme, with the logistic support of the Australian National Antarctic Research Expeditions.

16.7 REFERENCES

Barmore, F.E. (1975). The filling in of Fraunhofer lines in the day sky. *Journal of the Atmospheric Sciences 32*:1489-1493.

Barmore, F.E. (1977). High resolution studies of the 6300 A oxygen line in the day airglow. *Planetary and Space Science 25*:185-191.

Bens, A.R., Cogger, L.L. *and* Shepherd, G.G. (1965). Upper atmospheric temperatures from Doppler line widths III. *Planetary and Space Science 13*:551- 563.

Bevington, P.R. (1969). *Data reduction and error analysis for the physical sciences*. McGraw Hill Inc.

Cocks, T.D. (1983). Dual Fabry-Perot measurements of day-time thermospheric temperature and wind velocity: data analysis procedures. *Applied Optics 22*:726- 732.

Cocks, T.D., Creighton, D.F. *and* Jacka, F. (1980). Application of a dual Fabry-Perot spectrometer for day-time airglow studies. *Journal of Atmospheric and Terrestrial Physics 42*:499-511.

Cocks, T.D. *and* Jacka F. (1979). Day-time thermospheric temperatures, wind velocities and emission intensities derived from ground based observations of the OI λ 630 nm airglow line profile. *Journal of Atmospheric and Terrestrial Physics 41*:409-415.
Dickinson, R.E., Ridley, E.C. *and* Roble, R.G. (1981). A three dimensional general circulation model of the thermosphere. *Journal of Geophysical Research 86*:1499-1512.
Fuller-Rowell, T.J. *and* Rees D. (1980). A three dimensional time dependent global model of the thermosphere. *Journal of the Atmospheric Sciences 37*:2545-2567.
Grainger, J.F. *and* Ring, J. (1962). Anomalous Fraunhofer line profiles. *Nature 193*:762.
Hedin, A.E. (1983). A revised thermospheric model based on mass spectrometer and incoherent scatter data: MSIS-83. *Journal of Geophysical Research 88*:10170- 10188.
Hedin, A.E. (1987). MSIS-86 thermospheric model. *Journal of Geophysical Research 92*:4649-4662.
Hunten, D.M. (1970). Surface albedo and the filling in of Fraunhofer lines in the day sky. *The Astrophysical Journal 159*:1107-1110.
Jacka F. (1984). *Applications of Fabry-Perot spectrometers for measurement of upper atmosphere temperature and winds*. Handbook for MAP, Volume 13.
Noxon, J.F. (1964). A study of the 6300 A oxygen line in the day airglow. *Journal of Geophysical Research 69*:3245-3255.
Noxon, J.F. (1968). Day airglow. *Space Science Reviews 8*:92-134.
Roble, R.G., Ridley, E.C. *and* Dickinson, R.E. (1987). On the global mean structure of the thermosphere. *Journal of Geophysical Research 92*:8745-8758.
Wilksch, P.A. (1975). Ph.D. thesis, University of Adelaide.

17. CORRELATION BETWEEN WINDS AT 80 TO 108 KM ABOVE MAWSON AND GEOMAGNETIC ACTIVITY

G. Price[1,2], G. B. Burns[1], F. Jacka[2] and R.A. Vincent[3]

[1]Antarctic Division
Kingston Tas 7050
Australia

[2]Mawson Institute for Antarctic Research
University of Adelaide
Adelaide SA 5000
Australia

[3]Department of Physics
University of Adelaide
Adelaide SA 5000
Australia

ABSTRACT

Measurements of the horizontal wind velocity, throughout the *D* region and into the lower *E* region of the ionosphere, have been obtained using the spaced antenna partial reflection (SAPR) technique. The SAPR radar has been operated continuously at Mawson station (67°S, 63°E) since July 1984. This work investigates correlations between geomagnetic activity and the horizontal wind field. An 'apparent' correlation is seen in a data set covering the period from August to November 1985. This data set is used here to demonstrate the use of a randomisation technique to test the correlation.

17.1 INTRODUCTION

The upper thermosphere responds strongly to geomagnetic disturbances through the effects of direct heating and momentum transfer from the ions to the neutrals. In the mesosphere the motions of the neutral atmosphere are dominated by upward propagating tides and gravity waves. Little is known of the relation between geomagnetic disturbances and the neutral air motions in the upper mesosphere/lower thermosphere.

A number of studies have been aimed at assessing the extent of this coupling. Correlations between geomagnetic activity and various components of the wind field have been discussed by Balsley et al. (1982), Manson and Meek (1986), Johnson and Luhmann (1985a,b), Johnson et al. (1987) and Phillips and Vincent (1987c). Johnson and Luhmann (1985b) showed that ambiguous correlations were obtained if preliminary analysis was not carried out to remove the tidal components. However, the removal of the tides is complicated since the amplitude and phase of the tides, particularly the semidiurnal tide, can vary over a number of days (Forbes 1985). In this work a randomisation technique is developed which allows anomalous correlations to be identified, allowing a correlation between the raw wind data and geomagnetic activity to be demonstrated.

Establishing whether a correlation exists between a pair of geophysical phenomena is difficult, and determining whether a cause and effect relationship exists is even more so. One of the problems is that if two parameters are controlled by processes with similar but independent periodicities, then the two parameters may appear to be correlated if the matching periodicities are approximately in phase. Daily variations are found in local geomagnetic activity, the data acquisition rate and the horizontal wind speed, and may be responsible for producing an apparent correlation between geomagnetic activity and the horizontal wind field.

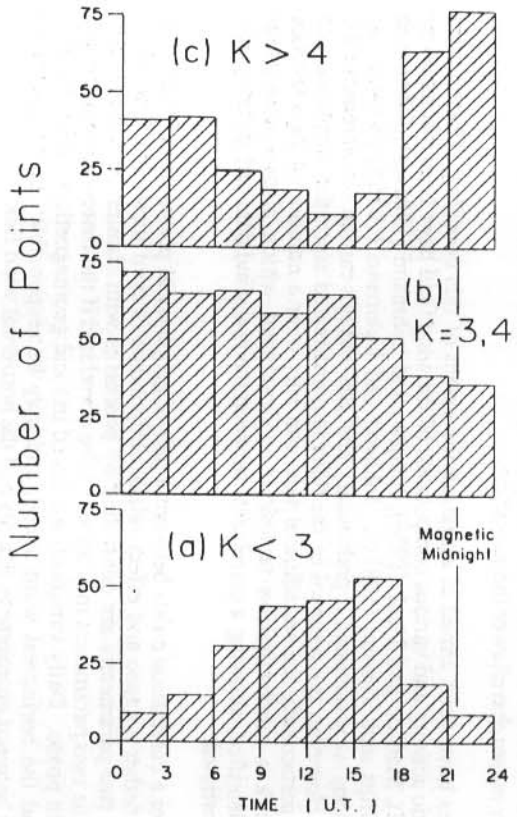

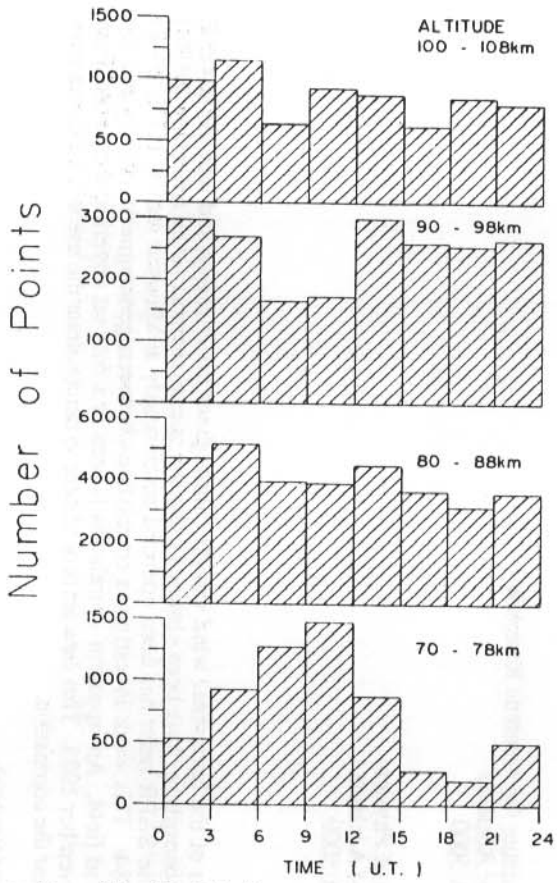

(left)
Figure 1. The distribution of high (K > 4), medium (K = 3, 4) and low (K < 3) K-indices throughout the day for the period August to November 1985.
(right)
Figure 2. Histogram showing the number of wind values, obtained using the SAPR radar, versus time of day for the period August to November 1985. The data points are divided into four altitude ranges; 70-78 km, 80-88 km, 90-98 km and 100-108 km.

17.2 THE SPACED ANTENNA PARTIAL REFLECTION RADAR

The spaced antenna partial reflection (SAPR) radar operates in a pulsed mode, at a frequency of 1.94 MHz, and records signals partially reflected from ionised irregularities in the lower ionosphere. Three receiving antennas are located at the apexes of an equilateral triangle. The full correlation analysis (Briggs 1984) is used to determine the horizontal velocity of the reflecting irregularities from measurements of the radio fading at the three receiving antennas.

Data are obtained over the height range 70 to 108 km with a height resolution of approximately 2 km. The heights are sampled using three overlapping height intervals such that heights between 80 and 100 km are sampled eight times an hour and heights outside this range four times an hour. Data acquisition shows a seasonal variation, but generally maximises between 80 to 90 km, where typically two to three measurements per hour are obtained (Phillips and Vincent 1987a).

17.3.1 *Daily variations*

The local K-index is used to indicate the intensity of geomagnetic activity at Mawson. The difference between the highest and lowest deviations of the magnetic field from the regular daily variation, over a 3 hour period, is used to determine the K-index for that period. An integer value between 0 and 9 is assigned to the measured 'difference' using a conversion scale which varies between stations. The local K-indices for Mawson are compiled by the Australian Bureau of Mineral Resources. In this work, low, medium and high K values are defined as $K < 3$, $K = 3$ or 4, and $K > 4$ respectively. These groupings were chosen to give an even distribution of data points between the three K-index groups.

The distributions of high, medium and low K-indices throughout the day were calculated for the four month period under consideration (Figure 1). There is a clear tendency for low K-indices to be concentrated between 0900 and 1800 UT, and for high K indices to occur between 1800 and 2400 UT. Magnetic midnight at Mawson occurs at around 2210 UT and thus the high K-indices tend to occur around magnetic midnight.

The number of wind data points in each 3 hour period throughout the day is plotted for the four height ranges; 70-78 km, 80-88 km, 90-98 km and 100-108 km (Figure 2). In the 70 to 78 km height range there is a strong daily variation in the data acquisition rate, with most data being obtained between 0600 and 1200 UT (1200 to 1800 LT). There is far less variation in the data acquisition rate above 80 km throughout the day.

The wind speed shows a regular daily variation also, due to the presence of diurnal and semidiurnal tidal oscillations. The amplitude of the semidiurnal tide is large, typically 10 to 20 ms^{-1} with a broad maximum around 85 to 95 km, while the diurnal tide is smaller, with an amplitude of 5 to 10 ms^{-1} (Phillips and Vincent 1987b). The semidiurnal tide exhibits a large phase shift during Spring (Tetenbaum et al. 1986). A phase change of about 50° was observed in the Mawson data over an eight day period in early October (Price et al. 1987).

In summary, a strong daily variation is seen in both the local K-index and the horizontal wind speed, where the strongest influence on the wind field is due to the semidiurnal tide. In addition, the data acquisition rate varies strongly with the time of day at heights below 80 km. The data below 80 km were rejected on two grounds. Firstly, because a geomagnetic effect is least likely to be observed at the lower altitudes and secondly, due to the large variability of the data acquisition rate with time of day.

17.3.2 *An apparent geomagnetic effect*

The measured wind values were classified according to the corresponding value of the local K-index into high, medium and low K groups. The wind speed distributions for the different K

groups were then compared. Visual inspection of the speed distributions revealed no obvious difference between the three K value distributions at heights below 100 km. However, in the height range 100 to 108 km the peak of the high K value distribution appears broader than that of the medium and low K distributions and there is a greater proportion of points in the high velocity wing of the distribution (Figure 3). The wind speed is clearly not normally distributed, particularly during periods of high geomagnetic activity, and therefore non-parametric statistics are required to compare the distributions.

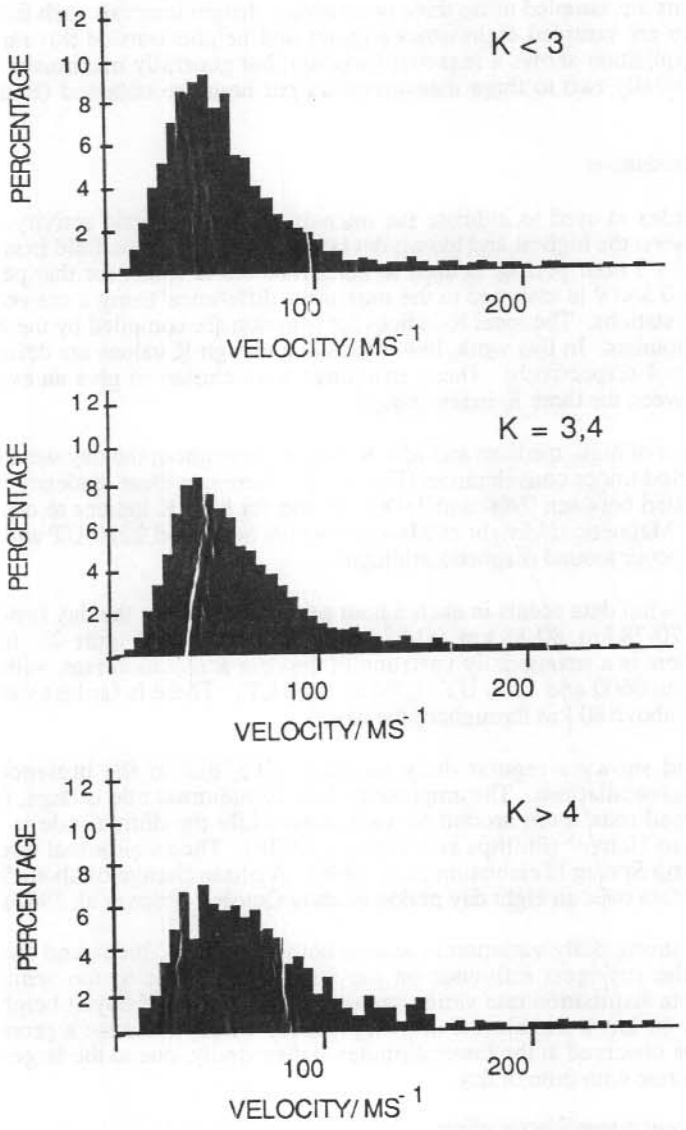

Figure 3. The distribution of horizontal wind speeds in the height range 100 to 108 km during periods of high (K>4), medium (K = 3, 4) and low (K<3) geomagnetic activity.

The 50th and 75th percentiles of the high, medium and low K-index speed distributions were calculated for each 2 km height interval from 80 to 108 km. The 50th percentile is equivalent to the median of the distribution. The difference between the 75th and 50th percentile gives a measure of the 'spread' of the distribution, and is here referred to as such. The median and spread of the high, median and low K-index distributions are plotted as a function of height in Figures 4a and b respectively. The medians of the high K distributions are greater than those of both the medium and low K distributions at all altitudes above 90 km. At these altitudes there is in fact very little difference between the medians of the medium and low K distributions. Below 88 km the situation changes; the medians of the low K distributions are greater than the medians of the medium and high K distributions.

The spreads of the speed distributions show a similar height dependence to that of the medians. Above 88 km, there is a larger spread in the high K distributions than in the medium or low K distributions. However, unlike the medians, the spread becomes progressively larger from low to high K values at all altitudes above 100 km. Below 100 km there is little difference between the spread of the low and median distributions.

The Mann-Whitney U test was used to determine the probability that the low and high K distributions are drawn from the same population (Siegel 1956). The test is nonparametric and involves ranking a combined distribution and, in this case, counting the number of speeds from the high K distribution which precede each speed from the low K distribution, and summing. The test was used to compare the high and low K distributions only, as the percentile analysis had shown that the values of parameters describing the medium K-index distributions generally lay between those describing the high and low K-index distributions.

The null hypothesis under test, H_0, is that the speed distributions are the same under conditions of low and high K. An alternative hypothesis, H_1 was that the speeds associated with larger K-indices are larger. A 'p-value' is determined which represents the probability, under H_0, of an observation occurring by chance. Evidence for the rejection of H_0 is considered to be: weak for a p-value of 10%, moderate for a p-value of 5%, strong for a p-value of 1% and very strong for a p-value of 0.1%.

The Mann Whitney U test was used to compare the low and high K distributions at each 2 km height interval. The p-values are plotted against height on a logarithmic scale in Figure 4c. P-values of less than 5% were obtained at all heights greater than 90 km, and p-values of less than 0.1% were obtained at 94 km and at the three heights above 102 km. Thus there is very strong evidence for the rejection of H_0 in favour of H_1 at the top three altitudes, and moderate evidence for rejection at all heights above 90 km. These results indicate an apparent correlation between the horizontal wind field and geomagnetic activity.

17.3.3 *Application of a randomisation technique*

To test further the likelihood that the trends observed in the previous section were obtained by chance, the results could be compared with those obtained by grouping the wind data according to a set of randomly selected indices. However, a stronger test of the results would be attained if the wind data were grouped according to a randomly selected set of 'K like' indices i.e. a random distribution of numbers which have a similar auto-correlation function to the distribution of K-indices. In this way any correlation which resulted from periodicities in the wind values matching with periodicities in K would be preserved, and any correlation which occurred over and above this would be seen only in the correlation with the 'real' K-indices.

Although it would be possible to generate a set of random 'K-like' values it is much simpler to use the 'ready-made' source which exists in the past records of local K-indices from Mawson. Nineteen intervals, each of four months duration, were selected from records dating back to 1963 (Bureau of Mineral Resources, Geology and Geophysics, 1963-1986) (Table 1). Eight of these were chosen to cover different 4 month intervals throughout the year, and eleven sets were

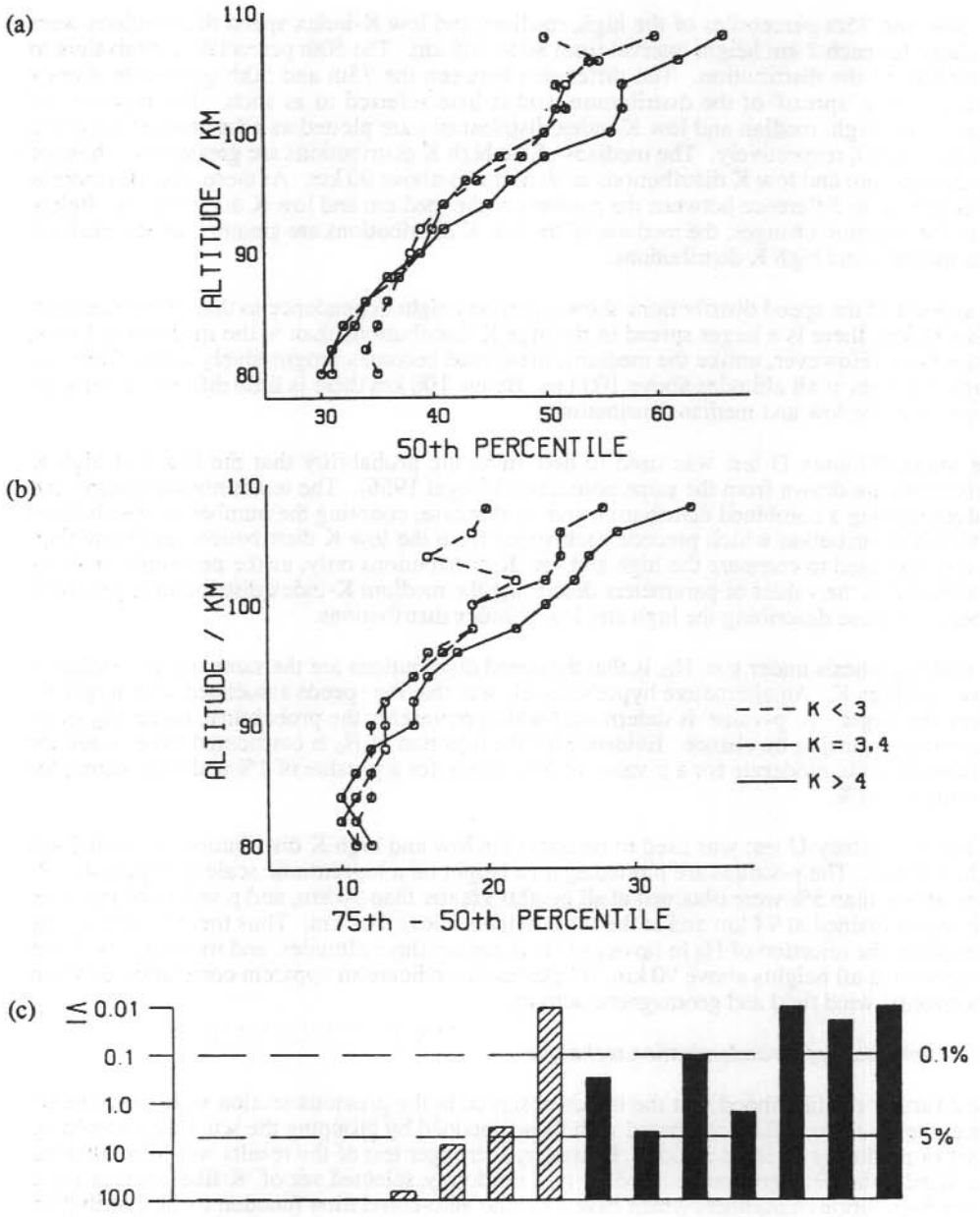

Figure 4. August to November 1985: The height variation of (a) the 50th percentile or median and (b) the difference between the 75th and 50th percentiles or spread, during periods of high, (K>4), medium (K = 3, 4) and low (K<3) geomagnetic activity.
(c). The results of the Mann Whitney U test which is used to compare the high and low K-index speed distributions. The p-value is plotted on a logarithmic scale against altitude, and the 0.1% and 5% levels are marked.

chosen to cover the same 4 month period (August to November) as the wind data. There were two sets (marked with an asterisk in Table 1) which covered the same months of the year and the same epoch of the solar cycle as the wind data. A sequential number was assigned to each 4 month interval, where the 'real' set of K-indices (i.e. those appropriate to the wind data) are designated sequence 1.

The 4 months of wind data were divided into three K-index groups, as defined earlier, according to each of the nineteen sets of K-indices in sequences 2 to 20. The Mann Whitney U test was applied to the low and high K distributions at each height for each of the nineteen different groupings of the wind data. The results are plotted in Figure 5 along with the results obtained in the previous section for sequence 1 (Figure 4c).

At altitudes above 96 km there were three sequences (1, 10 and 18) for which p-values of less than 5% were obtained for at least three successive heights. In the case of sequence 1, the p-value was less than 0.1% for the highest three altitudes, and less than 5% for the four height levels below these. Thus a consistent trend was evident with the null hypothesis being rejected very strongly at levels above 102 km, and being rejected less strongly at heights between 94 km and 102 km. For sequence 10, the p-value was less than 5% at all heights greater than 94 km, except 102 km where it was 45%. The p-value was less than 0.1% at 96, 98 and 106 km. For sequence 18 the p-value was less than 5% at the top four altitudes and at 96 km it was less than 0.1% at 96 and 106 km.

At altitudes below 96 km, nine out of twenty sequences resulted in p-values of less than 5% for at least three consecutive heights. On seven of these a p-value of less than 0.1% occurred for at least three successive heights. Thus for nearly half of the sequences, very strong evidence for the rejection of the null hypothesis was obtained for at least three successive height levels below 96 km. Generally, the heights for which strong evidence for the rejection of H_0 were obtained covered altitude ranges of up to 18 km, rather than being distributed randomly with height. For example, for sequence 18 p-values were less than 0.1% for eight consecutive heights and less than 5% for nine.

The question to be answered is whether the results obtained for sequence 1 are any more significant than those obtained for the other nineteen sequences. Sequence 1 is the only one which shows a p-value of less than 5% at all heights greater than 96 km and the only one which shows a p-value of less than 0.1% for three consecutive heights above 96 km. Sequences 4, 10 and 18 are the only others which show p-values of less than 0.1% at altitudes greater than 96 km. These occur at one, three and two height levels respectively, but on none of these are they at the highest altitudes, or consistent with altitude for three consecutive heights.

Below 96 km however, there is an apparent correlation between the wind field and K-indices evident in a number of the randomly selected K-index data sets. The most likely cause of this apparent correlation is a matching of the daily variation of the wind due to the semidiurnal tide with the daily variation of the K-index. There are two trends in the results which support this hypothesis. Firstly, p-values of less than 0.1% occurred most frequently in the height range 84 to 94 km which is the height range at which the semidiurnal tide maximises. Secondly, p-values of less than 5% tended to occur over a height range of typically 6 to 16 km. This height range is approximately a quarter of the vertical wavelength, which is approximately 50 km, of the semidiurnal tide at Mawson during the Spring (Phillips 1987b). Since we would expect the phase of the tide to be approximately constant over a quarter of a wavelength across the peak then this observation is also consistent with a tidal related cause for the apparent correlation.

17.4 CONCLUSION

Wind motions in the upper thermosphere are strongly influenced by geomagnetic activity through the process known as ion drag. In the lower mesosphere ion drag is completely ineffective in driving the neutral winds. Thus a geomagnetic effect on the wind field is most likely to be

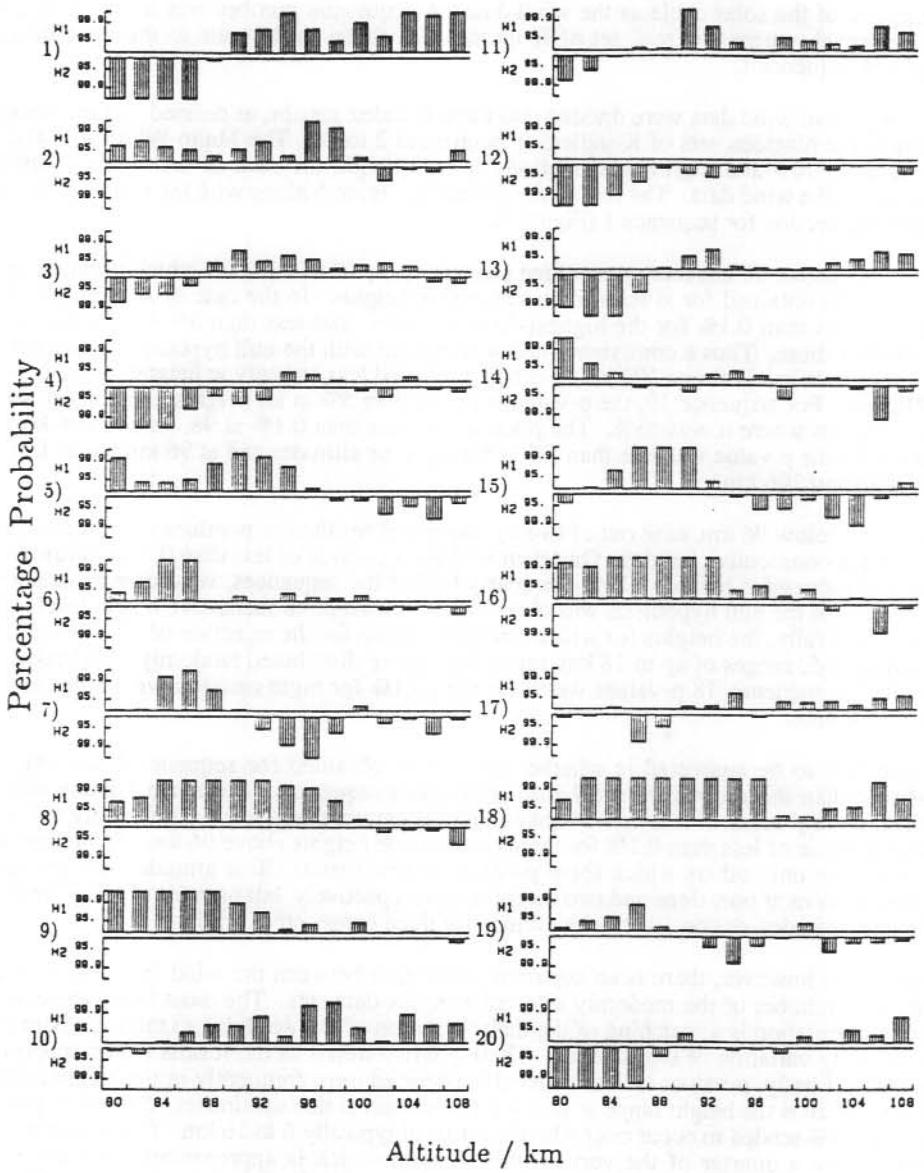

Figure 5. August to November 1985: The results of applying the Mann-Whitney U test to each 2 km height interval in the range 80 to 108 km for the wind speeds grouped according to the K-indices in each of the sequences 1 to 20 as indicated. A pair of histograms describes the results associated with each set of K-indices where the top histogram gives the probability that the hypothesis H_1 is true, with the probability increasing up the page. The bottom histogram gives the probability that the hypothesis H_2 is true, with the probability increasing down the page. Probabilities are plotted on a logarithmic scale.

strongest at higher altitudes. The authors would also expect it to be fairly consistent over a number of altitudes rather than to 'single out' heights. These two conditions are better met in the results for sequence 1, than they are for any other sequence. Below 96 km an apparent correlation is produced which is most likely caused by an approximate matching of the periods of the semidiurnal tide and the daily variation of the local K-index. Since a total of twenty cases have been examined it can be concluded, at a significance level of 5%, that results most consistent with a geomagnetic effect are obtained when the wind data are grouped with the 'real' set of K-indices. The evidence for larger winds during geomagnetically active periods is very strong above 104 km and moderate to strong between 96 and 102 km.

ACKNOWLEDGMENTS

The observations discussed here were carried out at the Australian National Antarctic Research Expedition's station at Mawson. The authors thank the Director, Antarctic Division, for logistic support and B. Brown and B.H. Briggs for their valuable comments. This work was supported by the Australian Research Grants Scheme.

17.5 REFERENCES

Balsley, B.B., Carter, D.A. *and* Ecklund,W.L. (1982). On the relationships between electrojet intensity fluctuations and the wind field near the mesopause. *Geophysical Research Letters 9*(3):219-222.

Briggs, B.H. (1984). The analysis of spaced sensor records by correlation techniques. *Middle Atmosphere Program Handbook 13*:166-186.

Forbes, J.M. (1985). Atmospheric tides between 80 km and 120 km. *Middle Atmosphere Program Handbook 16*:166-186.

Johnson, R.M. *and* Luhmann, J.G. (1985a). Neutral wind spectra at the auroral zone mesopause: Geomagnetic effect? *Journal of Geophysical Research 90*(A2):1735- 1743.

Johnson, R.M. *and* Luhmann, J.G. (1985b). High-latitude mesopause neutral winds and geomagnetic activity: A cross-correlation analysis. *Journal of Geophysical Research 90*(A9):8501-8506.

Johnson, R.M., Wickwar, V.B., Roble, R.G. *and* Luhmann, J.G. (1987). Lower thermospheric winds at high latitude: Chatanika radar observations. *Annales Geophysicae 5A*(6):383-404.

Manson, A.H. *and* Meek, C.E. (1986). Comparisons between neutral winds near 100 km at Saskatoon (52°N, 107°W, L = 4.4) and variations in the geomagnetic field (1979-1983). *Annales Geophysicae 4A*(3):281-286.

Phillips, A. *and* Vincent, R.A. (1987a). Winds in the middle atmosphere at Mawson, Antarctica: Mean Circulation and large scale motions. In: G.B. Burns and M. Craven (Eds). Australian upper atmospheric and space physics research in Antarctica, 1987. *ANARE Research Notes Number 48*. Pp. 86-92.

Phillips, A. *and* Vincent, R.A. (1987b). Winds in the middle atmosphere at Mawson, Antarctica: II. Tides. In: G.B. Burns and M. Craven (Eds). Australian upper atmospheric and space physics research in Antarctica, 1987. *ANARE Research Notes Number 48*. Pp. 93-106.

Phillips, A. *and* Jacka, F. (1987c). Winds in the middle atmosphere at Mawson, Antarctica: Geomagnetic and 'meteorological' effects. In: G.B. Burns and M. Craven (Eds). Australian upper atmospheric and space physics research in Antarctica, 1987. *ANARE Research Notes Number 48*. Pp. 107-120.

Price, G.D., Vincent, R.A. *and* Jacka, F. (1987). Winds and temperatures in the mesosphere and lower thermosphere at Mawson, Antarctica. In: G.B. Burns and M. Craven (Eds). Australian upper atmospheric and space physics research in Antarctica, 1987. *ANARE Research Notes Number 48*. Pp.148-159.

Siegel, S. (1956). *Nonparametric statistics for the behavioural sciences*. Chapter 6. McGraw Hill.

Tetenbaum, D., Avery, S.K. *and* Riddle, A.C. (1986). Observations of mean winds and tides in the upper mesosphere during 1980-1984, using the Poker Flat, Alaska, MST radar as a meteor radar. *Journal of Geophysical Research 91*:14539-14555.

18. PRESENT AND FUTURE COSMIC RAY RESEARCH OF THE AUSTRALIAN ANTARCTIC DIVISION

M.L. Duldig
Antarctic Division
Kingston Tas 7050
Australia

ABSTRACT

The Geiger counter telescope systems at the Mawson Cosmic Ray Observatory have been progressively replaced over the past few years by low maintenance proportional counter telescopes. In addition, the electronics at the observatory have been upgraded to allow computer control and plug in replacement of parts should a failure occur. Completion of this observatory automation program was achieved during the 1987-88 summer. From 1989 the observatory will run on an operator-less basis with a brief 10 minute daily check by the station electronics engineer. Repairs and maintenance as well as new equipment installation will only be carried out during the summer shipping season.

A large air shower array is being installed at South Pole by US/UK researchers. Known as the South Pole Air Shower Experiment, it aims to search for ultra high energy gamma ray induced showers from SN1987a and from a number of X-ray binaries. The Antarctic Division has agreed, in principal, to install a large area (>50m^2) muon telescope within the array to detect the muon content of such showers. In addition, the muon telescope design is being optimised for modulation studies.

18.1 INTRODUCTION

The Mawson observatory was designed as a stable, long-term operation, making use of the unique features of the polar location for observations of high energy variations of the cosmic ray intensity. It is the largest and most sophisticated observatory of its kind in the Southern Hemisphere, contributing more than half of the total count rate at moderately high energies for the hemisphere.

Continuous hourly observations commenced in 1973 and have been maintained since that time with a short break early in 1978 caused by a fire in the building.

18.2 THE MAWSON AUTOMATED COSMIC RAY OBSERVATORY (MACRO)

The observatory building (Figure 1) houses the high zenith angle north and south pointing telescopes and the University of Tasmania neutron monitor. Beneath the building is the underground vault with 11 m of granite, equivalent to a vertical absorber depth of 40 m of water equivalent (m.w.e.), above. The vault houses north and south-west pointing telescopes. Details of all the muon telescopes are summarised in Table 1 and the directional responses of the telescopes are shown in Figure 2.

The surface north pointing telescope views through approximately 40 m.w.e. of atmosphere, scanning equatorially and thus maximising the response to semi-diurnal variations characteristic of bi-directional anisotropies and diurnal variations due to uni-directional anisotropies.

The surface south point telescope takes advantage of its polar location to view mid-latitudes in the opposite hemisphere of longitude, normal to the geomagnetic field. The phase angle of response varies sensitively with the energy spectrum of the anisotropy, assisting in the differentiation between high energy galactic and lower energy solar phenomena.

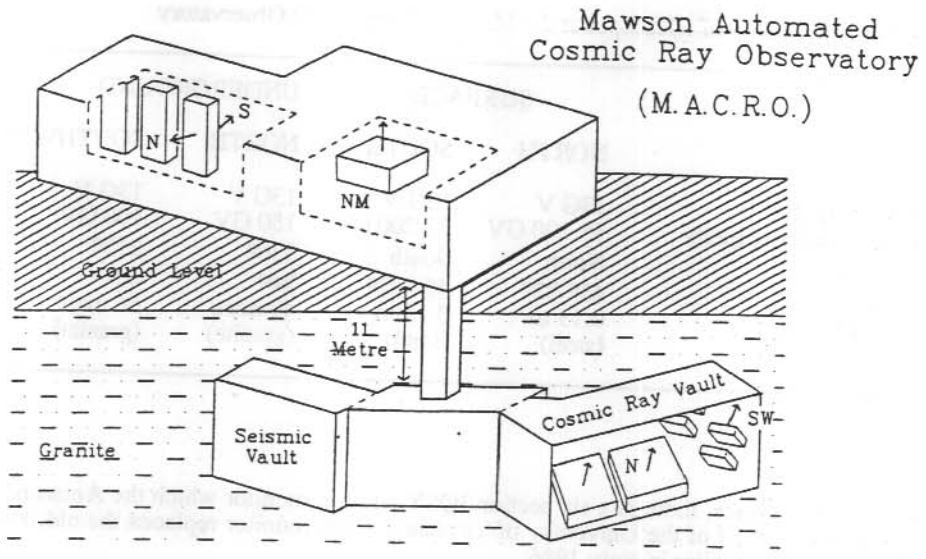

Figure 1. Schematic representation of the Mawson Automated Cosmic Ray Observatory (MACRO).

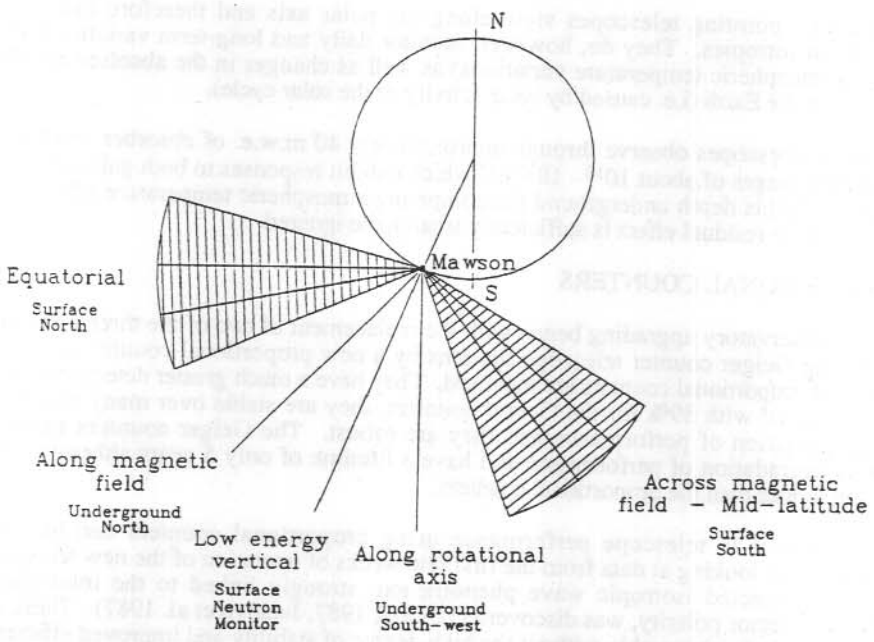

Figure 2. Viewing directions of the surface and underground muon telescopes and the neutron monitor located at the Mawson observatory.

Table 1. Summary of telescopes at the Mawson Cosmic Ray Observatory

	SURFACE		UNDERGROUND	
	NORTH	SOUTH	NORTH	SOUTHWEST
Cutoff rigidity	13G V	13G V	13G V	13G V
Effect. median rigidity	35-200 GV	35-200 GV	180 GV	190 GV
Azimuth	North	South	330°	215°
Zenith	45°-82°	45°-82°	24°	40°
Absorber	0.13 m (steel)	0.13 m (steel)	49 mwe (granite)	56 mwe (granite)

Also at the surface, there is a six section IQSY neutron monitor which the Antarctic Division operates on behalf of the University of Tasmania. This monitor replaced the old, lower count rate, IGY type monitor in early 1986.

Underground, the north pointing telescopes view along the geomagnetic field and thus have no geomagnetic phase displacements in their observed anisotropies. Furthermore, with the telescope viewing at mid-latitudes, their response to amplitudes of bi-directional anisotropies are maximised.

The south-west pointing telescopes view along the polar axis and therefore have a small response to anisotropies. They do, however, monitor daily and long-term variations of local origin (i.e. atmospheric temperature variations) as well as changes in the absolute cosmic ray flux arriving at the Earth (i.e. caused by solar activity or the solar cycle).

All the muon telescopes observe through approximately 40 m.w.e. of absorber and therefore sample energy ranges of about 10^{10} - 10^{12} eV which exhibit responses to both galactic and solar phenomena. At this depth underground the competing atmospheric temperature effects almost cancel out and the residual effect is sufficiently small to be ignored.

18.3 PROPORTIONAL COUNTERS

In 1982 the observatory upgrading began with the replacement of two of the three underground north pointing Geiger counter telescope sections by a new proportional counter system. The advantages of proportional counters are manifold. They have a much greater detection efficiency of 98% compared with 89% for the Geiger counters, they are stable over many tens of years with no degradation of performance and they are robust. The Geiger counters suffer from continuous degradation of performance and have a lifetime of only 5 years although they are smaller and lighter than the proportional counters.

The improvement in telescope performance using proportional counters can be readily appreciated when looking at data from the first few weeks of operation of the new telescope. A previously undetected isotropic wave phenomenon, strongly linked to the inter-planetary magnetic field sector polarity, was discovered (Duldig 1987, Jacklyn et al. 1987). These waves would not have been observable without the high degree of stability and improved efficiency of the proportional counters.

All of the telescopes have been upgraded.

18.4 MICRO-COMPUTER CONTROL

In mid-1982 a micro-computer system was installed for data collection. The data from all telescope sections, together with pressure, wind and time, are stored on floppy disk and in memory. Operator commands on the keyboard are employed to print any given day's data or punch it for subsequent telex transmission to Hobart. Some operator warnings of ill-conditioned data or error conditions are also produced along with check-sums for telex transmission.

With the addition of computer control and a complete replacement of the counting electronics it has been possible to convert the observatory to full automation. All electronics are now modular in design and a unit may be quickly and easily replaced should it fail. Thus it is no longer necessary for the observatory to be permanently manned. The observatory will be checked daily by the station electronics engineer, who will replace any faulty units, change printer paper and floppy discs etc. as required. Failed modules will be returned to Hobart for repair during the next summer.

Observatory repairs, maintenance and future upgrades will be carried out during the summer shipping season by Antarctic Division personnel.

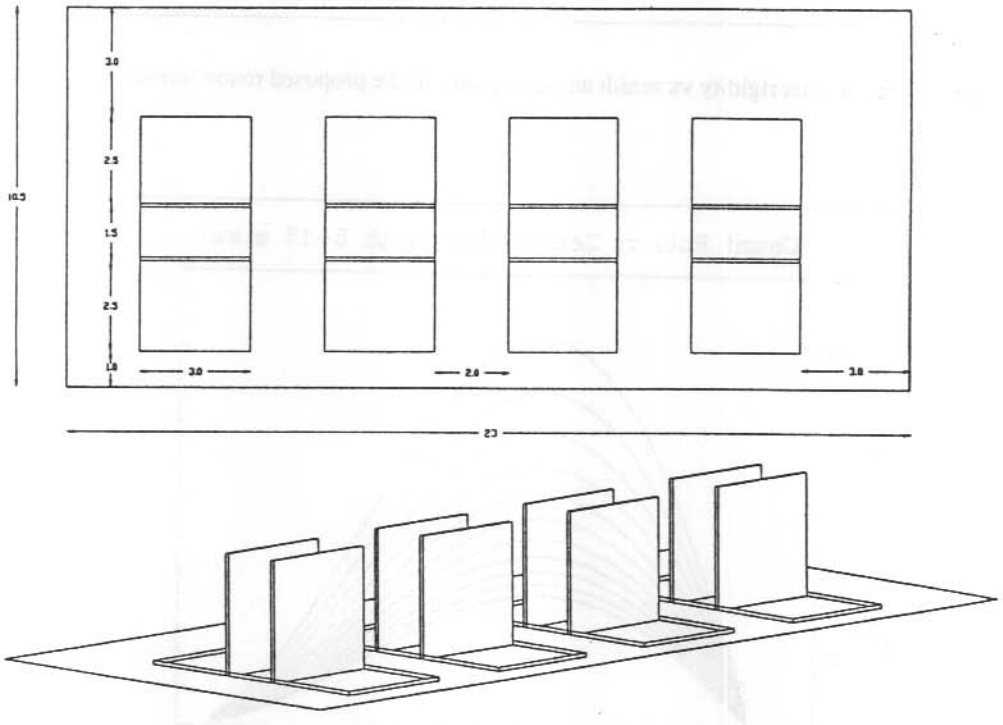

Figure 3. Proposed Four Section Muon Detection Experiment to be housed in the ice at a depth of 7 m.w.e. as part of the SPASE project.

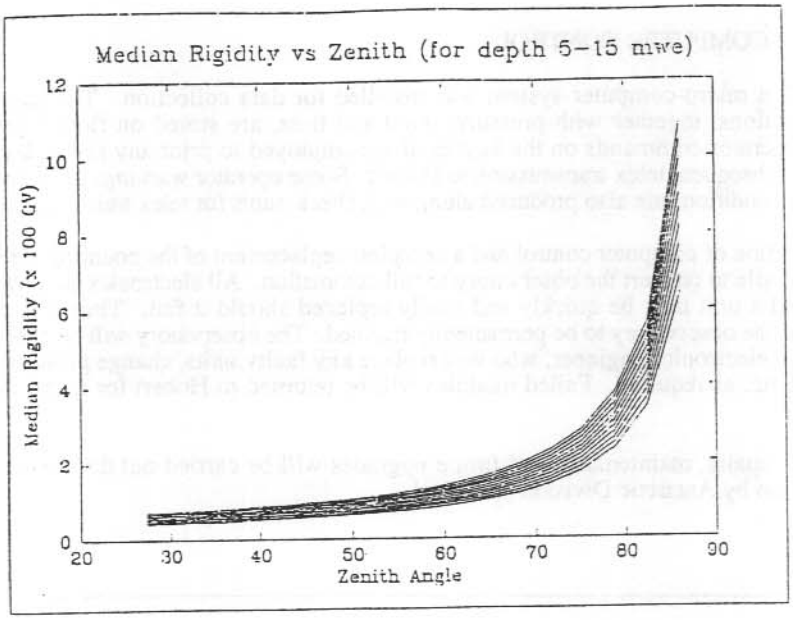

Figure 4. The median rigidity vs zenith angle response of the proposed muon telescopes.

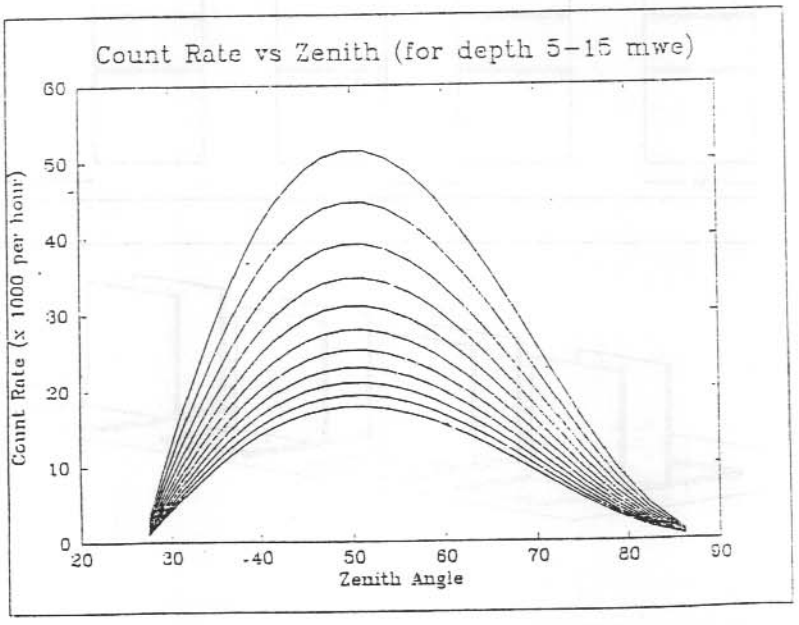

Figure 5. The count rate vs zenith angle response of the proposed muon telescopes.

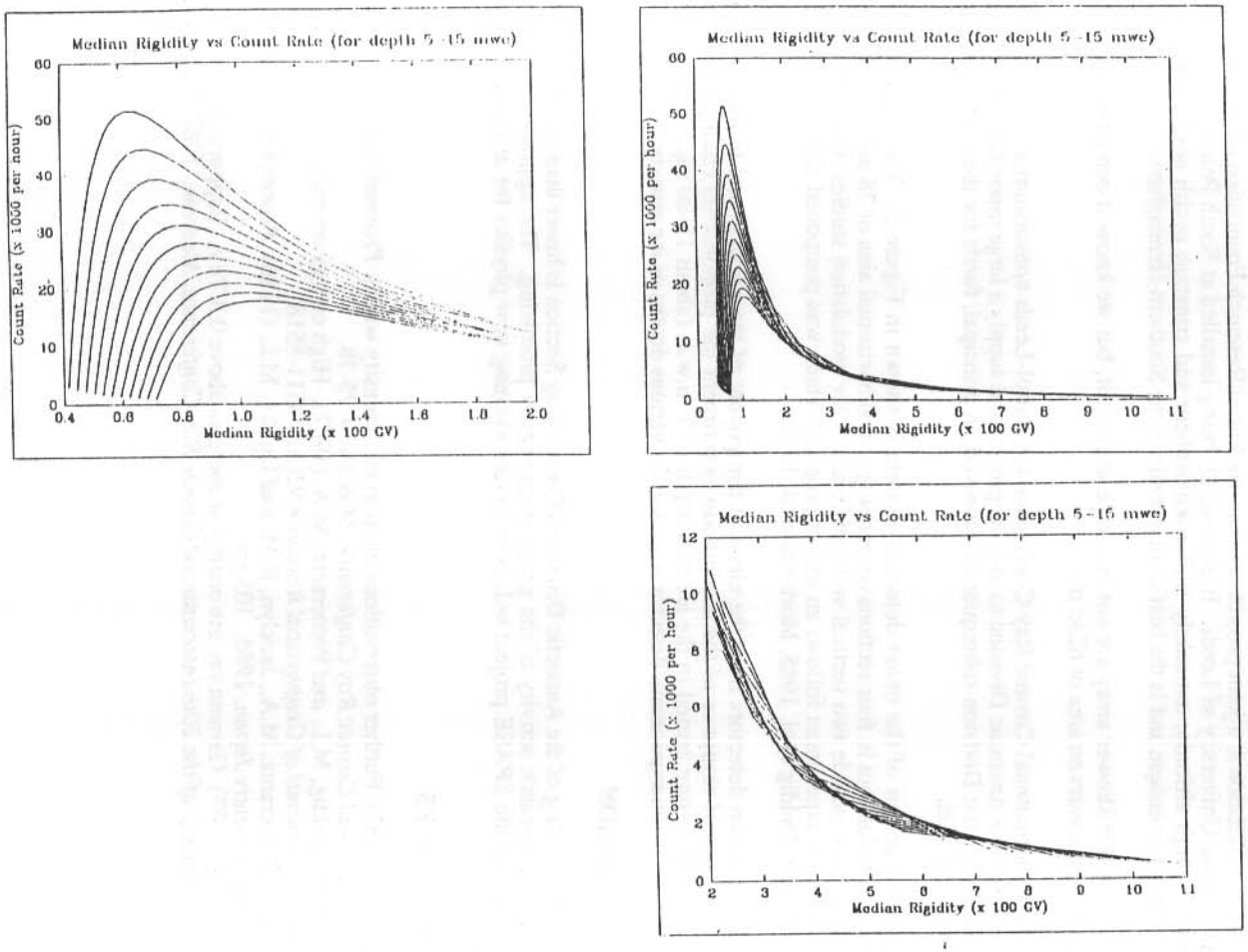

Figure 6. The count rate vs rigidity response over different ranges of rigidity of the proposed muon telescopes.

18.5 THE SOUTH POLE AIR SHOWER EXPERIMENT (SPASE)

Over the past 5 years a number of binary X-ray sources have been shown to produce ultra-high energy (UHE) gamma ray emission (Protheroe 1987). No satisfactory mechanism to explain these emissions has yet been developed due in large part to the paucity of data. The recent supernova, SN1987a, may also produce UHE gamma rays and as a result several experiments are being initiated to search for these emissions.

The SPASE installation is a joint project between the Bartol Research Foundation of the Franklin Institute and the University of Leeds. It is presently being installed at South Pole station. This site, with its high altitude, extremely stable atmosphere and constant zenith angles for each celestial source, is unique and is the best available site in the Southern Hemisphere.

Details of the Air Shower array are not available at present, but we know it comprises sixteen scintillators and covers an area of 6235 m^2.

At the 20th International Cosmic Ray Conference the Bartol-Leeds consortium approached the author to invite the Antarctic Division to join the project and supply a large muon detector for the array. The Antarctic Division subsequently approved, in principal, funds for the muon detector extension to SPASE.

The proposed design of the muon detection system is shown in Figure 3. The proportional counters will be laid out in four sections comprising a total horizontal area of 78 m^2. In addition, each section will include two vertical walls of counters for modulation studies of cosmic rays. This modulation experiment follows an earlier proposal which was postponed as a result of the SPASE project (Duldig et al. 1985, Morishita et al. 1986).

To shield the muon detectors from the electron component of the showers and to increase the median rigidities of response of the modulation experiment the proportional counters will be housed in an enclosure buried in the ice at a depth of 7 m.w.e. (about 15-20 m). Figures 4-6 show the modulation experiment detector response for various depths of ice absorber.

18.6 CONCLUSION

Although the staffing of the Antarctic Division's Cosmic Ray Section is lower than may be hoped for, the future research activity of the group is extremely promising. The upgraded Mawson observatory and the SPASE project will both ensure exciting new physics for at least another decade.

18.7 REFERENCES

Duldig, M.L. (1987). Further observations of isotropic intensity waves. *Proceedings of the 20th International Cosmic Ray Conference, Moscow. 4*:75-78.

Jacklyn, R.M., Duldig, M.L. *and* Pomerantz, M.A. (1987). High energy cosmic ray intensity waves. *Journal of Geophysical Research 92*(A8):8511-8518.

Morishita, I., Pomerantz, M.A., Jacklyn, R.M. *and* Duldig, M.L. (1986). *Proceedings of the Physics Society Japan, 1986.* 105 pp.

Protheroe, R.J. (1987). Gamma ray astronomy at energies above 0.3 TeV. Rapporteur Paper. *Proceedings of the 20th International Cosmic Ray Conference, Moscow, 1987 8*:21-44.

19. COSMIC RAY ENHANCED DIURNAL VARIATIONS - NEUTRON MONITOR AND UNDERGROUND OBSERVATIONS

J.E. Humble[1], M.L. Duldig[2], K.B. Fenton[1] and A.G. Fenton[1]

[1]Physics Department
University of Tasmania
Sandy Bay Tas 7005
Australia

[2]Antarctic Division
Kingston Tas 7050
Australia

ABSTRACT

A preliminary analysis of data from surface and underground detectors at Hobart and Mawson for the period 1982 to 1986 has been undertaken. At least nine episodes of enhanced diurnal variation are found with durations of more than 5 days. The significance of these short term enhancements is briefly discussed.

19.1 INTRODUCTION

The solar diurnal variation is generally accepted as resulting from co-rotation of the cosmic ray 'gas' with the solar field and the added effects of convection and diffusion (Somogyi 1981). Forbush (1969) noted that the solar diurnal variation showed a 22-year periodicity in its phase which was subsequently explained by employing a changing particle drift dependent on the solar field direction (Levy 1976, Kota 1985). However, the role of the upper limiting rigidity, sometimes referred to as the cut-off, is not yet clear.

There have been numerous reports of trains of enhanced diurnal variations (see for example Jacklyn and Humble 1981, Swinson 1981, Mori et al. 1975, Mishra and Agrawal 1987, Iucci et al. 1983) comprising amplitude increases of between two and five times the mean annual values.

Numerous explanations for such enhancements have been proposed including:

- fast solar wind streams (Iucci et al. 1981, Iucci et al. 1983)
- perpendicular gradients (Murayama 1981)
- N-S anisotropy enhancement (Mori 1975, Swinson 1981)
- transverse diffusion (Alania et al. 1981)

None of these models can satisfactorily explain all events and in particular the event reported by Jacklyn and Humble (1981) would appear to be unexplained by any of these mechanisms.

The present work is a preliminary analysis of data from the Hobart underground vertical and Mawson underground north muon telescopes and the Mt Wellington and Mawson neutron monitors.

19.2 OBSERVATIONS

The data analysed in this preliminary study cover the period 1982-1986. The neutron monitors are the IQSY instrument at Mt Wellington and the IGY instrument at Mawson. The underground muon detectors are the Mawson north-pointing telescopes aligned along the magnetic field (zenith angle 24°, azimuth 330°) at a mean depth of 50 hg/cm^2 and the Hobart vertical telescopes at a mean depth of 70 hg/cm^2.

Table 1. Maximum and mean amplitudes of enhanced diurnal variation for the Mt Wellington and Mawson neutron monitors and the Mawson and Hobart underground muon telescopes.

Period		Amplitude % (Max/Mean) Mt Wellington IQSY	Mawson IGY	Mawson MUON	Hobart MUON
1982	330-340	2.64/1.17	2.82/1.30	0.60/0.35	0.58/0.37
	20-30	1.59/0.54	1.10/0.48	0.35/0.22	0.47/0.28
1983	50-60	0.96/0.49	0.61/0.34	0.43/0.25	0.48/0.27
	218-228	1.12/0.60	0.96/0.61	0.36/0.26	1.35/0.43
	26-46	1.85/0.76	1.29/0.69	0.49/0.32	0.56/0.31
1984	74-84	0.98/0.70	1.37/0.78	0.40/0.29	0.48/0.29
	102-112	0.96/0.55	1.11/0.58	0.46/0.33	1.81/0.52
1985	76-86	1.08/0.76	1.18/0.65	0.37/0.24	1.18/0.61
1986	46-56	2.55/1.08	-	0.65/0.32	1.68/0.50
QUIET					
1985	335-345	0.61/0.30	0.67/0.39	0.25/0.16	0.36/0.18
POISSON ERROR		0.04/0.01	0.15/0.05	0.06/0.02	0.10/0.03

Table 2. Annual diurnal variations for the Mt Wellington and Mawson neutron monitors and the Mawson and Hobart underground muon telescopes.

Year	Amplitude % Mt Wellington IQSY	Mawson IGY	Mawson MUON	Hobart MUON
1982	0.28	0.29	0.09	0.10
1983	0.29	0.25	0.09	0.11
1984	0.36	0.31	0.11	0.15
1985	0.33	0.29	0.06	0.09
1986	0.18	0.17	0.02	0.08
POISSON ERROR	0.002	0.008	0.003	0.005

Nine periods of enhanced diurnal variations lasting more than five days are shown in Table 1 together with a quiet period. The maximum and mean amplitudes in percent for each period are shown for each telescope. The last entry gives typical poisson errors for these data. For comparison the annual diurnal responses for these telescopes are shown in Table 2.

Figures 1 to 10 show the pressure corrected data for the periods described in Table 1 for each of the telescopes. No data for the Mawson neutron monitor were available in 1986 between days 44 and 55. This was the period during which the older IGY monitor was replaced by a six section IQSY monitor. In addition to the count rate data the solar mean field direction at the Earth, derived from the Stanford inferred interplanetary magnetic field data, are also shown for all the plots up to the end of 1985 except the period 1983 days 218-238 when these data were not recorded.

19.3 DISCUSSION

As this is a preliminary investigation the enhanced variations have not yet been reduced to their free space amplitudes. Using the coupling coefficients of Yasue et al. (1982) for the neutron monitors and those of Fujimoto et al. (1984) for the underground detectors, and the technique of Jacklyn and Humble (1965), it should be possible to derive the rigidity dependence, upper limiting rigidity and free space parameters of the anisotropy for each of the periods described. It should also be possible, where the data exist, to compare these free space parameters with the interplanetary magnetic field and solar wind. Of particular interest will be the presence or absence of high speed streams in the solar wind and abnormal field intensities or structures.

Some points of interest are readily apparent without this detailed analysis. The two largest mean amplitudes observed by the neutron monitors represent an increase over the quiet period amplitude of a factor of 3 to 4. This is in contrast to the underground enhancement for the same events by a factor of about 2. The underground detectors have a median energy of response of about 170 GV whilst the neutron monitors are closer to 10 GV. As the solar diurnal anisotropy is known to have a spectral index, γ, close to zero the implication is that the upper limiting rigidity of these events must be relatively low, probably less than 100 GV. Unlike these enhancements the period 1984 days 102-112 shows an underground response enhancement of more than 2 whilst the neutron monitor response enhancement is somewhat less than 2. In such a case the upper limiting rigidity must be high and possibly the spectrum is significantly different.

It is noteworthy that all but one of the seven periods for which solar field data were available show an initial solar sector boundary crossing from the away field to the toward field during the enhancement. Without more detailed information on the solar field structure there is no obvious reason why this should be so.

The annual vectors appear to be small when compared with the quiet period results. Such a result is not unexpected because the annual result is a weighted vector sum of the yearly data and noise during the year will average out to a vector of zero magnitude leaving only a true resulting vector with a slightly larger error. Interestingly the annual vector amplitudes for the latter years are very much smaller than for the earlier years. A similar reduction in amplitude toward solar minimum was observed during the previous solar cycle by Riker and Ahluwalia (1987). This is in part due to the latter years approaching solar minimum but the sudden and quite dramatic change from 1985 to 1986 needs further investigation.

A detailed study of these enhanced variations is being conducted and the results of these analyses will be published elsewhere.

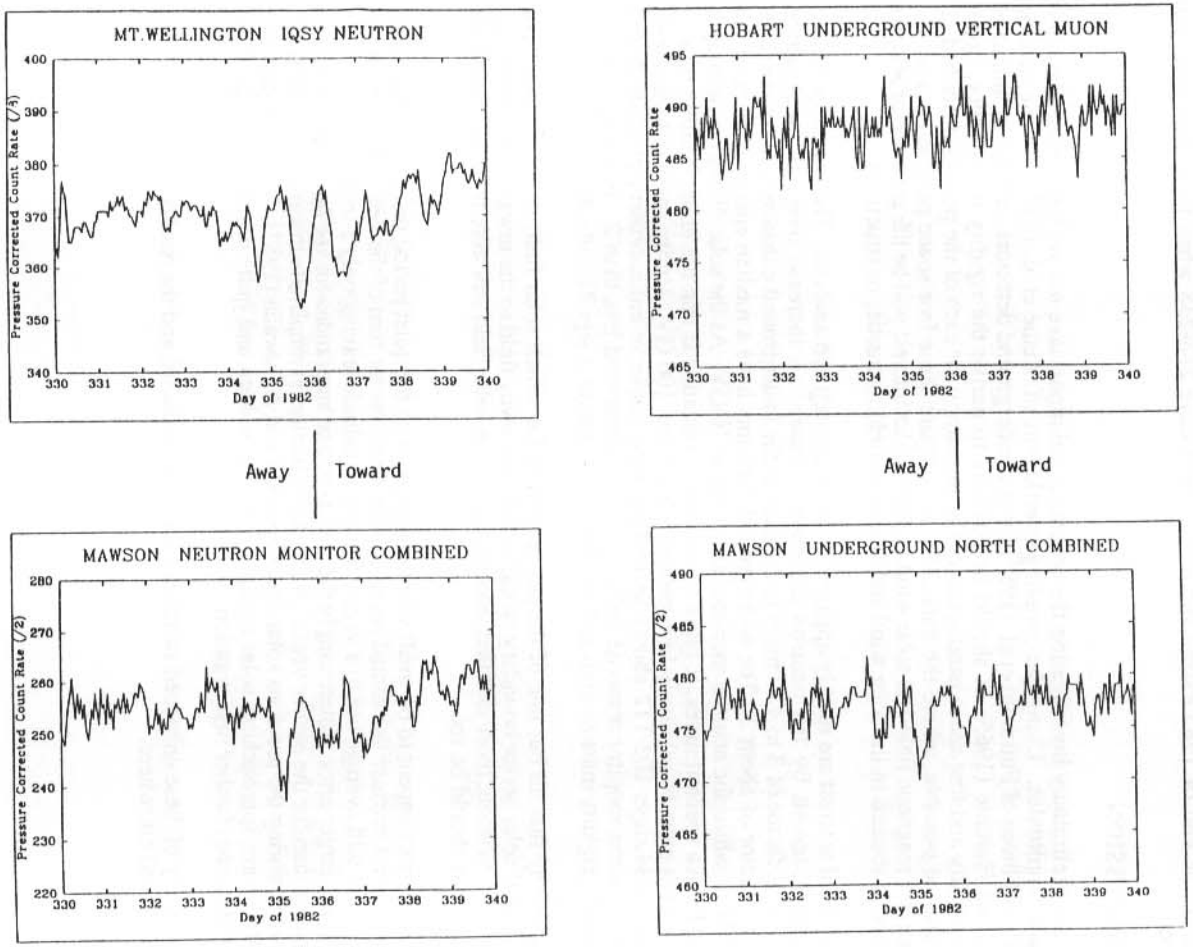

Figure 1. Pressure corrected count rates from the four telescope systems described in the text for the period 1982, days 330 to 340. The solar sector structure is also shown.

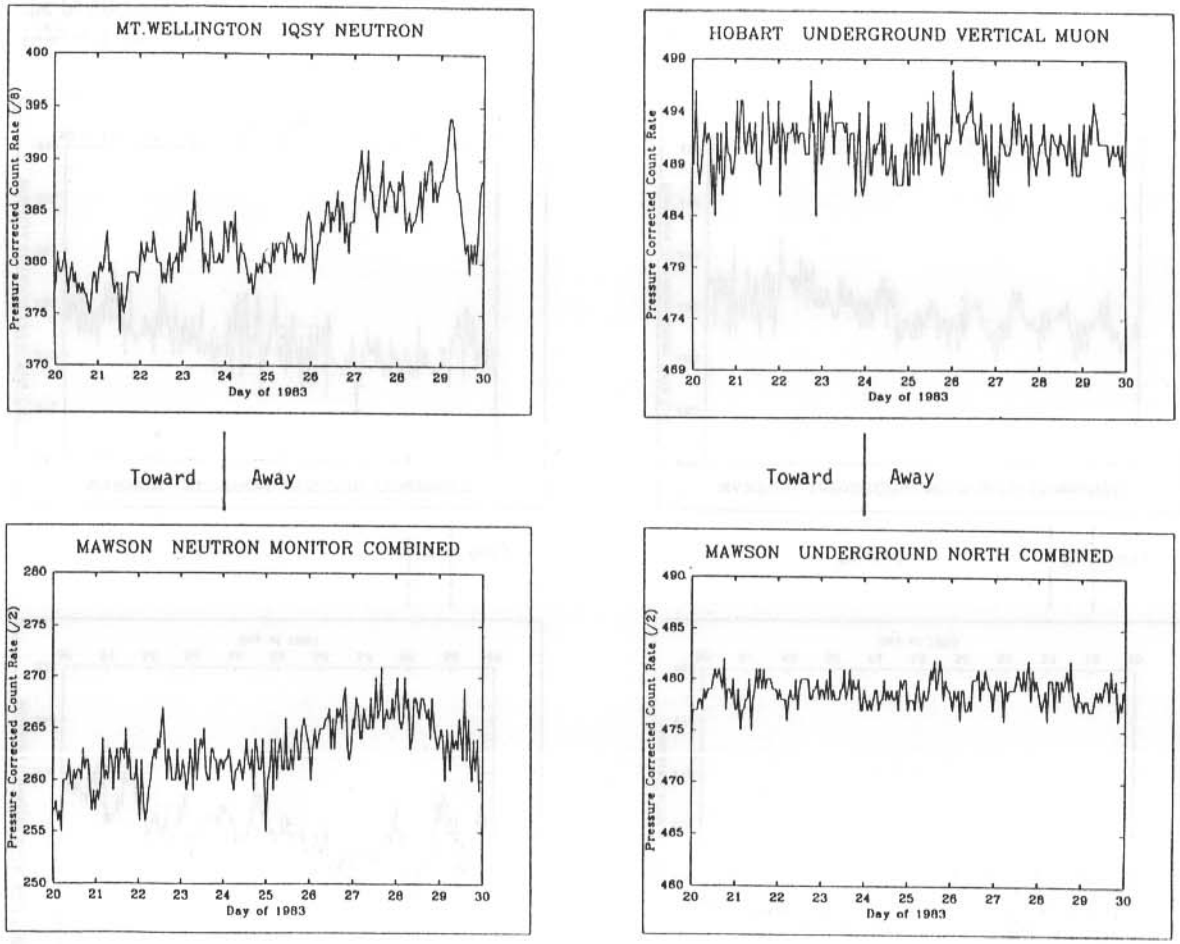

Figure 2. Pressure corrected count rates from the four telescope systems described in the text for the period 1983, days 20 to 30. The solar sector structure is also shown.

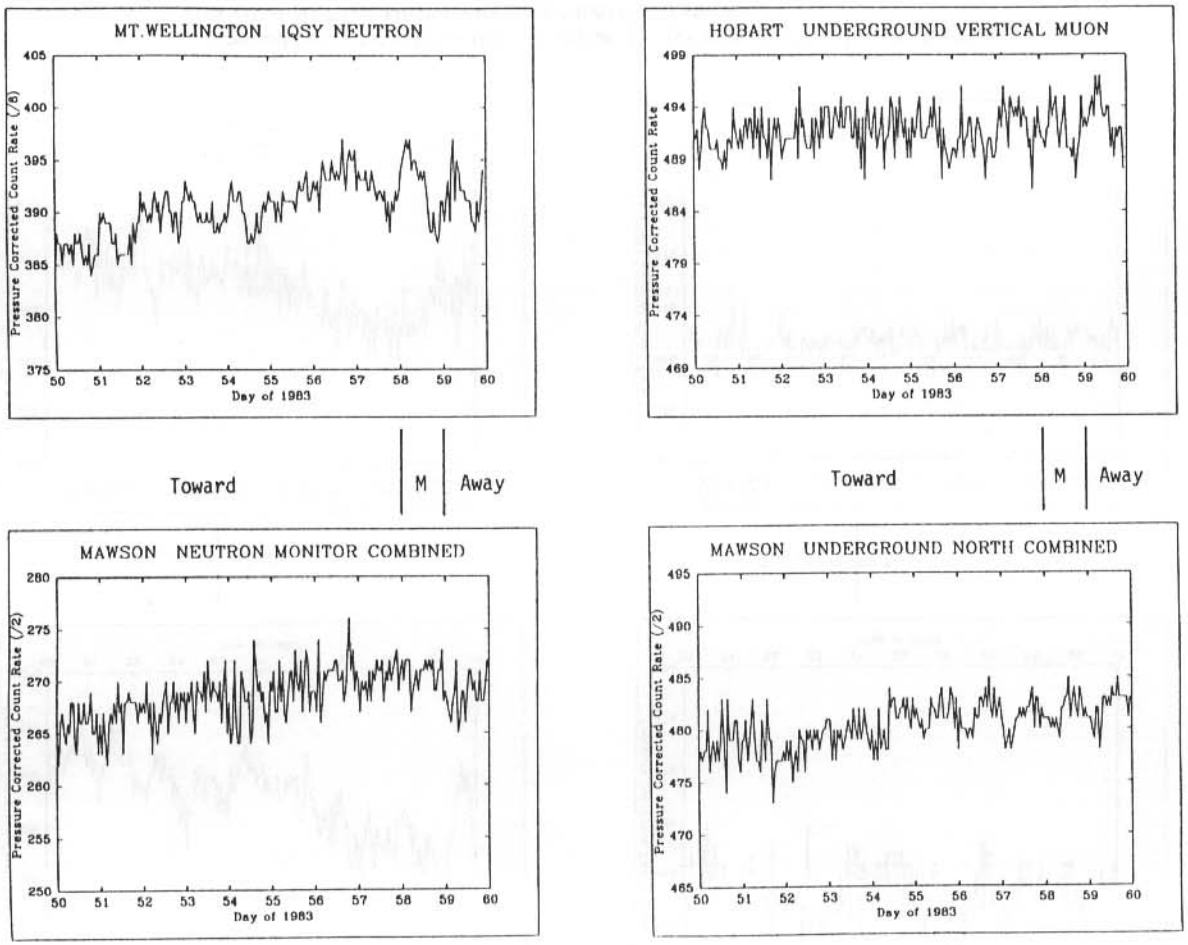

Figure 3. Pressure corrected count rates from the four telescope systems described in the text for the period 1983, days 50 to 60. The solar sector structure is also shown. (M = Mixed)

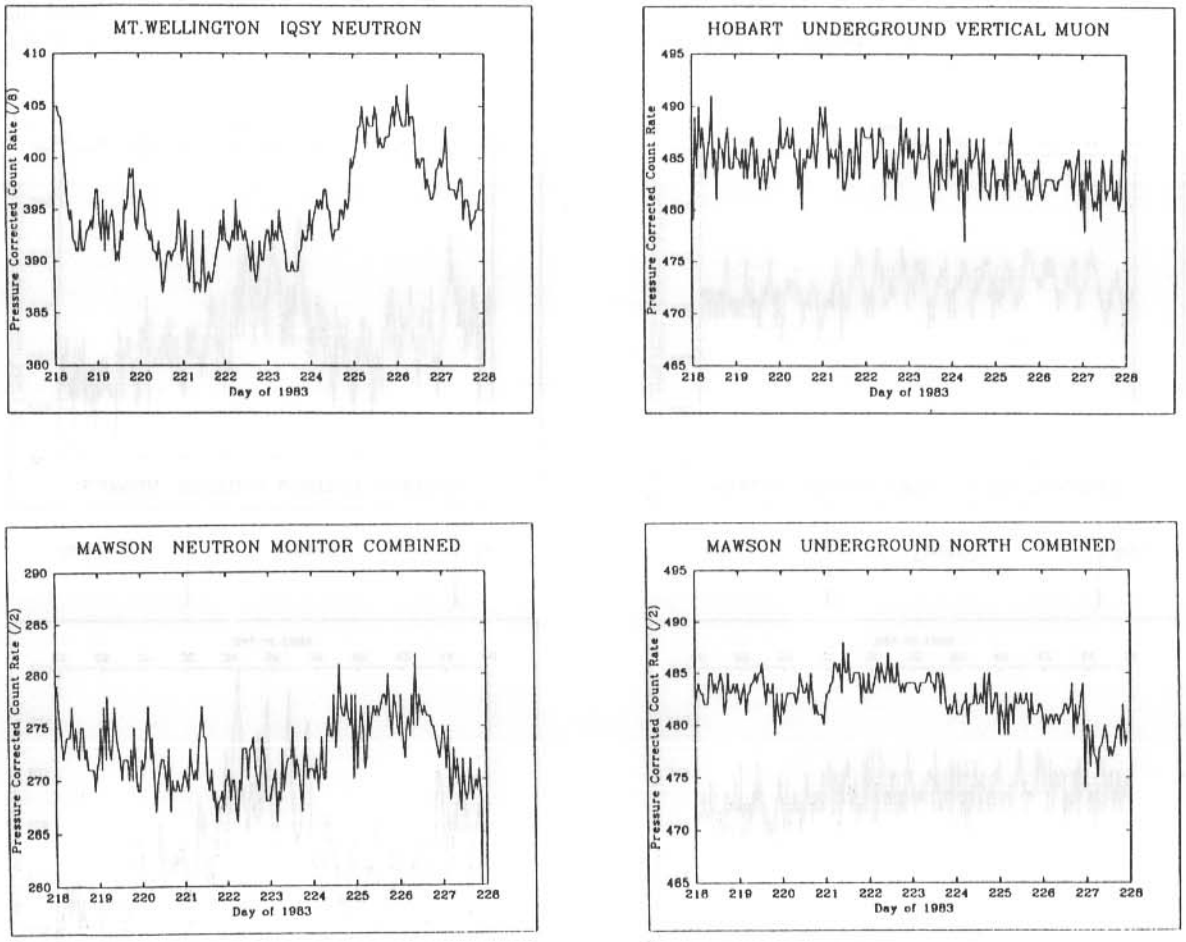

Figure 4. Pressure corrected count rates from the four telescope systems described in the text for the period 1983, days 218 to 228. No solar sector structure data are available.

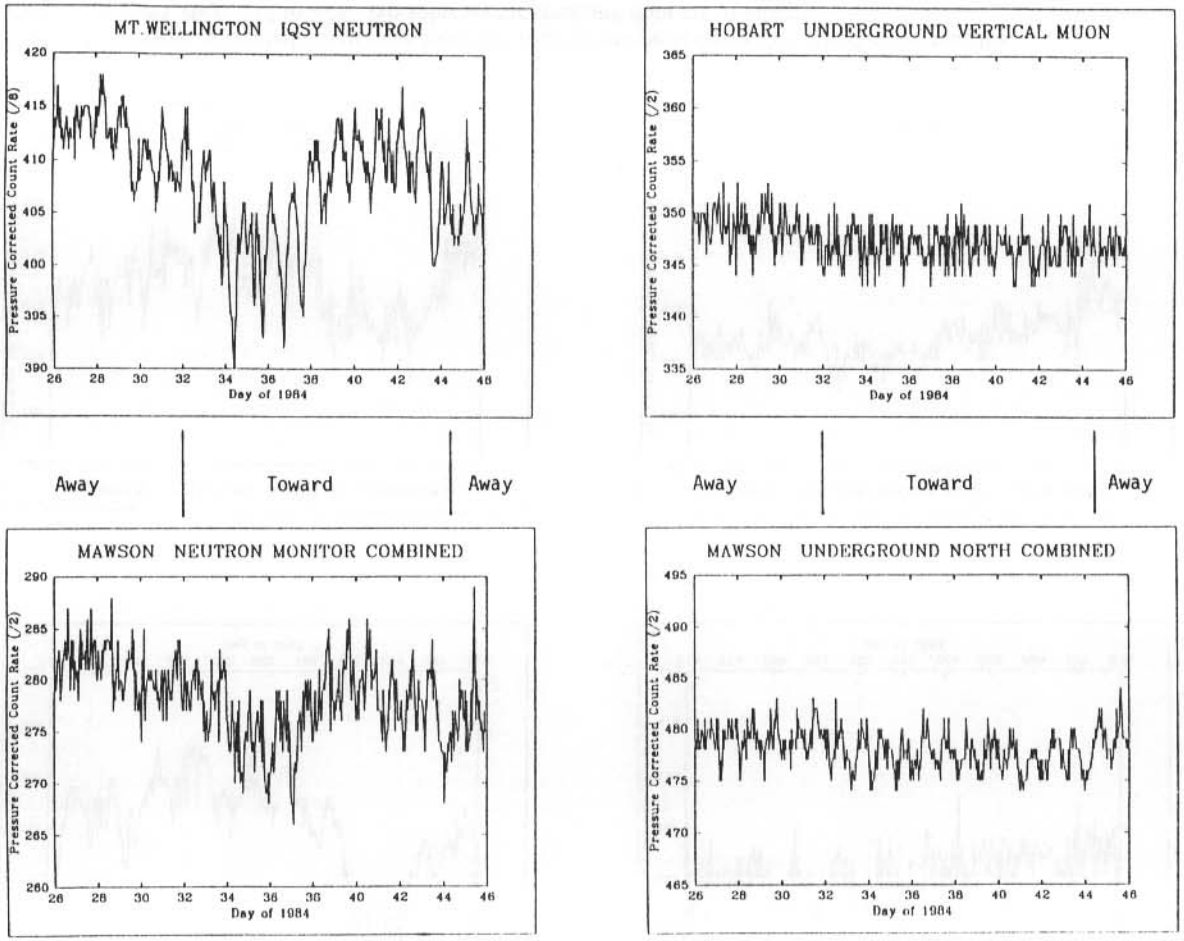

Figure 5. Pressure corrected count rates from the four telescope systems described in the text for the period 1984, days 26 to 46. The solar sector structure is also shown.

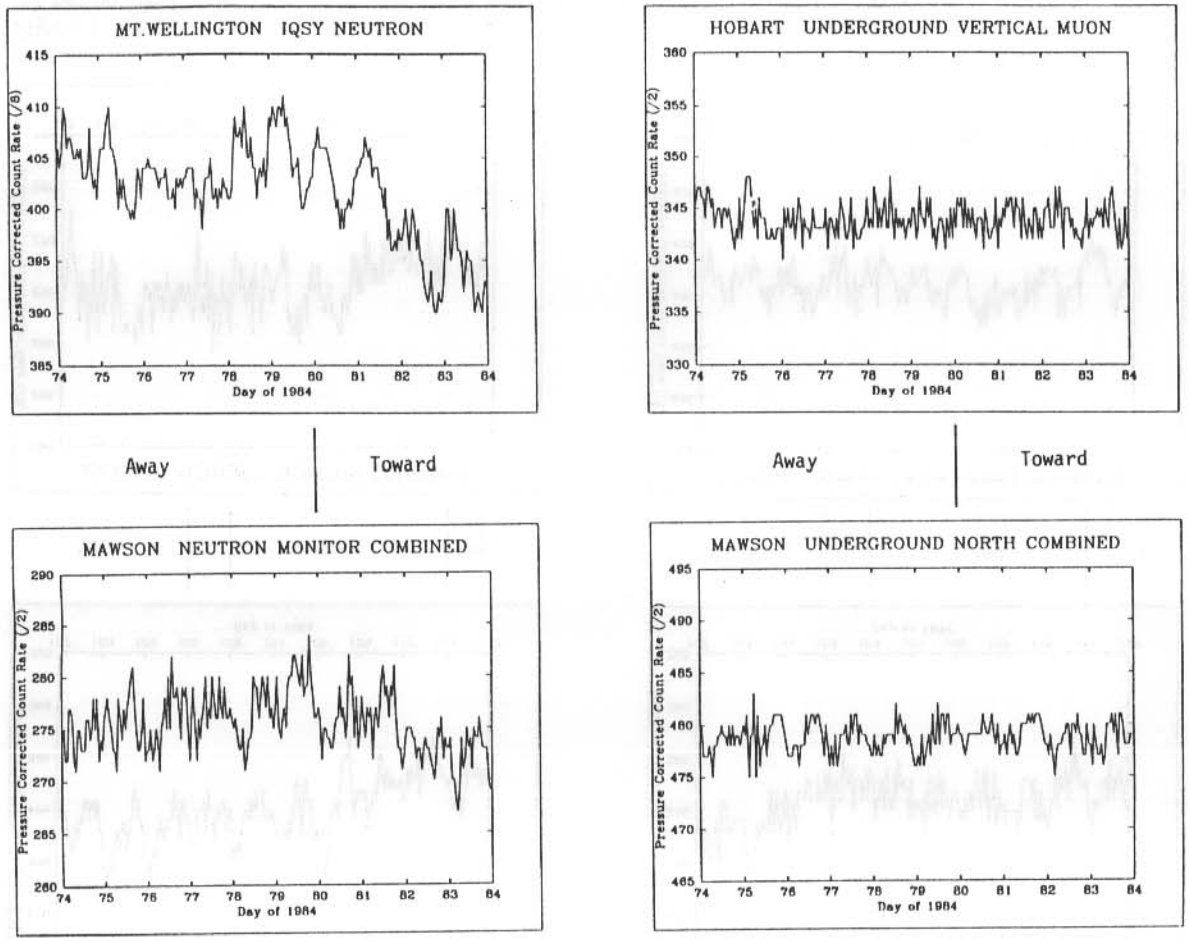

Figure 6. Pressure corrected count rates from the four telescope systems described in the text for the period 1984, days 74 to 84. The solar sector structure is also shown.

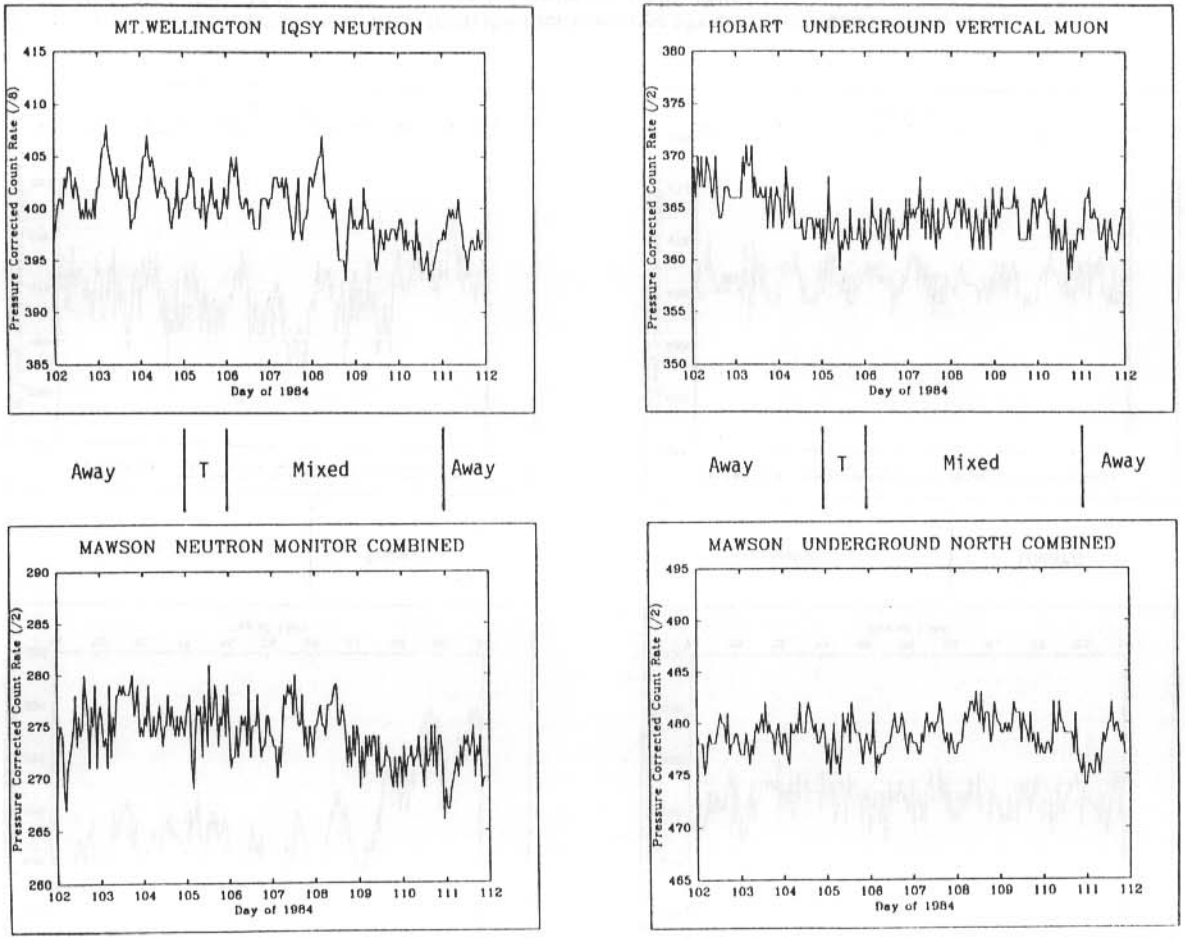

Figure 7. Pressure corrected count rates from the four telescope systems described in the text for the period 1984, days 102 to 112. The solar sector structure is also shown. (T = Toward)

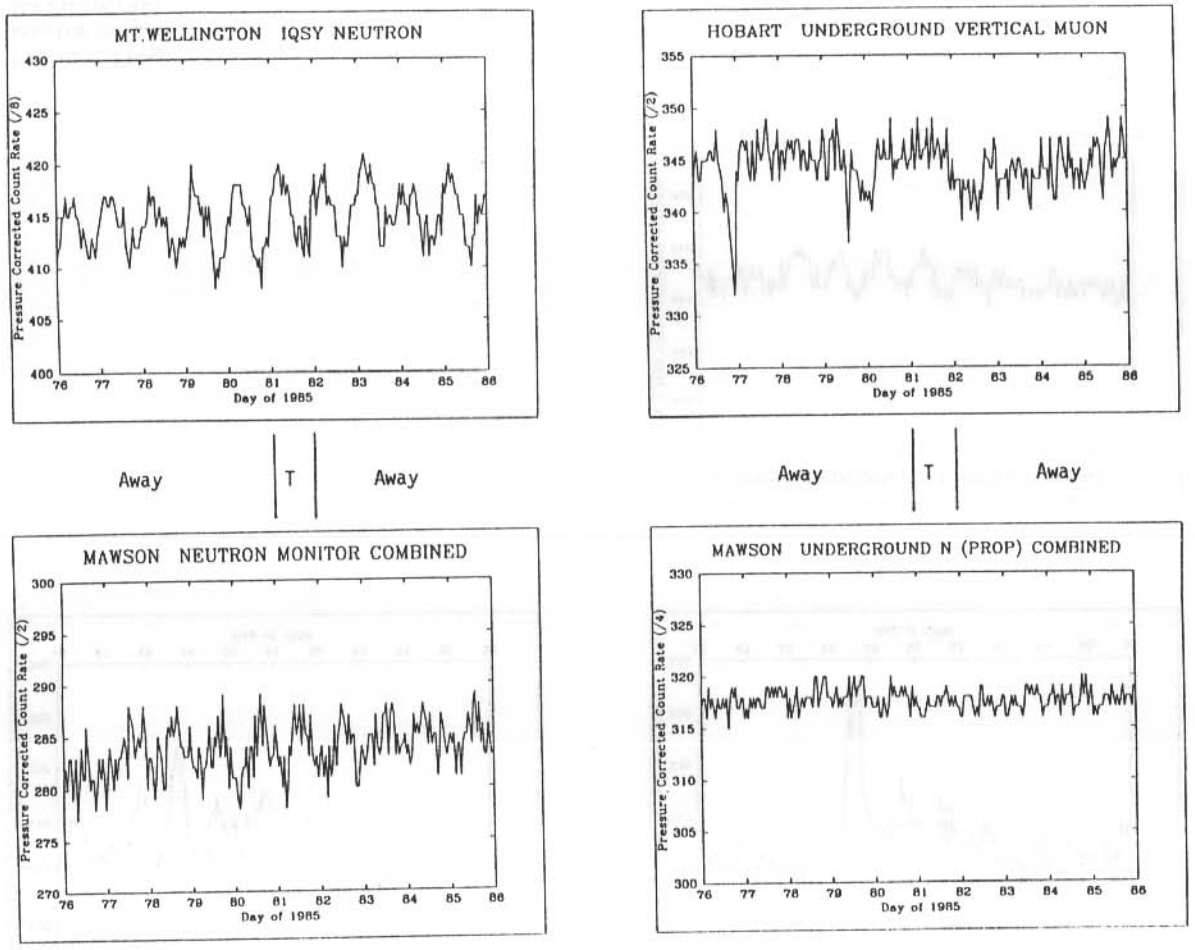

Figure 8. Pressure corrected count rates from the four telescope systems described in the text for the period 1985, days 76 to 86. The solar sector structure is also shown. (T = Toward)

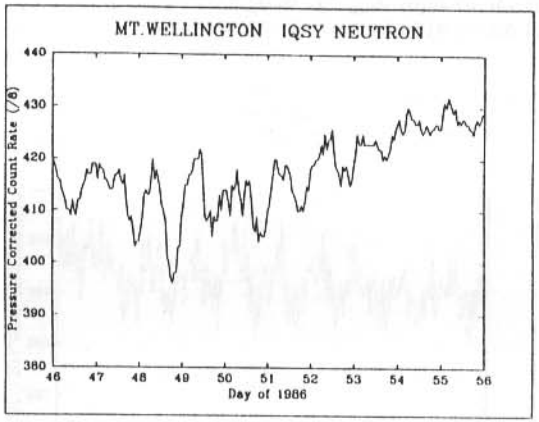

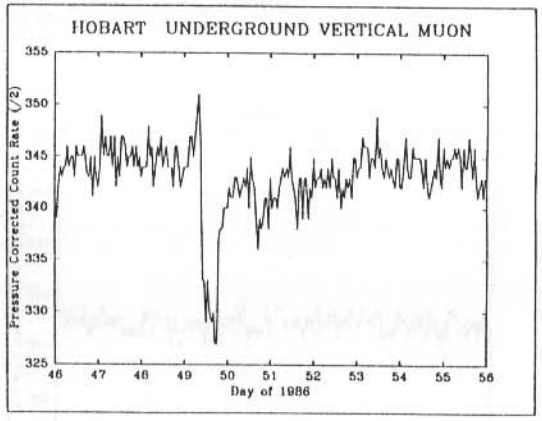

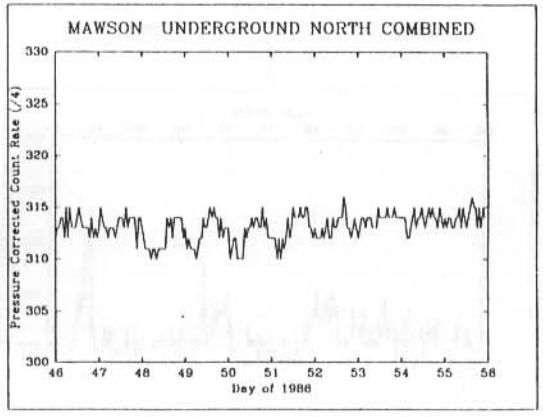

Figure 9. Pressure corrected count rates from three of the four telescope systems described in the text for the period 1986, days 46 to 56. No data are available from the Mawson neutron monitor for this period. No solar structure data were available for this period.

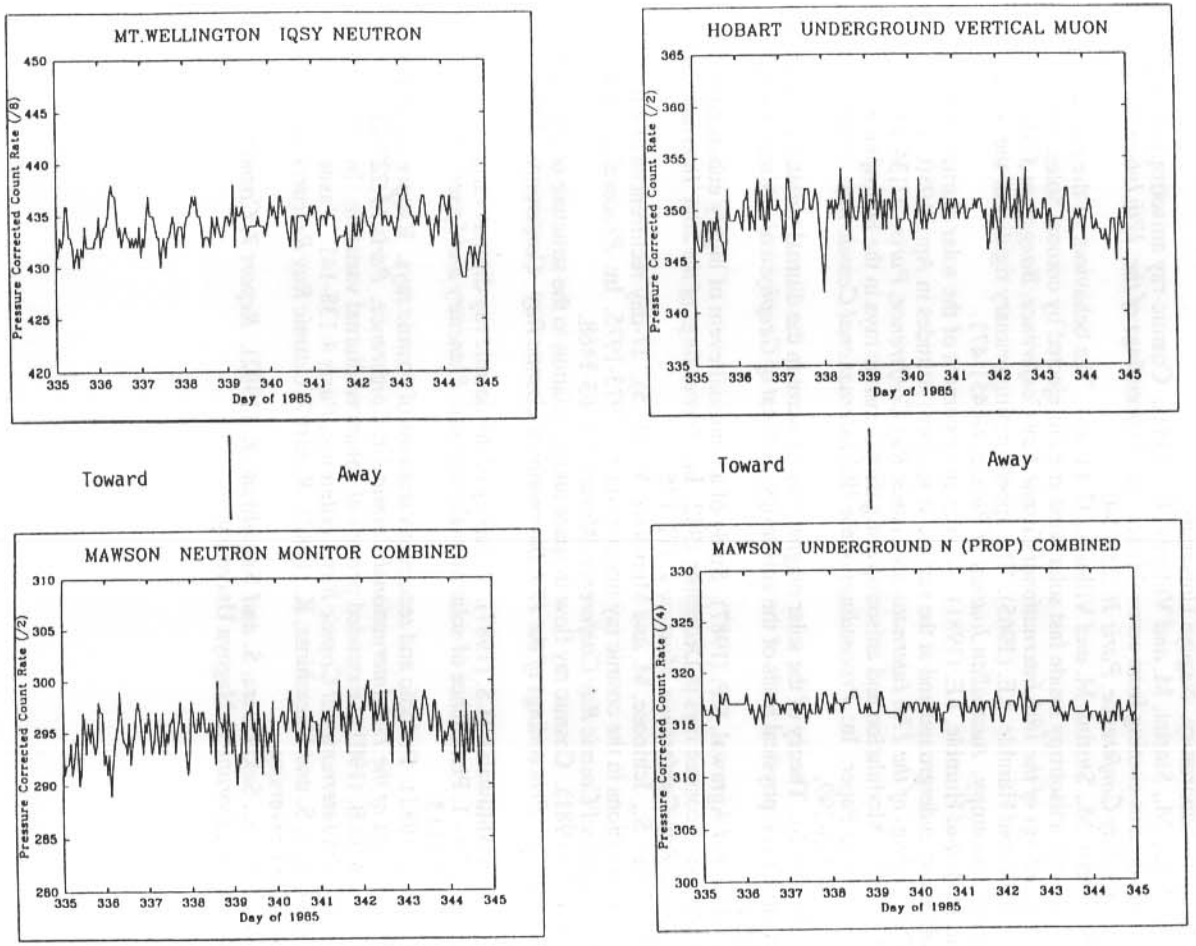

Figure 10. Pressure corrected count rates from the four telescope systems described in the text for the quiet period 1985, days 335 to 345. The solar sector structure is also shown.

19.4 REFERENCES

Alania, M.V., Aslamazashvili, R.G. *and* Djapiashvili, T.V. (1981). A new type of the quasiperiodic changes of cosmic ray anisotropy due to the particle drift in the sectors of the interplanetary magnetic field. In: *Proceedings of the 17th International Cosmic Ray Conference, Paris 4*:64-47.

Forbush, S.E. (1969). Variation with a period of two solar cycles in the cosmic-ray diurnal anisotropy and the superposed variations correlated with magnetic activity. *Journal of Geophysical Research 74*:3451-3468.

Fujimoto, K., Inoue, A., Murakami, K. *and* Nagashima, K. (1984). *Report 9, Cosmic Ray Research Laboratory*. Nagoya University.

Iucci, N., Parisi, M., Storini, M. *and* Villoresi, G. (1981). Cosmic-ray anisotropy during high–speed streams coming from coronal holes. In: *Proceedings of the 17th International Cosmic Ray Conference, Paris 10*:238-240.

Iucci, N., Parisi, M., Storini, M. *and* Villoresi, G. (1983). The behaviour of the cosmic ray equatorial anisotropy inside fast solar wind streams ejected by coronal holes. In: *Proceedings of the 18th International Cosmic Ray Conference, Bangalore 3*:354-357.

Jacklyn, R.M. *and* Humble, J.E. (1965). The upper limiting primary rigidity of the cosmic ray solar anisotropy. *Australian Journal of Physics 18*:451-471.

Jacklyn, R.M. *and* Humble, J.E. (1981). A large enhancement of the solar diurnal variation observed underground and at the surface at southern latitudes in April 1980. In: *Proceedings of the 17th International Cosmic Ray Conference, Paris. 4*:134-137.

Kota, J. (1985). Modulation and anisotropy of galactic cosmic rays in the heliosphere. Rapporteur Paper. In: *Proceedings of the 19th International Cosmic Ray Conference,* La Jolla *9*:275-299.

Levy, E.H. (1976). Theory of the solar magnetic cycle wave in the diurnal variation of energetic cosmic rays: physical basis of the anisotropy. *Journal of Geophysical Research 81*:2082-2088.

Mishra, B.L. *and* Agrawal, S.P. (1987). Study of an unusual event of highly enhanced daily variation of cosmic rays in December 1982. In: *Proceedings of the 20th International Cosmic Ray Conference, Moscow 4*:172-175.

Mori, S., Yasue, S., Ichinose, M. *and* Munakata, Y. (1975). 27-day recurrences of enhanced daily variations in the cosmic ray intensity during 1973-1975. In: *Proceedings of the 14th International Cosmic Ray Conference, Munich 4*:1463-1468.

Murayama, T. (1981). Cosmic ray flow in space and its relation to the structure of interplanetary plasma. In: *Proceedings of the 17th International Cosmic Ray Conference, Paris 4*:155-158.

Riker, J.F. *and* Ahluwalia, H.S. (1987). A survey of the cosmic ray diurnal variation during 1973-1979 - 1. Persistence of solar diurnal variation. *Planetary and Space Science 35*:1111-1115.

Somogyi, A.J. (1981). Periodic and recurrent variations of cosmic rays. Rapporteur Paper. In: *Proceedings of the 17th International Cosmic Ray Conference, Paris 13*:227-237.
Swinson, D.B. (1981). Extended periods of enhanced diurnal variation. In: *Proceedings of the 17th International Cosmic Ray* Conference, *Paris 4*:138-141. Yasue, S., Mori, S., Sakakibara, S. *and* Nagashima, K. (1982). *Report 7, Cosmic Ray Research Laboratory*. Nagoya University.

Yasue, S., Mori, S., Sakakibara, S. *and* Nagashima, K. (1982). *Report 7, Cosmic Ray Research Laboratory*. Nagoya Univerisy.

20. INSTRUMENTATION FOR THE STUDY OF THE GEOELECTRIC FIELD AT DAVIS, ANTARCTICA

R.G. McLoughlin[1], S. Malachowski[2] and G.B. Burns[1]

[1]Antarctic Division
Kingston Tas 7050
Australia

[2]Physics Department
La Trobe University
Bundoora Vic 3083

ABSTRACT

A rotating dipole sensor for the measurement of the global vertical electric field has been deployed at Davis, Antarctica. The reasons for selecting Davis for the deployment of the device and a description of the equipment layout, together with some examples of the data being collected, are presented.

20.1 INTRODUCTION

Modern studies of atmospheric electric phenomena can reasonably be said to begin with the work of Franklin and D'Alibard in the 1750s. From that time until well into the space-age in the 1970's the main thrust of atmospheric electric research was directed towards an understanding of lower atmosphere electric fields in terms of an 'electrostatic' model. Researchers concentrated on the study of thunderstorm electrification and its relationship to the global electric circuit. In particular, considerable effort was expended in an attempt to determine the value and characteristics of the global 'fair weather' electric field. This state of affairs arose from the fact that a relatively highly conducting layer exists in the atmosphere at a height of 40-60 km and it was believed that this 'equipotential' layer would act as a shield, preventing any electric fields which existed above this layer from having an effect inside this so-called electrosphere; that is, in the region between the Earth and the upper conducting layer.

A slow accumulation of evidence from a variety of ground-based, balloon-born and rocket launched experiments, supported by some of the predictions of the computer models being developed, has led to a broader, more dynamic, view of atmospheric electric phenomena. In particular, this electrodynamic view allows for the possibility of electromagnetic fields penetrating the atmosphere from the ground to the magnetosphere and varying in response to both terrestrial and extra-terrestrial influences in a complex and far from fully understood manner. Coincident with the development of this view, which results from the drawing together of some previously distinct areas of research into both terrestrial and other planetary atmospheres, was a rekindling of interest in reports supporting the idea of direct Sun-weather relationships. In examining what we know of solar upper atmosphere interactions, in an attempt to define plausible means by which these interactions may influence our weather, the focus of attention has fallen on the possible coupling of solar influenced upper atmosphere electric fields and the thunderstorm generated lower-atmosphere electric field. It is therefore important to fully investigate the nature and extent of any solar influences on the lower atmosphere electric field.

20.2 SITE SELECTION

When undertaking measurements of atmospheric electric phenomena it is important to measure as many parameters as possible so as to assist in differentiating between global and local effects, be they meteorological, anthropogenic, ionospheric or magnetospheric in origin. A considerable amount of evidence has been accumulated which indicates that oceanic or polar sites are the best

locations if one wishes to measure the global fair weather electric field. This places the observation sites as far away from thunderstorm activity as possible, bearing in mind that thunderstorms are the generators for the global lower atmosphere electric field. Oceanic and polar sites also tend to suffer less from anthropogenic sources of chemical and electromagnetic pollution which can influence the measured electric field. Obviously sites on land have an advantage over ship based sites in terms of logistic support and long term cost. Stability of the weather also has a bearing on the selection of a suitable site, since local meteorological effects tend to dominate in the measured electric field. Where one wishes to make measurements of any ionospheric or magnetospheric electric effects, a site which maximises these effects, in terms of frequency of occurrence and likely intensity, is desirable. The Australian Antarctic station Davis, which is situated on the seaward edge of the Vestfold Hills approximately 20 km from the polar cap, is almost ideal as a site from which to undertake atmospheric electric studies as it already has a sophisticated laboratory for atmospheric physics and adequate logistic support for implementation of such a program. The weather at Davis also tends to be better than that at either Mawson or Casey and with an invariant latitude of 74°36'S it is well located to observe any variation in the vertical electric field resulting from the dawn-dusk horizontal electric field generated by the solar wind/magnetosphere interaction. It is also located well away from areas of thunderstorm activity.

20.3 INSTRUMENTATION

The equipment deployed at Davis to monitor the vertical electric field consists of a rotating dipole sensor of the field mill type, similar in design to that employed by Park (1976). The motor drive and electronic pre-amplifiers are housed in an aluminium tube approximately 40 cm long by 15 cm in diameter. The shaft carrying the dipole protrudes 11 cm from the end of the tube and the whole assembly is mounted 52 cm above a 15 m by 15 m ground plane constructed of steel mesh. The ground plane is located approximately 200 m east (up wind) of the main laboratory site and sits approximately 1 m above the surrounding ground level. The ground plane serves a dual purpose; in this instance it not only provides a uniform ground reference for the electric field measurements but also should minimise interference from electrode effects common at ground level. The site itself is on a small knoll in the middle of a large, flat area of bare rock and snow. Because of problems defining electrical ground a section of steel mesh has been immersed in a saline tarn nearby and a cable run from it to the ground plane. Tests have shown that this provides a better ground reference than is otherwise obtainable.

It was originally intended that the local conductivity and air-earth current would also be measured but technical difficulties have prevented this being done at present. As part of the experiment, wind speed, wind direction, air temperature and humidity are also continuously monitored at the site. The signals from the various transducers and the field mill are fed to the main physics laboratory via a remote data acquisition system located in a controlled environment enclosure beneath the ground plane. The re.note data acquisition system is a multichannel device which digitises the incoming signals and transmits them via a twisted pair cable to the main laboratory where they are recorded at 10 second intervals using a LSI-11/02 computer. Data analysis may be carried out at Davis using one of the LSI-11/23 computers or the MICROVAX located in the physics laboratory. Further computing facilities may be accessed at the Antarctic Division headquarters at Kingston, Tasmania via a permanent satellite link. This link is also used to transmit the data to Kingston for further analysis by researchers based there and elsewhere.

In assessing the sensitivity of the field mill the problem of absolute calibration is encountered. The field mill output is dependent on the local field which is in turn related to its physical surroundings. That is, there is a compression factor associated with the immersion of the field mill in what is hopefully otherwise an undisturbed field representative of the global fair-weather field. The authors have tackled this problem from two directions. As a matter of routine, at regular intervals, a small metal box containing two floating electrodes is placed over the end of the field mill and an electric field impressed between the plates, which are by 44 cm apart. This then provides a relative calibration and performance check of the field mill. In order to relate the field mill output to the mean potential difference between the ground plane and the centre-line of the

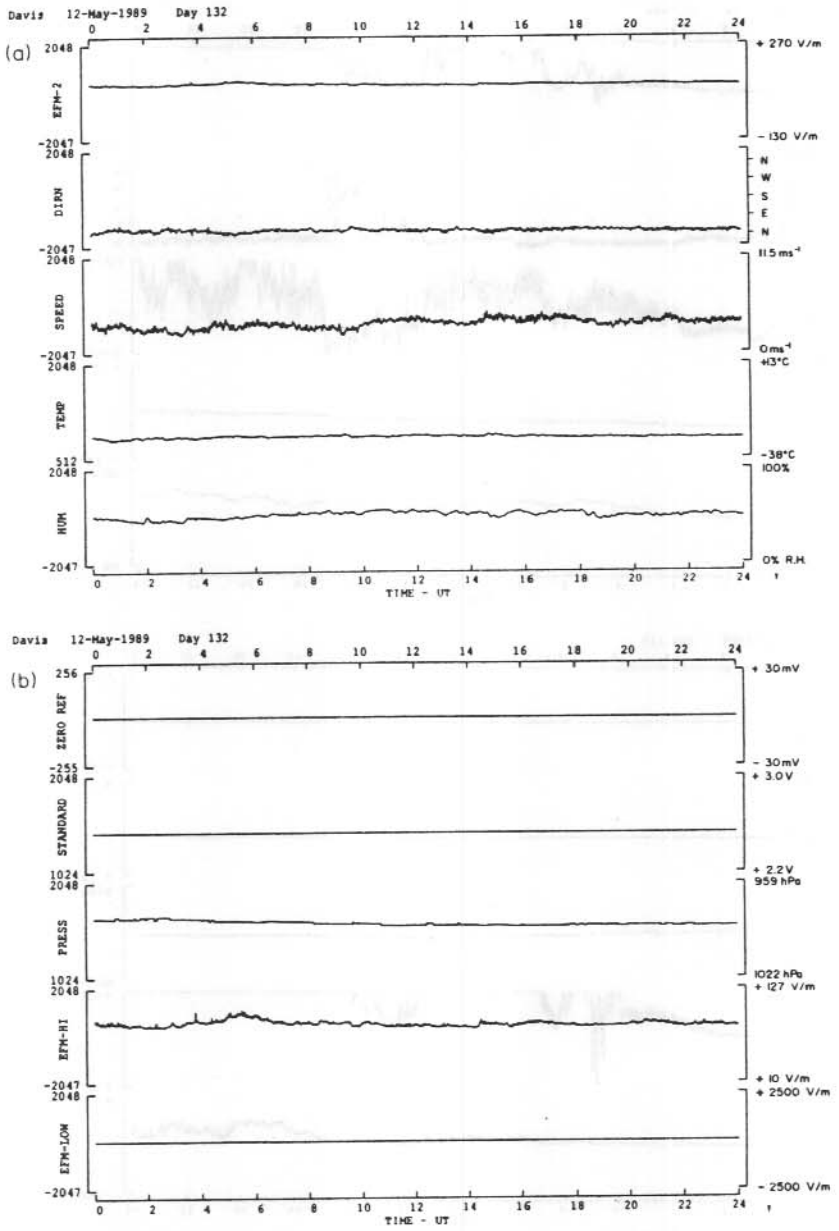

Figure 1. Field mill data acquired on a 'quiet' or fair-weather day (12 May 1989, Day 132). Parameters which are routinely monitored for the electric field study, from top to bottom are: (a) electric field mill output, wind direction, wind speed, ambient temperature and relative humidity; (b) a channel with shorted input to monitor amplifier offset changes, a channel to which a fixed reference voltage is applied to monitor temperature gain changes (if any), a channel monitoring atmospheric pressure as measured by a DIGIQUARTZ sensor and two further channels monitoring the electric field at different gains and/or offsets from the channel in (a) Preliminary calibration values for the data are on the right-hand edge.

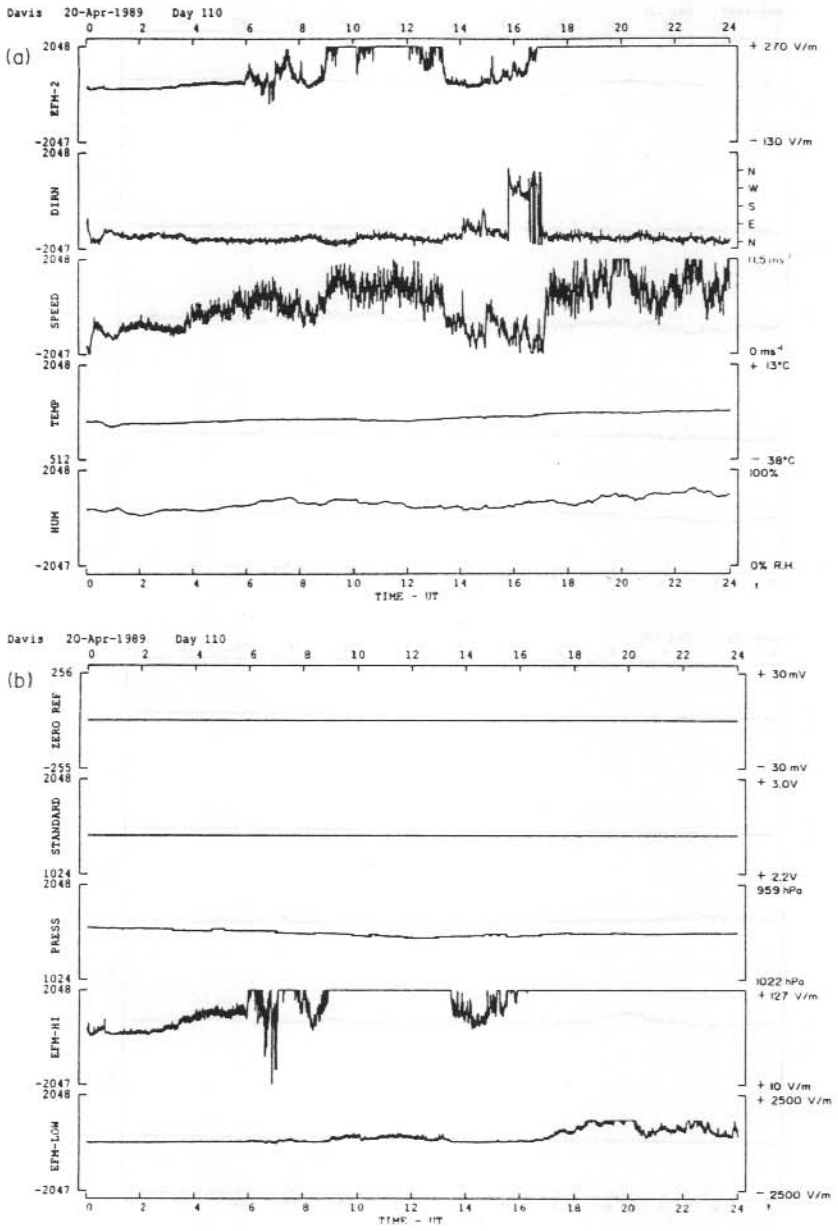

Figure 2. Field mill data acquired on a day when local meteorological generators were active (20 April 1989, Day 110). The channels are in the same order and at the same gain as in Figure 1(a) and Figure 2(b). Note the saturation evident between about 1830 UT and 2030 UT on the bottom trace of resulting from saturation at the field mill during a period of heavily blowing snow when the local field exceeded a value of approximately 1000 V/m.

field mill, a passive detector is periodically placed at the same height above the ground plane at a distance of 7 m from the field mill. At this distance it is reasonable to expect no interference between the devices.

Although a detailed analysis of the data from Davis has not yet been undertaken, the equipment has been operating there for almost 18 months without trouble (March 1988 to June 1989). Some examples of the data quality are displayed in Figures 1 and 2 which present, respectively, a 'quiet' day's data and data from a day when local meteorological generators were active, i.e. a blizzard.

20.4 REFERENCE

Park, C.G. (1976). *Geophysical Research Letters 3*:475.

21. PROJECTS OPERATED BY THE AUSTRALIAN ANTARCTIC DIVISION'S UPPER ATMOSPHERE PHYSICS SECTION AT ANARE STATIONS

R.Mc Loughlin, G.B. Burns, I.F. Grant and M. De Deuge
Antarctic Division
Kingston Tas 7050
Australia

ABSTRACT

Summaries of the projects operated in recent years by the Upper Atmosphere Physics Section at the ANARE stations Macquarie Island, Mawson, Davis and Casey are given. These experiments are often operated on behalf of, or in conjunction with, external agencies. These associations have been indicated.

21.1 INTRODUCTION

Much of the information contained here was obtained from the principal researchers of projects and was presented in poster paper format at the Bicentennial AIP Congress in Sydney. The station-by-station format leads to substantial repetition but is maintained for convenience of reference. Projects operated at the stations are continually being initiated, upgraded and withdrawn. The accuracy of the information will rapidly decrease with time.

21.2 THE MACQUARIE ISLAND OBSERVATORY

21.2.1 *Macquarie Island*

Geographic coordinates: 54°30'S, 158°57'E
Invariant coordinates: 64°28'S, 177°40'E
L value: 5.4
Local midnight: 13:24 UT
Approximate magnetic midnight: 12:15 UT (seasonal variation ± 15 minutes)
Approximate magnetic noon: 00:15 UT (seasonal variation ± 15 minutes)

Macquarie Island is located in the Southern Ocean about 1500 km south-east of Hobart, Tasmania. The island is a long narrow ridge of land some 33 km long by 3 km wide. Politically Macquarie Island is part of the Municipality of Esperance in the State of Tasmania and is a Nature Reserve administered by the Tasmanian Department of Lands, Parks and Wildlife.

The station is built on a narrow isthmus near the northern extremity of the island. The main physics laboratory is located on the southern outskirts of the station in the middle of the isthmus. Most of the physics equipment is situated further to the south. A small facility housing an ionosonde and providing temporary refuge for other experiments, is located on Wireless Hill to the north of the station.

Macquarie Island has an oceanic climate with temperatures generally just above 0°C and with little seasonal or diurnal variation. Rain, drizzle and snow are frequent with only a few days each year having no precipitation. Cloud cover at Macquarie Island makes photometric observations difficult.

Macquarie Island is located just to the north of the auroral zone. The displacement of the invariant magnetic pole towards Australia means that Macquarie Island has a relatively low geographic latitude associated with a high invariant latitude.

21.2.2 *Laboratory facilities*

The general laboratory facilities include a reasonably comprehensive range of maintenance and test equipment such as CROs, frequency counters, function generators etc. At present there are two operational computer systems; a micro PDP (LSI-11/23+) and a GRC (LSI-11/02) with data storage via RX01 and RL02 (10 MByte removable) disk systems. Data input to the computers occurs via A/D and parallel digital interface cards. A HP-7475A digital plotter is used for on-site data analysis in conjunction with one of the LSI-11/23+ systems. Accurate timing information for all experiments is provided via an Austron 8120 Time Code Generator with high stability crystal, day ID number, DC backup and external synchronisation options. This system gives timing signals with less than 10 µsec/day drift and is referenced to time signals received from WWVH. An option being investigated at present is to reference the laboratory Time Code Generator to transmissions from the Omega navigation system.

Communications between Australia's Antarctic stations and the Australian mainland have been upgraded to include direct dedicated satellite links for both voice and data transmission. This system is called ANARESAT. Transmission to and from the Pacific Ocean satellite occurs in the 5.9 to 6.4 GHz and 3.4 to 3.7 GHz bands respectively. There is currently one 4 kHz bandwidth voice channel and one 4800 BPS data channel in operation. This system allows selective transmission of digital data from Macquarie Island to Australia for instrument verification and analysis.

21.2.3 *All-sky camera*

Controlling agency: Antarctic Division

The camera used is a modified version of the 1962 model all-sky camera developed by the Dominion Physical Laboratory of the DSIR, New Zealand. The modifications provide full solid-state electronic control of the camera functions. The camera is operated to record a 25 mm diameter circular image of the night sky at one minute intervals on 35 mm format B&W negative stock. The camera is normally operated whenever the cloud cover is less than 5/8. With the Ilford HP5 film an eight second exposure time is used. The field of view of the camera extends from 0° to 88° zenith angle. A zenith-filler provides the image from 0° to 26° zenith angle. Day number and time information is recorded with each frame. The Macquarie Island all-sky camera incorporates a modified drive mechanism which will be incorporated in the other cameras as they are routinely rotated for servicing.

21.2.4 *Riometer*

Controlling agency: Antarctic Division

This is an all solid-state electronic device developed by Antarctic Division staff to monitor ionospheric cosmic noise absorption. The antenna used consists of two horizontal half-wave centre-fed aluminium dipoles spaced 0.4λ apart and 0.15λ above a wire mesh ground plane. This gives a -3 dB half-angle of 35° about the zenith. The riometer operates at a fixed frequency in the range 29.9 MHz to 30.1 MHz, the exact frequency being selected to minimise interference from local noise sources. The maximum selectable bandpass of 40 kHz is normally reduced to 20 kHz as a compromise between sensitivity and local noise rejection. A daily calibration cycle is initiated at 1630 UT, consisting of four 1.25 mA increments in the noise diode current lasting one minute each. Data are recorded continuously on chart at 6 cm/hr and digitally at 10 second intervals via a LSI-11/02 computer system.

21.2.5 *The Earth's magnetic field*

Controlling agency: Bureau of Mineral Resources

X, Y and Z magnetic field components are measured using a Photo-Electric Magnetograph. Data are collected in analogue form and digitally at one sample every minute. These data are also being digitally recorded at 10 second intervals on the Antarctic Division LSI-11/02 computer system. Absolute measurements of the H, D and F parameters are routinely taken at approximately weekly intervals. These measurements, made using a Quartz Horizontal Magnetometer and a Proton Precession Magnetometer, are used to monitor secular variations in the magnetic field and also to provide baseline calibration of the magnetic variometer records. The nominal accuracy of these measurements is 1 nT.

21.2.6 *Ionosonde - model 4B*

Controlling agency: IPS Radio and Space Services

This instrument is a largely solid-state, swept frequency, 5 kW peak-power pulsed ionosonde designed for routine vertical incidence sounding of the ionosphere using the pulse-echo technique. A complete frequency sweep from 1 MHz to 23 MHz takes 12 seconds of a 20 second program cycle. In the normal mode of operation one sounding cycle is performed every 15 minutes, synchronised to the hour. The echoes received during each cycle are displayed on a cathode ray tube along with a graticule indicating virtual height along one axis and frequency along the other. This trace is then recorded on 16 mm format B&W negative stock, Ilford HP5, together with day number and time information. Two orthogonally mounted, centre-fed, vertical delta-antennas are used; one each for transmitting and receiving the radio signals.

21.2.7 *Magnetic pulsations*

Controlling agency: joint program between Newcastle University, Antarctic Division, La Trobe University and the Institute of Physics of the Earth Moscow.

This equipment has been set up to study small scale (generally less than 5 nT peak amplitude) oscillations in the Earth's magnetic field resulting from disturbances in the magnetosphere and ionosphere. The period of these oscillations varies from seconds to minutes. At present the system is being substantially upgraded. The sensor coils used consist of 250 000 turns wound over a high-permeability mu-metal core giving a response of approximately 350 μV/nT/Hz at frequencies of less than 1 Hz. Provision has been made for automatic frequency response calibration by two methods. On a daily basis a series of low frequency signals are sent to internal calibration coils (500 turns) and once every 5 days a motor driven magnet is rotated through a range of frequencies. This method gives both a daily relative and a five-daily absolute sensor calibration. Timing signals accurate to better than 5 m sec are provided to permit propagation times to be calculated from data recorded at different locations. The data are recorded on chart at 30 cm/hr and on FM audio tape (25 Hz centre frequency) at 200 in/hr. During periods of special interest data may also be recorded digitally at up to 20 Hz using a LSI-11/02 computer system.

21.2.8 *Wide-angle photometer*

Controlling agency: Antarctic Division

This is an Antarctic Division developed instrument for monitoring the 427.8 nm (N_2^+ 1NG(0,1)) and 557.7 nm ($O(^1S\text{-}^1D)$) emissions. It is a zenith-oriented instrument with a 30^0 half-angle field of view and is used for general auroral emission observation. Data are recorded on chart at nominally 15 cm/hr and provision exists for digital data collection at up to 20 Hz via a LSI-11/02 computer system. This experiment was removed at the end of 1988.

21.2.9 *Narrow-angle photometer*

Controlling agency: Antarctic Division

A narrow angle (1° half-angle), field aligned photometer was operated at Macquarie Island during 1988 to study the dominant auroral emission feature, the O(^{1}S-^{1}D) line emission at 557.7 nm. A single optical front-end and a beam-splitter are used to compare the 557.7 nm emission with the 'instantaneous' N_2^+ 1NG(0,1) band emission from the same narrow region of the sky. This comparison enables the determination of the effective lifetime of the metastable O(^{1}S) state under auroral conditions and gives some indication of the excitation process(es) involved. These measurements will be compared with model predictions. Our understanding of the chemistry of the auroral regions is at present insufficient to explain the intensity of this, the brightest, auroral emission.

21.2.10 *Total electron concentrations by the Faraday rotation technique*

Principal investigator: Dr E.A. Essex, La Trobe University

By monitoring the plane of polarisation of a radio signal from a geostationary satellite, variations in the 'line-of-sight' electron concentration are determined. Ionospheric studies from this program consist of comparisons with URSI model ionospheres, studies of the mid-latitude ionospheric trough and the incidence and properties of medium and large-scale travelling ionospheric disturbances. A knowledge of the behaviour of the ionosphere to the south of Australia is important for satellite communications and proposed satellite search and rescue services. The monitoring of ionospheric disturbances propagating from auroral regions over Australia may lead to improved prediction services for HF communications in the Australian region. This experiment was removed from Macquarie Island at the end of 1988, for upgrading and possible redeployment at Casey.

21.2.11 *Differential phase studies using satellites*

Principal investigator: Dr E.A. Essex, La Trobe University

During 1988, a study of the near Earth plasma in the south-eastern Australia to Southern Ocean region of Macquarie Island was conducted utilising the coherent transmissions on 150 MHz and 400 MHz from the five polar orbiting Navy Navigation Satellite System satellites. This Macquarie Island study will enable the occurrence, latitude location, extent and shape of the mid-latitude ionospheric trough to be determined in this region. The ionospheric signatures of gravity waves and the occurrence of scintillation irregularities are also of interest. A commercially available JMR geodetic receiver coupled with a La Trobe University developed data acquisition system was used to conduct this project.

21.2.12 *Oblique propagation ionosphere studies*

Principal investigator: Dr E.C. Butcher, La Trobe University

Atmospheric gravity waves in the neutral atmosphere manifest themselves as travelling ionospheric disturbances (TIDs) in the ionosphere. In this experiment, conducted during 1987, the properties of TIDs generated in the auroral region were studied by observing changes in the phase path and amplitude of an obliquely propagated, double-side-band modulated CW transmission. A 30 watt transmitter on 3.399 MHz was operated remotely at Hurd Point on the southern end of Macquarie Island and received 31 km away on Wireless Hill near the station.

21.2.13 *OPALNET (VLF-OMEGA)*

Principal investigators: Prof. R.L. Dowden and Mr C.D.D. Adams, University of Otago

The Omega Phase and Amplitude Logger (OPAL) was designed and built at the University of Otago for studying small ionisation enhancements at the base of the ionosphere produced by electron precipitation. Each OPAL unit receives and logs all signals (five frequencies) from four Omega transmitters. Electron precipitation produces a slight lowering (approximately 1 km) of the top 'plate' of the Earth-ionosphere waveguide and so an advancement of the VLF phase of the Omega signals. The Macquarie Island installation is one of five units located so that the deconvoluted signals can map the electron precipitation in the southern Tasman region.

21.2.14 *Atmospheric trace gases (CO_2)*

Principal investigators: Dr G.I. Pearman, Dr. P.J. Fraser and Mr. D.J. Beardsmore, CSIRO Division of Atmospheric Research

A CO_2 infra-red gas analyser has been operated since 1979 for periods of 8 or 30 hours, three or four times a month when the wind is such that there is no contamination from station activities or local wildlife. Approximate values of CO_2 concentrations are calculated monthly; more accurate results are determined after the comparison gases are returned to CSIRO for recalibration. This program provides part of a data set from which sources and sinks of CO_2 can be determined, providing an understanding of the global carbon budget, and ultimately the impact of atmospheric CO_2 changes on global climate.

21.2.15 *CO_2 isotopes*

Principal investigator: Dr R.J. Francey, CSIRO Division of Atmospheric Research

Dry, clean air samples are collected in 5 L flasks, one or two per month. These are analysed at CSIRO, Aspendale, for CO_2 concentrations and the $^{13}C/^{12}C$ and $^{18}O/^{16}O$ isotope ratios in the CO_2. The $^{13}C/^{12}C$ data, coupled with the CO_2 concentrations distinguish between nett biospheric and oceanic exchange of CO_2. The $^{18}O/^{16}O$ ratio appears to be a potentially important new bio-geographical signal. One aim of this project is to improve our knowledge of the physical and biological processes involved in determining future levels of atmospheric CO_2. As a matter of course, CO, CH_4 and halocarbon concentrations are also determined.

21.2.16 *Atmospheric aerosols*

Principal investigator: Dr J.L. Gras, CSIRO Division of Atmospheric Research
An automated Nolan-Pollak counter and diffusion battery is operated to measure concentrations of atmospheric submicron aerosol particles in several size ranges. Many physical properties of clouds are strongly dependent on the concentration, composition and size distribution of the aerosol particles upon which they are formed. Aerosol particles also play a direct role in the global cycle of several important chemical species. The long term objective is to use this data to help define the mechanisms of production and transport of natural atmospheric particles, and refine models of particle production appropriate to the Australia-Southern Ocean region.

21.2.17 *Natural radon concentrations*

Principal investigator: Dr S. Whittlestone, Australian Nuclear Science and Technology Organization

Naturally occurring radon concentrations are measured continuously. Radon is a useful tracer of continental air and provides information on the long range transport of air masses. This experiment is operated in conjunction with the atmospheric aerosols experiment.

21.3 THE MAWSON OBSERVATORY

21.3.1 *Mawson*

Geographic coordinates: 67°36'S, 62°53'E
Invariant coordinates: 70°07'S, 19°37'E
L value: 8.6
Local midnight: 19:48 UT
Approximate magnetic midnight: 22:19 UT (seasonal variation of approximately ± 20 minutes)
Approximate magnetic noon: 10:19 UT (seasonal variation of approximately ± 20 minutes)

Mawson is the ANARE station furthest from continental Australia, lying 5200 km south-south-west of Perth. Mawson was established in February 1954 and is the longest continuously operated station south of the Antarctic Circle. The station lies on a horseshoe-shaped rock area which encloses a small deep-water harbour. The rock rises as in an amphitheatre to the edge of the continental ice sheet just 400 m inland. Mawson is one of the windiest places on Earth. A katabatic wind travelling down the ice plateau gives Mawson a yearly average wind speed of 40 km/hr. During blizzards wind gusts may exceed 260 km/hr. Mawson is generally located under the auroral oval around magnetic midnight. This, and its generally clear skies, make it an ideal site for photometric auroral observations.

21.3.2 *General laboratory facilities*

The aeronomy laboratory at Mawson is located behind the main station facilities and close to the ice plateau. The laboratory area will be almost doubled this year with the completion of an extension incorporating an electronics workspace, storage area and darkroom. Ground level air sampling is carried out in a separate clean air laboratory situated 50 m upwind from the main building.

The Mawson laboratory contains a large facility established by the Mawson Institute for Antarctic Research (MIAR), Adelaide, to investigate the dynamics of the upper atmosphere. A number of post-graduate students have assisted in the establishment, operation and maintenance of the equipment since 1981. MIAR provided computing systems include two PET Commodore personal computers and three Data General NOVA 2 systems.

The general laboratory facilities at Mawson include a reasonably comprehensive range of maintenance and test equipment such as CROs, frequency counters, function generators, etc. Two micro PDPs (LSI-11/23+) with twin RLO2 disk drives and a single HP-7475A plotter are being established this year to provide digital data collection and research facilities compatible with other stations. From the establishment of a riometer at Mawson during 1989, and by collecting magnetometer data from the Bureau of Mineral Resources operated system at the station (21.3.4), it is intended to supply 10 second digital data in the form now collected at all other stations. A direct satellite link between Mawson and mainland Australia was installed during the 1987-88 summer season. This system provides one 4 kHz bandwidth voice channels and four 4800 BPS data channels.

Accurate timing information for some experiments is provided via an Austron 8120 Time Code Generator with high stability crystal, day ID number, DC backup and external synchronisation options. The system is referenced to time signals received from WWVH. An option being investigated at present is to reference the laboratory Time Code Generator to transmissions from the Omega navigation system.

21.3.3 *All-sky camera*

Controlling agency: Antarctic Division

The camera used is a modified version of the 1962 model all-sky camera developed by the Dominion Physical Laboratory of the DSIR, New Zealand. The modifications provide full solid-state electronic control of the camera functions. The camera is operated to record on 35 mm format B&W negative stock a 25 mm diameter circular image of the night sky at 1 minute intervals. The camera is normally operated whenever the cloud cover is less than 5/8. With the Ilford HP5 film an 8 second exposure time is used. The field of view of the camera extends from 0° to 88° zenith angle. A zenith-filler provides the image from 0° to 26° zenith angle. Day number and time information is recorded with each frame.

21.3.4 *The Earth's magnetic field*

Controlling agency: Bureau of Mineral Resources

X, Y and Z magnetic field components are measured using a Photo-Electric Magnetograph. The F component is measured using a Proton Precession Magnetometer. Data are collected in analogue form and digitally at one sample every minute. These variometers are calibrated twice weekly using a Quartz Horizontal Magnetometer, a Declinometer and a second Proton Precession Magnetometer. Mawson is one of the stations which contributes data used in the evaluation of the planetary magnetic field disturbance index, K_p.

21.3.5 *Ionosonde - Model 4B*

Controlling agency: IPS Radio and Space Services

This instrument is a largely solid-state, swept frequency, 5 kW peak-power pulsed ionosonde designed for routine vertical incidence sounding of the ionosphere using the pulse-echo technique. A complete frequency sweep from 1 MHz to 23 MHz takes 12 seconds of a 20 second program cycle. In the normal mode of operation one sounding cycle is performed every 15 minutes, synchronised to the hour. The echoes received during each cycle are displayed on a cathode ray tube along with a graticule indicating virtual height along one axis and frequency along the other. This trace is then recorded on 16 mm format B&W negative stock, Ilford HP5, together with day number and time information. Two orthogonally mounted, centre-fed, vertical delta-antennas are used; one each for transmitting and receiving the radio signals.

21.3.6 *Magnetic pulsations*

Controlling agency: joint program between Newcastle University, Antarctic Division, La Trobe University and Institute of Physics of the Earth, Moscow

This equipment has been set up to study small scale (generally less than 5 nT peak amplitude) oscillations in the Earth's magnetic field resulting from disturbances in the magnetosphere. At present the system is being substantially upgraded. Provision has been made for automatic frequency response calibration by two methods. On a daily basis a series of low frequency signals are sent to internal calibration coils (500 turns) and once every five days a motor driven magnet is rotated through a range of frequencies. This method gives both a daily relative and a five-daily absolute sensor calibration. The sensor coils used consist of 250 000 turns wound over a high-permeability mu-metal core giving a response of approximately 350 μV/nT/Hz at frequencies of less than 1 Hz. Timing signals accurate to better than 5 m sec are provided to permit propagation times to be calculated from data recorded at different locations. The data are recorded on chart at 30 cm/hr and on FM audio tape (25 Hz centre frequency) at 200 in/hr. It is intended that during periods of special interest data may also be recorded digitally at up to 10 Hz using a Micro PDP 11/23+ computer system which is being installed during 1989.

21.3.7 *Fabry-Perot spectrometer*

Principal investigator: Dr F. Jacka, Mawson Institute for Antarctic Research, University of Adelaide

A large aperture, dual etalon, scanning Fabry-Perot spectrometer has been used to measure the winds and temperatures at the 95 km and 250 km levels by recording the Doppler shift and broadening of the atomic oxygen spectral lines emitted at these levels. The dual etalon nature of this instrument has enabled day-time observations of the oxygen emissions at 558 nm and 630 nm, which are superimposed on the solar Fraunhoffer absorption lines. The program has been extended to include observation of the 'twilight' atomic sodium emissions at 85 km.

21.3.8 *2 MHz partial reflection radar*

Principal investigators: Dr. R.A. Vincent, Department of Physics, University of Adelaide, and Dr F. Jacka, Mawson Institute for Antarctic Research, University of Adelaide

Winds are measured in the height range 60 km to 110 km using a spaced antenna, partial reflection radar. This makes use of pulsed 2 MHz radio waves which are partially reflected from ionisation irregularities carried with the wind. The signal is transmitted from the ground and received, after reflection, by three spaced antennas. Full correlation analysis of the three received signals enables the motion of the reflection signal strength pattern through the array to be determined. From this the winds at the reflection height may be inferred.

21.3.9 *Photometric observations of internal gravity waves*

Principal investigator: Dr F. Jacka, Mawson Institute for Antarctic Research, University of Adelaide

A three field photometer is used to monitor airglow intensity variations of the 558 nm and 630 nm lines of atomic oxygen emitted from heights of approximately 95 km and 250 km. The three regions observed are centred 5.2° off vertical and each field is 3.3° in extent. Comparison of the phases of the fluctuations in the three fields of view permits determination of the phase velocity and other characteristics of gravity waves at the optical emission heights.

21.3.10 *Atmospheric trace gases*

Principal investigators: Dr G.I. Pearman, Dr P.J. Fraser and Mr D.J. Beardsmore, CSIRO Division of Atmospheric Research

One or two half-litre gas flasks have been filled with dried air two or three times a month since 1978. These are analysed at CSIRO, Aspendale to determine the concentrations of CO_2, CH_4 and CO. An understanding of the sources, sinks and exchanges of these gases is important in assessing mankind's impact on climate. The experiment is part of an international monitoring program.

21.3.11 *CO_2 isotopes*

Principal investigator: Dr R.J. Francey, CSIRO Division of Atmospheric Research

Dry, clean air samples are collected in 5-L flasks, one or two per month from eight stations spread between 80° N and 90° S. These are analysed at CSIRO, Aspendale, for CO_2 concentrations and the $^{13}C/^{12}C$ and $^{18}O/^{16}O$ isotope rations in the CO_2. The $^{13}C/^{12}C$ data, coupled with the CO_2 concentrations distinguish between nett biospheric and oceanic exchange of CO_2. The $^{18}O/^{16}O$ ratio provides a potentially important new bio-geochemical signal. The aim is to improve knowledge of the physical and biological processes involved in determining future

levels of atmospheric CO_2. As a by-product, CO, CH_4 and halocarbon concentrations are also determined.

21.3.12 *Atmospheric aerosols*

Principal investigator: Dr J.L. Gras, CSIRO Division of Atmospheric Research

An automated Nolan-Pollak counter and a manually operated diffusion battery measure concentrations of atmospheric submicron aerosol particles in several size ranges. Many physical properties of clouds are strongly dependent on the concentration, composition and size distribution of the aerosol particles upon which they are formed. Aerosol particles also play a direct role in the global cycle of several important chemical species. The long term objective is to use these data to help define the mechanisms of production and transport of natural atmospheric particles, and refine models of particle production appropriate to the Australia-Southern Ocean region. This experiment has been operating continuously at Mawson since 1981.

21.3.13 *Environmental monitoring*

Principal investigator: Prof. J.M. Prospero, University of Miami

A high-volume aerosol sampling apparatus is operated and filters are collected each week for later analysis to determine the aerosol concentration of a number of natural and anthropogenic species. Principal measurements made are the concentrations of nitrate, sulfate (total and non-sea-salt), methane sulfonic acid (MSA), ammonium, ^{7}Be and ^{210}Pb. The overall objective is to attempt to assess the major sources and sinks of particles in the marine atmosphere and their transport, removal and geochemical cycling.

21.4 THE DAVIS OBSERVATORY

21.4.1 *Davis*

Geographic coordinates: 68°35'S, 77°58'E
Invariant coordinates: 74°29'S, 29°36'E
L value: 14.0
Local midnight: 18:48 UT
Approximate magnetic midnight: 21:25 UT (seasonal variation of approximately ± 15 minutes)
Approximate magnetic noon: 09:26 UT (seasonal variation of approximately ± 15 minutes)

Davis station is located on the seaward edge of an ice-free region known as the Vestfold Hills. The Vestfold Hills cover a roughly triangular area of about 400 km^2. Being separated from the plateau by some 20 km of low rocky hills, the weather at Davis is relatively benign by Antarctic standards. Logistic support is provided over summer by visits from ice-strengthened research and resupply vessels and on occasion by helicopters operating from the station. The station maintains self-sufficient operations from March to November/December, when sea-ice conditions prevent access to the station.

Of prime significance, from an upper atmosphere physics point of view, Davis passes under the dayside projection of the auroral oval in a region known as the magnetospheric cusp.

21.4.2 *General laboratory facilities*

The laboratory consists of a series of seacontainer modules which provide a workable but less than desirable laboratory environment. A new laboratory, which will provide facilities comparable with a well equipped mainland laboratory, has been designed and partially shipped to Davis. The general laboratory facilities include a reasonably comprehensive range of maintenance

and test equipment such as CROs, frequency counters, function generators. At present there are four operational computer systems; a micro-PDP (LSI-11/23+), a MDB (LSI-11/23+), a GRC (LSI-11/02) and a micro-VAX with data storage via RX02, RX01 and RL02 (10 MByte removable) disk systems. Data input to the computers occurs via A/D and parallel digital interface cards. A HP-7475A digital plotter is used for on-site data analysis in conjunction with one of the LSI-11/23+ systems. Accurate timing information for all experiments is provided via an Austron 8120 Time Code Generator with high stability crystal, day ID number, DC backup and external synchronisation options. This system gives timing signals with less than 10 μsec/day drift and is referenced to time signals received from WWVH. An option being investigated at present is to reference the laboratory Time Code Generator to transmissions from the Omega navigation system.

Communications between Australia's Antarctic stations and the Australian mainland have been upgraded to include direct, dedicated satellite links for both voice and data transmission. This system is called ANARESAT. The Davis ground station consists of a control room in the operations building and a 7.2 m dish inside a 12 m dome located nearby. Transmission to and from the Indian Ocean satellite occurs in the 5.9 to 6.4 GHz and 3.4 to 3.7 GHz bands respectively. There is currently one 4 kHz bandwidth voice channels and two 4800 BPS data channels in operation. This system allows selective transmission of digital data from Davis to Australia for instrument verification and analysis. In addition, the micro-VAX has recently been networked, via an ANARESAT link, to the Antarctic Division, Hobart, computer system.

21.4.3 *All-sky camera*

Controlling agency: Antarctic Division

The camera used is a modified version of the 1962 model all-sky camera developed by the Dominion Physical Laboratory of the DSIR New Zealand. The modifications provide full solid-state electronic control of the camera functions. The camera is operated to record a 25 mm diameter circular image of the night sky on 35 mm format B&W negative stock at 1 minute intervals. The camera is normally operated whenever the cloud cover is less than 5/8. With the Ilford HP5 film an 8 second exposure time is used. The field of view of the camera extends from 0° to 88° zenith angle. A zenith-filler provides the image from 0° to 26° zenith angle. Day number and time information is recorded with each frame.

21.4.4 *Riometer*

Controlling agency: Antarctic Division

This is an all solid-state electronic device developed by Antarctic Division staff to monitor ionospheric cosmic noise absorption. The antenna used consists of two horizontal half-wave centre-fed copper dipoles spaced 0.4λ apart and 0.15λ above a wire mesh ground plane. This gives a -3 dB half-angle of 35° about the zenith. The riometer operates at a fixed frequency in the range 29.9 MHz to 30.1 MHz, the exact frequency being selected to minimise interference from local noise sources. The maximum selectable bandpass of 40 kHz is normally reduced to 20 kHz as a compromise between sensitivity and local noise rejection. A daily calibration cycle is initiated at 1630 UT, consisting of four 1.25 mA increments in the noise diode current lasting 1 minute each. Data are recorded continuously on chart at 10 cm/hr and digitally at 10 second intervals via a LSI-11/02 computer system.

21.4.5 *Magnetometer*

Controlling agency: Antarctic Division

An Antarctic Division modified EDA FM100C fluxgate magnetometer is used to record large scale variations in the X,Y and Z components of the Earth's magnetic field. The modifications include provision of temperature stabilisation of the fluxgate sensors and daily calibration of the unit at 1630 UT by means of a predetermined current fed to a coil mounted in the sensor unit. Absolute calibration of the unit is obtained by reduction of the weekly magnetic absolute measurements made on behalf of the Bureau of Mineral Resources. Data are recorded on chart at 10 cm/hr at a sensitivity of approximately 2000 nT/V and digitally at 10 second intervals via a LSI-11/02 computer system.

21.4.6 *Magnetic absolutes*

Controlling agency: Bureau of Mineral Resources

Absolute measurements of the H, D and F parameters of the Earth's magnetic field are routinely taken at approximately weekly intervals for the Geomagnetism Section of the BMR. These measurements, made using a Quartz Horizontal Magnetometer and a Proton Precession Magnetometer, are used to monitor secular variations in the magnetic field and also to provide baseline calibration of the magnetic variometer records. The nominal accuracy of these measurements is 1 nT.

21.4.7 *Ionosonde - Model 4B*

Controlling agency: IPS Radio and Space Services

This instrument is a largely solid-state, swept frequency, 5 kW peak-power pulsed ionosonde designed for routine vertical incidence sounding of the ionosphere using the pulse-echo technique. A complete frequency sweep from 1 MHz to 23 MHz takes 12 seconds of a 20 second program cycle. In the normal mode of operation one sounding cycle is performed every 15 minutes, synchronised to the hour. The echoes received during each cycle are displayed on a cathode ray tube along with a graticule indicating virtual height along one axis and frequency along the other. This trace is then recorded on 16 mm format B&W negative stock, Ilford HP5, together with day number and time information. Two orthogonally mounted, centre-fed, vertical delta-antennas are used; one each for transmitting and receiving the radio signals.

21.4.8 *Magnetic pulsations*

Controlling agency: joint program between Antarctic Division, Newcastle University, La Trobe University and the Institute of Physics of the Earth, Moscow

This equipment has been set up to study small scale (generally less than 5 nT peak amplitude) oscillations in the Earth's magnetic field resulting from disturbances in the magnetosphere. At present the system is being substantially upgraded. Provision has been made for automatic frequency response calibration by two methods. On a daily basis a series of low frequency signals are sent to internal calibration coils (500 turns) and once every 5 days a motor driven magnet is rotated through a range of frequencies. This method gives both a daily relative and a five-daily absolute sensor calibration. The sensor coils used consist of 250 000 turns wound over a high-permeability mu-metal core giving a response of approximately 350 μV/nT/Hz at frequencies of less than 1 Hz. Timing signals accurate to better than 5 m sec are provided to permit propagation times to be calculated from data recorded at different locations. The data are recorded on chart at 30 cm/hr and on FM audio tape (25 Hz centre frequency) at 200 in/hr. During periods of special interest data may also be recorded digitally at up to 10 Hz using a LSI-11/02 computer system.

21.4.9 *Wide-angle photometer*

Controlling agency: Antarctic Division

This is an Antarctic Division developed instrument for monitoring the 427.8 nm (N_2^+ 1NG (0,1)) and 557.7 nm ($O(^1S-^1D)$ emissions. It is a zenith oriented instrument with a 30^σ half-angle and is used for general auroral emission observation. Data are recorded on chart at nominally 10 cm/hr and provision exists for digital data collection at up to 20 Hz via a LSI-11/23+ computer system.

21.4.10 *OH Photometer and scanning spectrometer*

Controlling agency: Antarctic Division

The aim of this project, operated at Davis during 1987, is to obtain detailed spectra of the night-time hydroxyl radical airglow, specifically the OH Meinel (8-3) band, at Davis. From a comparison of the relative intensities of the $P_1(2)$ to $P_1(5)$ lines, and assuming a thermalised atmosphere, it is possible to derive temperatures for the region of the upper atmosphere known as the mesopause. This project was first attempted at Davis in 1984 using a six-channel (OH) photometer employing various band-pass filters as the wavelength selecting elements. Unfortunately, inconsistencies in the temperature derived from different ratios indicated the possibility of spectral contamination. In 1987 a Spex Model 1269 scanning spectrometer was employed to obtain a better understanding of contaminant contributions in the region of the OH emission lines. From a preliminary analysis of the 1987 data it seems that mesopause temperatures are generally very close to 200°K. Further studies will hopefully provide information on daily and seasonal variations in the mesopause temperature and further contribute to our knowledge of neutral species dynamics in this region.

21.4.11 *Atmospheric electric field project*

Controlling agency: Antarctic Division in conjunction with La Trobe University, Melbourne

This project has been set up to study some aspects of the electrical processes occurring in our atmosphere. The principal aim is to determine whether any variation in the geoelectric field observed at ground level can be correlated with the direction of the IMF or ionospheric/magnetospheric activity. Equipment currently deployed includes; a rotating dipole induction mill for sensing the vertical electric field; and sensors for measuring relative humidity, wind speed and direction and air temperature and pressure. The signals from all sensors, which are located at a site remote from the main scientific laboratory, are fed to an Intersil REMDAC remote data acquisition system. Following digitisation and transmission along a twisted pair line to the main laboratory computer system, the data are stored on RL02 disks at 10 second intervals.

21.4.12 *Satellite scintillations*

Controlling agency: La Trobe University

During 1987 a project was operated to obtain basic propagation information at VHF (244 MHz) and L-Band (1.5 to 1.6 GHz) frequencies from satellites at relatively high southern latitudes. This information is of relevance to the proposed AUSSAT-B Land Mobile Satellite Service which is scheduled to come into operation, utilising L-Band frequencies, in the 1990s.

To study L-Band signal propagation, use was made of the standby signal received by the 1 m dish antenna provided as part of the INMARSAT communications system. The 10.5 MHz signal from a suitable testpoint on the INMARSAT receiver was down-converted to 2-3 kHz for transmission from the main radio room, via the station telephone network, to the Upper Atmosphere Physics Laboratory. The signal then passed through a buffer/level-shifter amplifier

before being logged on computer, and through high and low pass filters (>0.1 Hz, <0.017 Hz) before being logged on a twin-channel chart recorder.

To study VHF signal propagation a ten element, horizontal polarised, Yagi antenna was used to monitor the standby signal at 244.18 MHz transmitted by the Fleetsat satellite. The antenna was mounted on a 2 m mast adjacent to the laboratory and employs a masthead amplifier to boost the signal before transmission to the laboratory via co-axial cable. Again the signal was down-converted before being buffered/level-shifted and logged on chart and computer. A second antenna was set up some distance from the first to give an estimate of the velocities of the plasma 'blobs' passing through the field of view. From a preliminary analysis of the data there seems to be some evidence for scintillations originating in the F and E regions and also for lensing effects occurring in the E region.

21.4.13 *Multiple-beam imaging riometer (Rio-imager)*

Controlling agency: Dr E. Nielsen, Max Planck Institute for Aeronomy, West Germany

The Rio-imager is a German-designed riometer system utilising RF beam-forming techniques to generate four narrow-angle (16°) beams to simultaneously monitor cosmic noise absorption in four directions. Three beams are oriented along the invariant north-south meridian at angles of 39° north, 7° north and 22° south of zenith. A fourth beam is oriented along the east-west invariant parallel at an angle of 30° East of zenith. Four receivers, operating on 50.4 MHz, monitor cosmic noise absorption events. The signals are sampled at approximately 4 Hz by a dedicated computer. By measuring delays in cosmic noise absorption events recorded at adjacent receiving beams, the velocity and direction of movement of precipitating electrons can be studied.

21.5 THE CASEY OBSERVATORY

21.5.1 *Casey*

Geographic coordinates: 66°12'S, 110°21'E
Invariant coordinates: 80°38'S, 85°17'E
L Value: 37.8
Local midnight: 16:38 UT
Approximate magnetic midnight: 17:43 UT (season variation ± 10 minutes)
Approximate magnetic noon: 05:25 UT (seasonal variation ± 10 minutes)

Casey is located on the coast of the Antarctic mainland, 3750 km south of Perth. The new station is being located on a hill overlooking Newcombe Bay. The old station, consists of a line of buildings running across the wind line up the slope from the bay. The buildings are linked by a tunnel and raised off the rock to prevent the station being buried by snow. The present physics laboratory is located near the top of the building line. Plans for the relocation of the physics laboratory when the old station is closed have not been finalised. In 1989 an engineer supports an expanded program, and a wintering physicist is proposed for 1990.

Casey is generally located in the polar cap but may traverse beneath the magnetospheric cusp near magnetic midday.

21.5.2 *General laboratory facilities*

The general laboratory facilities include a reasonably comprehensive range of maintenance and test equipment such as CROs, frequency counters and function generators. Timing information is provided via an Austron 8120 Time Code Generator with a high stability crystal with day ID number and DC backup. The system gives timing signals with less than 10 µsec/day drift and, following the demise of VNG, is referenced to time signals received from WWVH. Due to the

long propagation delays from this transmitter, and conflicting broadcasts on the same frequency, an option being investigated is to reference the laboratory Time Code Generator to transmissions from the Omega navigation system.

Communications between Australia's Antarctic stations and the Australian mainland have been upgraded to include direct, dedicated satellite links for both voice and data transmission. This system is called ANARESAT. Transmission to and from the Pacific Ocean Satellite occurs in the 5.9 to 6.4 GHz bands respectively. There is currently one 4 kHz bandwidth voice channels and a 4800 BPS data channel in operation. This system allows selective transmission of digital data from Casey to Australia for instrument verification and analysis.

An LSI 11/02 and a micro PDP computer system were installed over the 1988–89 summer to provide a routine data logging facility, a Casey - ANARESAT - HO data link, a fast data logging facility (at least to 20 Hz) and an on site analysis system.

21.5.3 *Magnetometer*

Controlling agency: Antarctic Division

An Antarctic Division modified EDA FM100C fluxgate magnetometer is used to record large scale variations in the X, Y and Z components of the Earth's magnetic field. The modifications include provision of temperature stabilisation of the fluxgate sensors and daily calibration of the unit at 1630 UT by means of a predetermined current fed to a coil mounted in the sensor unit. Absolute calibration of the unit is obtained by reduction of the weekly magnetic absolute measurements made on behalf of the Bureau of Mineral Resources. Data are recorded on chart at 10 cm/hr at a sensitivity of approximately 2000 nT/V.

21.5.4 *Magnetic absolutes*

Controlling agency: Bureau of Mineral Resources

Absolute measurements of the H, D, Z and F parameters of the Earth's magnetic field are routinely taken at approximately weekly intervals for the Geomagnetism Section of the Bureau of Mineral Resources. These measurements, made using a Quartz Horizontal Magnetometer, Balanced Magnetic Zero Magnetometer and a Proton Precession Magnetometer, are used to monitor secular variations in the magnetic field and also to provide baseline calibration of the magnetic variometer records. The nominal accuracy of these measurements is 1 nT.

21.5.5 *Magnetic pulsations*

Controlling agency: joint program between Antarctic Division, Newcastle University, La Trobe University and the Institute of Physics of the Earth, Moscow

This equipment has been set up to study small scale (generally less than 5 nT peak amplitude) oscillations in the Earth's magnetic field resulting from disturbances in the magnetosphere. The system has recently been substantially upgraded. Provision has been made for automatic frequency response calibration by two methods. On a daily basis a series of low frequency signals are sent to internal calibration coils (500 turns) and once every 5 days a motor driven magnet is rotated through a range of frequencies. This method gives both a daily relative and a five-daily absolute sensor calibration. The sensor coils used consist of 250 000 turns wound over a high-permeability mu-metal core giving a response of approximately 350 μV/nT/Hz at frequencies of less than 1 Hz. The data are recorded on chart at 30 cm/hr and on FM audio tape (25 Hz centre frequency) at 200 in/hr.

21.5.6 *Ionosonde - Model 4B*

Controlling agency: IPS Radio and Space Services

During 1989 a Model 4B ionosonde was installed at Casey. This instrument is a largely solid-state, swept frequency, 5 kW peak-power pulsed ionosonde designed for routine vertical incidence sounding of the ionosphere using the pulse-echo technique. A complete frequency sweep from 1 MHz to 23 MHz takes 12 seconds of a 20 second program cycle. In the normal mode of operation one sounding cycle is performed every 15 minutes, synchronised to the hour. The echoes received during each cycle are displayed on a cathode ray tube along with a graticule indicating virtual height along one axis and frequency along the other. This trace is then recorded on 16 mm format B&W negative stock, Ilford HP5, together with day number and time information. Two orthogonally mounted, centre-fed, vertical delta-antennas are used; one each for transmitting and receiving the radio signals.

22. ROUTINE OBSERVATORY OPERATIONS BY THE AUSTRALIAN ANTARCTIC DIVISION

G.B. Burns and R. McLoughlin
Antarctic Division
Kingston Tas 7050
Australia

ABSTRACT

In recent years considerable effort has gone into upgrading, calibrating and improving the access to Antarctic Division's routine observatory experiments. The present status and future plans are briefly discussed.

22.1 TIMING SYSTEMS

An Austron 8120 Time Code Generator with high stability crystal, day ID number, DC back-up and external synchronisation options is now provided at all stations. The system gives timing signals with less than 10 nanoseconds per day drift and by reference to time signals received from WWVH an accuracy of ± 5 milliseconds is maintained. The recent demise of VNG and the difficulty inherent in using WWVH (multiple time pulses due to more than one transmitting station, along with large propagation delays to Antarctica) have meant that timing references to either the Omega navigation system or via fixed delay satellite links to the Antarctic stations are being investigated.

Over the years, each station has developed decoder units to provide initiation and timing marks as required by the experiments being operated at the stations. In an effort to standardise and to improve on these units, a prototype Time Decoder has been developed by Antarctic Division in association with Component Resources, Hobart. Units have now been deployed at all stations. The equipment has not operated totally as planned and upgrades are likely in the future. Researchers interested in conducting experiments at ANARE stations should inquire if their timing requirements can be met by these units. This can be done either by taking one of the buffered Austron outputs and providing their own electronics, or by picking off appropriate timing clicks. The present profusion of timing systems at the stations, often with their own battery back-up systems, is adding to the list of items expeditioners are required to align and repair.

22.2 COMPUTER SYSTEMS

The Antarctic Division operates LSI based computing systems for the rapid collection, checking and preliminary analysis of specific research project data and for the routine continuous collection of riometer and magnetometer data. An LSI 11/02 and a Micro PDP 23+ are operational at Casey, Davis and Macquarie Island. Two Micro PDP 23+ systems are installed at Mawson. Davis also has a Micro VAX, which has recently been networked to the Antarctic Division computer system, and an MDB 11/23+ system which will not be supported in the long term.

Each system has twin RL02 disk drives, (10 M Byte removable hard disks), a VT101 or VT220 terminal and an LA36 or LA120 lineprinter. A HP-7475A digital plotter is available at all stations. An RT 11 Version 5.4 operating system is currently used. The only 'higher level' language supported by the systems at the stations is FORTRAN IV.

Antarctic Division runs two generic types of data acquisition programs. LOGALL.FOR versions are for slow data logging, generally of riometer and magnetometer data at one sample per 10 seconds. Timing information is fed to the microcomputer via an optically isolated sixteen bit parallel interface from the Austron station clocks. Thus the program sampling times have the accuracy of the station master timing system. EARS.MAC generic programs sample at fast rates

generally in the range of 2 Hz to 20 Hz. A sampling rate and an initiate pulse are decoded from the master timing system, thus data collection is again locked to an accurate timing system. For 'EARS-type' programs however, the LSI internal clock, from which file headers are derived, drifts with the station mains. In both generic sampling programs, data can be input either via a parallel interface or via analog to digital conversion.

At all stations the Antarctic Division operates a version of TRANSFER (DEC proprietary software) for transferring computer files between stations and HO via the ANARESAT links.

Difficulties with the computer systems revolve essentially around the approximate equality of the time taken to develop versatile, accurate time, sampling systems and the obsolescence time in the computer industry.

Upgrading to FORTRAN 77 and changing to 32 bit parallel interface cards is in progress.

22.3 DIGITAL DATA ACQUISITION

Riometer (one channel) and magnetometer (four channels X, Y, Z and T) data are now collected routinely at one sample every 10 seconds at Casey, Davis and Macquarie Island. It is planned to collect similar data from Mawson by the end of the 1988-89 summer. While the data are presently being collected the system for archiving and retrieving has yet to be established.

Data are collected in a riometer (date/time plus 1 channel) and magnetometer (date/time plus four channels) file for each station and each UT day. Each record has a date and time recorded with it. The file name contains station, instrument, year and day number information. It is proposed, that each station/year/instrument will have a README.LOG file which will give details of the instrument used and carry data calibration information. The Antarctic Division does not have the resources to routinely reduce the digital data to absorption values in the case of the riometer data or to fully calibrated magnetic field data in the case of the magnetometer data but it is proposed that the README.LOG files will contain enough information to enable this to be done. As proposed, the system greatly improves the access to the riometer and magnetometer data routinely collected by the Antarctic Division.

At Casey, Davis and Macquarie Island, data are presently being transmitted to Antarctic Division, Hobart, via an ANARESAT multiplexed, 4800BPS, data channel on a nominally weekly basis.

22.4 RIOMETERS

The riometer units operated by the Antarctic Division are all solid-state electronic devices developed by I.G. Bird, B.R. Morton and H.A. Williams to monitor ionospheric cosmic noise absorption. The antenna used consists of two horizontal, half-wave, centre fed dipoles spaced 0.4λ apart and 0.15λ above a wire mesh ground plane. This gives a 3 dB half-angle of approximately 35^{o} about the zenith. The riometer operates at a fixed frequency in the range 29.9 MHz to 30.1 MHz, the exact frequency being selected to minimise interference from local noise sources. Local noise sources may be considerably reduced as the Antarctic Division moves from HF communications to a satellite communications system (ANARESAT). The maximum selectable bandpass of 40 kHz is normally reduced to 20 kHz as a compromise between sensitivity and local noise rejection. A daily calibration cycle is initiated at 1630 UT. This consists of four 1.25 mA increments in the noise diode current. Each calibration step is of 1 minute duration.

The Antarctic Division plans to deploy riometers at all stations. They are currently operated at Casey, Davis and Macquarie Island. Data will be recorded on charts at 10 cm/hr and digitally at 10 second intervals.

The digital recording of riometer data was commenced at Macquarie Island in September 1987, at Davis in March 1988 and at Casey in February 1989.

22.5 MAGNETOMETERS

Antarctic Division operates modified EDA FM 100C fluxgate magnetometers to record the large scale variations in the X, Y and Z (geographic) components of the Earth's magnetic field at Casey and Davis. The modifications include provision of temperature stabilisation for the fluxgate sensors and daily calibration of the unit. Daily calibration at 1630 UT is achieved by means of a predetermined current fed to a coil mounted in the sensor unit. Chart data collected at 10 cm/hr with a sensitivity of approximately 2000 nanotesla per volt is collected at both stations. The Casey unit is not, as yet, fully calibrated.

Information written on the charts includes provisional baseline and scaling values, sufficient information for determining the calibration levels, and the H, D, Z and F absolute values of the Earth's magnetic field at the times they were determined. Antarctic Division does not have the resources to routinely check the consistency of the data, but the information to do so is provided on the charts.

The Geomagnetism Section of the Bureau of Mineral Resources (BMR) measures the X, Y and Z components of the magnetic field at Macquarie Island and Mawson using Photo-Electronic Magnetographs.

Digital data have been collected at Macquarie Island since September 1987, at Davis since March 1988 and at Casey since February 1989. It is proposed to collect digital data from the BMR system at Mawson by the end of the 1989-90 summer.

22.6 ALL-SKY CAMERAS

The Antarctic Division operates much modified 1962 model all-sky cameras developed by the Dominion Physical Laboratory of the Department of Science and Industrial Research, New Zealand. All-sky cameras (ASCs) are currently operated at Davis, Mawson and Macquarie Island. Consideration is being given to operating an ASC at Casey in association with a proposed expanded program at that station. The modifications provide full solid-state electronic control of the camera functions. The camera is operated to record a 25 mm diameter circular image of the night sky at one minute intervals on 35 mm format film. The camera is normally operated whenever the cloud cover is less than 5/8ths. Ilford HP5 film with an 8 second exposure is used. The field of view of the camera extends from 0° to 88° zenith angle. Day number and time information is recorded with each frame.

Over the years, difficulties with timing accuracy, the drive mechanism and inadequate data labelling procedures have made the data difficult to use. The task of film developing also makes this a relatively time consuming experiment to operate.

The cameras are rotated out of service approximately once every four years for repairs, maintenance and upgrading. This had resulted in cameras which are individualistic in their electronics and temperament.

The Antarctic Division investigated the feasibility of installing a video All Sky System, to reduce the workload and improve access to the data. The limited research value in one minute ASC images did not justify the cost of developing a suitable video system and producing units for the stations. However, this decision is again under review. Imaging at the rate of at least 1 Hz is required for foreseeable research programs. Data storage and handling becomes a major problem if this type of data rate is operated on a routine basis. The Antarctic Division will attempt to develop a CCD (implying a linear relation between intensity and output) system where data can either be directly digitally collected or stored in a video format. It is proposed that this unit be operated on a specific research program basis.

To improve the mechanical reliability of the cameras, a new drive system has been developed. The direct drive between the motor and gearbox has been replaced by a toothed belt and slipping clutch which protects the motor and gearbox in the event of a jam in the film drive. This system has been installed on cameras deployed at Macquarie Island and Davis and will be incorporated in other cameras on a rotation basis. To improve timing control for the Mawson camera, the timebase for the internal clock is derived from an opto isolated 1 Hz signal from the Austron laboratory clock. The ease of access to the data has been improved by the simple expedient of measuring and including camera orientation information with each film.

The ad hoc electronic upgrading of the cameras has meant that no electronics manual exists for the present individual cameras. Poor electronics layout and the close proximity of mechanical motors have led to further difficulties with operating some cameras. A new electronic control unit for the camera is being designed by the Antarctic Division to overcome these difficulties. When this new electronics is available consideration will be given to reducing the considerable workload inherent in operating the ASCs by reducing the data collection rate from one frame per minute to one frame every 3 minutes. The cameras will continue to be operated, but perhaps at this reduced rate, at least for the next 5 years.